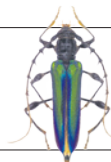


THIS WEEK

EDITORIALS

POLITICS Scottish referendum should give scientists brave hearts **p.460**

WORLD VIEW Istanbul canal scheme must be properly investigated **p.461**



SURVEILLANCE Insect traps at ports reveal early wood warning **p.462**

First response, revisited

The Ebola outbreak in West Africa has starkly exposed major gaps in plans to tackle emerging infectious diseases. Lessons must be learned.

It is encouraging that the United States last week committed 3,000 military personnel and US\$750 million to lend logistical support to civilian efforts to tackle the Ebola outbreak in West Africa. Civilian efforts also received a major, if belated, boost from United Nations intervention, with a Security Council resolution (see page 469).

Six months into the outbreak, this massive deployment of the US military and the combined resources of the UN is a damning indictment of the World Health Organization (WHO), the UN's health arm charged with tackling outbreaks of potential international concern.

The international community has debated pandemic planning and outbreak response intensely over the past decade, following the SARS (severe acute respiratory syndrome) epidemic and the increased awareness of the threat of avian flu.

In 2005, the WHO member states agreed the International Health Regulations (IHR), designed to help the international community to respond better to outbreaks. And last year, the WHO adopted an Emergency Response Framework to guide its own actions.

These frameworks have failed miserably in this outbreak, and the WHO has been slow and, so far, ineffective. There has been some progress in disease surveillance, but the world is little better prepared to quickly stamp out a threatening outbreak than it was a decade ago.

Earlier this month, WHO director-general Margaret Chan told *The New York Times*: "We are not the first responder... the government has first priority to take care of their people and provide health care. WHO is a technical agency." Fair enough, but if the WHO is not the first responder to an emergency such as this, then who is? The Ebola outbreak clearly demonstrates that response to such events cannot be left to the non-governmental organizations (NGOs) and governments of some of the poorest countries in the world.

The IHR states that countries must boost their surveillance and outbreak-response capacities, and that individual governments must foot the bill. The aspirations are correct: strengthening health-care systems everywhere will be the best defence against outbreaks of potential international concern. But the reality is that few poor countries have anything that resembles a working outbreak-response system.

Rich countries must make a greater effort to help poor countries to boost their health-care systems to defend against outbreaks, which would also contribute to the UN's Millennium Development Goals of achieving reductions in child and maternal mortality and other causes of morbidity and mortality. The case is strong for a new global health fund to help build functioning health systems, on the scale of the multibillion-dollar Global Fund to Fight AIDS, Tuberculosis and Malaria.

But building better health-care systems will take time. One immediate step should be to create an international contingency fund. A 2011 independent review of the IHR called for the creation of a pot of at least \$100 million that the WHO could immediately tap in the event of a public-health emergency. But that sensible proposal has been taken nowhere by the WHO's member states. It should be resuscitated, and its

size realistically estimated — \$100 million is probably on the low side.

Also lacking is the capacity to quickly deploy medical supplies, emergency field hospitals, and people trained in the many aspects of outbreak response — from surveillance, epidemiology and virology to implementing public-health control measures, patient care and biosafety.

Rapid emergency response to outbreaks must inevitably be done on a case-by-case basis, drawing on the resources of individual country donors, the UN and NGOs. Flexible international plans and agreements should be put in place to allow this. A large reserve corps of appropriately trained staff should also be established. Lack of personnel has been the biggest bottleneck in the Ebola response.

In principle, the WHO should be the body best placed to oversee international response to outbreaks. It has a total budget of \$4 billion for 2014 and 2015, less than many large Western hospitals, but it also spreads itself too thin by trying to do too much. The organization's budget for outbreak response is just \$110 million a year, and funding for preparedness and surveillance is just \$140 million. Moreover, funds have dwindled and the organization has lost vital in-house expertise and talent for responding to outbreaks.

If member states want the WHO to be more active in outbreak response, they must fund it adequately. But the slow and bureaucratic WHO must also demonstrate that it is up to the task, and can spend its money wisely and act fast. ■

"Strengthening health-care systems everywhere will be the best defence against outbreaks."

Staff support

German research organizations need to help their workers to defend animal research.

Last year, an animal activist code-named Pawel got a job as an animal carer at one of Germany's leading neuroscience laboratories. Pawel stayed at the Max Planck Institute for Biological Cybernetics in Tübingen for more than six months, secretly filming the monkeys that are used there to study how the brain works.

On 10 September, a seven-minute film purporting to show immense cruelty and suffering was aired on German television. The scenes of animals bleeding from surgery and apparently being manhandled into restraining chairs were hard to watch.

The impact on the institute was immediate. Staff members were threatened, and politicians were called on to shut down the research.

With increasing frequency, animal activists are infiltrating labs where

research is done with non-human primates. Four such operations have been conducted in the past 18 months alone by the media-savvy British Union for the Abolition of Vivisection in London, which has also produced an English-language film clipped from Pawel's footage.

The Max Planck Society (MPS) — the Tübingen institute's umbrella organization — was taken off guard by the furor, but it has responded well. It immediately set up an independent expert investigation into conditions for animals in the institute, and published its initial conclusions on 18 September. It said that the film gave a false impression and that the monkeys are particularly well treated at the institute — although veterinary staff are working at the limits of their capacity. The MPS declared that no new research projects will be initiated there until another vet is hired, and until a computer system to record the animals' consumption of food and drink is in place. And rather than insisting that scientists keep their heads down, as it has in the past, it sent the institute's animal-welfare officers to a television debate on 17 September.

More concerning is the fact that the MPS was taken off guard at all. The society has delayed moves by the German scientific community to create an organization to lobby appropriately for animal research and provide professional support in crises such as this one. The moves had in any case been much too slow, given Germany's ambition to become a biomedical powerhouse, which activist campaigns are undermining.

Nature has long advocated for professional animal-research lobbies to combat such campaigns with openness. To battle diseases from Ebola to Alzheimer's — which most of society wants to see conquered — researchers need to use monkeys. It is a difficult issue, and it is understandable that some people think research using non-human primates is too high a price for human health. Some animal activists distort the true facts of such work, or threaten scientists, to promote their cause. Researchers who use monkeys realize that keeping quiet about their work is ineffective. They believe that a more effective — and honest — strategy requires them to show the world what they do, and explain why.

The United Kingdom, France and the Netherlands all have national organizations that support and advocate on behalf of animal research.

The powerful US Society for Neuroscience (SfN) and its European counterpart, the Federation of European Neuroscience Societies, have specialist committees. "We all know we need to come out of the closet," says Mickey Goldberg, a neuroscientist at Columbia University in New York, who is chair of the SfN committee of animal research and has spoken in support of the Tübingen scientists.

The Max Planck Institute in Tübingen has, independently of the nervous MPS leadership, done a good job of explaining on its website why it uses monkeys, and how they are cared for. Yet

"German scientists have led the European discussion on openness about animal research, but they have not been served well by their organizations."

coverage of the recent incident suggests that journalists did not turn to it for information. They might have used an authoritative and independent professional organization — had it existed. Such a group could also have given media training to those who might be targeted by animal activists, or might need to speak up, including research leaders. The representatives who took part in the television debate did a splendid job of defending the Tübingen institute's work, but they did not seize the initiative to match the activists' skills in appealing to the emotions of their audience by explaining that animal research is needed to save lives and alleviate suffering. That is what media training can teach you.

German scientists have led the European discussion on openness about animal research, but they have not been served well by their organizations, which have stalled for time, worried and quarrelled among themselves. The Tübingen debacle must be a wake-up call for them. There are encouraging signs. Last week, the chastened Alliance of Science Organisations in Germany — whose members include the MPS as well as universities and granting agencies — agreed to present plans for an independent organization in the "foreseeable future". It should do this fast. Animal-activist groups in Europe are becoming ever more professional, well organized, coordinated and well funded. The research community needs to match them. ■

German scientists have led the European discussion on openness about animal research, but they have not been served well by their organizations, which have stalled for time, worried and quarrelled among themselves. The Tübingen debacle must be a wake-up call for them. There are encouraging signs. Last week, the chastened Alliance of Science Organisations in Germany — whose members include the MPS as well as universities and granting agencies — agreed to present plans for an independent organization in the "foreseeable future". It should do this fast. Animal-activist groups in Europe are becoming ever more professional, well organized, coordinated and well funded. The research community needs to match them. ■

Special interest

As the Scottish referendum showed, scientists' views can influence political debate.

It is natural for local and specialist media to seek a relevant position on national and international events. Taken too far, such an approach breeds satire — see the 'local man lost at sea' line, a possibly apocryphal headline from a regional newspaper's report on the sinking of the *Titanic*. But it can sometimes help to drill into general-interest topics; what is the wider world if not an ever-shifting collection of individual groups of special interests?

To some outside the British Isles (and some inside), last week's decision by the people of Scotland to remain with the United Kingdom merely saw the status quo continue. No iceberg, no shipwreck. Yet there are lessons for scientists; they just have to see them.

As is normal in independence debates, the political fight over Scotland's future was rancorous. And when the result — 55% no to independence, 45% yes — came in early on Friday morning, many scientists were among those either elated or mourning a lost opportunity.

It would be going too far to say that debates about how science would fare in an independent nation became central to the decision. But the prospects for research did provide an intriguing and relevant subplot.

Pressure groups on both sides — Academics for Yes and rivals Academics Together — received significant airtime. Heavyweights from UK learned societies were wheeled out to make the case for the union in that most British of political statements: a letter to *The Times*

newspaper. Scientific leaders were presented front and centre as part of the dialogue, and both research and academic freedom in Scottish universities were held by both sides as a prize to value and fight for. In the days leading up to the vote, Alex Salmond, leader of the Scottish government and the independence movement, was attacked over claims that he bullied the head of the University of St Andrews, Louise Richardson, because of her unfavourable (to him) views.

The media, and through them the UK public, were interested in more than just researchers' political opinions and analysis of their funding streams: scientists' daily work was also enlisted. Estimates of the size of the oil reserves in an independent Scotland became front-page news and even the subject of conspiracy theories, with allegations that the unionist UK government was concealing the true, vast scale of Scotland's potential future wealth.

The story has some way yet to run. Scotland will get extra powers to tax and spend — a sop promised to separatists in the desperate campaigning (see *Nature* <http://doi.org/vvm>; 2014). These may even end up resulting in more money for science. But the message from the politicians and the public is already clear: science is important and the views of scientists occupy a privileged place in debates. This may not surprise anyone but it is worth saying, especially at a time when researchers from Australia to Canada feel under-served by their political masters.

Lobbying for science is too important to be left to the science lobby alone, as effective as it can be. Every scientist can do more to talk up the importance of what they do. Researchers who care nothing for

Scotland and have no comprehension of the differences between the United Kingdom, Great Britain, England, Scotland, Wales and Northern Ireland should still care about this message. Your voices carry great weight: use them. ■

➔ **NATURE.COM**
To comment online,
click on Editorials at:
go.nature.com/xhunqv



Istanbul canal needs environmental study

Scientists must ensure that the ambitious plan of Turkey's president does not move forward without a thorough impact assessment, says **Derin Orhon**.

For centuries, Turkish rulers in Istanbul have realized the strategic importance of the narrow Bosphorus strait, which famously divides east and west, and have pledged to build a waterway that bypasses the channel to more efficiently connect north and south. The latest proposed version of this crazy scheme is called the Kanal Istanbul, and is the brainchild of Turkey's new president (and former prime minister) Recep Tayyip Erdoğan.

Erdoğan wants to dig an equivalent of the Suez Canal in western Istanbul. Some 400 metres wide and 25 metres deep, the artificial waterway would stretch nearly 50 kilometres to connect the Sea of Marmara with the Black Sea.

He would like to see the canal open for the 2023 centenary of the Turkish republic. Erdoğan's election last month, and his stated intention to bolster the power of the previously mostly ceremonial presidential role, will inevitably give the canal idea a political boost.

But details of the project are murky. It certainly has no legal basis, mainly because a metropolitan plan laid out for Istanbul in 2006 (and amended slightly in 2009) has no provision for it. It might be no coincidence that Erdoğan's government modified planning-related regulations in 2013 to exempt selected large projects from legally required environmental-impact assessments.

Scientists worldwide should put pressure on Turkey and Erdoğan to carry out such an assessment of the proposed Istanbul canal, and to make the results public. The project must prove itself to be environmentally sustainable before it proceeds.

The surrounding marine environment is already under severe threat of pollution. Not long ago, the shores of the Sea of Marmara were lined with quiet coves, beaches, small fishing villages and clusters of summer homes. I consider myself lucky to have spent my entire youth, in the 1950s and 1960s, in the glorious natural surroundings of Istanbul; I still enjoy remembering the magnificent beaches that extended along the coastline.

This is now nothing but history. In the past few decades, the rapid population growth and urban expansion of Istanbul has extended to the entire shoreline — as residential areas, industrial zones, energy plants and shipyards. The water body is now dangerously polluted owing to several wastewater discharges from Istanbul and other sources along the coastline.

And an unusual physical feature of the Marmara could be its downfall. It is permanently and strongly stratified into two separate layers. So, too, is the Bosphorus, which flows in two directions at once. The lower layer carries water north, from the Marmara to the Black Sea; the upper layer brings less dense water back the other way.

Istanbul is unusual among major cities in that it still discharges much of its sewage and wastewater untreated directly into the environment. In the early 1970s, on the basis of the limited scientific data available at the time, a series of master-plan studies concluded that all discharges made to the lower layer of the Bosphorus and the Marmara would be transported to the Black Sea, without significant mixing or interference with the upper layer, and consequently with no detrimental effect on the water quality of the Marmara.

Every day, more than two-thirds of the Istanbul's raw effluent is poured into the Marmara and the Bosphorus — some 1,100 tonnes of organic matter, 130 tonnes of nitrogen and 20 tonnes of phosphorus, as well as a wide spectrum of other chemicals and hazardous materials.

Contrary to the 1970s findings, much of this pollution does not get carried away to the Black Sea. Significant mixing between the two layers of the Bosphorus does occur, particularly where it meets the Marmara. From a scientific perspective, the most unsuitable location for wastewater disposal would undoubtedly be the mixing zone between the Bosphorus and the Marmara. However, two major untreated discharges, from the districts of Kadıköy and Yenikapı, and which account for around 40% of the total wastewater load in Istanbul, are directly located in this mixing zone.

In total, about 40% of Istanbul's waste does a U-turn and is dumped into the once-picturesque sea on its doorstep. Erdoğan's canal could worsen the situation. First, in opening a channel for the waters of the Black Sea to mix with the Marmara, it offers a new route for polluted water to head south. The Black Sea is already a substantial pol-

luter of the Marmara. Monitoring studies indicate more than 30 tonnes of nitrogen and 9 tonnes of phosphorus are carried south each day in the upper current of Bosphorus.

Second, there will be an indirect increase in the amount of wastewater generated in and around Istanbul, because work on a new canal will probably catalyse further development. At present, much of this extra waste will finish in the Marmara.

Erdoğan himself has called the idea of the canal "crazy and magnificent". He talks of diverting all tanker traffic through it, and the Bosphorus being restored to a river that the city can be proud of, complete with water sports.

Magnificent? We certainly cannot afford to just wait and see. Crazy? Rigorous science would not allow a proposed plan such as this to remain so. ■

Derin Orhon is emeritus professor at the Istanbul Technical University in Turkey, and a member of The Science Academy in Istanbul.
e-mail: orhon@itu.edu.tr

**ISTANBUL
STILL DISCHARGES
MUCH OF ITS
SEWAGE
UNTREATED
DIRECTLY INTO THE
ENVIRONMENT.**

➔ **NATURE.COM**
Discuss this article
online at:
go.nature.com/xcfbfb8

RESEARCH HIGHLIGHTS

Selections from the
scientific literature

STEM CELLS

Cord-blood cells made plentiful

A group of small molecules can spur the growth of stem cells from umbilical cord blood. These could one day be used as transplants to treat, for example, certain blood cancers.

Guy Sauvageau at the University of Montreal in Canada and his colleagues screened a library of small molecules for ones that stimulate the proliferation of human cord-blood stem cells that drive the long-term production of all blood cells. They found one molecule that worked particularly well and synthesized an optimized version, UM171, that performed even better. This molecule triggered the expansion of cord-blood stem cells that, when transplanted into mice, generated the full array of mature blood cells.

Cord-blood stem cells could be an alternative to bone-marrow transplants, which are currently in short supply, the authors say.

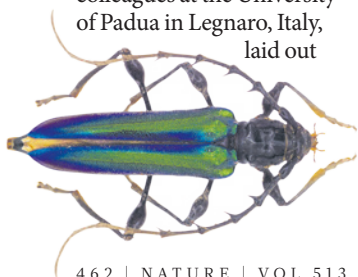
Science 345, 1509–1512 (2014)

ECOLOGY

Boring invaders held at the border

Insect traps near busy ports could provide crucial early warnings of the arrival of invasive tree-boring beetles.

These pests can damage forests and can travel around the world hidden in wood. So Davide Rassati and his colleagues at the University of Padua in Legnaro, Italy, laid out



bait to lure the beetles into traps at 15 Italian ports and in the surrounding forests. They caught 14 alien species, including *Cordylomera spinicornis* (pictured), along with native beetles from the Scolytinae, Cerambycidae and Buprestidae families, including four species never before found in Italy. The number of alien species correlated with the volume of imports at the ports.

The authors suggest that traps in busy ports could help the fight against these economically damaging invasive pests.

J. Appl. Ecol. <http://doi.org/vrj> (2014)



ZOOLOGY

Clock ticks for tiny group of fish

One of Earth's rarest fish, the Devil's Hole pupfish, is often cited as an unusual example of a small but long-lasting population of animals. But these fish may not have been isolated for as long as once thought.

Less than 100 adult pupfish (*Cyprinodon diabolis*, pictured) live in a small pool in the southwestern United States, and they have supposedly been there for 10,000 to 20,000 years. Michael Reed at Tufts University in Medford, Massachusetts, and Craig

Stockwell at North Dakota State University in Fargo analysed genetic data from *C. diabolis*, along with their numbers over time. They concluded that the fish have been living in this pool for only a few hundred to a few thousand years, and will probably become extinct within the next 400 to 3,000 years.

This means that *C. diabolis* is no exception to the rule that small, isolated populations cannot persist for long.

Proc. R. Soc. B 20141648 (2014)

VIROLOGY

Flu virus comes in various flavours

The proteins that make up the influenza viral particle differ depending on which species the virus was generated in.

The composition of a virus is important for its ability to infect and spread. Edward Hutchinson, Ervin Fodor and their colleagues at the University of Oxford, UK, used mass spectrometry to identify and quantify the proteins in seven different flu viruses derived from either mammalian tissue or chicken

eggs. The authors found a common core architecture of proteins, but some components were unique to the host.

The finding suggests that flu vaccines grown in chicken eggs or mammalian tissue could have different compositions.

Nature Commun. 5, 4816 (2014)

CANCER IMMUNOLOGY

Therapy broadens immune response

A drug that activates the immune system against a type of skin cancer does so by promoting new immune responses to cancer, rather than

STONE NATURE PHOTOGRAPHY/ALAMY

PAOLO PAOLUCCI

amplifying pre-existing ones.

The melanoma drug ipilimumab boosts the activity of immune-system cells called T cells, which recognize a variety of molecules on tumour cells, marking them for destruction. Pia Kvistborg and Ton Schumacher of the Netherlands Cancer Institute in Amsterdam and their team compared T cells from melanoma patients before and after treatment and found that the drug broadened the range of melanoma targets recognized by T cells. But melanoma-specific T cells that were already present before treatment did not expand their ranks, suggesting that the drug stimulates new responses.

Boosting the range of T cells could be a useful strategy for other cancer immunotherapies, the authors say.

Sci. Transl. Med. 6, 254ra128 (2014)

QUANTUM OPTICS

Photons made to dance together

Physicists have made two beams of light interact at the level of individual photons.

Getting photons to interact is important for all-optical computation and for producing new quantum states of light. Kristin Beck at the Massachusetts Institute of Technology in Cambridge and her colleagues crossed two beams of light inside a cavity filled with trapped and cooled caesium atoms. When photons from each beam tried to pass through the system at the same time, the trapped atoms changed their internal state, allowing only one photon to be transmitted, while the other one was reflected or scattered.

The interaction creates two entangled beams of light, which the authors say could eventually be used to improve the accuracy of measurements, such as of a gyroscope's rotation, that would otherwise be limited by the laws of quantum mechanics.

Phys. Rev. Lett. 113, 113603 (2014)

CHEMISTRY

On the trail of a drug in plants

The painkiller tramadol is not made naturally by plants despite last year's surprising finding that the drug was present in the roots of a Cameroonian plant (*Nauclea latifolia*).

Michael Spiteller from the Technical University of Dortmund in Germany and his team analysed plant, water and soil samples in Cameroon and interviewed local residents to track down the true explanation. Farmers in the far north area have been giving tramadol to their cattle, which then excrete the drug and its metabolites into soil and water. The painkiller is subsequently absorbed by plant roots.

The authors say this off-label use of tramadol poses a risk to health because it also contaminates local water supplies.

Angew. Chem. Int. Ed. <http://doi.org/f2t7tg> (2014)

GENOMICS

Mutation has big disease effect

A genetic mutation is associated with a change in a person's risk of heart disease from high to low — one of the first rare gene variants found, by sequencing large numbers of people, that has a sizable impact on disease risk.

Nicole Soranzo of the Wellcome Trust Sanger Institute in Hinxton and Nicholas Timpson of the University of Bristol, both in the United Kingdom, led a team that sequenced the genomes of 3,202 Europeans with known levels of blood triglycerides — fatty acids linked to increased risk of heart disease. They discovered that one variant of the *APOC3* gene, found in less than 0.2% of the study participants, was associated with reductions in triglyceride levels that they estimated were large enough to significantly lower an

SOCIAL SELECTION

Popular articles on social media

How to draw perfect figures

Jumbled charts and misleading graphs — illustrations in a paper can go wrong in many ways. Now, a treatise that attempts to rescue science from bad figures has been getting rave reviews on social media.

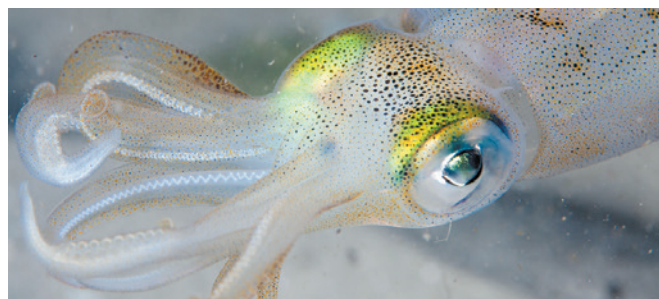
Using original illustrations — some elegant, some clunky — to prove key points, 'Ten simple rules for better figures' tries to steer researchers away from common pitfalls. The first tip: know your audience. A stripped-down graph that might make sense to your closest colleagues could prove baffling to anyone else. Many researchers on social media were grateful for the advice. Andrew Jackson, an evolutionary ecologist at Trinity College Dublin, tweeted: "Magic. Using that in lectures for sure. Incoming students take note!"

PLoS Comput. Biol. 10, e1003833 (2014)



Based on data from altmetric.com. Altmetric is supported by Macmillan Science and Education, which owns Nature Publishing Group.

➔ **NATURE.COM**
For more on popular papers:
go.nature.com/vmht2t



individual's risk level.

The results support the idea that sequencing large populations can uncover rare genetic mutations that have a major impact on disease risk.

Nature Commun. 5, 4871 (2014)

MATERIALS

Squid skin inspires colourful display

A flexible material can display patterns much in the same way that cuttlefish, octopuses and squid (**pictured**) form colourful spots in their skin.

To quickly change their appearance and camouflage themselves, such cephalopods use their muscles to stretch and relax small sacs of pigment under their skin. A team led by Xuanhe

Zhao of the Massachusetts Institute of Technology in Cambridge developed an artificial equivalent using silicone rubber and organic compounds called spiropyran mechanophores, which glow when exposed to force. The researchers control the display by applying an electric field to deform the silicone, causing the mechanophores to glow in various repeated patterns including lines, circles and letters.

The display size and resolution could be scaled up for use as a camouflaging coating, the authors say.

Nature Commun. 5, 4899 (2014)

➔ **NATURE.COM**
For the latest research published by Nature visit:
www.nature.com/latestresearch

SEVEN DAYS

The news in brief

POLICY

Scotland stays

On 18 September, voters in Scotland decided by a majority of 55% to remain part of the United Kingdom. Many scientists cheered the result, saying it would give Scotland continued access to its current levels of research funding from UK-wide sources. See *Nature* <http://doi.org/vt2> (2014) and page 460 for more.

Ebola threat

The Ebola virus strain spreading throughout West Africa could be deadlier than thought, with a death rate of about 70% instead of 50%, epidemiologists report (WHO Ebola Response Team *N. Engl. J. Med.* <http://doi.org/vvw>; 2014). Patients treated in hospital seem to have the best chance of surviving, the authors say. Meanwhile, the United States and the United Nations have pledged to ramp up their response to the crisis. See page 469 and go.nature.com/qak4pe for more.

Antibiotics push

The US government released a national strategy on 18 September to combat antibiotic-resistant bacteria. The plan includes improved methods for diagnosing and tracking antibiotic-resistant infections, and incentives for researchers and drug companies to develop new antibiotics. See page 471 and go.nature.com/bguvaz for more.

GM crops approved

The US Department of Agriculture approved on 17 September the commercialization of genetically modified (GM) maize (corn) and soya beans that are engineered to tolerate two herbicides. The agency also announced

that it would deregulate the traits, developed by Dow AgroSciences of Indianapolis, Indiana. The Environmental Protection Agency has yet to rule on the company's herbicide — a mix of glyphosate and 2,4-D — to be used on the plants. The GM crops and herbicide mix will probably be used to combat the rise in glyphosate-resistant weeds, but some worry that overuse will lead to weeds that are resistant to both herbicides (see *Nature* **510**, 187; 2014).

HFC sunset

To accelerate the phase-out of potent greenhouse gases used in refrigerants and air conditioning, US President Barack Obama announced on 16 September pledges from

major chemical companies and retail firms to shift rapidly away from the use of hydrofluorocarbons (HFCs). The voluntary commitments are expected to reduce global HFC consumption by the equivalent of 700 million tonnes of carbon dioxide by 2025, the White House says.

Rules for whaling

At a meeting last week in Portoroz, Slovenia, the International Whaling Commission passed tougher rules for proposed 'scientific' whaling projects, adding a list of criteria that includes consideration of whether lethal catches are scientifically reasonable. Scientific whaling is controversial, and some

researchers allege that Japan has used it as a cover for commercial whaling. The International Court of Justice ruled earlier this year that Japan's hunts were not for scientific purposes, but Japan has pledged to revise its scientific-hunting scheme.

EVENTS

Sea-ice minimum

Arctic sea-ice coverage reached its probable annual minimum on 17 September, spanning 5.02 million square kilometres. The measurement, reported by the US National Snow and Ice Data Center in Boulder, Colorado, continues a trend of lower-than-average coverage, and is the sixth-lowest in the satellite record.



NOAH BERGER/REUTERS/CORBIS

Extreme drought fuels California fires

Firefighters in California last week battled to gain control of several large wildfires that raged through the central and northern parts of the drought-stricken state. The most significant blaze, the King Fire near Placerville (pictured), started on 13 September, and by 23 September had burned more than 350 square kilometres. The California

drought, now in its third year, has wreaked havoc on native ecosystems (see *Nature* **512**, 121–122; 2014) and exacerbated seasonal fire risks. On 16 September, in response to the water shortage, Governor Jerry Brown signed a series of bills that would begin to regulate the extraction of groundwater, which supplies 40–60% of California's water usage.

LOCKHEED MARTIN

Meanwhile, sea ice around Antarctica continues to follow an opposite trend, exceeding the record maximum extent set last year. See go.nature.com/urlbe6 for more.

RESEARCH

NIH cleared

US government inspectors have concluded that the National Institutes of Health (NIH) did not interfere in the oversight of a controversial clinical trial in premature infants. A public watchdog organization had alleged that the NIH acted inappropriately in 2013 when the agency disputed findings from the Office for Human Research Protections, which said that consent forms failed to fully disclose the trial's risks (see *Nature* <http://doi.org/vt3>; 2014). In a report last week, inspectors concluded that the NIH merely argued its case without overstepping its bounds.

Arrival at Mars

Mission scientists and engineers (pictured at Lockheed Martin in Littleton, Colorado) cheered the insertion of NASA's MAVEN spacecraft (Mars Atmosphere and Volatile Evolution) into orbit around Mars on 21 September, after a ten-month journey. The mission will focus on studying the



upper atmosphere of the red planet. See go.nature.com/px22mw for more.

FUNDING

US spending bill

The US Congress has passed a US\$1.012-trillion stopgap spending bill, which would fund government operations from 1 October — the start of the 2015 fiscal year — until 11 December. The bill includes \$30 million to send health workers and resources to fight the Ebola outbreak in West Africa, and \$58 million to develop drugs and vaccines against the disease. See go.nature.com/pg1oxq for more.

AWARDS

Genius grants

The MacArthur Foundation in Chicago, Illinois, announced the recipients of its 2014 'genius

grants' on 17 September. Winners include Yitang Zhang, a mathematician at the University of New Hampshire in Durham, who in May 2013 made a major breakthrough towards proving that prime numbers follow a particular pattern, called the 'twin-prime conjecture' (see *Nature* <http://doi.org/vrs>; 2013). Each MacArthur Fellows Program award comes with a no-strings-attached US\$625,000 stipend paid over five years. See go.nature.com/arjf37 for more.

BUSINESS

Pharma firm fined

A Chinese court has fined drug giant GlaxoSmithKline £297 million (US\$485 million) after finding it guilty of bribery, the London-based firm said on 19 September. The verdict follows an investigation into whether the company bribed physicians and officials to

COMING UP

26–30 SEPTEMBER

The European Society for Medical Oncology holds its 2014 meeting in Madrid. Researchers will discuss blood biomarkers of cancer, genetic heterogeneity in tumours and advances in clinical-trial design. go.nature.com/l9rynbn

boost sales in China. Five of the company's managers were convicted of bribery-related charges and received suspended prison sentences, according to the state-run Xinhua news agency.

Focus on bioscience

German chemical company Bayer said on 18 September that it would spin off its materials-science division as a separate company, and focus solely on life sciences. The Leverkusen-based firm will shift resources towards expanding its health-care and crop-science divisions, which together generated about €29 billion (US\$36 billion) in sales last year — roughly 70% of the company's total sales.

Space taxis

US astronauts will soon fly to and from the International Space Station on spacecraft operated by two private companies, NASA announced on 16 September. Since the agency retired the space-shuttle programme in 2011, astronauts have been relying on Russian Soyuz vehicles. Now NASA has given grants of US\$4.2 billion to Boeing of Chicago, Illinois, and \$2.6 billion to SpaceX of Hawthorne, California; each will demonstrate at least one crewed test flight and then conduct between two and six crewed missions to the space station. The flights are slated to begin in 2017.

NATURE.COM

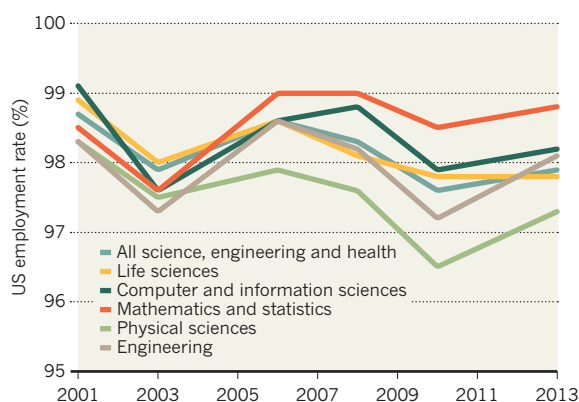
For daily news updates see:
www.nature.com/news

TREND WATCH

US employment rates for PhD recipients in science, engineering and health increased slightly from 97.6% in 2010 to 97.9% in 2013, according to statistics published this month by the National Center for Science and Engineering Statistics in Arlington, Virginia. Mathematics and statistics doctorates had the highest rates of employment, while physical scientists and engineers saw the steepest increases in employment since 2010.

BACK TO WORK

Employment rates for most US science PhDs rose in 2013, but prospects stayed flat for biology graduates.



SOURCE: NSF/NCSES

NEWS IN FOCUS

POLICY Transformation at the heart of Chinese science **p.468**

TECHNOLOGY Business beckons for cheap easy solar power **p.470**

HEALTH Drug-safety surveillance tool gets green light **p.472**



WIND POWER United States struggles to harness its vast resource **p.478**

LEO CORREA/AP



Environmental icon Marina Silva may struggle to advance her environment agenda if elected president.

ELECTIONS

Brazil warming to 'green' policies

Activist Marina Silva is gaining ground in presidential polls.

BY JEFF TOLLEFSON

Marina Silva rose from poverty deep in the Amazon jungle to become a prominent politician and the advocate who kick-started Brazil's battle against deforestation. Now she is clashing with an old foe, President Dilma Rousseff, in a wild election that could reshape the nation's environmental policy.

Silva's sudden ascent is almost as shocking as the event that prompted it: a plane crash on 13 August that killed presidential candidate Eduardo Campos. That pushed Silva, his running mate, to the top of the centre-left Brazilian

Socialist Party. Although the Campos-Silva ticket had struggled to gain traction, Silva is now in a statistical dead heat with Rousseff going into the election on 5 October; the two women are expected to face off in a runoff vote three weeks later.

As a third-party contender, Silva has promised a break from traditional politics amid growing anger over Brazil's stagnant economy and political corruption that has tainted the Workers' Party led by former president Luiz Inácio 'Lula' da Silva and his successor, Rousseff. But the campaign has also shown that Silva's grassroots 'socio-environmentalism' has wider appeal than many once believed.

Almost one-fifth of Brazilians supported Silva when she ran for president under the Green Party banner in 2010, but she seemed destined to remain a protest vote. After briefly trying to form her own party, she joined forces this year with Campos, a popular governor from the northeastern state of Pernambuco and Lula's former science minister.

"There has been a sea change in the political culture in Brazil, and Marina is one of the people who has brought it about," says Steve Schwartzman, an anthropologist with the Environmental Defense Fund, a non-profit advocacy group in New York, who began working with Silva in the 1980s.

Silva's impoverished childhood stands in stark contrast to that of Rousseff, an economist who grew up in a well-off family and received a solid education. Born into a poor forest community in 1958, Silva suffered mercury poisoning, hepatitis and malaria as a child and moved to the city of Rio Branco to receive hepatitis treatment at the age of 16. There she began her education at a Catholic convent and went on to earn a degree in history.

DEFORESTATION CAMPAIGNER

In 1984, she joined forces with environmentalist Chico Mendes, a rubber tapper whose 1988 murder helped to put the destruction of the Amazon rainforest onto the geopolitical map.

Silva was elected to the Brazilian Senate in 1994, at the age of 36, as a member of the Workers' Party. Lula appointed her as environment minister when he took office in 2003, and Silva quickly transformed Brazil's governance of the Amazon, pulling multiple government branches into a new enforcement regime that has helped to drive a 79% decrease in deforestation over the past decade.

"She was always directly engaged, very smart, and she listens a lot," says Thelma Krug, who served as Silva's chief climate-change adviser and is now assistant director at the National Institute for Space Research in São José dos Campos.

A devout evangelical, Silva speaks softly but commands attention. She is not afraid to stand up for her goals and values: she resigned as environment minister in 2008, feeling her agenda had been ignored in repeated battles over dams and development plans with other administration officials, Rousseff included. Krug's only concern is how Silva will cope with the harsh political realities in ►

► Brasília. “Marina does not negotiate on principles,” she says.

Others go a step farther. “I think she is a little too radical,” says Pedro Alves Vieira, a geologist at the State University of Goiás and environment secretary for the municipality of Goiás. Although Silva has hewed to the centre during the campaign, Vieira fears that she may be too focused on the environment, too religious and too rigid for the presidency.

“I think it’s time for a change.”

But some of Silva’s major stances have evolved. As environment minister, she opposed the introduction of genetically modified soya beans, but has since sought to mend fences with the powerful agribusiness industry — stressing that modern agriculture, practised legally, is not at odds with forest protection.

Her plan for sustainable development focuses on stemming Brazil’s gradual shift toward fossil fuels: renewable energy fell from 95% of the nation’s energy mix in the 1990s to 78% in 2013, according to her campaign. To reverse that trend, she is calling for the installation of solar panels on 1 million homes and the revitalization of the sugarcane ethanol sector, which has struggled to compete with heavily subsidized petrol. She is also pushing for sustainable forest concessions geared toward biomass energy.

By contrast, Rousseff has put more emphasis on dozens of large-scale hydroelectric dams that would increase development pressure on the Amazon rainforest. “We need more energy, but Brazil’s current strategy is really based on big infrastructure,” says Mercedes Bustamante, an ecologist at the University of Brasília who spent two years at the science ministry under Rousseff. “I think it’s time for a change.”

Science policy has received little attention in the presidential campaign, although Silva has called for federal and private investments in research and development to expand from 1.1% of Brazil’s gross domestic product to 2%. The government’s science spending has increased over the past decade, but researchers say that it has also been spread thin by new programmes.

Even if she takes the helm, Silva will have to tackle shifting political winds in Brasília. In 2012, the nation’s congress voted to weaken the country’s forest law, and some lawmakers are now pushing to scale back protected lands to allow mining and energy development.

But Schwartzman warns against underestimating Silva’s political skills should she win. “She and the others who worked with Chico Mendes in Acre really came through a crucible,” he says. “In some ways, looking back on that experience, I’m not surprised that she is where she is now.” ■



The Chinese Academy of Sciences, which employs 60,000 people, opens its 2014 congress in Beijing.

POLICY

Chinese science gets mass transformation

Teamwork at centre of Chinese Academy of Sciences reform.

BY DAVID CYRANOSKI IN BEIJING

Change is coming to the institute that has been at the heart of China’s scientific development since the communist state began. The Chinese Academy of Sciences (CAS) is making unprecedented structural reforms to foster collaboration and turbocharge research. Proponents say that the initiative will make China a world leader in areas from neuroscience to particle physics; detractors question whether modern China needs such a sprawling organization at all.

The CAS, headquartered in Beijing, employs 60,000 people, and has 104 research institutes and a budget of roughly 42 billion renminbi (US\$6.8 billion). Just under half comes from the government, to cover overhead costs and salaries; the rest comes from competitive government grants. It is “the biggest reform in the academy’s history”, CAS president Chunli Bai told *Nature*’s news team in an interview on 22 September.

The initiative — which was designed by Bai — follows an appeal by Chinese president Xi Jinping in July 2013 for the CAS to become a world leader in science. Although China’s spending on science now outpaces that of all countries except the United States, many agree that the country is not getting a good return on its investment, in terms

of both basic-science breakthroughs and commercialization of those findings.

Some underperformance might result from low salaries for scientists — including those at the CAS, says Bai — who scramble to supplement their incomes with multiple grants. “Their research becomes very fragmented,” he said.

Scientists also shy away from collaborations because co-authorship dilutes their achievements in the eyes of grant committees. At a conference in 2012, Bai discovered that researchers across 20 different CAS institutes were working on related projects, but often did not know each other — duplicating work and missing opportunities to share knowledge. He also notes that they had little interest in discussing applications with industry representatives.

To deal with these issues, Bai has grouped research into four categories, and promising CAS scientists are being selected to work together under them. They will see their salaries jump, relying on grants for only 30% of their income, rather than for 70%. The idea is to encourage scientists to collaborate on fewer, large problems, rather than to churn out marginal advances in disparate projects that can be used to seek multiple grants. “Teamwork is the key word,” says Mu-Ming Poo, director of the CAS Institute of Neuroscience in Shanghai.

The first category is devoted to establishing centres of excellence focused on basic science,

PANG XINGLEI/XINHUA PRESS/CORBIS

and will target areas in which China has a chance to dominate. One team, for which Poo has already selected 40 researchers from 11 different CAS institutes, specializes in brain science — one goal is to produce a transgenic monkey model that could be useful for neurodegenerative-disease research.

Tandong Yao, director of the Institute of Tibetan Plateau Research in Beijing will head another centre focused on the seismically active plateau: his team wants to probe how the crust underneath deformed over time. Other centres will focus on particle physics, thorium-based molten-salt reactors, and quantum information. The plan is to take the count up to 20 centres by 2020.

A second category will target areas with underdeveloped commercial potential, including microsatellites, marine information technology and drug development. A third category will establish collaborations around large-scale facilities: a synchrotron and a protein-science centre, for example, both in Shanghai, will be linked to make it easier to carry out high-precision protein studies and support academic and industry researchers, including some from abroad.

The fourth category, still in its design phase, will be devoted to initiatives that assist local development and sustainability. Its first will probably focus on work by the Institute of Mountain Hazards and Environment in Chengdu, which could help communities to prepare for natural disasters such as landslides.

But not everyone agrees that the changes tackle the key problems at the CAS. One Chinese university scientist, who is familiar with the reforms and did not want to be identified, says that the source of the problems is that the CAS hires too many young scientists who then go through little or no review, and essentially receive tenure without having to prove themselves. Bai counters that the opportunities offered by his initiatives will “encourage the underperformers to be better”. He says that he has steered away from a US-style system in which underperformers can be fired: “It is a reform with Chinese characteristics.”

Cong Cao, a science-policy specialist at the University of Nottingham, UK, says that the CAS is too big and unwieldy. “There’s no organization in the world with so many functions,” he says. He says that universities and individual research institutes, which are increasingly competing with the CAS for leading scientists, can offer a better management environment for scientists. “There probably is no reason for the CAS in China right now.”

But Bai uses the same trait to justify the academy’s existence: he argues that it allows the CAS to make wide contributions to China’s development. “You have to understand the history,” he says. ■

INFECTIOUS DISEASE

Global Ebola response kicks into gear at last

US and UN mobilizations are welcome but overdue.

BY DECLAN BUTLER

The international community is responding to the Ebola outbreak — at long last. On 18 September, the United Nations Security Council adopted a resolution declaring the outbreak a “threat to international peace and security”; two days before, the United States had said that it will send 3,000 military personnel to West Africa and spend US\$750 million to support civilian efforts. Both moves are unprecedented for a disease outbreak and just what is needed, say experts. But there are fears that quelling the outbreak now will be more difficult than if it had been tackled earlier.

The Ebola outbreak was first detected in March, but only the humanitarian group Médecins Sans Frontières (MSF, or Doctors Without Borders) has so far deployed substantial relief in the affected region, which centres on Liberia, Sierra Leone and Guinea (for more, see nature.com/ebola). MSF has repeatedly demanded that the international community launch a major effort to tackle the outbreak.

The UN resolution calls on member states to respond urgently. As it was passed, UN secretary-general Ban Ki-moon launched the United Nations Mission for Ebola Emergency Response to deploy resources from UN agencies in coordination with efforts from member nations and donors. The mission’s remit includes “stopping the outbreak, treating the infected, ensuring essential services, preserving stability and preventing further outbreaks,” said Ban.

The United States plans to establish military-run command and control headquarters in Liberia and build 17 treatment centres of 100 beds each in the affected region. It hopes to recruit medical staff to run them, and train up to 500 health-care workers a week.

The public-health community tends to view military involvement “with suspicion and mistrust”, says Adam Kamradt-Scott, a health-policy researcher at the University of Sydney in Australia. But he welcomes the US plan: “Military forces have unique skill sets that can assist civilian authorities.” If the operation does help to counter Ebola, he adds, it could set a new precedent for responding to disease outbreaks of international concern.

Training forces in outbreak response will take time, warns Daniel Bausch, who studies infectious diseases at Tulane University in New Orleans, Louisiana, and is caring for people with Ebola in Sierra Leone. He adds that

the situation is too dire for the United States alone to solve, and that other nations must step in, something that the UN resolution should catalyse. It was passed by unanimous vote and had a high number of member-state sponsors.

Jean-Clément Cabrol, director of operations for MSF in Geneva, Switzerland, says that both efforts are welcome, but that the situation has worsened in the past few weeks, so speed is key. Treatment centres in the three countries most affected are completely overwhelmed

“Military forces have unique skill sets that can assist civilian authorities.”

(see page 474). This is fuelling the spread of the disease, because centres are forced to send away infected people, who then contaminate others.

Conventional public-health measures are no longer working, says Bausch. It has become next to impossible to detect and isolate those infected, and to monitor all the people they have been in contact with. He recommends focusing surveillance on areas next to affected zones to prevent further geographical spread of Ebola. He adds that international efforts will be effective only if they include training for health-care staff, for example in biosafety. Money and supplies are welcome, but by themselves, they are not enough. ■ [SEE EDITORIAL P.459](#)

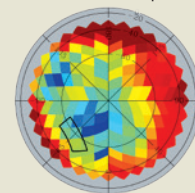
MORE ONLINE

TOP NEWS

- Population boom to last all century go.nature.com/xnsblj
- Male astronomers get bigger share of Hubble go.nature.com/v9e8o7

IMAGE OF THE WEEK

This map measures dust in the southern Galactic hemisphere. It suggests that



a signal of gravitational waves from the Big Bang previously observed in the black rectangle

could have been spurious. go.nature.com/ifalmw



OLGA MALINKIEWICZ, UNIV. VALENCIA

Perovskite solar cells, currently postage-stamp sized, must be scaled up to be practically viable.

SOLAR POWER

Cheap solar cells tempt businesses

Easy-to-make perovskite films rival silicon for efficiency.

BY RICHARD VAN NOORDEN

Olga Malinkiewicz, a PhD student studying photovoltaics at the University of Valencia in Spain, first heard about perovskites, the latest hope for low-cost solar power, in April last year. Unlike the slabs of purified silicon at the heart of the solar cells that currently dominate the market, perovskites form thin films that are easily made in the lab by mixing together cheap salts. “I couldn’t believe it was so simple,” says Malinkiewicz, who immediately tried it herself.

A year later, she won a European student innovation prize, for coating flexible foil with perovskites. “After that, my telephone didn’t stop ringing,” she says. “Investors were asking me all the time if I was going to start a company.” By May 2014, the excited 31-year-old had decided to do just that. In the past three months, she has moved from Spain to her native Poland, rented laboratory space in Wrocław, founded the privately backed company Saule Technologies, and rebuffed an offer of €1 million (US\$1.3 million) for 10% of the fledgling firm — although she is yet to complete her PhD.

Malinkiewicz’s bold venture epitomizes how fast perovskites have zipped from academic curiosity to the brink of commercialization. In three years, competing research groups have tripled the cells’ efficiency, achieving what took decades to accomplish for other solar materials.

Large, commercial silicon modules convert 17–25% of solar radiation into electricity, and much smaller perovskite cells have already reached a widely reproduced rate of 16–18% in the lab — occasionally spiking higher. They are expected to top 20% in a few months, says Sang Il Seok at the Korea Research Institute of Chemical Technology in Daejeon, whose lab holds the current record of 17.9%. “The results so far are truly spectacular,” says David Ginley, a researcher at the US National Renewable Energy Laboratory in Golden, Colorado.

The combination of low cost and efficiency means that perovskite cells could, in theory, make solar power — which currently provides less than 1% of the world’s electricity — cheaper to generate than fossil-fuel energy, according to Henry Snaith, a physicist at the University of Oxford, UK (see *Nature* **504**, 357–365; 2013). At a conference he convened in Oxford on 11–12 September, perovskite researchers discussed the remaining barriers to the technology’s commercial success.

The cells, composed of perovskite film sandwiched between conducting layers, are still about the size of postage stamps. To be practical, they must be scaled up, which causes efficiency to drop. Seok says that he has achieved 12% efficiency with 10 small cells wired together.

Doubts remain over whether the materials

can survive for years when exposed to conditions outside the lab, such as humidity, temperature fluctuations and ultraviolet light. Researchers have also reported that ions inside some perovskite structures might shift positions in response to cycles of light and dark, potentially degrading performance.

Oxford Photovoltaics (Oxford PV), a company that Snaith co-founded, says that its unpublished tests show that the cells can meet industry stability standards if encapsulated in glass, as silicon panels are. By 2017, the company’s commercial partners aim to be using perovskites trapped in glass to produce transparent cells that could hug the exteriors of buildings. And on 16 September, Snaith and his colleagues published another way to protect a perovskite cell from heat and moisture, by replacing one of its layers with carbon nanotubes embedded in insulating plastic (S. N. Habisreutinger *et al.* *Nano Lett.* <http://dx.doi.org/10.1021/nl501982b>; 2014).

The need for this engineering might create another setback, says Arthur Nozik, a chemist at the University of Colorado Boulder. After plummeting in past years, the price of crystal-line silicon modules — which make up 90% of the solar-cell market — has levelled off but is expected to keep falling slowly. As a result, most of the cost of today’s photovoltaic systems is not in the material itself, but in the protective glass and wiring, racking, cabling and engineering work.

When all these costs are factored in, perovskites might save money only if they can overtake silicon in efficiency. In the short term, firms are focusing on depositing the films on silicon wafers, with the perovskites tuned to capture wavelengths of light that silicon does not. On 10 September, Oxford PV announced that it was working with companies to make prototypes of these ‘tandem’ cells by 2015, and that this could boost silicon solar cells’ efficiencies by one-fifth, so that they approach 30%. Malinkiewicz’s hope is to find a niche that silicon cannot fill: ultra-cheap, flexible solar cells that might not last for years, but could be rolled out on roof tiles, or used as a portable back-up power source.

There is another potential snag: perovskites contain a small amount of toxic lead, in a form that would be soluble in any water leaching through the cells’ protection. Although Snaith and others have made films with tin instead, the efficiency of these cells is only just above 6%.

Researchers say that many major electronics and chemicals firms are studying perovskites. Japan’s space agency JAXA is also testing them for their potential to power satellites. But as Malinkiewicz has found, perovskites’ low-cost, simple recipe means that anyone has a shot at commercializing them. “It is not just in the hands of the big chemical companies, or the silicon companies,” says Mohammad Khaja Nazeeruddin, a chemist the Swiss Federal Institute of Technology in Lausanne. “It is everybody’s technology.” ■

“I couldn’t believe it was so simple.”

PUBLIC HEALTH

US vows to combat antibiotic resistance

Strategy lauded, but some fear it is lax on agricultural use.

BY SARA REARDON

A push by the US government to stop the rise of antibiotic resistance has drawn broad praise from advocates who have long warned about this public-health threat. Some, however, are concerned that the plan might not do enough to curb the use of these drugs in livestock.

Released by the White House on 18 September with an accompanying report by a presidential science advisory panel, the executive order instructs leaders of several US agencies to develop a five-year plan to limit the spread of resistance, using strategies such as developing new antibiotics and finding better ways to diagnose antibiotic-resistant infections quickly. It received the nod of approval from many experts.

"I find this report surprisingly detailed and surprisingly on target," says Stuart Levy, a physician and microbiologist at Tufts University in Boston, Massachusetts, who has long campaigned for prudent antibiotic use. It hits all the most important topics, he says: increased surveillance, better diagnostics, development of new drugs and more judicious use of existing antimicrobials — measures also outlined by the World Health Organization in April.

The use of antibiotics in animal husbandry is addressed in the White House strategy and in the report by the President's Council of Advisors on Science and Technology (PCAST). The report calls for collection of more data on the use of antibiotics on farms, and monitoring of whether policies to curb antibiotics affect the spread of resistance. But some advocates for careful antibiotic use feel that the plan will not do enough to stop the threat quickly. "They haven't proposed anything new," says Steven Roach of Carbondale, Illinois, who is an analyst for Keep Antibiotics Working, a coalition of advocacy groups that campaigns against antibiotic overuse. "The things they're saying people should do are endorsing the status quo."

Farmers sometimes give antibiotics to healthy livestock to prevent infection and boost growth, a controversial practice that is banned in some countries because it is thought to

contribute to the development of resistant bacteria. In December, the US Food and Drug Administration (FDA) issued voluntary guidance asking pharmaceutical firms to change labelling so that drugs cannot be marketed to fatten up farm animals, and requiring a veterinary surgeon to prescribe the drugs. According to the PCAST report, all 26 major manufacturers of antibiotics used in US farm animals have adopted these rules.

Two bills pending in the House of Representatives and the Senate would entirely ban farm-animal use of antibiotics that are also given to humans. But justifying more-stringent limits is hampered by a poor understanding of the link

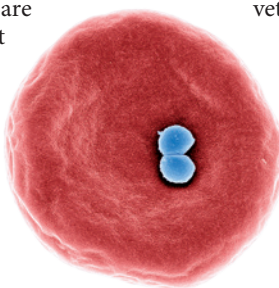
between agricultural antibiotic use and resistance in bacteria that infect humans.

"If I could wave my hand and ban it, I'd say let's do it," says Henry Chambers, an infectious-disease physician at the University of California, San Francisco. "But it's a very complicated area."

The PCAST report suggests that the FDA should continue to track whether the existing voluntary measures decrease agricultural antibiotic use, and investigate the extent to which giving the drugs to healthy animals contributes to resistance in human pathogens.

"It will be difficult to rigorously attribute changes in human antibiotic resistance patterns to changes in agricultural use — at least until much better surveillance systems are in place and until the flow of antibiotic resistance between reservoirs is much better understood," the PCAST report says.

PCAST's analysis, which is intended to guide the US agencies in their five-year plan, suggests spending US\$900 million per year on national monitoring systems — double the current level — and developing infrastructure to speed clinical trials of new antibiotics. The report also recommends spending \$150 million per year for 7 years on basic research into the spread of resistance and alternative strategies for growth promotion in livestock. To kick off the initiative, the White House announced a \$20-million prize for the first team to develop a rapid diagnostic tool for antibiotic-resistant infections. ■



Staphylococcal bacteria (blue) on a red blood cell.

STANLEY FLEGER/VISUALS UNLIMITED/GETTY



Medical records can provide information about harmful side effects that is not available elsewhere.

MEDICAL RESEARCH

Drug-safety pilot makes the grade

FDA will continue to monitor safety from health records.

BY HEIDI LEDFORD

A tool that allows US regulators to assess drug safety from the health records of more than 175 million people is set to become an integral part of the nation's drug-safety surveillance.

On 1 October, a US\$116-million pilot that the US Food and Drug Administration (FDA) has been running since 2009 will become a fully fledged initiative to mine the electronic medical data held by insurers and health-care providers for signs that a medicine has harmful side effects. Investigators will also begin to explore ways to use this growing pool of information for research on other issues.

But the project, known as Mini-Sentinel, has faced challenges over who should be allowed to analyse the data and publicize the results. It creates a valuable resource, says epidemiologist Bruce Psaty of the University of Washington in Seattle, but the FDA will need to decide how to weigh up the new data against other types of information. "These are difficult scientific questions," he says.

The FDA currently monitors drug safety mainly through clinical trials and voluntary reporting of possible side effects. Both approaches have limitations. Although the gold standard, data from randomized clinical trials are expensive to obtain and do not always

reflect the conditions under which the drug will be used in daily practice. And voluntary reports might alert the FDA to possible side effects, but they cannot reveal how common the reactions are or provide any firm evidence linking them to the drug.

In 2007, the US Congress became concerned that some approved drugs might be increasing the risk of heart attacks and strokes, and ordered the FDA to add electronic medical data to its drug-safety monitoring arsenal. The result was Mini-Sentinel: a 'dispersed data' system involving 18 large health-care organizations. Each organization analyses its own data and reports the results to a team at the Harvard Pilgrim Health Care Institute in Boston, Massachusetts. The Pilgrim team then combines the analyses and sends the pooled result to the FDA. The process is meant to ensure the privacy of patients and to prevent outside researchers from drawing their own conclusions from their data. "It's really an impressive system," says Joshua Gagne, an epidemiologist who works on the project at Brigham and Women's Hospital in Boston. "It's going to change the way in which FDA looks at drug safety."

But there are some trade-offs, he adds. Pooled analyses have less statistical power than would be possible if all of the patients were combined into a single massive population. They also require sophisticated methods to allow the

integration of analyses from different groups.

Mini-Sentinel's protocols are likely to serve as models for other projects, such as a \$93.5-million database network that is being developed in Washington DC to compare the effectiveness of different treatments using medical records. (see *Nature* 512, 18; 2014).

JOHN MOORE/GETTY

DECIDING FACTORS

Scientists are still wrestling with when, and how, to apply the data that Mini-Sentinel unearths to actual drug-safety decisions. The FDA has so far issued five drug-safety updates that were based on Mini-Sentinel analyses. In one case, it used the system to investigate an unusually high number of reports of serious bleeding associated with the anti-clotting drug Pradaxa (dabigatran) after the drug was approved in 2010. Mini-Sentinel's conclusion was that the drug, made by the German drug company Boehringer Ingelheim, was no more likely to cause bleeding than warfarin, a medicine that has been used for decades.

The FDA announced its finding in an official communication to physicians and consumers, but acknowledged separately that the analysis was preliminary and had not considered potential confounding factors, such as the tendency of doctors to prescribe the newer drug to younger, and thus presumably healthier, patients. The analysis was done before Mini-Sentinel had the tools to support a more sophisticated study, says Mini-Sentinel principal investigator Richard Platt. Those tools are now in place, and the FDA is analysing the data more thoroughly.

Some, however, are not convinced that the tool adds any insight. Cardiologist İlke Sipahi of Acibadem University Medical School in Istanbul, Turkey, for instance, says that his analysis of all available clinical-trial data comparing the two drugs showed a higher risk of bleeding from Pradaxa than from warfarin — a direct contradiction to the Mini-Sentinel analysis. He does not believe that Mini-Sentinel needed to be brought in because the answer was already available in the higher-quality clinical-trial data (I. Sipahi, S. Celik & N. Tozun *JAMA Intern. Med.* 174, 150–151; 2014).

And David Madigan of Columbia University in New York has different concerns. He faults the FDA for issuing an official communication on the Pradaxa results to physicians and consumers — in effect, he says, sending a premature all-clear signal. "I have no idea whether that drug is dangerous or not," he says. "But I sure as hell know that particular analysis didn't shed any light on the question." ■

CLARIFICATION

The graphic in the News Feature 'The fusion upstarts' (*Nature* 511, 398–400; 2014) omitted to note that the deuterium–deuterium reaction has a 50% chance of producing tritium and a proton.



TOMMY TRENCHARD/THE NEW YORK TIMES/REDUX/EYEVINE

EBOLA'S LOST WARD

A hospital in Sierra Leone has struggled to continue its research amid the worst Ebola outbreak in history.

BY ERIKA CHECK HAYDEN

Robert Garry had a bad feeling about the tin roof teetering above his head. It was June, and he and a colleague, Sheik Humarr Khan, were surveying a makeshift shelter that was to serve as a temporary Ebola ward for Kenema Government Hospital in Sierra Leone. They could see that the only thing holding the metal sheets to a 5-metre-tall wooden frame was a handful of thin, twisted wires.

Half an hour later, at a meeting in the main hospital building, the men were interrupted by a tremendous crash. As the sound reverberated through the hospital grounds, Garry and Khan rushed back outside to see what had seemed inevitable: the precarious structure had collapsed.

It was an omen of things to come. In less than a month, the hospital's operations would topple under the weight of the worst Ebola outbreak in history. The wards were overwhelmed with

patients and Khan, an infectious-disease physician at Kenema, and many of his staff were among those fighting for their lives.

The epidemic has killed more than 2,600 people since it began in December 2013, and it could infect tens of thousands more by the end of this year, according to the World Health Organization (WHO). Three countries — Guinea, Liberia and Sierra Leone — have been the epicentre, struggling with weak health systems and a wholly inadequate global aid response, even after the WHO declared the epidemic an international public-health emergency in early August (see *Nature* <http://doi.org/vsc>; 2014).

Khan and his team came to the fight against Ebola armed with experience battling another virus: Lassa, which like Ebola causes a life-threatening illness that sometimes results in haemorrhagic fever. But Lassa has much more predictable annual infection cycles. Along with Garry, a virologist at Tulane University in New Orleans, Louisiana,

One of the general wards at Kenema Government Hospital was abandoned by staff and patients owing to fears over Ebola.

NATURE.COM
For a video about some of the people involved, see: go.nature.com/kaInp6

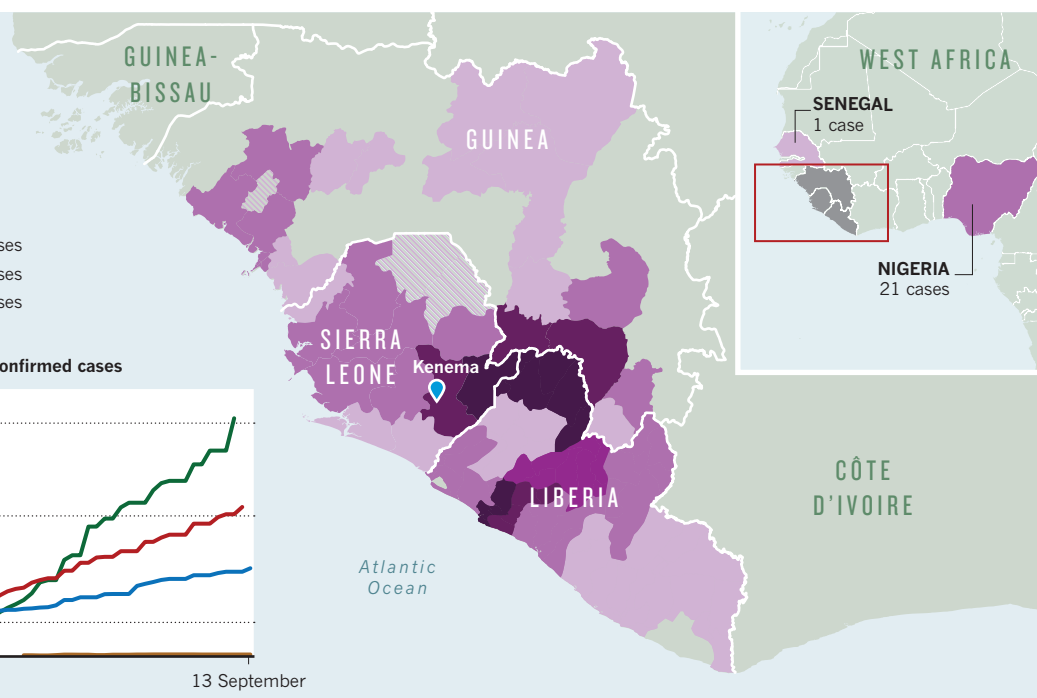
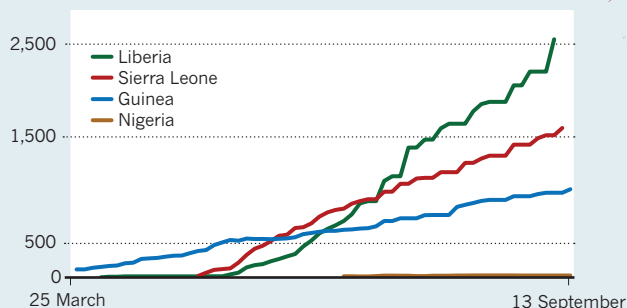
SOURCE: RELIEFWEB.INT

EBOLA'S EPICENTRE

Since Guinea saw the first confirmed case of Ebola in March, the number of people who have become infected has climbed steadily. Kenema Government Hospital identified Sierra Leone's first case in May.



Cumulative suspected, probable and confirmed cases



and an international team of scientists, Khan had spent the better part of a decade building a Lassa treatment and research programme at Kenema, including a dedicated ward and a modern diagnostic laboratory. The ward they were adding was the next step in their arsenal against the disease.

But before it could be completed, the Lassa lab diagnosed Sierra Leone's first case of Ebola. Hundreds more followed. And a medical facility that had been set up to study one disease suddenly found itself overwhelmed by another.

Researchers worked hard to study the disease that was filling the wards — to trace its path into and through the country. But the outbreak consumed the hospital, and research was put on hold. It became clear that even if science could inform the outbreak response, the much more pressing need was for health resources and humanitarian aid.

"There's a question of research's role here," says Pardis Sabeti, a computational geneticist at the Broad Institute in Cambridge, Massachusetts, who has worked with the Kenema team since 2008. Too frustrated to stand on the sidelines, she and other US researchers called for more aid to be sent to Kenema, but found the response painfully slow. "Our friends needed support and every international organization we turned to was stretched too thin."

A SHINING EXAMPLE

Khan knew the risks of working on haemorrhagic fevers: he became the lead Lassa doctor at Kenema after his predecessor died of the disease. Lassa infects 300,000 to 500,000 people a year and kills between 5,000 and 20,000 of those.

The hospital in Kenema had been treating patients in its Lassa ward for decades, even struggling through a bloody civil war that lasted from 1991 to 2002. Its expertise made it an ideal nucleus for a group called the Viral Haemorrhagic Fever Consortium, which started in 2010 and included scientists from Kenema, Tulane and other partners in West Africa and the United States.

One of the main obstacles that doctors faced was diagnosing diseases quickly enough to treat them; after the war, no lab in Africa had the technology to detect Lassa in a patient's blood. So in 2005, Kenema

built a lab and developed a diagnostic test. Sabeti, one of the founding members, began to sequence samples to understand how the disease spread through West Africa.

In May, Sabeti, Khan and Garry met in Nigeria to celebrate an enormous step forward for their work. In October, the World Bank and the US National Institutes of Health had funded a Centre for Genomics of Infectious Disease led by a collaborator in Ogun State, Nigeria, and the institute was hosting its inaugural meeting. The centre would use genetic technologies to study microbes in West Africa; it would soon acquire the first high-throughput sequencer in the region, mean-

ing that Kenema would no longer have to send samples of Lassa and other viruses overseas for in-depth sequencing. The partnership was becoming a shining example of scientific collaboration on the continent, building infrastructure and experience from within rather than importing it all from abroad.

Everyone was buoyed by the news, and by the progress in Sierra Leone, where, with a grant from the US Navy, Kenema was building its new Lassa ward. The ward would have 48 beds — almost double the capacity of the current

ward. It would have air conditioning to help nurses and doctors, who often had to wear stifling protective gear in oppressive equatorial heat. And it would be safer, with features such as a tiled floor and a drainage system, so that a worker could clean it out just by hosing it down. People with haemorrhagic fevers shed the virus in their blood, vomit, diarrhoea, sweat and tears. In the old Lassa ward, with its concrete floors, staff risked infection every time they slogged through the waste with a broom.

But the team knew that trouble was coming. When Guinea, to the north, notified the WHO about its Ebola cases in March (see 'Ebola's epicentre'), Garry predicted that Kenema would be next. He and Sabeti shipped trunks of protective gear to Kenema. Researchers from Sabeti's lab travelled there with the genetic probes needed to diagnose Ebola.

In May, the first cases arrived. A woman turned up with a fever, and was bleeding heavily after a miscarriage. She and 13 others had become infected at the funeral of a traditional healer who had been treating Ebola victims in neighbouring Guinea. On 25 May, Augustine Goba, head of the Lassa diagnostic lab, confirmed that these people had brought the virus into Sierra Leone. They were admitted to Kenema's Lassa ward.

"Our friends needed support and every international organization we turned to was stretched too thin."



Pardis Sabeti (centre) worked with nurses at Kenema Government Hospital to study Lassa virus, but switched to studying Ebola once the outbreak began.

Garry flew in right away to help make sure that the Kenema staff were prepared. They needed to swap out their usual gowns and masks for Tyvek ‘bunny’ suits that cover the whole body in a waterproof barrier. Garry also made sure that the technicians were collecting, decontaminating and packing blood samples from patients after they had been used in diagnosis, so that Sabeti could sequence the DNA at the Broad Institute.

At first, the patients arrived slowly — too slowly. In early June, workers tracing the contacts of infected individuals could see that there were many more people who were potentially infected than there were in the hospital. But Ebola had never before come to West Africa, and people were spreading the disease without knowing it, simply by caring for the sick and burying the dead. Whole villages would be wiped out.

Khan suspected that Kenema would soon see a wave of cases, so he ordered the construction of the new, temporary ward. (After the first structure collapsed, workers rebuilt it with a shorter, sturdier roof). His prediction was right: by the end of June, the old Lassa ward was overwhelmed and suspect cases were being admitted to the temporary one. Patients began to flood in from all over eastern Sierra Leone. Everyone was sending patients to Kenema Government Hospital; there was nowhere else to go.

Supplies and staff were thin on the ground: Médecins Sans Frontières (MSF) and other aid groups were already stretched beyond capacity treating patients in Guinea and Liberia. The WHO had sent some staff to Kenema in June, but supplies were dwindling, and Khan was often the only doctor in charge of treating 80 people. He felt alone and afraid for his life. But he continued to care for his patients as best he could. “If I refuse to treat them, who would treat me?” he told his sister.

A DEADLY CHAIN OF EVENTS

Back in Cambridge, Sabeti was analysing data from the samples that Garry had shipped out of Kenema. Her group now had 99 Ebola virus samples from the first 78 patients in the country’s outbreak. The researchers were performing in-depth genetic sequencing to track the way the virus mutated as it passed from person to person. No one had ever gathered these kinds of data on an outbreak while it was unfolding.

Important information was already emerging — for instance, that the whole outbreak could be traced to a single event in which an animal, probably a bat, transmitted the virus to a human. They also saw that the virus had accumulated hundreds of mutations since separating from an ancestral Ebola virus in Central Africa a decade ago (see *Nature* <http://doi.org/vsd; 2014>).

It is the sort of work that could eventually change the way in which outbreaks are fought, says Anthony Fauci, head of the US National Institute of Allergy and Infectious Diseases (NIAID) in Bethesda, Maryland, which funded the work. “We would normally come out with an analysis like this two years after an outbreak is over,” he says. “To be able to do this is just extraordinary.”

Sabeti’s team released its data as quickly as it could, by 31 July. Among the first users were researchers who had been developing experimental drugs and vaccines for Ebola. These include the antibody cocktail ZMapp, which has since been given to seven individuals, not all of whom have survived, and a NIAID vaccine that entered human trials in early September. None of the mutations seen in the virus

so far would render these products less effective, although some affect regions of the virus that are targeted by current diagnostic tests.

Sabeti was in close contact with Khan throughout, and knew that the situation in Kenema was deteriorating fast. “He was concerned, and he was sort of still by himself, and not really getting the support he needed,” Sabeti says.

In late June, a feverish local chief was admitted to a private ward in Kenema that lacked the infection-control measures used in the Lassa ward. That started a deadly chain reaction: he infected five staff members, including a pregnant nurse. A midwife, Mbalu Fonnies, who was also the chief Lassa nurse, worked with three others to deliver the nurse’s stillborn baby. She and the other nurses were all infected, almost certainly during the delivery. They all died.

Fonnies’s death on 21 July and the deaths of other senior nurses snapped a thread that had kept the hospital together. ‘Aunty Mbalu’ had been treating Lassa at Kenema for 25 years — throughout the civil war — and had survived a Lassa infection herself. Now she was gone.

“A lot of these people spent a good part of their childhoods hiding out in the bush from the rebels.”



Mbalu Fonnies (left), Veronica Koroma and Sheik Humarr Khan all contracted Ebola while working to treat patients at Kenema General Hospital.

The next day, while in a lab meeting, Sabeti glanced at her e-mail and saw that there was a message about Khan. She opened it immediately: Khan had Ebola. "I just broke down and started bawling," she says.

Sabeti felt helpless. She wanted to do something — anything. So she wrote a white paper urging US officials to commit more supplies and money to fighting the outbreak, and sent it to Broad Institute director Eric Lander and other members of a board of science advisers to the US president. She and Garry had already travelled to Washington DC to ask health officials and Congress to send more aid; Garry had asked officials to send experimental vaccines and medicines.

Now they urged doctors from MSF and the WHO to treat Khan with ZMapp. But the doctors feared that if something went wrong, it would undermine the already-fragile public trust in them, so they decided not to do it.

With Khan now very ill, the Kenema hospital was on the verge of collapse. There were too many patients and too few staff to treat them, and supplies were dwindling. Fearing for their lives and feeling ill-equipped to do their jobs, the remaining nurses and lab technicians went on strike. The hospital as a whole had virtually shut down, except for its Ebola work.

Tulane physician Daniel Bausch was working in the Ebola ward around that time. One day, he went into the ward with a WHO worker. "There were 50 patients and no nurses or other health workers in there. My first reaction was, we just need to close this centre. We can't say this offers any care." Still, they soldiered on, knowing full well that Kenema was a place of last resort for patients, who would only spread the disease if released.

Meanwhile, hearing rumours that Ebola was a hoax or a conspiracy, people from the surrounding city attacked the hospital, throwing rocks at the building. Police used tear gas to drive the rioters away.

On 29 July, Sabeti received a second e-mail from an epidemiologist in Sierra Leone. The message simply read: "Dr. Khan is gone."

LASSA LOOMING

The period after Khan's death was the nadir of the outbreak in Kenema. The loss of its leader and of so many others was devastating. "It completely demoralized the community. It has completely torn them apart," says Joseph Fair, a virologist who has been working in Sierra Leone since 2004 and advised the country on its response to the current outbreak. Sabeti and her team were also shocked. "We loved that man," Sabeti says.

By the time the paper on the sequencing of the first 78 cases was

published (S. K. Gire *et al. Science* **345**, 1369–1372; 2014), on 28 August, six of its authors, including Khan and Fonnies, had died.

But by then, help had started to arrive. Workers from the WHO and MSF began to restock supplies of protective equipment. The International Committee of the Red Cross began building a treatment centre just outside Kenema. Kenema is still treating roughly 50 Ebola patients, but it is trying to wind down that work and reopen its general wards.

But with all the attention now on Ebola, physicians who work in Kenema are concerned about Lassa. The peak Lassa season, November to April (J. G. Shaffer *et al. PLoS Negl. Trop. Dis.* **8**, e2748; 2014), is approaching, and of the hospital's original 36 specialized Lassa staff, 11 have now been infected and 6 have died. Surveillance staff, doctors, nurses, drivers, cleaners and lab technicians have all lost their lives to Ebola. New trainees and the remaining staff — including Ebola survivors — are stepping up to treat the cases that do arrive. But the hospital is seeing fewer Lassa patients than it would have expected for this time of year. "We think the patients are reluctant to come in," says Garry. "That's not good."

Garry still hopes to make Kenema a centre of excellence for Lassa research by training African staff to carry out clinical trials on the best ways to track, diagnose and treat the disease. And the haemorrhagic-fever consortium plans to name the new ward after Khan when it is finally completed. The goal is to outfit it with a high-throughput genetic sequencer so that researchers there can study the circulating viruses all the time, and perhaps detect the next outbreak, of Ebola or otherwise, before it grows out of control. Garry has faith in Kenema's survivors. "A lot of these people spent a good part of their childhoods hiding out in the bush from the rebels," Garry says, thinking back to the days of civil war. "You're talking about a very resilient group of individuals."

Sabeti, Garry and their colleagues are now preparing for the next step in their research: sequencing samples from every Ebola patient seen at Kenema since 18 June. They hope that the data will reveal whether the virus is continuing to mutate at the same rate and in the same genetic regions as before, and whether the mutations seen in the current outbreak made different circulating viruses more or less able to transmit between people and cause death. The data will also tell a more personal story, revealing the precise path taken by the virus as it infected Khan, Auntie Mbalu and so many of their colleagues. They, too, are represented in the samples. ■

Erika Check Hayden is a reporter for Nature in San Francisco, California.



Wind power tests the waters

The United States has plenty of strong winds offshore, but it has struggled to harness them for energy.

BY GENE RUSSO

The town of Castine, Maine, feels like a place bypassed by time. First settled in the early seventeenth century, its streets are lined with buildings hundreds of years old. Boats bob in its small harbour and a white lighthouse, constructed of rough-hewn stone, stands guard from a high hill.

But just half a kilometre offshore, a harbinger of the future pokes out of the grey mist. A

canary-yellow wind turbine rocks in the waves, its thin blades slowly rotating. Installed in June last year, the 20-metre-tall structure is an experimental floating design just one-eighth in scale. It provides a maximum of 20 kilowatts of electricity, barely enough to power half a dozen US homes. But the structure, called VolturnUS, stands out because it is the only offshore wind turbine in US waters.

ROBERT F. BUKATY/AP/PRESS ASSOCIATION

A floating turbine in Castine, Maine, is the only existing offshore wind facility in the United States.

Other countries, such as Belgium, the United Kingdom, Denmark and Germany, have built massive turbine farms off their coastlines in the past few decades. In the United States, however, efforts to tap the power of coastal winds have gone nowhere because of environmental concerns, bureaucratic tangles and political opposition. That may soon change. Ecological studies indicate that carefully planned wind farms should not significantly harm birds or marine mammals. And business and politicians are increasingly interested in exploring and investing in offshore wind power.

This May, the US Department of Energy awarded money to three demonstration projects, planned for the coasts of New Jersey, Oregon and Virginia. Several state governments are forging ahead with their own ambitions for offshore wind farms, and commercial developers say that they could start planting turbines in the ocean as early as next year.

In theory, the potential is tremendous. Including harder-to-reach deep-water sites, the offshore territory of the United States has the capacity to generate an estimated 4,200 gigawatts of electricity, enough to supply four times the nation's current needs. But before the field can take off, proponents will have to prove that offshore wind can compete financially against other energy sources, and can clear the thicket of state and federal regulations that govern projects in coastal waters.

"I don't think we're looking at easy street here," says Walt Musial, a long-time offshore-wind researcher at the National Renewable Energy Laboratory in Louisville, Colorado. "We really need to demonstrate that it can be done."

SEA TEST

No project encapsulates the challenges facing offshore wind power better than Cape Wind, being developed by Energy Management of Boston, Massachusetts. The venture aims to take advantage of the strong winds and relatively calm waters of Nantucket Sound near Cape Cod, Massachusetts, some 350 kilometres southwest of Castine.

The plan for Cape Wind consists of 130 turbines, each standing nearly 80 metres tall, over an area of 65 square kilometres. Energy Management says that the completed wind farm will have a capacity of 468 megawatts, able to produce 75% of the electricity for Cape Cod and the nearby islands of Martha's Vineyard and Nantucket.

But the project has faced strong opposition for more than a decade. Organizations including the non-profit group Save Our Sound have brought dozens of lawsuits against Cape Wind, claiming that the project would harm birds and other wildlife, increase electricity rates for consumers and endanger aeroplanes flying into local airspace. Except for one temporary

decision, all of the judicial rulings have been in favour of Cape Wind. Spokesperson Mark Rodgers says that even with court appeals coming, the project intends to commence construction by spring 2015. "There are no merits to any of these legal complaints," he says.

Cape Wind has already broken new ground by being the first US offshore wind project to complete a major environmental assessment. That study — thousands of pages long — and independent analyses have helped to appease some groups that were sceptical of the initial proposal.

The conservation group Mass Audubon in Lincoln, Massachusetts, for example, spent three years tracking roseate terns (*Sterna dougallii*), migratory songbirds and sea ducks

wintering in the area, and found little cause for concern. The songbirds typically fly above 300 metres, making collisions unlikely. And the terns and ducks stay close to shore during migration and breeding.

The effects on marine mammals may be harder to predict. Researchers and environmentalists have worried in particular about the construction stage of offshore wind farms, which so far have almost exclusively used turbines fixed to the ocean floor. Pounding huge steel beams into the seabed generates sounds equivalent to a small explosion — enough to disrupt the behaviour of some marine mammals, at least temporarily.

In the early 2000s, Jakob Tougaard, a marine bioacoustician at Aarhus University in Roskilde, Denmark, studied the effects of wind-farm construction on harbour porpoises (*Phocoena phocoena*) off the coast of Denmark. Using recordings of porpoise vocalizations, he found¹ evidence that animals shied away from the construction site even up to distances of 21 kilometres. "In most cases, there's a strong effect from construction," says Tougaard. But his work and follow-up studies by other researchers show² that porpoise visits to the wind-farm area increase once construction has finished.

To avoid severe problems such as damaging the hearing of marine mammals, Cape Wind is required as part of its lease to have at least one observer monitoring each turbine installation. The company will delay pile driving if a marine mammal comes within 750 metres of the site, says Rachel Pachter, a permitting and environmental project manager for Cape Wind.

Other projects might have to take stronger measures to accommodate the endangered North Atlantic right whale (*Eubalaena glacialis*). Cape

Wind is outside the whales' typical migration path, but the animals pass closer to many other potential wind-farm sites along the East Coast. In 2012, several environmental groups and developers agreed to guidelines that would minimize risks to the whales. For example, during certain migratory periods, developers are expected to mitigate the noise through measures such as generating curtains of bubbles around the project to dissipate sound waves.

Peter Tyack, a marine biologist at the Woods Hole Oceanographic Institution in Massachusetts, says that these and other measures will reduce the effects of construction on whales. "I would be surprised if it has a big impact on them," he says, although he advocates putting measures in place to reduce the risk.

"I don't think we're looking at easy street here."

Once construction is over, wind farms could even provide benefits to the marine animals. Researchers have suggested that forests of offshore turbines can become artificial reefs, and a study published³ this year using tracking data found that seals sought out turbines at active wind farms in Germany and the United Kingdom, perhaps to forage around them. "What really shocked me was the pattern they showed," says Deborah Russell, a marine biologist at the University of St Andrews, UK, who led the study. The seals may like the protection that the wind farm provides from boats, she says.

Beyond concerns over wildlife, US proponents of offshore wind farms have had to address the issue of hurricanes, which could buffet turbines with gusts much stronger than those experienced by facilities in Europe. Although no East Coast hurricane has tested an offshore turbine, engineers say that wind farms can be built to withstand them. Experience with offshore structures such as oil platforms provides confidence that widespread failure of turbines should not be a problem, says James Manwell, a mechanical engineer and director of the Wind Energy Center at the University of Massachusetts Amherst. But fortifying turbines requires extra steel, which drives up expenses. Companies will have to determine how to balance the costs and benefits of reinforcing wind farms for infrequent hurricanes.

ROCKY WATERS

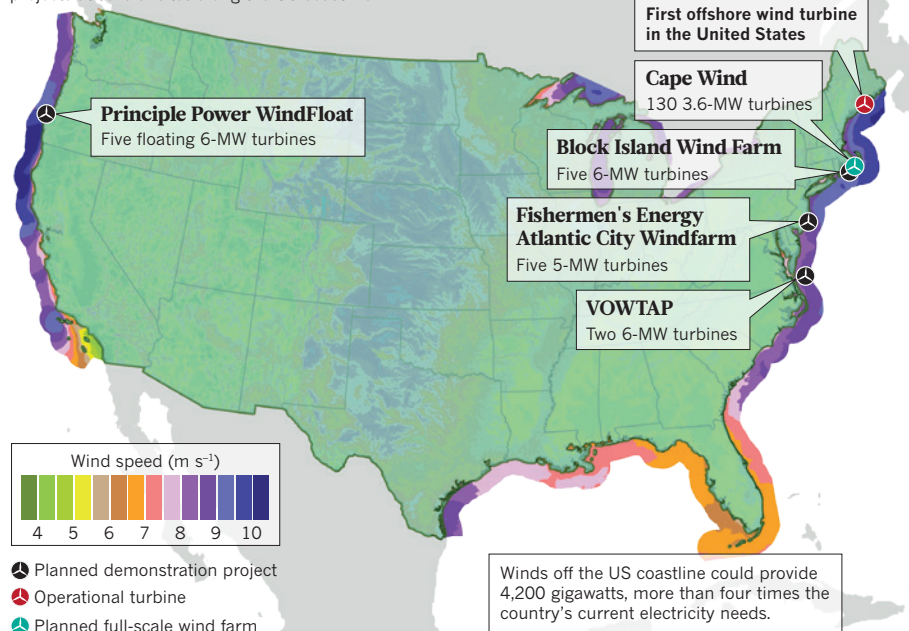
For developers, the big question is whether it makes economic sense to develop wind farms off US shores. Any extra effort associated with meeting environmental regulations or preparing for severe storms will increase the cost of construction, at a time when wind farms have to compete with a bounty of cheap natural gas.

So developers are experimenting with different designs in the hope of driving down costs.

➔ NATURE.COM
For a video about the
Castine turbine, see:
go.nature.com/m9hqng

Air power

Plans are moving forward to develop offshore wind projects at several sites along the US coastline.



Monopile foundations — made of a single huge tube driven into the seabed — are generally cheapest and well tested, but some developers are trying foundations that twist three piles around a central column, similar to structures used for offshore oil and gas platforms. As turbines get larger, these multi-pile designs may be more stable and cost effective than monopiles.

Another solution could be simply to float the turbines, as researchers have done with the experimental design in Castine. Habib Dagher, an engineer at the University of Maine in Orono, and his colleagues constructed the base of the turbine out of hollow concrete tubes; it is held steady in the waves by three cables attached to anchors on the sea floor. Such a design could operate in much deeper waters — where it is impractical to use a monopile that reaches all the way to the sea floor — and would be relatively cheap to construct, because it could be manufactured onshore and simply towed out to the designated location, says Dagher.

He and others will have to prove that the full-size floating structures can stay upright and stable during major storms. Measurements taken since the demonstration turbine's launch suggest that the design will perform well. Even in winds up to about 80 kilometres per hour, the turbine leans by only 5.9 degrees, which indicates that a full-sized device should remain stable during storms so powerful they are expected to strike only once every 500 years, says Dagher.

Floating turbines were not taken seriously ten years ago, but now they are emerging as serious contenders, says Musial. An experimental 2-megawatt floating turbine off the coast of Portugal has been working since 2012, and Japan

has two floating turbines already connected to the power grid. The US energy department has also expressed interest in the design: one of the three demonstration projects funded by the agency this year will station five 6-megawatt floating turbines in 350 metres of water off the coast of Coos Bay, Oregon (see 'Air power').

POLITICAL PROBLEMS

Experts say that the environmental and technical challenges for offshore wind are surmountable. The biggest barrier at the moment is the tangled fabric of policy rules that slow projects and provide insufficient certainty for developers and investors, says Willett Kempton, who studies offshore-wind policy at the University of Delaware in Newark. In New Jersey, a group of investors from the commercial fishing industry called Fishermen's Energy succeeded in securing one of the three Department of Energy grants, but has been locked in a court battle with the state Board of Public Utilities. The board has rejected the group's application for a demonstration project off the coast of Atlantic City, saying that the state's electricity users would bear too much of the cost. The most recent decision, handed down by a New Jersey appellate court on 18 August, will force the board to reconsider the application.

Other projects have also fallen prey, at least in part, to concerns over politics, policy and costs. In Maine, for example, a deal to build a US\$120-million wind farm, involving the Norwegian energy company Statoil, fell apart after the state's governor elected to reopen the bidding process to other developers.

Kempton lauds the energy policies and financial incentives of the European countries that have pushed ahead with offshore

wind. Denmark, for example, has set a target of getting 50% of its power from wind by 2020. To help meet that goal, it requires that the grid connect to offshore wind farms, and it sets a price for electricity from those facilities.

Such long-term support is much more attractive to the wind-energy industry than the kind of short-term tax credits offered by the US federal government, which appear and disappear depending on the whims of Congress as it moves through its two-year election cycle. Some US states are starting to provide better support for projects that could encourage investors and developers. For example, early efforts to build a large wind farm off the coast of Maryland have been buoyed by the state's offer of subsidies for developers. On 19 August, Italian energy company Renexia won an auction to lease 32,000 hectares off Maryland's coast, with a bid of \$8.7 million.

For now, however, the greatest chance of getting turbines into the water lies farther to the north. In September, developer Deepwater Wind received what it says is the final federal approval required to install turbines off the coast of Rhode Island in the middle of next year as part of a demonstration project. And Energy Management hopes to start constructing its much larger Cape Wind project even sooner.

To make that possible, the port of New Bedford, Massachusetts, is hurrying to finish preparations that will enable it to handle the 1,400-tonne cranes required to lift the turbines onto ships that will carry them to the Cape Wind site. Massive excavators are working 24 hours a day to deepen the port.

"I think in the next several months we're going to know whether Cape Wind is going to be real or not," says Bill White, senior director for offshore wind at the Massachusetts Clean Energy Center, which is managing the New Bedford site.

Out on a small boat touring the port, White says that Cape Wind is only the beginning for New Bedford's long-term plans. The hope is that the upgraded harbour will serve as a staging ground for offshore-wind projects all along the eastern seaboard.

White and the project engineers have visited ports in Europe, where they learned some valuable lessons — in particular, that loading areas for offshore-wind parts must handle a tremendous amount of weight. A carefully orchestrated sandwich of concrete, steel and sand has added many metres of sturdy land to the port.

The Europeans also taught him something else. "They said be careful with expectations," White says. "It's going to take some time." ■

Gene Russo is a former Nature editor.

1. Tougaard, J., Carstensen, J. & Teilmann, J. *Acous. Soc. Am.* **126**, 11–14 (2009).
2. Dähne, M. *et al. Environ. Res. Lett.* **8**, 025002 (2013).
3. Russell, D. J. F. *et al. Curr. Biol.* **24**, R638–R639 (2014).

COMMENT

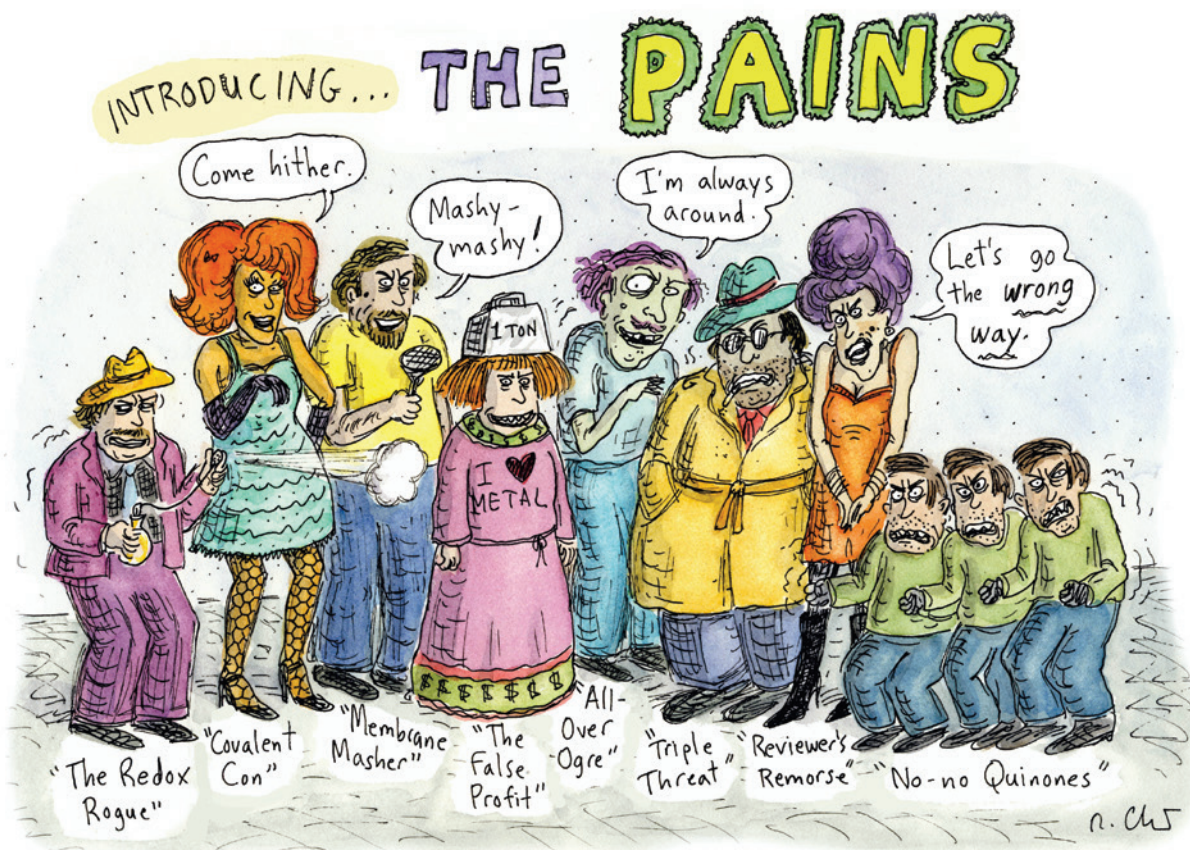
ETHOLOGY Julian Huxley's animal-behaviour classic at 100 **p.484**



ASTROPHYSICS Literary experiment conveys cosmology in few words **p.485**

MUSIC Tree-ring expert authenticates priceless violins **p.486**

PALAEONTOLOGY 'Hobbit' scientists urge Twitter critics to read the literature **p.487**



Chemical con artists foil drug discovery

Naivety about promiscuous, assay-duping molecules is polluting the literature and wasting resources, warn **Jonathan Baell** and **Michael A. Walters**.

Academic researchers, drawn into drug discovery without appropriate guidance, are doing muddled science. When biologists identify a protein that contributes to disease, they hunt for chemical compounds that bind to the protein and affect its activity. A typical assay screens many thousands of chemicals. 'Hits' become tools for studying the disease, as well as starting points in the hunt for treatments.

But many hits are artefacts — their activity

does not depend on a specific, drug-like interaction between molecule and protein. A true drug inhibits or activates a protein by fitting into a binding site on the protein. Artefacts have subversive reactivity that masquerades as drug-like binding and yields false signals across a variety of assays^{1,2}.

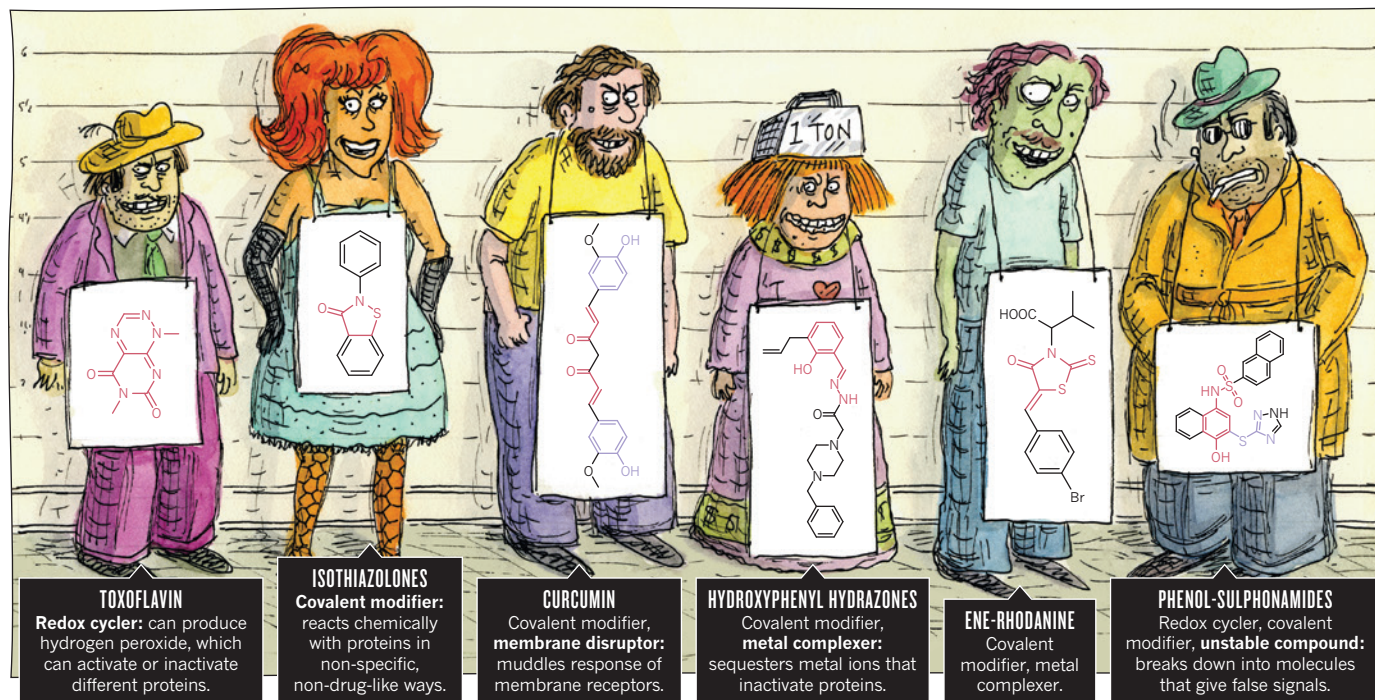
These molecules — pan-assay interference compounds, or PAINS — have defined structures, covering several classes of compound (see 'Worst offenders'). But biologists

and inexperienced chemists rarely recognize them. Instead, such compounds are reported as having promising activity against a wide variety of proteins. Time and research money are consequently wasted in attempts to optimize the activity of these compounds. Chemists make multiple analogues of apparent hits hoping to improve the 'fit' between protein and compound. Meanwhile, true hits with real potential are neglected.

Until the past decade or so, screening ►

WORST OFFENDERS

Pan-assay interference compounds (PAINS) fall into hundreds of chemical classes, but some groups occur much more frequently than others. Among the most insidious are the eight shown here (reactive portions shown in red and purple). These and related compounds should set off alarm bells if they show up as 'hits' in drug screens.



► work was mainly performed at pharmaceutical companies, and supported by experienced chemists. It is now increasingly common in academic environments, in which the same support may not exist. An example of this trend, the Academic Drug Discovery Consortium, founded in 2012, already boasts more than 115 centres in 9 countries. Unfortunately, growing numbers of academic drug researchers are typically not trained to separate hits into compounds good, bad and ugly³.

The apparent activity of PAINS is so seductive that work continues despite published reports explaining that a compound interferes with assays. One under-appreciated study⁴ identified half-a-dozen molecules that showed activity against one-third or more of the proteins that they were screened against.

Repeated identification of the same types of molecule as promising hits against different proteins is polluting the chemical literature. Publications falsely revalidate molecules as good drug leads and feed Sisyphean cycles of 'screen, publish, flounder'. Chemical companies include these artefacts in their sales catalogues as published protein inhibitors, and other biologists start using them in their own studies.

Often termed 'bad actors', PAINS are actually excellent actors: they impersonate promising leads only too well. One of us (J.B.) first published a guide¹ to identifying PAINS in 2010, after his lab spent the equivalent of two or three employee years on futile work. The other of us (M.A.W.) became an

anti-PAINS advocate after preparing a manuscript and patent application for a potential fungicide, only to realize that many of the compounds identified as 'actives' were not. For instance, some compounds underwent non-specific chemical reactions with proteins. More than a year was spent working out what was really going on, using assays for confounding properties such as aggregation, chemical decomposition, protein reactivity and fluorescence.

Better awareness of these molecules and a few precautionary practices could, we estimate, save years of biomedical-research work and millions of dollars in wasted experiments (see 'PAINS-proof drug discovery').

MISLEADING MIRAGE

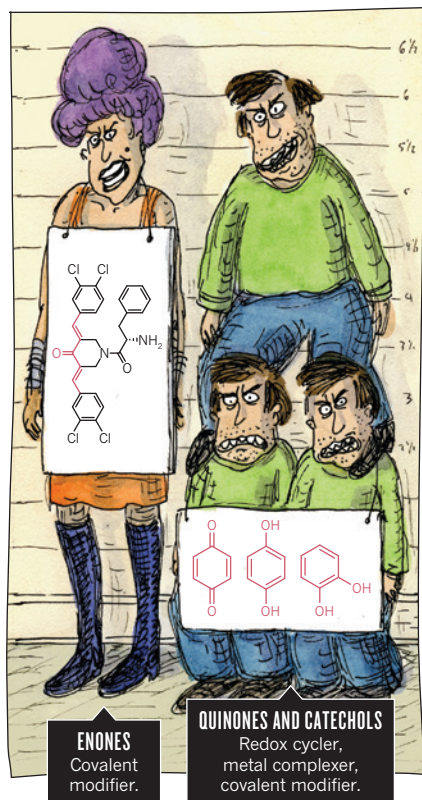
In a typical academic screening library, some 5–12% of compounds are PAINS¹, which can be rediscovered in multiple assays. This reflects the proportions in the pre-assembled libraries that most academic laboratories buy or access, for example the Library of Pharmacologically Active Compounds (LOPAC) from chemical-supply company Sigma-Aldrich, and the Molecular Libraries Small Molecule Repository (MLSMR) from the US National Institutes of Health.

Most PAINS function as reactive chemicals rather than discriminating drugs. They

give false readouts in a variety of ways. Some are fluorescent or strongly coloured. In certain assays, they give a positive signal even when no protein is present. Other compounds can trap the toxic or reactive metals used to synthesize molecules in a screening library or used as reagents in assays. These metals then give rise to signals that have nothing to do with a compound's interaction with a protein. Other PAINS coat a protein or sequester metal ions that are essential to a protein's function, or they may alter proteins chemically without fitting specifically into a binding site. All of these mechanisms thwart further attempts to improve a molecule's biological activity by tweaking its structure (the art known as medicinal chemistry).

PAINS often interfere with many other proteins as well as the one intended. For example, under certain assay conditions, some molecules — redox cyclers — produce hydrogen peroxide⁵, an antiseptic that is also produced by certain immune cells. The hydrogen peroxide inactivates the target protein and makes the compound look like a good inhibitor. But the compound itself may not bind to the protein at all.

After a hit is identified, often the next step is to test it in cells. PAINS frequently have more than one interference mechanism. They might produce a desired cellular readout, such as growth inhibition, even without acting as expected. Researchers are too readily convinced that a compound has potent activity against a protein target. They purchase similar compounds from commercial



suppliers and use expensive medicinal-chemistry resources to make and test more analogues. Sometimes a molecule fails only after going through patenting and assessment in animals⁶. It is regrettably easy, in our experience, to get a misleading readout in an animal model that is not related to the anticipated mechanism of action.

In fact, real hits — molecules that do interact specifically with the desired protein — often do not show activity in cells until structures are modified to bind more efficiently or to enter cells more readily⁷.

ALL PAIN, NO GAIN

Some of the compounds that should ring the most warning bells are toxoflavin and polyhydroxylated natural phytochemicals such as curcumin, EGCG (epigallocatechin gallate), genistein and resveratrol. These, their analogues and similar natural products persist in being followed up as drug leads and used as 'positive' controls even though their promiscuous actions are well-documented^{8,9}.

Rhodanines exemplify the extent of the problem. A literature search reveals 2,132 rhodanines reported as having biological activity in 410 papers, from some 290 organizations of which only 24 are commercial companies. The academic publications generally paint rhodanines as promising for therapeutic development. In a rare example of good practice, one of these publications¹⁰ (by the drug company Bristol-Myers Squibb) warns researchers that these

types of compound undergo light-induced reactions that irreversibly modify proteins. It is hard to imagine how such a mechanism could be optimized to produce a drug or tool. Yet this paper is almost never cited by publications that assume that rhodanines are behaving in a drug-like manner.

Very occasionally, a PAINS compound does interact with a protein in a specific drug-like way. If it does, its structure could be optimized through medicinal chemistry. However, this path is fraught — it can be difficult to distinguish when activity is caused by a drug-like mechanism or something more insidious. Rhodanines also occur in some 280 patents, a sign that they have been selected for further drug development. However, to our knowledge, no rhodanine plucked out of a screening campaign is in the clinic or even moving towards clinical development. We regard the effort to obtain and protect these patents (not to mention the work behind them) as a waste of money.

In a move partially implemented to help editors and manuscript reviewers to rid the literature of PAINS (among other things), the *Journal of Medicinal Chemistry* encourages the inclusion of computer-readable molecular structures in the supporting information of submitted manuscripts, easing the use of automated filters to identify compounds' liabilities. We encourage other journals to do the same. We also suggest that authors who have reported PAINS as potential tool compounds follow up their original reports with studies confirming the subversive action of

THREE TIPS

PAINS-proof drug discovery

Learn disreputable structures.

Pan-assay interference compounds (PAINS) encompass some 400 structural classes, but more than half of PAINS in a typical library fall into just 16 easily recognizable categories^{1,2}. Software tools can filter PAINS from screening libraries, but they are no match for sharp-eyed scientists.

Researchers should familiarize themselves with the most common structures and consult with PAINS-savvy medicinal chemists when these structures show up in hits. Scan compounds for functional groups that could have reactions with, rather than affinity for, proteins. These may not be flagged as PAINS, but can be similarly misleading.

Check the literature. Search by both chemical similarity and substructure to see if a hit interacts with unrelated proteins or has been implicated in non-drug-like mechanisms. Online services such as

SciFinder, Reaxys, BadApple or PubChem can assist in the check for compounds (or classes of compound) that are notorious for interfering with assays.

Assess assays. For each hit, conduct at least one assay that detects activity with a different readout. Be wary of compounds that do not show activity in both assays. If possible, assess binding directly, with a technique such as surface plasmon resonance.

Drill into further details. Compounds that become more active over time are probably acting through non-drug-like mechanisms. When a compound is tested with a protein and then diluted away, its activity should decrease. If not, it might be a PAINS.

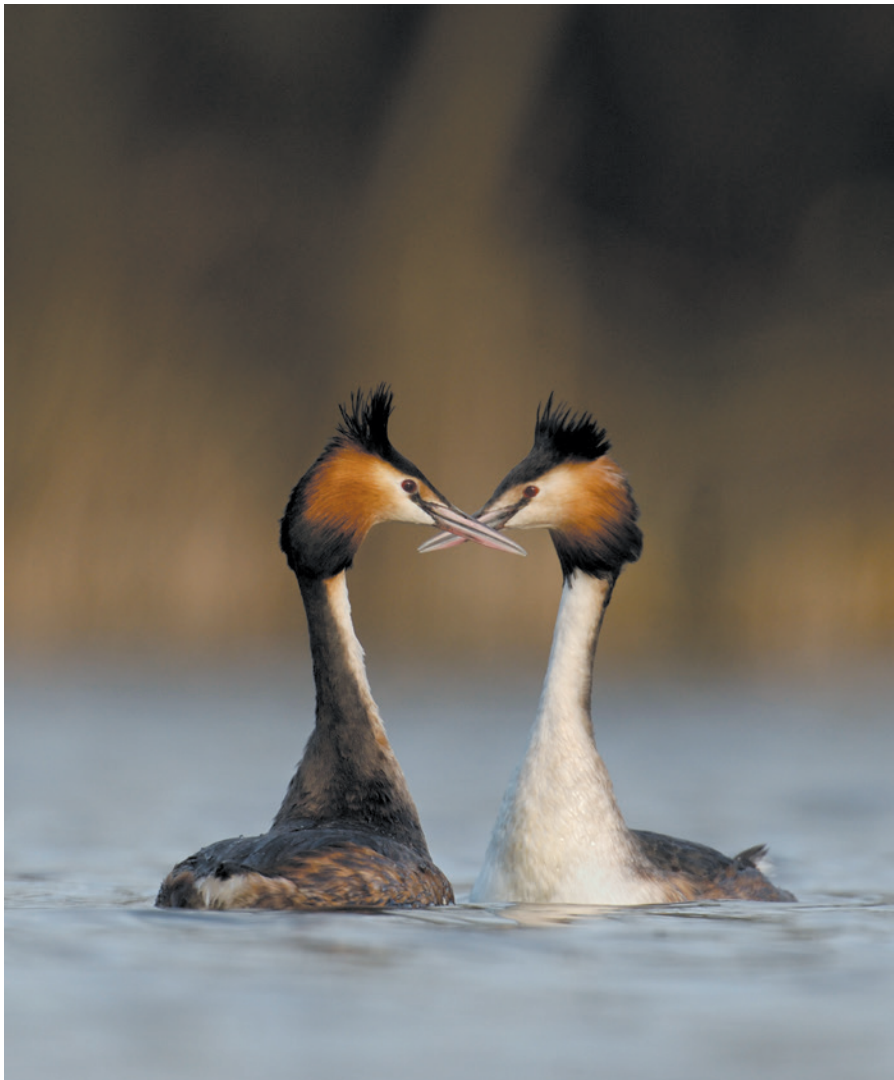
Verify the identity and purity of hits. Sometimes a positive readout is due to an unstable breakdown product of the chemical identified from the screening library^{1,2}. Remake or repurify these molecules and test them again. **J.B. & M.A.W.**

these molecules. Labelling these compounds clearly should decrease futile attempts to optimize them and discourage chemical vendors from selling them to biologists as valid tools.

Most of all, academic drug discoverers must be more vigilant. Molecules that show the strongest activity in screening might not be the best starting points for drugs. PAINS hits should almost always be ignored. Even trained medicinal chemists have to be careful until they become experienced in screening. Take it from us: do not even start down these treacherous routes. ■

Jonathan Baell is professor of medicinal chemistry at Monash University in Melbourne, Australia. **Michael A. Walters** is research associate professor of medicinal chemistry at the University of Minnesota in Minneapolis, USA.
e-mails: jonathan.baell@monash.edu; mwalters@umn.edu

1. Baell, J. B. & Holloway, G. A. *J. Med. Chem.* **53**, 2719–2740 (2010).
2. Baell, J. B. *Future Med. Chem.* **2**, 1529–1546 (2010).
3. Dahlin, J. L. & Walters, M. A. *Future Med. Chem.* **6**, 1265–1290 (2014).
4. Hu, Y. & Bajorath, J. *AAPS J.* **15**, 808–815 (2013).
5. Baell, J. B. *Drug Discovery Today* **16**, 840–841 (2011).
6. Ramesh, C. et al. *J. Med. Chem.* **53**, 1004–1014 (2010).
7. Baell, J. B., Ferrins, L., Falk, H. & Nikolakopoulos, G. *Aust. J. Chem.* **66**, 1483–1494 (2013).
8. Priyadarsini, K. I. *Curr. Pharm. Des.* **19**, 2093–2100 (2013).
9. Ingólfsson, H. I. et al. *ACS Chem. Biol.* **9**, 1788–1798 (2014).
10. Voss, M. E. et al. *Bioorg. Med. Chem. Lett.* **13**, 533–538 (2003).



Great crested grebes performing head-shaking, part of their courtship ritual.

IN RETROSPECT

The Courtship Habits of the Great Crested Grebe

Michael Brooke reappraises Julian Huxley's pioneering classic of animal behaviour on its centenary.

As a scion of the family that produced 'Darwin's Bulldog' Thomas Henry Huxley, novelist Aldous Huxley and Nobel-prizewinning biologist Andrew Huxley, Julian Huxley (1887–1975) seemed destined to shine. He did, notably as an architect of the mid-twentieth-century evolutionary synthesis that merged Darwin's ideas on natural selection with population genetics.

Decades before that, however, he helped to pioneer the field of animal behaviour with his groundbreaking work on avian ethology, the 1914 *Courtship Habits of the Great Crested Grebe*. In it, he demonstrated how detailed observations of individual birds can prompt profound biological questions, and sometimes reveal the outline of the answers.

Huxley was keenly interested in

ornithology from his youth. In 1911, while away from lecturing duties at the University of Oxford, UK, he began observing the courtship of the redshank *Tringa totanus* in Cardigan Bay, Wales. He found that although female redshanks did not actively select a mate from among competing males, they had the power to accept or reject each suitor — supporting part of Darwin's theory of sexual selection. The following April, Huxley and his brother Trevenen spent two weeks watching the courtship of great crested grebes (*Podiceps cristatus*). They did so at a reservoir near the Hertfordshire town of Tring, now renowned as home to the matchless bird collections of the Natural History Museum. The result was a paper published in the *Proceedings of the Zoological Society of London* in 1914 and later, in slightly abbreviated form, as a pocket-sized book.

By the month of the brothers' observations, the grebes had already paired. Nevertheless, male and female, whose plumages are virtually identical, engaged in striking behaviours such as the "cat attitude" and the "penguin dance", as Huxley colourfully labelled them. These he interpreted as necessary to bring the two birds into what he perceived as the emotional synchrony needed for coition, nest-building and egg-laying. To achieve this, some behaviours have undergone a gradual change from useful action to symbol to ritual.

It was Huxley's landmark paper that identified this process of ritualization in animal behaviour (he organized a Royal Society symposium to discuss it in 1965). Huxley also realized that ritualization extended to mammals, including people. With a sprinkling of references to Dante, Plato and Shakespeare's *Romeo and Juliet*, he digresses to muse on how human courtship so often and so predictably proceeds from hand-holding to kissing to more. More formally, he realized that behaviours may be shaped by evolution.

Darwin conceived sexual selection as having two principal components. The first, which still prevails, was that males would compete among themselves for access to females — leading, for example, to the huge size of belligerent bull elephant seals striving to monopolize a stretch of breeding beach. Second, he thought that ornamentation in one sex, most often the male, might be favoured by a mating preference of the other sex.

Huxley found this concept more difficult because of the similar breeding plumage in both sexes of great crested grebe, and because courtship continues well after the birds have paired off. Huxley's difficulties barely surface in the book, although he does presage the idea of runaway sexual selection, in which female preference for a male trait leads to ever more extravagant male traits. This latter idea was subsequently developed by Ronald Fisher in *The Genetical Theory of Natural Selection* (1930). But in 1938, Huxley



Julian Huxley in 1914.

published a paper in *The American Naturalist* that effectively poured cold water on any enthusiasm for female choice, and even more for mutual choice.

There matters largely rested until the early 1980s, when Malte Andersson showed that female choice did select for extreme male tail length in the African widowbird (*Euplectes progne*). Ten years later, Ian Jones and Fiona Hunter studied the crested auklet (*Aethia cristatella*), a monogamous seabird in which both sexes are ornamented. The parallels with the great crested grebe are obvious. Jones and Hunter showed that both males and females responded to accentuated models of the opposite sex with more frequent displays — confirming that ornaments in both sexes could be favoured by mutual mating preferences. Although beyond the scope of that study, it also seemed possible that ornament size influenced the likelihood of re-pairing the following year. That would have further undermined Huxley's reluctance to concede a role for sexual selection in any display after birds had paired for the season.

In 1946, Huxley became the first director of the fledgling United Nations Educational, Scientific and Cultural Organization (UNESCO), and he was instrumental in the 1961 founding of the World Wildlife Fund, now known as WWF. In the field of evolution, his overwhelming influence may have put a brake on the study of sexual selection, and his grebe-courtship observations have largely been superseded by those of zoologist Ken Simmons. But nobody has put two weeks' birdwatching in the spring sunshine beside an English reservoir to greater heuristic effect. ■

Michael Brooke is Strickland Curator of Ornithology at the University Museum of Zoology in Cambridge, UK.
e-mail: m.brooke@zoo.cam.ac.uk

COSMOLOGY

A few words on infinity

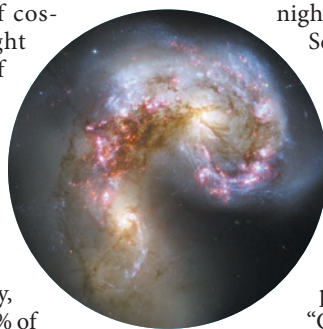
Lucy Fortson enjoys a slim primer on cosmology that uses a cleverly constrained lexicon.

When we think of cosmology, we might think of some of its most complex scientific theories, such as inflation or the general theory of relativity. Or we might consider its astounding discoveries, such as the twinned mysteries of dark matter and dark energy, which together comprise 96% of the contents of the Universe. We may then have the unsettling idea that the remaining 4% (including the stuff of which humanity is made) is insignificant in the grand scheme of things — a thought all the more remarkable when we consider the extent to which the bits of recycled stars known as humans understand cosmology.

The extraordinary story of the Universe and our journey to understand it is not an easy one to tell to the general public. But because it is the story that binds us all together, it is important to tell it in myriad ways to reach as many people as possible. *The Edge of the Sky* is an inventive, enjoyable and thought-provoking contribution to that effort.

Inspired by 'Up Goer Five' — an instalment of the webcomic *xkcd*, by former NASA roboticist Randall Munroe — theoretical cosmologist Roberto Trotta uses fewer than 90 pages to take the reader through a strange, yet sometimes compelling, exercise. He translates our current understanding of cosmology into the 1,000 most popular words in English (or as the book would say, "the ten hundred most-used words in our tongue"). Effectively, this approach demanded the invention of a new language through renaming of common objects: aeroplanes, for instance, become flying cars. It is as if we are reading a book by an observer on a different planet. Paradoxically, this simplicity of language encourages us to think outside the familiar.

So we follow a "student-person" (scientist) through one



The Antennae galaxies.

night of observation using a "Big-Seer" (telescope), and her reflections on the series of "Why? questions" (science) that have led her, and humanity, to the point of understanding as much as we do about the "All-There-Is" (Universe).

We move from early (Western) cosmology that the "old people" believed in, centred on "Crazy Stars" (planets), to the discoveries of planets outside the Solar System and today's search for new "Home-Worlds". We then follow a fairly conventional path with the usual suspects, including the "student-people" Mr Hubble, Mr Einstein and Mrs Rubin, as Trotta brings us through discoveries from the expansion of the Universe to Big Bang nucleosynthesis — all using a total of just 707 different words (and 42 names).

This linguistic constriction left me wondering about the intended readership. At times, the exercise feels like just that, yielding pained oversimplifications that give the impression of inaccuracy, such as "tired light" for redshift. We begin to wonder whether Trotta embarked on the project merely as an intellectual puzzle, proving to himself that he could write a satisfactory explanation of cosmology with an arbitrary constraint on vocabulary. (There are faint echoes here, for instance, of the French writer and filmmaker Georges Perec's experimental 1969 novel *La Disparition*, which excludes the letter e.)

In reading this book, do the cosmologically uninitiated really gain a clearer understanding of the workings of the Universe, and could they then explain this to someone else using ordinary terminology? Probably not. But, as with a well-told folk tale, perhaps some of the passion and poetry of this ultimate quest will be conveyed, inspiring a new student-person to ask the right Why? questions. This would be no small success. ■

Lucy Fortson is associate professor of physics at the University of Minnesota in Minneapolis, where she teaches cosmology. She is also committed to improving the scientific literacy of the general public through the citizen-science project Zooniverse (www.zooniverse.org).
e-mail: fortson@physics.umn.edu



The Edge of the Sky: All You Need to Know about the All-There-Is
ROBERTO TROTTA
Basic Books: 2014.



Peter Ratcliff restores and investigates violins from his workshop in Hove, UK.

Q&A Peter Ratcliff

Violin detective

Peter Ratcliff uses dendrochronology — tree-ring dating — to pin down the age and suggest the provenance of stringed instruments. As he prepares to speak at the Woodmusic instrument-identification conference in Cremona, Italy, on 30 September, he talks about the science of spotting fakes, and the 14 Stradivarius instruments made from the same spruce tree.

How do you use dendrochronology for dating?

The bellies of most Western stringed instruments are made from spruce, whose tight, even growth is easy to analyse. When I am sent an instrument, I measure the width of each ring in the varnished wood. The unique pattern formed by the rings can be matched with those on thousands of instruments in databases, as well as cores extracted from the oldest living trees and ancient timber. The year of the most recent ring on an instrument is the earliest it could have been built.

How do you pin down the school of making?

Ring patterns depend on weather, climate, soil composition and other local factors, so the pattern in any tree resembles those of its neighbours. I list other instruments whose wood grain is the closest match. Occasionally, I will find some by the same maker or, more rarely, by different makers who used the same tree — such as a 1744 violin made by Giuseppe Guarneri Del Gesù from Cremona, for instance, matched to a 1746 Sanctus Seraphin from Venice, and surprisingly, a 1767 José Contreras from Madrid. I am cautious not to make hard claims about authenticity, but if I examine a violin and 90% of instruments that match dendrochronologically are from, say, seventeenth-century

England, I will suggest that the owner show it to an expert who can assess whether style, varnish and construction conform to that school.

What have you learned about the habits of old violin makers?

To make a violin today, you buy a wedge of spruce, split it down the middle and align the halves so you have a symmetrical pattern — a ‘book match’. It is clear that many early makers did not work in this way. In a study of 13 violins and violas made by Andrea Amati, the sixteenth-century grandfather of modern violin-making, investigator John Topham and I found that 5 came from the same tree and only one was a true book match. I have also found that at least 14 violins and violas built by Antonio Stradivari between 1695 and 1705 are made from a single tree. My guess is that these old masters would buy a log, split it into wedges thick enough for half the soundboard, and hang them on a rack, sometimes for years, without worrying about book matches. Many soundboards are mismatched or come from different trees.

Have you spotted fakes?

Several — including two violins falsely attributed to Stradivari, and some that could not have been made before 1920. But two

instruments have gone up in value after I found that their soundboards matched trees known to have been used by Stradivari; one subsequently sold at auction for more than four times its estimate. Many convincing forgeries were made in the nineteenth and early twentieth centuries, but the science did not exist then. Forgers now are aware of dendrochronology, and it could be a problem if they use wood from old chalets to build sophisticated copies of historical instruments.

KAMILA RATCLIFF

How about unintentional deceit?

I never like to ‘kill’ a violin — reveal it as not what it seems. But if the wood does not match the claims, I investigate. I was recently sent photos of a violin supposedly made by an Italian craftsman who died in 1735. The wood dated to the 1760s, so I knew he could not have made it. But I did see strong correlations to instruments made by his sons and nephews who worked in the 1770s. So I deduced that the violin might have been damaged and an entirely new soundboard made after the craftsman’s death. The violin was pulled from auction, but not before it had received bids of more than US\$100,000.

Will dendrochronology change the market?

I think it already has, and has called into question some incorrect historical assumptions. Large violins of the Brescian school, which have a double line of inlaid decoration, were thought to have faded out with the death of maker Giovanni Paolo Maggini in about 1630. But I have tested 4 of these instruments and found that they were made at least 50 years after his death. Several important UK and US dealers and auction houses have found the information useful, especially when it confirms what they already believe. Others have knowingly sold instruments that were not quite what was claimed, and many of these are nervous about dendrochronology. Eventually, I’m hoping, this analysis will become routine. If you are spending £400,000 on a violin, what’s another £500 for a scientific report?

Can you identify violins made from the same tree by their sound?

I don’t believe this has been tested, but I would wager that a musician would not be able to select a pair of same-tree violins from a crowd. Incidentally, there does not seem to be any scientific or acoustic evidence that older instruments sound better. In an experiment reported this year by researcher Claudia Fritz, six old violins, including five Strads, were compared with six new ones in a double-blind test. Experienced players could not tell old from new. The new instruments seemed to be the favourites. I suspect that these results are not going to revolutionize the violin world. ■

INTERVIEW BY JASCHA HOFFMAN

Correspondence

Social change affects Antarctic priorities

New research priorities will arise for Antarctic science as a result of climate change and possible tensions between conservation and resource utilization. These priorities are not captured in the Scientific Committee on Antarctic Research's Antarctic and Southern Ocean Horizon Scan (see M. C. Kennicutt *et al. Nature* **512**, 23–25; 2014).

Over the next 20 years, the climate debate is likely to shift towards mitigation and adaptation strategies to offset economic, environmental and social impacts. This shift will prioritize efforts to improve forecasts of the most important elements of the scale, nature and consequences of climate change, and will compel research into potentially high-risk adaptation options such as geo-engineering.

By 2034, the Antarctic Treaty System will probably comprise an increased membership, with internal dynamics driven by parties' priorities. There will be more speculation on resource extraction in the lead up to 2048, which is the earliest juncture at which the indefinite ban on mining under the Madrid Protocol on Environmental Protection to the Antarctic Treaty can be reviewed. Fuelling speculation about exploitation will be a probable increase in ice-free rock, easier access to Antarctica with reductions in seasonal sea ice, and new technologies and drivers for exploration, extraction and visitation. This trend is already evident in the Arctic.

In the Southern Ocean, an expanding krill fishery responding to a growing human population will test the precautionary management regimes that account for dependent predators such as whales, seals and penguins. Science will need to support

sustainable fishery models that integrate the ecological consequences of krill catches with those of climate change.

Adding the social dimension to Kennicutt and colleagues' Horizon Scan in our view reprioritizes some of their pressing questions, as well as raising new and important ones.

Nick Gales *Australian Antarctic Division, Hobart, Australia.*
nick.gales@aad.gov.au

Phil Trathan *British Antarctic Survey, Cambridge, UK.*

Anthony Worby *Antarctic Climate and Ecosystems Cooperative Research Centre, Hobart, Australia.*

Intensive dairy farms becoming greener

I disagree with some of the assertions made by Mark Eisler and colleagues about how to provide a growing human population with high-quality protein from limited arable land (see M. C. Eisler *et al. Nature* **512**, 371; 2014). Their conjecture that cutting animal productivity by 20% would result in 80% better welfare and environmental impact is particularly unrealistic.

On the contrary, milk production is being sustainably intensified by effective management of high-yielding herds. Dairy cows have become more productive through genetic selection and better nutrition, housing and health, with a concomitant drop of 63% in greenhouse-gas emissions per unit of milk produced (J. L. Capper *et al. J. Anim. Sci.* **87**, 2160–2167; 2009).

Typically, the diet of dairy cows in intensive farming systems is 60% forage fibre by weight (see go.nature.com/h3w7yy). Feeding these cows grain does not divert an equivalent mass of food away from humans, because the concentration of protein and other nutrients in milk surpasses that in grain. The

male calves of Holstein dairy cows are already used for meat production, and manure is widely used as fertilizer on dairy farms (see go.nature.com/ebm5a9).

Stephen LeBlanc *University of Guelph, Canada.*
sleblanc@uoguelph.ca

Research critics to be properly informed

You highlight social-media activity following publication of our papers on *Homo floresiensis* (dubbed hobbits), quoting a tweet that dismisses our conclusions as “based seemingly on zilch” (see *Nature* **512**, 235; 2014). Critics of our findings, which question the taxonomic validity of *H. floresiensis* as a separate species, should have at least read the papers and checked the facts.

Our first report (R. B. Eckhardt *et al. Proc. Natl Acad. Sci. USA* **111**, 11961–11966; 2014) shows that specimen LB1, the individual originally designated as representing *H. floresiensis*, is developmentally abnormal; the second (M. Henneberg *et al. Proc. Natl Acad. Sci. USA* **111**, 11967–11972; 2014) presents a diagnosis of Down's syndrome for LB1.

These interpretations are based on detailed comparative skeletal morphology (see the papers' supplementary information) and on earlier diagnoses of Down's syndrome from skeletons (see, for example, A. Czarnetzki *et al. Lancet* **362**, 1000; 2003; and M. Rivollat *et al. Intl J. Paleopathol.* **7**, 8–14; 2014).

Objectivity is key in controversial fields, particularly when the evidence is so hard-won. Crucial evidence in this case would come from radiocarbon dating of tissue from LB1 and from unrestricted access to the skeletal remains of the other 14 *H. floresiensis* individuals so that their details can be studied independently.

Robert B. Eckhardt *Pennsylvania*

State University, University Park, USA. **Maciej Henneberg** *University of Adelaide, Australia.*
eyl@psu.edu

Science should boost well-being, not GDP

To achieve a more socially equitable society in which science benefits everybody, we need structural changes in the way that our economy works to remove the quest for constant growth of gross domestic product (see www.positivemoney.org). Spending billions of dollars on better versions of existing facilities risks entrenching unsustainable and destructive industries, which will not address the global challenges we face (see go.nature.com/kyamxu).

Consider, for example, the eviction of indigenous communities in parts of the world where increasingly large areas of land are being sacrificed to mining activity — a situation currently facing populations in southeastern Ecuador (see go.nature.com/1mlkki). Furthermore, poverty and ill health are on the rise in affluent countries such as the United Kingdom, despite resource-intensive technologies (see go.nature.com/xznlmi).

If science is to serve the public good, we have to shift to more ecosystem-centred systems that also take human rights and well-being into account. Good examples include the farmer field schools set up by the United Nations, engaging farmers in agro-ecological research (see T. MacMillan and T. Benton *Nature* **509**, 25–27; 2014).

Mark A. de Vries *Edinburgh, UK.*
m.a.devries@mail.com

CONTRIBUTIONS

Correspondence may be submitted to correspondence@nature.com after consulting the author guidelines at go.nature.com/cmchno.

Mitochondrial Ca^{2+} uniporter and CaMKII in heart

ARISING FROM M. A. Joiner *et al.* *Nature* **491**, 269–273 (2012); doi:10.1038/nature10234

The influx of cytosolic Ca^{2+} into mitochondria is mediated primarily by the mitochondrial calcium uniporter (MCU)¹, a small-conductance, Ca^{2+} -selective channel^{2–6}—MCU modulates intracellular Ca^{2+} transients and regulates ATP production and cell death¹. Recently, Joiner *et al.* reported that MCU is regulated by mitochondrial CaMKII, and this regulation determines stress response in heart⁷. They reported a very large

current putatively mediated by MCU that was about two orders of magnitude greater than the MCU current (I_{MCU}) that we previously measured in heart mitochondria³; furthermore, the current traces presented by Joiner *et al.* showed unusually high fluctuations incompatible with the low single-channel conductance of MCU. Here we performed patch-clamp recordings from mouse heart mitochondria under the exact

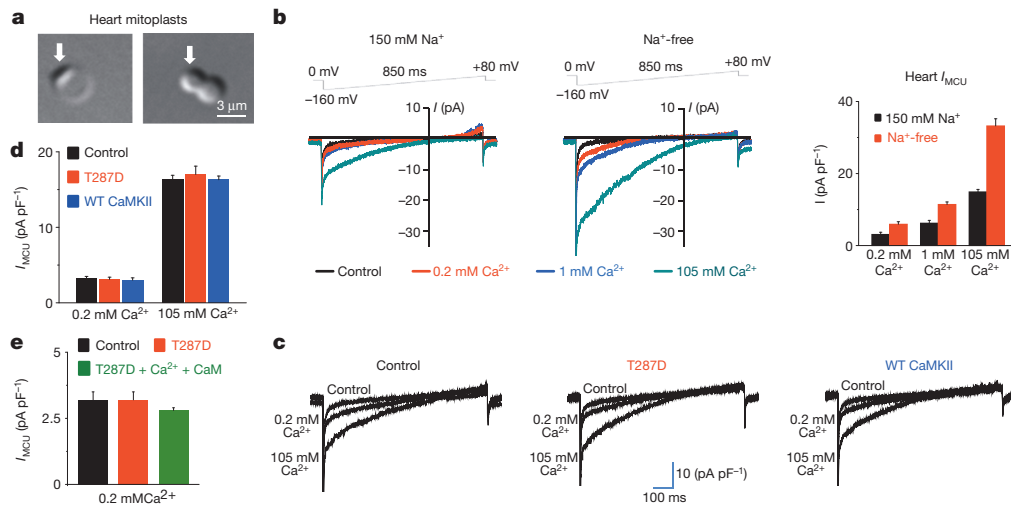


Figure 1 | Heart MCU current and CaMKII. **a**, Transmitted image of heart mitoplasts obtained by exposure of mitochondria to 5-min hypotonic shock. Both round (left) and ‘figure-8-shaped’ (right) mitoplasts were present in this preparation and used for electrophysiological experiments. Arrows indicate remnants of the outer mitochondrial membrane. The average diameter of heart mitoplasts in this preparation is $\sim 4.5 \mu\text{m}$ ($n = 65$), which corresponds well with the average membrane capacitance (C_m) measurements of 0.67 pF that we previously reported. **b**, Representative heart whole-mitoplast MCU currents (I_{MCU}) recorded in the presence (left) or absence (middle) of 150 mM Na-gluconate in both the pipette and bath solutions. I_{MCU} was recorded with different bath Ca^{2+} concentrations: 0.2 mM (red), 1 mM (blue) and 105 mM (green). I_{MCU} was blocked by 50 nM RuR added to the 0.2 mM Ca^{2+} bath solution (control, black). Currents in left and middle panels are not normalized and were recorded from two different mitoplasts with comparable membrane capacitance ($C_m = 0.80 \text{ pF}$ and 0.84 pF , respectively). The voltage ramp protocol used to elicit I_{MCU} is indicated at the top. With Na^+ in the recording solutions we also observed a small outward current at high positive voltages. This current was absent in Na^+ -free conditions (middle and ref. 3). **c**, Pipette solution (in mM): 150 Na-gluconate , 40 HEPES , 2 NaCl , 1.5 EGTA , tonicity 450 mmol per kg with sucrose, $\text{pH } 7.2$ with NaOH . Bath Ca^{2+} solutions with 0.2 and 1 mM Ca^{2+} were prepared by addition of 1 M stock solution of CaCl_2 into the bath solution containing (in mM): 150 Na-gluconate , 40 HEPES , tonicity 300 mmol per kg , $\text{pH } 7.4$ with NaOH . The bath solution with 105 mM Ca^{2+} contained 105 mM CaCl_2 and 10 mM HEPES , $\text{pH } 7.2$ with Tris base. Right: histogram representing average MCU current densities (I_{MCU} normalized to C_m) obtained in the presence (black) or absence (red) of 150 mM Na-gluconate in recording solutions with different bath Ca^{2+} concentrations (0.2 , 1 and 105 mM). Current amplitudes were measured at 5 ms after stepping from 0 to -160 mV . I_{MCU} densities were as follows: at bath 0.2 mM Ca^{2+} , $3.3 \pm 0.4 \text{ pA pF}^{-1}$ ($n = 8$) with 150 Na-gluconate in recording solutions and $6 \pm 0.7 \text{ pA pF}^{-1}$ without Na-gluconate in recording solutions; at bath 1 mM Ca^{2+} , $6.2 \pm 0.7 \text{ pA pF}^{-1}$ ($n = 9$) with Na-gluconate and $11.4 \pm 0.7 \text{ pA pF}^{-1}$ ($n = 6$) without Na-gluconate; at bath 105 mM Ca^{2+} , $14.2 \pm 0.7 \text{ pA pF}^{-1}$ ($n = 12$) with Na-gluconate and

$33.2 \pm 2 \text{ pA pF}^{-1}$ ($n = 7$) without Na-gluconate in the pipette solution. Statistical data are presented as mean \pm s.e.m. **c**, Representative I_{MCU} in control (left), in the presence of a constitutively active monomeric CaMKII (T287D mutant) in the patch pipette (middle), and in the presence of wild-type monomeric CaMKII previously activated (autophosphorylated) with Ca^{2+} /calmodulin (CaM) and Mg^{2+} /ATP (γ -thiol-ATP) (right) in the patch pipette. I_{MCU} was elicited by a voltage ramp protocol (see panel **b**) in the presence of 0.2 and 105 mM Ca^{2+} . I_{MCU} amplitude was monitored for up to 35 min after formation of the whole-mitoplast configuration as in Joiner *et al.*⁷ (however, the calculated diffusion time¹⁵ for the 35-kDa monomer of CaMKII from the pipette into the mitoplast is only $\sim 25 \text{ s}$). Pipette solution contained (in mM): 150 Na-gluconate , 40 HEPES , 2 NaCl , 1.5 EGTA , tonicity 450 mmol per kg with sucrose, $\text{pH } 7.2$ with NaOH . The recombinant T287D and wild-type CaMKII were added to the control solution at 0.5 or $1 \mu\text{M}$, in the presence of 2 mM Na_2ATP and 3 mM MgCl_2 . (Addition of ATP and Mg^{2+} alone did not affect I_{MCU} .) **d**, Histogram showing average I_{MCU} current densities obtained in the absence (black, control) or presence of T287D (red) or wild-type monomeric CaMKII pre-autophosphorylated with thiol-ATP (blue) in the pipette. Currents were measured in 0.2 and 105 mM Ca^{2+} as described in **c**, and amplitudes were determined at 5 ms after stepping from 0 to -160 mV . I_{MCU} densities were as follows: at bath 0.2 mM Ca^{2+} , $3.2 \pm 0.3 \text{ pA pF}^{-1}$ ($n = 17$) in control, $3.2 \pm 0.3 \text{ pA pF}^{-1}$ ($n = 14$) for T287D, and $3.0 \pm 0.3 \text{ pA pF}^{-1}$ ($n = 8$) for autophosphorylated wild-type CaMKII; at bath 105 mM Ca^{2+} , $16.4 \pm 0.5 \text{ pA pF}^{-1}$ ($n = 16$) in control, $17.9 \pm 1.1 \text{ pA pF}^{-1}$ ($n = 11$) for T287D, and $16.2 \pm 0.5 \text{ pA pF}^{-1}$ ($n = 5$) for autophosphorylated wild-type CaMKII. Statistical data are presented as mean \pm s.e.m. **e**, Histogram showing average I_{MCU} current densities in control (black) and in the presence of a constitutively active monomeric CaMKII (T287D mutant) in the patch pipette either alone (red) or with $1 \mu\text{M}$ CaM and $5\text{--}10 \mu\text{M}$ free Ca^{2+} (green). I_{MCU} densities were as follows: at bath 0.2 mM Ca^{2+} , $3.2 \pm 0.3 \text{ pA pF}^{-1}$ ($n = 17$) in control, $3.2 \pm 0.3 \text{ pA pF}^{-1}$ ($n = 14$) for T287D, and $2.8 \pm 0.1 \text{ pA pF}^{-1}$ ($n = 5$) for T287D in the presence of $1 \mu\text{M}$ CaM and $5\text{--}10 \mu\text{M}$ free Ca^{2+} . Current amplitudes were measured at 5 ms after stepping from 0 to -160 mV . Statistical data are presented as mean \pm s.e.m.

conditions used by Joiner *et al.*⁷, and confirm that I_{MCU} in cardiomyocytes is very small and is not directly regulated by CaMKII; thus, the currents presented by Joiner *et al.* do not appear to correspond to MCU, and there is no direct electrophysiological evidence that CaMKII regulates MCU. There is a Reply to this Brief Communication Arising by Joiner, M. A. *et al.* *Nature* **513**, <http://dx.doi.org/10.1038/nature13627> (2014).

The main differences in the experimental conditions used by Joiner *et al.*⁷ and in our previous study³ were: the use of hypotonic shock to prepare mitoplasts (versus French press in our study), the presence of high Na^+ concentration in recording solutions (versus Na^+ -free solutions), and the age of the mice (2–3 months versus 3–4 weeks).

Figure 1a shows mouse heart mitoplasts obtained by exposure of mitochondria to hypotonic shock. The measured average membrane capacitance (C_m) was 0.65 ± 0.03 pF (\pm s.e.m., $n = 65$), which correlates well with C_m measurements reported for heart mitoplasts obtained with French press³, as well as with measurements of the inner mitochondrial membrane surface area using electron microscopy^{8,9} and with estimated measurements of idealized cardiac mitochondria¹⁰. Therefore, the values reported by Joiner *et al.*⁷ seem to be abnormally high (5–9 pF), indicating inaccuracy in monitoring C_m leading to faulty values of I_{MCU} densities throughout the paper.

We recorded I_{MCU} from heart mitoplasts isolated by hypotonic shock with 150 mM Na-gluconate in the pipette and bath solutions (as in Joiner *et al.*⁷; Fig. 1b, left panel) and without Na^+ (conditions previously used by us³; Fig. 1b, middle panel). I_{MCU} recorded in the presence of Na-gluconate was significantly smaller than in its absence (Fig. 1b). Our data support the observation that elevated Na^+ may regulate heart mitochondrial Ca^{2+} concentration^{11,12}. Notably, the whole-mitoplast I_{MCU} was about two orders of magnitude lower than the current reported by Joiner *et al.*⁷ (~ 2 pA at -160 mV in 0.2 mM Ca^{2+} versus ~ 180 pA) and did not exhibit high fluctuations as expected for a small-conductance channel. Also, the current reported by Joiner *et al.*⁷ was not inhibited by Ru360 in the same fashion as the I_{MCU} (ref. 2). In 10 nM Ru360, I_{MCU} shows no immediate inhibition upon stepping from 0 mV to -120 mV (ref. 2), and the inhibition develops slowly over time², whereas the current of Joiner *et al.*⁷ was inhibited immediately upon stepping from 0 to -160 mV. All these observations indicate that Joiner *et al.*⁷ did not record I_{MCU} . We suggest that either they did not record from inner mitochondrial membrane or the integrity of their mitoplasts was compromised.

Next, we tested whether I_{MCU} is directly regulated by CaMKII, as claimed by Joiner *et al.*⁷, who reported that addition of a constitutively active monomeric form of CaMKII (T287D mutant) to the patch pipette potentiated their currents. When we applied T287D mutant CaMKII, we failed to observe any functional change in I_{MCU} , either without (Fig. 1c, middle panel, and Fig. 1d) or with Ca^{2+} plus calmodulin (Fig. 1e). We further verified these results using wild-type monomeric CaMKII pre-autophosphorylated with thiol-ATP to prevent de-autophosphorylation and again observed no change in I_{MCU} (Fig. 1c, right panel, and Fig. 1d).

The noisy currents presented by Joiner *et al.*⁷ do not appear to be carried by MCU, and their extremely high amplitude misrepresents the actual MCU activity in heart. Heart, with abundant mitochondria and frequently elevated cytosolic Ca^{2+} , has very low MCU current³, which is probably critical for avoiding disruption of cytosolic Ca^{2+} signalling and preventing mitochondrial Ca^{2+} overload and cell death. Finally, our electrophysiological experiments with MCU currents did not indicate that MCU is regulated by CaMKII.

Methods

Electrophysiological experiments were performed as in ref. 3. Recombinant δ -human monomeric CaMKII (1–317) was purified from baculovirus using an amino-terminal 6 \times -HN tag and Ni chromatography followed by gel filtration. Activity of recombinant CaMKII was measured in Na-gluconate pipette solution using the peptide substrate AC-2 (ref. 13). Constitutive activity (no Ca^{2+} /calmodulin) was undetectable for wild-type CaMKII and $4.6 \mu\text{mol min}^{-1} \text{mg}^{-1}$ for the T287D mutant. The Ca^{2+} /calmodulin stimulated activity of T287D CaMKII was $9.7 \mu\text{mol min}^{-1} \text{mg}^{-1}$. Wild-type CaMKII was autophosphorylated in γ -thiol-ATP to promote Thr287 autophosphorylation, which allows CaMKII to be active without Ca^{2+} /calmodulin (that is, autonomous activity)¹⁴. The autonomous activity of wild-type CaMKII was $19.4 \mu\text{mol min}^{-1} \text{mg}^{-1}$ ($\sim 91\%$ of the Ca^{2+} /calmodulin stimulated activity).

Francesca Fieni¹, Derrick E. Johnson², Andy Hudmon² & Yuriy Kirichok¹

¹Department of Physiology, University of California San Francisco, San Francisco, California 94158, USA.

email: yuriy.kirichok@ucsf.edu

²Department of Biochemistry and Molecular Biology, Stark Neuroscience Research Institute, Indiana University School of Medicine, Indianapolis, Indiana 46202, USA.

Received 1 August 2013; accepted 17 June 2014.

- Rizzuto, R., Bernardi, P. & Pozzan, T. Mitochondria as all-round players of the calcium game. *J. Physiol.* **529**, 37–47 (2000).
- Kirichok, Y., Krapivinsky, G. & Clapham, D. E. The mitochondrial calcium uniporter is a highly selective ion channel. *Nature* **427**, 360–364 (2004).
- Fieni, F., Bae Lee, S., Jan, Y. N. & Kirichok, Y. Activity of the mitochondrial calcium uniporter varies greatly between tissues. *Nature Commun.* **3**, 1317 (2012).
- Chaudhuri, D., Sancak, Y., Mootha, V. K. & Clapham, D. E. MCU encodes the pore conducting mitochondrial calcium currents. *eLife* **2**, e00704 (2013).
- De Stefani, D., Raffaello, A., Teardo, E., Szabo, I. & Rizzuto, R. A forty-kilodalton protein of the inner membrane is the mitochondrial calcium uniporter. *Nature* **476**, 336–340 (2011).
- Baughman, J. M. *et al.* Integrative genomics identifies MCU as an essential component of the mitochondrial calcium uniporter. *Nature* **476**, 341–345 (2011).
- Joiner, M. A. *et al.* CaMKII determines mitochondrial stress responses in heart. *Nature* **491**, 269–273 (2012).
- Page, E. Quantitative ultrastructural analysis in cardiac membrane physiology. *Am. J. Physiol.* **235**, C147–C158 (1978).
- Smith, H. E. & Page, E. Morphometry of rat heart mitochondrial subcompartments and membranes: application to myocardial cell atrophy after hypophysectomy. *J. Ultrastruct. Res.* **55**, 31–41 (1976).
- Williams, G. S., Boyman, L., Chikando, A. C., Khairallah, R. J. & Lederer, W. J. Mitochondrial calcium uptake. *Proc. Natl Acad. Sci. USA* **110**, 10479–10486 (2013).
- O'Rourke, B. & Maack, C. The role of Na dysregulation in cardiac disease and how it impacts electrophysiology. *Drug Discov. Today Dis. Models* **4**, 207–217 (2007).
- Maack, C. *et al.* Elevated cytosolic Na^+ decreases mitochondrial Ca^{2+} uptake during excitation-contraction coupling and impairs energetic adaptation in cardiac myocytes. *Circ. Res.* **99**, 172–182 (2006).
- Ashpole, N. M. & Hudmon, A. Excitotoxic neuroprotection and vulnerability with CaMKII inhibition. *Mol. Cell. Neurosci.* **46**, 720–730 (2011).
- Rokita, A. G. & Anderson, M. E. New therapeutic targets in cardiology: arrhythmias and Ca^{2+} /calmodulin-dependent kinase II (CaMKII). *Circulation* **126**, 2125–2139 (2012).
- Pusch, M. & Neher, E. Rates of diffusional exchange between small cells and a measuring patch pipette. *Pflügers Archiv.* **411**, 204–211 (1988).

Author Contributions F.F. and Y.K. conceived the project. F.F. performed electrophysiological experiments. D.E.J. and A.H. generated recombinant CaMKII and determined its activity under various conditions. All authors contributed to experimental design, discussed the results, and wrote the manuscript.

Competing Financial Interests Declared none.

doi:10.1038/nature13626

Joiner *et al.* replyREPLYING TO F. Fieni *et al.* *Nature* **513**, <http://dx.doi.org/10.1038/nature13626> (2014)

In our Letter¹ identifying mitochondrial CaMKII as a crucial component of a Ca²⁺-dependent process of heart disease, we used multiple methods to show that CaMKII modulates mitochondrial Ca²⁺ homeostasis, as outlined below. First, we carried out electrophysiology of the mitochondrial calcium uniporter (MCU) current in mitoplasts. In our report¹ we did not claim to measure capacitance of the mitoplast separately from the total capacitance of the mitoplast and pipette. Although we conceded that the approach of Fieni *et al.*² is preferable, we found that even after removing any correction for capacitance, dialysis with constitutively active CaMKII monomers increased MCU current whereas dialysis with catalytically dead CaMKII monomers did not.

Second, we identified candidate CaMKII sites on the MCU amino terminus (serine 57 and serine 92), and used a variety of approaches to provide evidence that both are functional and their phosphorylation by CaMKII increases MCU current. These approaches include transgenic mitochondrial-targeted expression of a highly selective CaMKII inhibitor (mtCaMKIIN), and dialysis of both constitutively active and catalytically inactive control CaMKII in cardiac mitoplasts, as well as in mitoplasts from HEK cells overexpressing wild-type MCU or a mutant form in which the two serines are replaced with alanines (S57A/S92A). We are uncertain why the dialysis by Fieni *et al.*², which used a constitutively active monomeric form of CaMKII, was ineffective in increasing MCU current, but given the tendency with which this kinase may lose activity we prefer a positive control experiment showing that the introduced CaMKII is active within a biological system.

Third, we measured a current from mitoplasts that we believe to be from MCU because: (1) it rectifies inwardly; (2) it displays greater Na⁺ than Ca²⁺ conductance; and (3) it is inhibited by Ru360 (albeit with a different kinetic signature than reported by Fieni *et al.*²). In addition to the voltage-clamp approach, we measured mitochondrial Ca²⁺ entry with Ca²⁺ green-5N dye and mitochondrial-targeted cameleon FRET, which also report on mitochondrial Ca²⁺ entry via the MCU pathway (that is, MCU current), as confirmed by a recent report on MCU knockout mice³. Indeed, mitochondrial Ca²⁺ uptake measured using Ca²⁺ green-5N, intramitochondrial Ca²⁺ sensitive probes and Ca²⁺-induced mitochondrial swelling are absent in MCU knockout mice, indicating that these approaches are reporting on MCU current. These approaches, deployed in a variety of systems, corroborated our findings with voltage clamp and supported the role of CaMKII in facilitating mitochondrial Ca²⁺ entry.

Since the time of our publication we have continued to study the role of CaMKII in mitochondria, including work to validate the Ser 57 and Ser 92 sites on MCU further. We note that our ongoing experiments support the concepts outlined in our original paper. The main finding in Joiner *et al.* was that CaMKII is present in cardiac mitochondria, where

it participates in mitochondrial Ca²⁺ homeostasis and contributes to pathological responses to stress, including myocardial infarction, ischaemia-reperfusion injury and catecholamine toxicity¹. We stand by the findings in our report, and look forward to future studies that will shed light on the contribution of MCU, its regulatory subunits and signalling pathways to mitochondrial biology and disease.

Mei-ling A. Joiner^{1†}, Olha M. Koval¹, Jingdong Li^{1†}, B. Julie He^{1†}, Chantal Allamargot², Zhan Gao¹, Elizabeth D. Luczak^{1†}, Duane D. Hall¹, Brian D. Fink³, Biyi Chen¹, Jinying Yang¹, Steven A. Moore^{4,5}, Thomas D. Scholz⁶, Stefan Strack⁷, Peter J. Mohler^{1†}, William I. Sivitz^{1,3}, Long-Sheng Song¹ & Mark E. Anderson^{1,4†}

¹Department of Internal Medicine and Cardiovascular Center, Carver College of Medicine, University of Iowa, Iowa City, Iowa 52242, USA.

email: mei-ling-joiner@uiowa.edu

²University of Iowa Central Microscopy Research Facility, Carver College of Medicine, University of Iowa, Iowa City, Iowa 52242, USA.

³Iowa City Veterans Affairs Medical, Iowa City, Iowa 52246, USA.

⁴Department of Molecular Physiology and Biophysics, Carver College of Medicine, University of Iowa, Iowa City, Iowa 52242, USA.

email: mark.anderson@jhmi.edu

⁵Department of Pathology, Carver College of Medicine, University of Iowa, Iowa City, Iowa 52242, USA.

⁶Department of Pediatrics, Carver College of Medicine, University of Iowa, Iowa City, Iowa 52242, USA.

⁷Department of Pharmacology, Carver College of Medicine, University of Iowa, Iowa City, Iowa 52242, USA.

†Present addresses: Department of Molecular Physiology & Biophysics, Carver College of Medicine, University of Iowa, 51 Newton Road, Iowa City, Iowa 52242, USA (M.A.J.); The Dorothy M. Davis Heart and Lung Research Institute, The Ohio State University, Columbus, Ohio 43210, USA (J.L., P.J.M.); Feinberg School of Medicine, Northwestern University, Chicago, Illinois 60611, USA (B.J.H.); Johns Hopkins University School of Medicine, 1830 East Monument Street, 9th Floor, Suite 9026, Baltimore, Maryland 21287, USA (E.D.L., M.E.A.).

1. Joiner, M. A. *et al.* CaMKII determines mitochondrial stress responses in heart. *Nature* **491**, 269–273 (2012).
2. Fieni, F., Johnson, D. E., Hudmon, A. & Kirichok, Y. Mitochondrial Ca²⁺ uniporter and CaMKII in heart. *Nature* **513**, <http://dx.doi.org/10.1038/nature13626> (2014).
3. Pan, X. *et al.* The physiological role of mitochondrial calcium revealed by mice lacking the mitochondrial calcium uniporter. *Nature Cell Biol.* **15**, 1464–1472 (2013).

doi:10.1038/nature13627

EARTH SCIENCE

A fresh look at river flow

A detailed survey of the Fraser River in Canada challenges preconceptions about how river water flows. The results call for a re-evaluation of how waterways carve through bedrock to form canyons. [SEE LETTER P.534](#)

NICOLE M. GASPARINI

Anyone who has ever hiked beside, fished in or floated down a bedrock river knows the beauty of the canyons that they create. But how exactly does a river incise through bedrock and cut a deep canyon? Venditti *et al.*¹ explore this question on page 534 of this issue, with their report of an extensive set of data on river-flow velocity through the canyons of the Fraser River in western Canada (Fig. 1). Their observations challenge standard assumptions about water-flow patterns and suggest a mechanism for how bedrock canyons evolve in space and time.

Although researchers have long hypothesized² about the processes that control bedrock incision, it was only in the past 20 years that bedrock rivers gained prominence in the scientific literature. A big reason for this is practical. Scientists and engineers tend to divide rivers into two types: bedrock and alluvial. Bedrock rivers cut directly into bedrock, and are often found in actively uplifting mountainous terrain and sparsely inhabited areas. By contrast, alluvial rivers are usually found in less mountainous — and therefore more habitable — terrain, where people build infrastructure that they want to protect. Understandably, extensive literature exists on the morphology and behaviour of alluvial rivers.

It is tempting to try to fit the behaviour of bedrock rivers into the mould of alluvial rivers, but the two differ in many respects. Venditti and colleagues highlight one example of this: flow patterns in narrow bedrock canyons can act both to locally increase incision rates into bedrock and to maintain nearly vertical bedrock walls through canyons.

To understand Venditti and colleagues' results, we must step back and review some fundamental ideas about flow velocity in rivers. Any student of fluid dynamics learns about the 'law of the wall', which states that the average velocity of turbulent flows increases logarithmically with distance away from a wall — or, for rivers, from the bed of the river channel³ (Fig. 2). This 'law' is ingrained in how scientists and engineers think about, sample and manage rivers. For example, the US



Figure 1 | The Fraser Canyon, Canada.

Geological Survey has developed widely used methods for measuring the average velocity of rivers on the basis of the 'typical' logarithmic velocity profile⁴. But not all velocity profiles are logarithmic. Venditti and colleagues' data illustrate important, previously unobserved aspects of velocity patterns in bedrock canyons that could influence how such canyons are built and maintained.

The authors used a boat-mounted acoustic Doppler current profiler (ADCP) to survey extensive reaches of the Fraser Canyon, which consists of 42 individual bedrock canyons. An ADCP uses the Doppler shift in multiple sound-wave beams to measure flow velocities from the water surface to the near-bottom. Originally deployed by oceanographers, this tool is now becoming more widely used by scientists studying rivers. In contrast to standard flow meters, which make velocity measurements one point at a time, ADCPs provide data on the entire velocity profile — not only saving time, but also providing a more detailed view of cross-sectional and longitudinal flow patterns.

Venditti *et al.* observe that a core of high-velocity flow is diverted downward from near the water surface towards the bed of the channel at places where the river enters a narrow

bedrock canyon (Fig. 2). This high-velocity core follows the channel bed downstream into a plunge pool (a locally deep part of the bed), where it then dissipates. Crucially, the shear stress (force per unit area) that the flow exerts on the bed is proportional to the square of the vertical gradient in velocity. A high-velocity core near the bed of the channel leads to locally higher shear stress — much higher than would be expected from a logarithmic profile — and suggests that bedrock-incision rates will be relatively high at this point.

Where the canyon deepens downstream, the high-velocity core dissipates, so that shear stress is lower and incision rates are also probably lower. This downstream change in incision rates could lead to increased erosion upstream of the plunge pool, or progressive deepening of the canyon upstream. Furthermore, Venditti and colleagues observed secondary cross-channel circulation patterns where the fast surface flow plunges downward: the downward flow in the centreline causes upward flow along the bedrock banks. Such upward flow might undercut the banks, leading to their collapse and maintaining nearly vertical bedrock-canyon walls. The researchers suggest that their findings are relevant beyond their study area, because similar bedrock-canyon shapes are

JARED HOBBS/ALL CANADA PHOTOS/ALAMY

STRUCTURAL BIOLOGY

Ribosome revelations

Proteins are synthesized in cells by the ribosome apparatus. A report of 16 yeast ribosome structures, each bound by a different inhibitor, broadens our understanding of how drugs affect ribosome activity. [SEE ARTICLE P.517](#)

NELSON B. OLIVIER

in the large subunit and the decoding centre in the small subunit. The chemistry conducted by the ribosome takes place in these centres. Garreau de Loubresse and colleagues find that the binding site of each compound in their structures is either within, or on the periphery of, the peptidyl transferase centre or the decoding centre (Fig. 1).

Visualizing the three-dimensional positions of a compound interacting with its biological target is crucial for understanding the nature of the interactions and improving the compound's therapeutic value. Over the past decade, crystal structures of the 70S ribosome and its isolated subunits have been the most successful platform for studying compound–ribosome interactions at atomic resolution^{2,3}. Through a combination of Garreau de Loubresse and co-workers' biophysical and biochemical experiments, we now have direct evidence for which surfaces in the chemical activity centres of the eukaryotic 80S ribosome support the binding of compounds that affect protein translation. This evidence can be used in combination with previous advances^{4,5}, and in parallel with further experimentation, to help design effective, non-toxic compounds for treating a variety of medical conditions, such as cystic fibrosis, tumour metastasis and severe haemophilia.

Perhaps the most interesting and revealing of Garreau de Loubresse and co-workers' results

The ribosome is the cellular machinery responsible for translating specific genetic codes into proteins by linking amino acids together, one by one. There are three types of ribosome: 70S, from prokaryotes (organisms whose cells do not have a nucleus, such as bacteria); 80S, from the cytoplasm of eukaryotes (organisms with nucleus-bearing cells, including fungi, plants and animals); and 55S, found in most eukaryotic mitochondria (the power plants of cells). On page 517 of this issue, Garreau de Loubresse *et al.*¹ report 16 X-ray crystal structures of the 80S ribosome from the yeast *Saccharomyces cerevisiae*. Each structure reveals the binding mode for a distinct compound known to inhibit or modulate the protein-translation function of the ribosome. The authors' analysis provides a rationale for how most of these compounds exert their effects, and allows a comparison with analogous, previously reported structures of prokaryotic ribosomes.

Much like a precisely operating watch, the ribosome is a conglomerate of many parts, all of which are necessary for efficient function. It forms by the reversible association of a small and a large subunit. Two key regions are targets for clinically used antimicrobial agents and for compounds that ameliorate the symptoms of genetic diseases: the peptidyl transferase centre

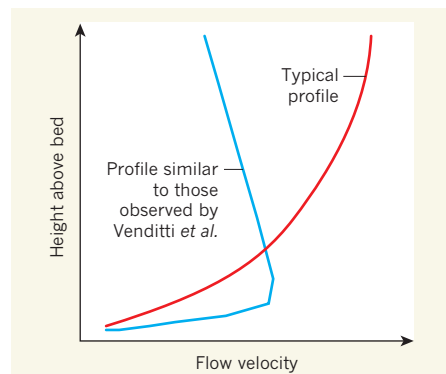


Figure 2 | Flow velocity in rivers. It is often assumed that the flow velocity of a river increases logarithmically with the distance from the bed. By contrast, Venditti *et al.*¹ report that the Fraser River flows fastest close to the bed at locations where the river enters a narrow bedrock canyon.

observed in other systems, and experimental data⁵ exhibit similar flow structures to those in the Fraser Canyon.

So what does this mean for our understanding of the long-term evolution of bedrock-river valleys? A convenient way to study the evolution of bedrock rivers and the mountainous topography that they shape is to use computational models. These models must calculate the evolution of topography over million-year timescales, and are limited to spatial resolutions of the order of 100 to 1,000 metres by currently available computational capabilities. So not only is the resolution of models wider than the width of a typical bedrock canyon, it is also longer than the flow patterns observed by Venditti and co-workers (the patterns occur over channel lengths of the order of 10–100 m). Computational limitations therefore mean that the spatial (and temporal) scale of the authors' observations are too small to be incorporated into current models that calculate incision over the timescales associated with bedrock-canyon formation. Nevertheless, this glimpse into flow through bedrock canyons will spur many ideas about how the processes of bedrock incision are affected by often-overlooked water-flow patterns, and will certainly be relevant for models of water flow that operate on much shorter timescales, such as days or months. ■

Nicole M. Gasparini is in the Department of Earth and Environmental Sciences, Tulane University, New Orleans, Louisiana 70118, USA.
e-mail: ngaspari@tulane.edu

1. Venditti, J. G. *et al.* *Nature* **513**, 534–537 (2014).
2. Gilbert, G. K. *Geology of the Henry Mountains, Utah* (US Gov. Printing Office, 1877).
3. Von Kármán, T. *Nachrichten von der Gesellschaft der Wissenschaften zu Göttingen, Mathematisch-Physikalische Klasse* 58–76 (1930).
4. Rantz, S. E. *US Geol. Surv. Wat. Supply Pap.* 2175 (1982).
5. MacVicar, B. J. & Rennie, C. D. *Wat. Resour. Res.* **48**, W02503 (2012).

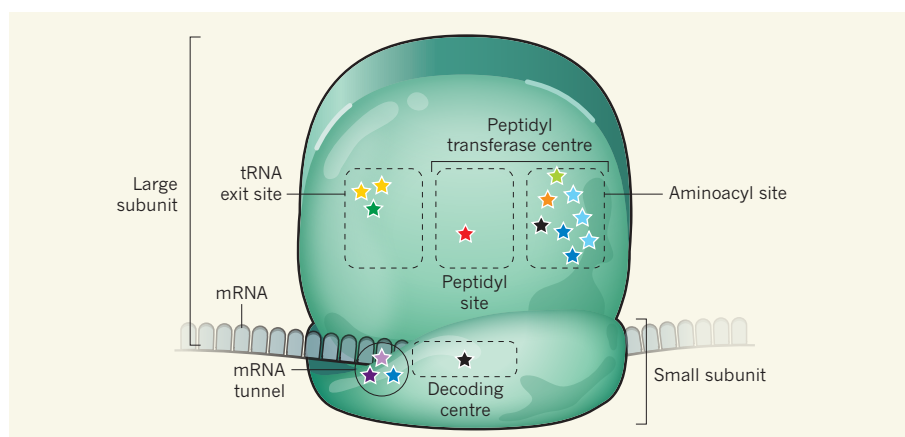


Figure 1 | Binding sites of protein-translation inhibitors in the yeast ribosome. Garreau de Loubresse *et al.*¹ report 16 crystal structures of the yeast ribosome, each in complex with a different inhibitor of protein translation. The binding sites of these inhibitors (indicated by stars) span key regions associated with protein translation: the peptidyl site and the aminoacyl site (the binding sites of transfer RNA in the peptidyl transferase centre), and the tRNA exit site, all of which are in the large subunit; and the decoding centre and the messenger RNA tunnel of the small subunit. Colours of stars represent different classes of inhibitor.

are those that focus on compounds that counter tumour proliferation *in vitro*⁶: the glutarimide compounds cycloheximide and lactimidomycin. Both of these inhibit protein synthesis by the 80S ribosome, but not by the 70S ribosome. The researchers' crystal structures identify the binding site for each compound at the exit of the peptidyl transferase centre. Comparisons with data for 70S structures⁷ show that the prokaryotic ribosome has components that occlude the glutarimide binding pocket, explaining these compounds' selectivity.

The authors' biochemical data also help to rationalize the different effects of each compound. Cycloheximide binds its ribosome pocket at any time during translation and blocks the exit of ribosome substrates from the peptidyl transferase centre. But the rate at which lactimidomycin binds its binding pocket is much lower than that of the substrates — so it cannot be accommodated in the ribosome during protein translation, but can bind and block the process before it starts. Because lactimidomycin is larger than cycloheximide, the authors propose that its binding is slower because of the extra effort needed to accommodate its greater bulk. In other words, when comparing the mechanism of action of the two compounds, size really does matter!

The inhibitor-bound structures reported by

Garreau de Loubresse and colleagues are by no means the end of the road to understanding the selectivity and mechanism of action of drugs that target ribosomes. For example, because these structures lack both messenger RNA and transfer RNA, it remains to be seen how compounds such as edeine and cryptopleurine — which inhibit ribosome activity by interacting with mRNA and/or tRNA — affect protein translation at the ribosome.

As techniques for studying the ribosome improve, there will undoubtedly be quantum leaps in our understanding of how these machines work and in our ability to modulate their activity. Indeed, such a breakthrough⁸ was made earlier this year when cryoelectron microscopy (cryoEM) was used to visualize the 80S ribosome from the malaria-causing protozoan *Plasmodium falciparum* bound to the translation inhibitor emetine, at a resolution of 3.2 ångströms. This demonstrated that cryoEM can achieve sufficiently high resolution to distinguish the details of electrostatic-bond formation between ribosomes and bound compounds. Unlike X-ray crystallography, cryoEM does not need crystals⁹, so the ability to use cryoEM removes a major hurdle to structural studies of ribosomes.

In the meantime, by successfully clearing this hurdle, Garreau de Loubresse *et al.* have

delivered groundbreaking data at atomic resolution that should further our understanding of how a diverse set of compounds affects the function of the 80S ribosome. It will be interesting to see which technique — X-ray crystallography or cryoEM — delivers the first 55S ribosome structure in the presence of an inhibitor. ■

Nelson B. Olivier is in the *Innovative Medicines and Early Development Unit, AstraZeneca Pharmaceuticals, Cambridge Science Park, Cambridge CB4 0FZ, UK.*
e-mail: nelson.olivier@astrazeneca.com

1. Garreau de Loubresse, N. *et al.* *Nature* **513**, 517–522 (2014).
2. Wilson, D. N. *Crit. Rev. Biochem. Mol. Biol.* **44**, 393–433 (2009).
3. Wimberley, B. T. *Curr. Opin. Invest. Drugs* **10**, 750–765 (2009).
4. Perez-Fernandez, D. *et al.* *Nature Commun.* **5**, 3112; <http://dx.doi.org/10.1038/ncomms4112> (2014).
5. Taguchi, A. *et al.* *ChemMedChem* <http://dx.doi.org/10.1002/cmdc.201402208> (2014).
6. Schneider-Poetsch, T. *et al.* *Nature Chem. Biol.* **6**, 209–217 (2010).
7. Schuwirth, B. S. *et al.* *Science* **310**, 827–834 (2005).
8. Wong, W. *et al.* *eLife* **3**, e03080 (2014).
9. Bai, X., Fernandez, I. S., McMullan, G. & Scheres, S. H. *eLife* **2**, e00461 (2013).

This article was published online on 10 September 2014.



BIODIVERSITY

Leaping lizards

Loss of biodiversity is a hallmark of the human-dominated era, but our influence can also alter the processes that generate biodiversity. On page 543 of this issue, Helmus *et al.* study human-assisted movement of lizards around Caribbean islands, and show that a major geographic parameter of a classic theory of biodiversity has been replaced by an economic one (M. R. Helmus, D. L. Mahler and J. B. Losos *Nature* **513**, 543–546; 2014).

The theory of island biogeography predicts that biodiversity is greatest on large and less-isolated islands (or other discrete habitat fragments), but the underlying processes of speciation and long-distance colonization are usually too slow for the theory to be tested directly.

The shipping trade has speeded things up for anole lizards in the Caribbean, transporting them around the islands as stowaways (pictured: *Anolis equestris*). The authors find that the resulting diversity of *Anolis* species fits theoretical predictions about island size, but that economic isolation — such as occurred on Cuba during the cold war — has overtaken geographic isolation as the other key factor. **Patrick Goymer**

EXTRASOLAR PLANETS

Window on a watery world

The first definitive signs of water have been seen in the atmosphere of a Neptune-sized exoplanet, paving the way towards the search for water on smaller Earth-like planets. [SEE LETTER P.526](#)

ELIZA M. R. KEMPTON

The molecules that make up the atmospheres of Neptune-sized exoplanets have remained elusive. Despite a protracted search for the atmospheric constituents of such planets using impressive instrumentation on world-class telescopes, observations have revealed only thick layers of clouds, haze or dust, which block astronomers' prying eyes and prevent a view of the world below^{1–4}. On page 526 of this issue, Fraine *et al.*⁵ now report observations of the Neptune-sized planet HAT-P-11b using the Hubble and Spitzer space telescopes that reveal a world without thick clouds and provide a clear confirmation that water vapour, along with copious amounts of hydrogen, is present in the atmosphere of this planet.

It should not be surprising that clouds are prevalent in the atmospheres of many exoplanets. In our own Solar System, clouds are practically ubiquitous. From Earth's puffy water-vapour clouds, to the hydrocarbon haze of Saturn's largest moon, to Jupiter's stratified clouds of ammonia compounds and water, clouds dominate the skies of most large Solar System bodies. These clouds, although interesting in their own right, are not always an astronomer's friend. It is easy to see why. A layer of clouds acts as a thick blanket, obscuring the deeper regions of a planet's atmosphere (and the planetary surface, if one exists). Despite being our neighbouring planet, almost nothing was known of Venus's surface until the 1970s for this very reason. The planet is enshrouded in clouds of noxious sulphuric acid, which prevented a view of its surface until the Soviet Venera landers were finally able to physically penetrate the clouds and transmit pictures back to Earth⁶.

The same problem exists for the study of exoplanets, but sending a lander to these distant worlds is not an option. To determine the gaseous composition of an exoplanet atmosphere, astronomers rely on spectroscopic studies and the fact that different gases absorb light at specific wavelengths. If clouds obscure the deeper regions of a planet's atmosphere, then no absorption will be seen, and the composition of the atmosphere cannot be readily determined (Fig. 1). Already, four exoplanets

of Neptune size or smaller, observed when passing in front of their host stars, have shown no absorption features^{1–4}, and clouds are a likely culprit. But when Fraine *et al.* observed a fifth such planet, HAT-P-11b, they hit on something markedly different. The observations of HAT-P-11b reveal the crystal-clear signature of water-vapour absorption. From the strength of the absorption, the authors conclude that the planet's atmosphere has a composition not dissimilar to those of the giant planets of our Solar System — mostly hydrogen, with trace amounts of heavier atoms, including oxygen in the form of water vapour.

The instrument that Fraine and colleagues used to unambiguously detect water vapour in the atmosphere of HAT-P-11b — the Wide Field Camera 3 (WFC3) on the Hubble Space Telescope — was commissioned in 2009 during the final servicing of the telescope. The device produced stunningly high-precision measurements and is providing astronomers with

a glimpse of what data might look like from next-generation space observatories. Searching for water-vapour absorption in the atmosphere of an exoplanet passing in front of its host star is akin to looking for a tiny insect passing in front of a bright coastal lighthouse lamp. To detect the minute signatures of molecular absorption, the WFC3 provides exceptional instrumental stability so as not to introduce spurious noise that could mask the signs of water vapour in an exoplanet's atmosphere. In 2018, NASA is due to launch the James Webb Space Telescope, which will carry instruments with sensitivity similar to that of the WFC3. The advantage of this new observatory is that the telescope itself will have a larger mirror than Hubble's, allowing it to detect even fainter signals than those detected by Fraine and colleagues. As a result, the telescope will be able to observe molecular absorption in the atmospheres of planets smaller than Neptune, but only if these planets do not have clouds.

The successful detection of water vapour in HAT-P-11b's atmosphere allows exoplanet researchers to breathe a sigh of relief. The finding that some of the smaller exoplanets do not have thick clouds bodes well for observations with the James Webb Space Telescope. However, there is still more work to be done in identifying suitable targets for these future observations. It has long been expected that water vapour should be present in the atmospheres of planets such as HAT-P-11b — those of Neptune size whose orbits carry them close to their host stars. But after multiple failed attempts to observe molecular absorption in

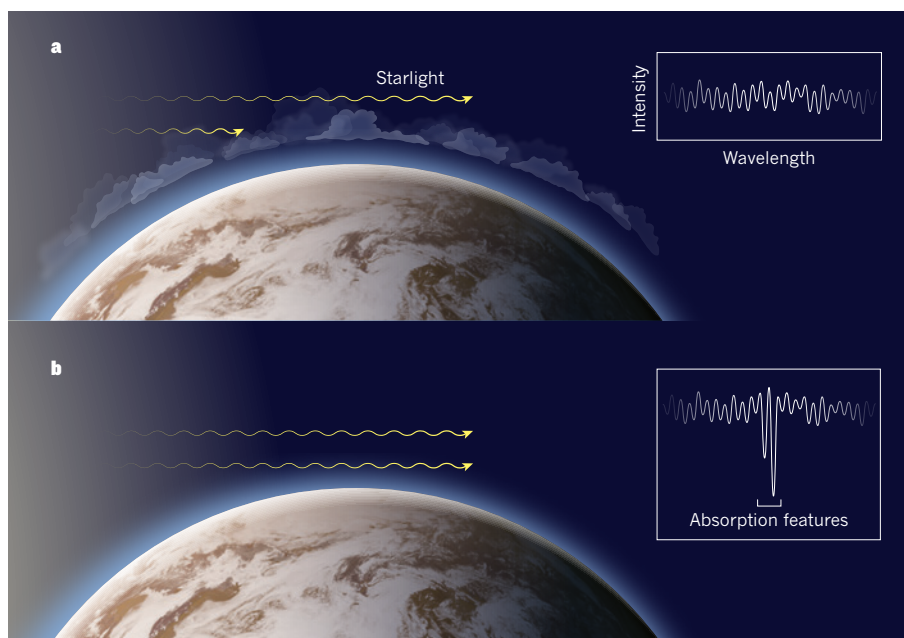


Figure 1 | Concealing clouds. **a**, An exoplanetary atmosphere with clouds blocks the transmission of starlight, producing a flat transmission spectrum with no features. **b**, A clear atmosphere with no clouds allows starlight to penetrate deeper into the atmosphere, where molecules such as water absorb light. The resulting transmission spectrum has absorption spectral features, which enable astronomers to infer the molecular composition of the atmosphere. This was the case for Fraine and colleagues' observations⁵ of exoplanet HAT-P-11b, which has water-absorption features.

the atmospheres of other similar planets, the surprise of Fraine and colleagues' results is that the atmosphere of HAT-P-11b is sufficiently devoid of clouds to allow the detection of water vapour.

Now that this planet has been shown to be free of clouds, despite their prevalence in the atmospheres of other similar planets, some questions arise. What fraction of Neptune-sized exoplanets has clouds? For the planets that do have clouds, what specific physical

processes are responsible for their formation? Understanding the answers to these questions will allow astronomers to better identify planets unmarred by clouds. By first pinpointing and studying those planets that provide a clear window into their atmospheres, researchers will ultimately be able to extend the search for water and other molecules to smaller planets — perhaps even Earth-sized planets — with the James Webb Space Telescope and beyond. ■

Eliza M. R. Kempton is at Grinnell College, Grinnell, Iowa 50112, USA.
e-mail: kemptone@grinnell.edu

1. Knutson, H. A. *et al. Nature* **505**, 66–68 (2014).
2. Kreidberg, L. *et al. Nature* **505**, 69–72 (2014).
3. Knutson, H. A. *et al. http://arXiv.org/abs/1403.4602* (2014).
4. Ehrenreich, D. *et al. http://arXiv.org/abs/1405.1056* (2014).
5. Fraine, J. *et al. Nature* **513**, 526–529 (2014).
6. Florensky, C. P. *et al. Proc. 8th Lunar and Planetary Sci. Conf.* 2655–2664 (1977).

chondrocytes from patients, but Yamashita and colleagues took advantage of improved cell-reprogramming techniques⁵ to do just that.

The authors isolated skin cells from three individuals with thanatophoric dysplasia and converted the cells to induced pluripotent stem cells, which can give rise to any cell type in the body. Next, Yamashita and co-workers stimulated the stem cells to become chondrocytes, which had the same genetic make-up as the original patients. They then took advantage of the chondrocytes' ability to aggregate into cartilage-forming particles⁶ to generate a system for analysing particles formed by thanatophoric dysplasia chondrocytes and by controls without the FGFR3 mutation. The authors compared the particles' similarities and differences as the different cells grew and matured over several weeks in culture (Fig. 1).

A major difference was that, compared to controls, thanatophoric dysplasia particles exhibited impaired maturation associated with degradation of cartilage. Remarkably, reducing FGFR3 levels or adding antibodies to block FGFR3 activity in dysplasia cultures restored growth and maturation of the cartilage-forming particles to normal levels. Yamashita and co-workers used their culture system to assay several molecules that affect either the response of cells to FGFR3 signals or the formation of chondrocytes from stem cells,

DISEASE MODELS

Statins give bone growth a boost

The development of stem-cell-based models of two diseases that cause dwarfism reveals that statins — drugs that are used to treat high levels of blood cholesterol — may also promote cartilage formation and bone growth. SEE ARTICLE P.507

BJORN R. OLSEN

Many medical conditions can cause short stature, but a faulty gene encoding the protein FGFR3 is responsible for two-thirds of all forms of dwarfism in humans. FGFR3 normally controls a brake signal in the molecular machinery that regulates the growth of limb bones during childhood and adolescence. In 1 in every 10,000–30,000 births, genetic mutations cause FGFR3 to become overactive and so brake too hard. Although our understanding of the cellular processes that go awry in dwarfism is good, development of treatments has been hampered by a lack of efficient methods for screening and testing potential drugs. In this issue, Yamashita *et al.*¹ (page 507) report

a major step forward in solving this problem, establishing a human-disease-based system for screening potential drugs to treat skeletal-growth defects.

In humans, the most common FGFR3 mutation results in achondroplasia, a disorder that causes short extremities, increased curvature of the spine and distortion of skull growth, resulting in substantial health problems². More-severe mutations in FGFR3 can cause thanatophoric dysplasia, in which a small chest, and respiratory problems, may cause death either at or shortly after birth³. In both dysplasias, skeletal defects are caused by decreased proliferation and impaired maturation of cartilage-forming cells called chondrocytes within growing regions of bone⁴. It has not previously been possible to obtain

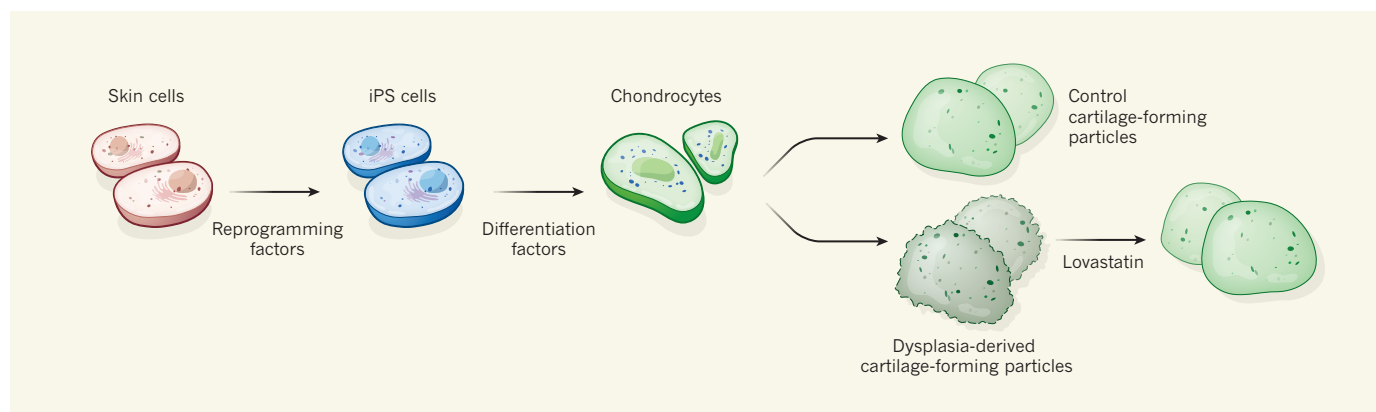


Figure 1 | A cell-based model of impaired bone growth. Yamashita *et al.*¹ isolated skin cells from people with thanatophoric dysplasia and from people with normal bone growth, and reprogrammed them to become induced pluripotent stem cells (iPS cells), which can give rise to every cell type of the body. They then added factors that caused the cells to differentiate into

cartilage-forming cells called chondrocytes. Chondrocytes derived from controls produced normal cartilage-forming particles, but the particles formed from dysplasia-derived chondrocytes showed impaired growth and maturation. However, normal particle formation was restored when the drug lovastatin was added to the culture dish, highlighting a possible treatment for this disease.

to determine which could promote cartilage development in dysplastic cells. Molecules that had positive effects included C-type natriuretic peptide (CNP) and several statins, including lovastatin and rosuvastatin.

CNP has a positive effect on bone formation and growth⁴, and its overexpression in chondrocytes counteracts dwarfism in a mouse model of achondroplasia⁷. As a result, CNP has been pursued as a potential achondroplasia treatment, although it is not an ideal candidate. A major obstacle is that the peptide, which must be injected, is degraded within minutes of being administered. A more stable version is effective in mouse models of achondroplasia and is currently in clinical trials, but still requires daily injections⁸. In addition, the effects of CNP on the cardiovascular system and the central nervous system raise the possibility of undesirable side effects if the drug is used long-term in children.

Statins — cholesterol-lowering drugs that are available in tablet form — provide an interesting alternative. Their safety has been evaluated in children with inherited high cholesterol⁹, and evidence¹⁰ suggests that early statin treatment improves the chances of children with this condition reaching the age of 30 without having a heart attack. In addition to their cholesterol-related properties, the drugs stimulate production of chondrocyte molecules that make up the structure of cartilage¹¹, and repress production of cartilage-degrading enzymes¹². In a series of compelling experiments, Yamashita *et al.* demonstrated that lovastatin stimulates production of cartilage components in thanatophoric dysplasia chondrocytes, and promotes the formation of chondrocytes from stem cells. It also restores cartilage formation by chondrocytes derived from people with achondroplasia. Finally, the authors showed that injecting rosuvastatin into mice with an achondroplasia-causing defect in FGFR3 partially restored bone growth in the limbs and head.

What are the mechanisms underlying these striking effects? Yamashita and colleagues' study does not provide the full answer. However, the authors do find that high levels of FGFR3 protein, but not messenger RNA, are reduced to normal levels when lovastatin is added to cultures of particles derived from people with either form of dysplasia. This suggests that statins stimulate degradation of FGFR3. Cellular protein-degradation machines called proteasomes might be involved, because adding a proteasome inhibitor to lovastatin-containing cultures increased levels of FGFR3. The researchers speculate that this is related to the ability of statins to lower cholesterol in cells, and to destabilize cell membranes so that FGFR3 (which spans the membrane) is more easily internalized and degraded, but this remains to be determined.

If the ability of statins to restore cartilage-particle growth is found to be independent of

their cholesterol-lowering properties, it may be possible to modify the drugs such that these two effects are separated. However, if the cartilage-promoting effect of statins is a direct consequence of a decrease in cholesterol, extreme care is needed before using the drugs to treat children with achondroplasia. It will be crucial to ensure that cholesterol levels in these children are maintained at reasonable levels.

Between the ages of 25 and 35, mortality related to heart disease is more than 10 times higher in people with achondroplasia than in the general population^{13,14}. The reasons for this are not understood, and limited data suggest that serum cholesterol levels in children with achondroplasia are in the high normal range¹⁵. Whether statin treatment would help to reduce this mortality is therefore unclear.

In summary, Yamashita *et al.* have established a disease model of achondroplasia and related dysplasias based on pluripotent stem cells. The results of the study raise the possibility that statins might be effective in treating children with these disorders. Furthermore, the authors' system allows screening of additional compounds in the search for even safer drugs. ■

INORGANIC CHEMISTRY

How calcium affects oxygen formation

Calcium is an essential component of the catalyst that forms oxygen from water during photosynthesis. It seems that part of calcium's job is to enable the release of oxygen from this catalyst.

DAVIDE LIONETTI & THEODOR AGAPIE

The mechanism of oxygen production in photosynthesis remains unresolved, despite many studies. The presence of a calcium ion in the inorganic active site of the complex that produces oxygen is particularly puzzling, because the reaction is a redox process involving the transfer of multiple electrons, whereas calcium is redox-inactive (it cannot transfer electrons under biological conditions). Writing in *Nature Chemistry*, Bang *et al.*¹ provide insight into the ion's possible role. They report that, under oxidative conditions, oxygen molecules can be released from iron peroxide complexes — which can be thought of as simplified models of the active site — in the presence of calcium ions, but not in the presence of other metal ions that are better Lewis acids (electron-pair acceptors) than calcium.

Oxygenic photosynthesis, the process by which plants convert carbon dioxide to organic matter using solar energy, has generated

Bjorn R. Olsen is in the Department of Cell Biology, Harvard Medical School, Boston, Massachusetts 02115, USA.
e-mail: bjorn_olsen@hms.harvard.edu

1. Yamashita, A. *et al.* *Nature* **513**, 507–511 (2014).
2. Shiang, R. *et al.* *Cell* **78**, 335–342 (1994).
3. Tavormina, P. L. *et al.* *Am. J. Hum. Genet.* **64**, 722–731 (1999).
4. Laederich, M. B. & Horton, W. A. *Curr. Opin. Pediatr.* **22**, 516–523 (2010).
5. Okita, K. *et al.* *Nature Methods* **8**, 409–412 (2011).
6. Koyama, N. *et al.* *Stem Cells Dev.* **22**, 102–113 (2013).
7. Yasoda, A. *et al.* *Nature Med.* **10**, 80–86 (2004).
8. Lorget, F. *et al.* *Am. J. Hum. Genet.* **91**, 1108–1114 (2012).
9. Eiland, L. S. & Luttrell, P. K. *J. Pediatr. Pharmacol. Ther.* **15**, 160–172 (2010).
10. Braamskamp, M. J. *et al.* *Circulation* **128**, A17837 (2013).
11. Hatano, H., Maruo, A., Bolander, M. E. & Sarkar, G. *J. Orthop. Sci.* **8**, 842–848 (2003).
12. Simopoulou, T., Malizos, K. N., Poultsides, L. & Tsezou, A. *J. Orthop. Res.* **28**, 110–115 (2010).
13. Hunter, A. G., Hecht, J. T. & Scott, C. I. *Jr Am. J. Med. Genet.* **62**, 255–261 (1996).
14. Wynn, J., King, T. M., Gambello, M. J., Waller, D. K. & Hecht, J. T. *Am. J. Med. Genet. A* **143A**, 2502–2511 (2007).
15. Collipp, P. J., Sharma, R. K., Thomas, J., Maddaiah, V. T. & Chen, S. Y. *Am. J. Dis. Child.* **124**, 682–685 (1972).

This article was published online on 17 September 2014.

most of the oxygen (O₂ molecules) in the atmosphere, enabling life on Earth as we know it. Oxygen forms when water is oxidized, a complex chemical reaction involving the transfer of four electrons and four protons (H⁺ ions; Fig. 1a). The reaction is catalysed by the oxygen-evolving complex (OEC) — an inorganic cluster of four manganese ions and one calcium ion bridged by oxide ligands², buried in a photosynthetic protein complex known as photosystem II (PSII). The mechanism of water oxidation is debated, particularly the role of calcium and the site at which the oxygen–oxygen (O–O) bond of the dioxygen molecule forms. Further insight might allow the rational design of effective catalysts for artificial photosynthesis³.

Chemists often synthesize small molecular complexes that display structural motifs similar to enzyme active sites and use them as models that can be systematically investigated. This approach has been challenging for the OEC because the cluster is structurally

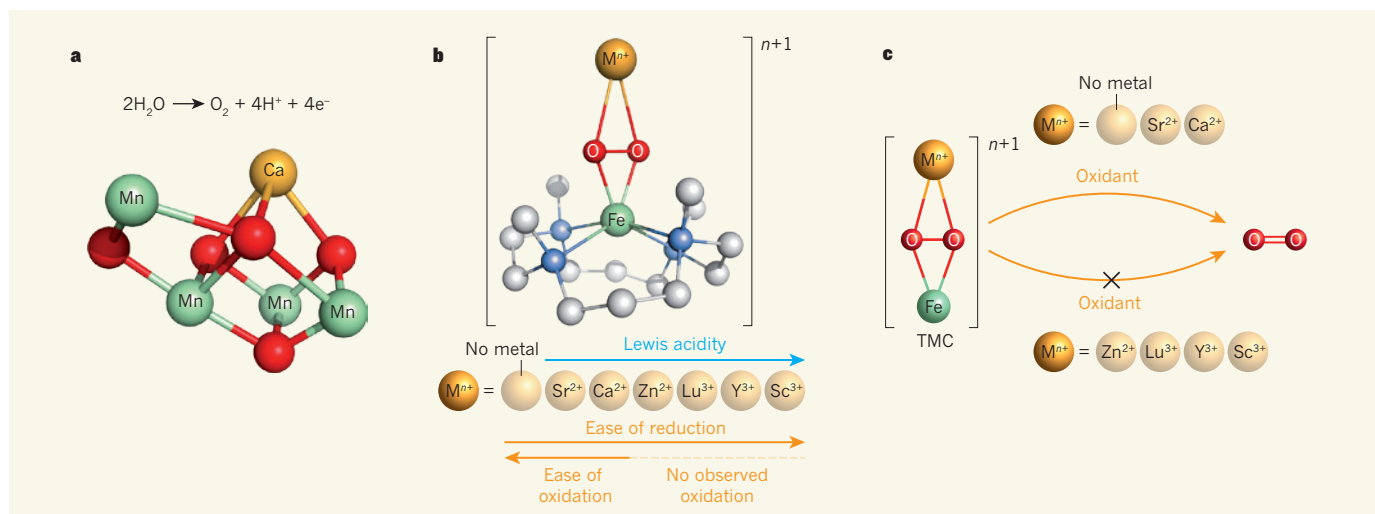


Figure 1 | Oxygen release from iron peroxide complexes. **a**, In the oxygen-evolving complex (OEC) of the photosynthetic apparatus, water is oxidized to produce oxygen — a reaction involving the transfer of four electrons (e^-) and four protons (H^+). The OEC contains four redox-active manganese ions and one calcium ion², which is redox-inactive under biological conditions. Oxygen atoms are shown in red. **b**, Bang *et al.*¹ prepared complexes that model the OEC in the final step of water oxidation. In these complexes, a redox-active iron atom (green) is bound

to a TMC ligand (1,4,8,11-tetramethyl-1,4,8,11-tetraazacyclotetradecane, shown in grey and blue) and a peroxide moiety (red), which binds a redox-inactive metal ion (M^{n+}). The charge on the complex is $n+1$. The ease with which the complexes can be reduced correlates with the Lewis acidity of the metals. Only the complexes that contained strontium ions (Sr^{2+}) or calcium ions (Ca^{2+}), or which lacked a redox-inactive metal, could be oxidized. **c**, When treated with an oxidant, only the oxidizable complexes reacted to produce oxygen.

complex and contains two types of metal. For their models, Bang *et al.* targeted complexes that contain one redox-active metal (iron) and one redox-inactive metal.

The authors focused on a step of water-oxidation chemistry that occurs after O–O bond formation, hypothesizing that it relates to the role of calcium in the OEC: the formation of oxygen from a peroxide moiety (O_2^{2-}). They added solutions of redox-inactive metal ions to a redox-active iron peroxide species, $Fe-(O_2^{2-})$, and obtained complexes containing the $Fe-(O_2^{2-})-M$ motif (Fe is iron; M can be ions of calcium, strontium, zinc, lutetium, yttrium or scandium). This series of compounds conceptually mimics a putative peroxide complex from the OEC, which allowed the authors to systematically compare the effects of the redox-inactive metals on the properties of these compounds (Fig. 1b, c). The models are structurally different from the OEC because they have one iron rather than four manganese ions. However, they distil the effect of redox-inactive metals on the peroxide moiety into a simple combination of two metal ions that is easier to interrogate than the OEC.

Using electrochemical analysis, Bang *et al.* showed that the redox-inactive metals have a significant effect on electron transfer to and from the complexes. The propensity of the complexes to be chemically reduced (that is, to accept an electron) increases with the Lewis acidity of the M ion. Conversely, the ease with which the complexes are oxidized (an electron is removed) shows the opposite trend: the researchers observed an oxidation event in the presence of calcium or strontium ions, or in the absence of a redox-inactive metal, but

not when the M ion was a stronger Lewis acid (zinc, lutetium, yttrium or scandium). Similar effects have been invoked previously to unravel the role of calcium ions in the OEC, in studies of complexes containing oxo (O^{2-}) or hydroxo (HO^-) motifs instead of peroxide moieties^{4–9}, but this is the first detailed study of a series of peroxide species in this context^{10,11}.

So what does this mean for oxygen release from the complex? In agreement with the electrochemical results, Bang and colleagues observed that the complexes incorporating zinc, lutetium, yttrium or scandium ions did not react with a chemical oxidant (ceric ammonium nitrate), so no oxygen was produced. By contrast, treatment with the same oxidant led to oxygen release from the calcium and strontium complexes, and from $Fe-(O_2^{2-})$ that was not bound to a redox-inactive metal ion.

The effects of calcium and strontium ions are of particular interest because they are biologically relevant: calcium is the native component of the OEC, and strontium is the only metal that can replace calcium and still generate a functional catalyst. Notably, the authors' calcium and strontium complexes not only have similar electrochemical properties, but also allow oxygen production from peroxide. The parallels between the biological and synthetic systems suggest that the study's conclusions may extend to the OEC — although the more complicated structure of the OEC and the different metals within it will affect the interactions with, and the chemical reactivity of, the peroxide moiety.

Do the findings reveal the mechanism of water oxidation? Not completely, but they shed light on the terminal step of the process. The

observation that the iron peroxide compound can be oxidized to generate oxygen molecules in the absence of any redox-inactive metal implies that the role of calcium ions in PSII cannot be to promote oxygen release alone. As the authors assert, the crucial point is that the calcium ion does not hinder oxygen release, whereas metals that are stronger Lewis acids do. The most elusive step in the water oxidation reaction, the formation of the O–O bond, remains a challenging but key target for future studies. Bang and colleagues' work nonetheless provides an insightful contribution to the debate about the role of calcium ions in PSII. ■

Davide Lionetti and Theodor Agapie are in the Division of Chemistry and Chemical Engineering, California Institute of Technology, Pasadena, California 91125, USA.
e-mail: agapie@caltech.edu

1. Bang, S. *et al.* *Nature Chem.* <http://dx.doi.org/10.1038/nchem.2055> (2014).
2. Umena, Y., Kawakami, K., Shen, J.-R. & Kamiya, N. *Nature* **473**, 55–60 (2011).
3. Lewis, N. S. & Nocera, D. G. *Proc. Natl Acad. Sci. USA* **103**, 15729–15735 (2006).
4. Fukuzumi, S. *et al.* *Nature Chem.* **2**, 756–759 (2010).
5. Yoon, H. *et al.* *J. Am. Chem. Soc.* **135**, 9186–9194 (2013).
6. Park, Y. J. *et al.* *Chem. Sci.* **4**, 717–726 (2013).
7. Kanady, J. S., Tsui, E. Y., Day, M. W. & Agapie, T. *Science* **333**, 733–736 (2011).
8. Tsui, E. Y., Tran, R., Yano, J. & Agapie, T. *Nature Chem.* **5**, 293–299 (2013).
9. Herbert, D. E., Lionetti, D., Rittle, J. & Agapie, T. *J. Am. Chem. Soc.* **135**, 19075–19078 (2013).
10. Lee, Y.-M. *et al.* *Chem. Sci.* **4**, 3917–3923 (2013).
11. Li, F. F., Van Heuvelen, K. M., Meier, K. K., Münck, E. & Que, L. Jr *J. Am. Chem. Soc.* **135**, 10198–10201 (2013).

This article was published online on 17 September 2014.

PLANT SCIENCE

Towards turbocharged photosynthesis

The development of tobacco plants that are genetically engineered to produce a more efficient form of Rubisco, an enzyme involved in photosynthesis, marks a step towards increasing crop yields. [SEE LETTER P.547](#)

G. DEAN PRICE & SUSAN M. HOWITT

As the world's population increases, the spectre of severe food shortages is growing, with the United Nations predicting¹ that food production will need to double by 2050. It has been proposed that cyanobacteria — which obtain their energy from a highly efficient form of photosynthesis — might hold the key to increasing the yield of our most important crops and vegetables. On page 547 of this issue, Lin *et al.*² report a major step towards realizing this possibility, finding that cyanobacteria can be used to improve photosynthesis in the leaves of crops.

Photosynthesis harnesses sunlight to convert carbon dioxide into simple sugars. Rubisco, the key enzyme for CO₂ fixation into sugar, is inefficient because it cannot easily discriminate between oxygen and CO₂ and

so wastes energy by fixing O₂. The enzyme evolved at a time when O₂ levels in the atmosphere were much lower than they are today, and there was therefore little evolutionary pressure to select for an ability to discriminate between the two molecules. Photosynthetic organisms have evolved to circumvent the problem of rising atmospheric O₂ levels in two ways: first, by making more of a slower-acting version of Rubisco with an improved ability to discriminate; or second, by using various 'add-ons', called CO₂-concentrating mechanisms (CCMs), to elevate CO₂ levels in the vicinity of the enzyme.

Most crops have adopted the first strategy, making Rubisco possibly the most abundant enzyme on Earth. This approach, however, results in a 30% reduction in photosynthetic efficiency through the associated O₂ fixation. That can be partly ameliorated

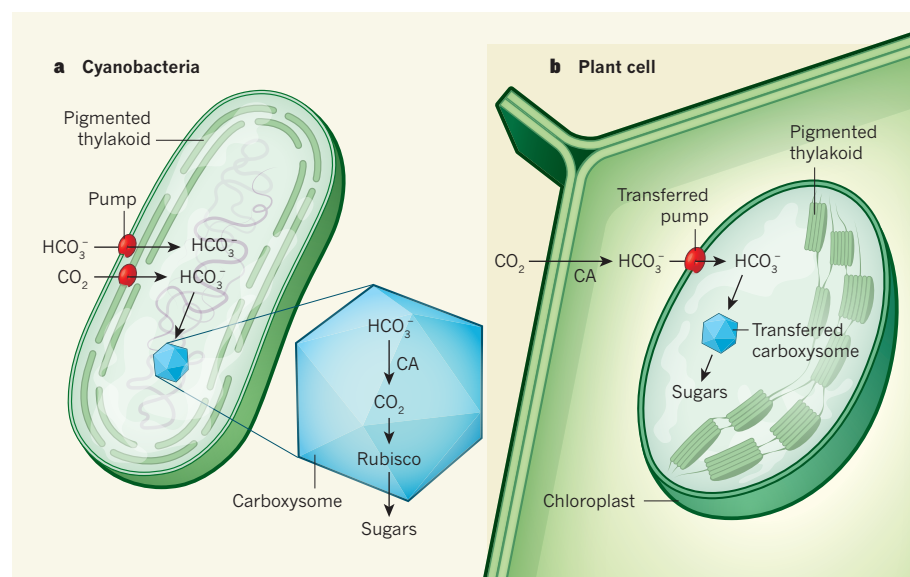


Figure 1 | A proposed method for improving photosynthesis in crops. **a**, In cyanobacteria, a carbon dioxide-concentrating mechanism (CCM) ensures that photosynthesis is effective (the energy for photosynthesis is provided through light harvesting by structures called pigmented thylakoids). The CCM includes pumps that take up CO₂ and bicarbonate (HCO₃⁻) molecules; the CO₂ pump also converts CO₂ to HCO₃⁻, which then enters microstructures called carboxysomes. Here, HCO₃⁻ is converted to CO₂ by the enzyme carbonic anhydrase (CA), elevating CO₂ concentrations around the Rubisco enzyme to increase the efficiency with which it converts CO₂ into sugars. **b**, Transfer of cyanobacterial carboxysomes or CCM pumps into plant cells has been posited as a way to improve crop yields. Lin *et al.*² took us a step closer to achieving this aim by replacing Rubisco in the chloroplasts of tobacco plants with a more efficient, cyanobacterial form of the enzyme. In the plant-cell cytoplasm, CA can also convert CO₂ to HCO₃⁻.



50 Years Ago

The capacity exhibited by all organisms to develop tolerance for new environmental conditions has been an important factor in the continuing existence of life on Earth. It has also had adverse effects on some creatures. To man, one of the most disturbing of these effects is being manifested through the resistance certain microbes develop for the 'wonder' drugs he uses to counteract microbial diseases. The peculiar capacity of pathogenic micro-organisms to develop strains which are resistant to drugs which on initial application are lethal to most individuals — and eventually to thrive on those drugs — did not come into clear focus until Paul Ehrlich *et al.* made their famous chemotherapeutic researches during the first decade of this century.
From Nature 26 September 1964

100 Years Ago

The council of the Senate of the University of Cambridge has offered to professors, teachers, and students of the University of Louvain such facilities in the way of access to libraries, laboratories, and lectures, together with the use of lecture-rooms, as may secure the continuity of the work of that University during the present crisis. Hospitality in the way of living accommodation and so forth will probably be offered by the individual colleges and by private residents. The professors of the University of Oxford have offered a home for the winter to the young children of the professors of the University of Louvain; and the academic staff of University College (University of London) offers hospitality to about seventy members of French and Belgian universities, whether professors, teachers, or students, men or women, who may find it necessary to take refuge in this country.
From Nature 24 September 1914

by raising CO₂ levels around the leaf³ in a manner conceptually similar to adding a CCM. There is currently increased focus on the second strategy — if a CCM could be introduced into crops, it might turbocharge photosynthetic CO₂ fixation. CCMs have evolved independently in cyanobacteria, microalgae and some plants (mostly those regarded by us as weeds). Although several types of CCM are being considered for introduction into crops, Lin and colleagues' work focuses on the cyanobacterial CCM.

This CCM involves a series of membrane-based pumps for CO₂ and bicarbonate (HCO₃⁻), and special microcompartments called carboxysomes, which contain Rubisco⁴. HCO₃⁻ is pumped into the cell, then converted to CO₂ in the carboxysomes by the enzyme carbonic anhydrase (Fig. 1). The resulting high local CO₂ concentrations increase Rubisco efficiency, and so almost eliminate O₂ fixation⁴. Furthermore, thanks to the CCM, cyanobacteria have retained an ancient form of Rubisco that is almost three times as efficient as that found in most crops⁵.

Lin *et al.* engineered tobacco plants to express a functional cyanobacterial form of Rubisco. This enzyme usually consists of a complex of eight large subunits and five to eight small subunits. The authors replaced DNA that encodes the large subunit of Rubisco in the tobacco plant with that encoding the cyanobacterial enzyme, ensuring that the photosynthesis and growth they observed occurred as a result of the introduced Rubisco, rather than the native version. This DNA is located in the cells' photosynthesizing factories, structures called chloroplasts.

Lin and colleagues' approach differs from those of earlier, unsuccessful efforts⁶ in several ways; most notably, the authors co-expressed the cyanobacterial Rubisco with proteins that are involved in the enzyme's assembly. They found that co-expression of cyanobacterial Rubisco with either the RbcX chaperone protein (which helps protein folding) or a carboxysomal protein called CcmM35 (a Rubisco-organizing protein) were equally effective at forming functional Rubisco. However, the latter approach produced large complexes of Rubisco, which seemed to be related to those that form during the assembly of pre-carboxysomes in cyanobacteria. This is because CcmM35 mimics three of Rubisco's small subunits and so is incorporated into Rubisco. But the protein also crosslinks to other Rubisco complexes, producing enzyme aggregates⁴.

The authors did not demonstrate whether the addition of CcmM35 or RbcX was the pivotal step in successfully expressing cyanobacterial Rubisco in tobacco, or whether other elements of the experimental design provided the crucial advantage. Earlier this year, the same group showed that co-expression of several carboxysomal

shell proteins in chloroplasts can produce structures suggestive of carboxysome self-assembly⁷. Thus, prospects for building functional carboxysomes in tobacco-plant chloroplasts are now quite good. However, extending this to crops would be greatly aided by the development of technologies for altering the chloroplast genomes of key crop species.

In the past two years, the sequence of events required to build a cyanobacterial CCM in the chloroplast has been identified in detail^{8,9}. Stand-alone addition of cyanobacterial Rubisco, or even of carboxysomes, to chloroplasts provides no obvious advantage. In fact, Lin *et al.* show that their modified plants survive only at high CO₂ concentrations. To provide an advantage, both CO₂ and HCO₃⁻ pumps are required, to elevate HCO₃⁻ levels in the chloroplast and so turbocharge CO₂ levels in the carboxysomes. And even when these remaining steps have been achieved in model plants such as tobacco, improved crops are still some way off. However, this work is a milestone on the road to boosting plant efficiency. The advance can be

likened to having a new engine block in place in a high-performance car engine — now we just need the turbocharger fitted and tuned. ■

G. Dean Price and Susan M. Howitt are in the Research School of Biology, Australian National University, Canberra, ACT 0200, Australia.

e-mails: dean.price@anu.edu.au;

susan.howitt@anu.edu.au

1. www.un.org/News/Press/docs/2009/gaef3242.doc.htm
2. Lin, M. T., Occhialini, A., Andralojc, P. J., Parry, M. A. J. & Hanson, M. R. *Nature* **513**, 547–550 (2014).
3. Long, S. P., Zhu, X.-G., Naidu, S. L. & Ort, D. R. *Plant Cell Environ.* **29**, 315–330 (2006).
4. Rae, B. D., Long, B. M., Badger, M. R. & Price, G. D. *Microbiol. Mol. Biol. Rev.* **77**, 357–379 (2013).
5. Tcherkez, G. G. B., Farquhar, G. D. & Andrews, T. J. *Proc. Natl Acad. Sci. USA* **103**, 7246–7251 (2006).
6. Kanevski, I., Maliga, P., Rhoades, D. F. & Gutteridge, S. *Plant Physiol.* **119**, 133–141 (1999).
7. Lin, M. T. *et al. Plant J.* **79**, 1–12 (2014).
8. Price, G. D. *et al. J. Exp. Bot.* **64**, 753–768 (2013).
9. McGrath, J. M. & Long, S. P. *Plant Physiol.* **164**, 2247–2261 (2014).

This article was published online on 17 September 2014.

NETWORK BIOLOGY

A compass for stem-cell differentiation

The development of CellNet — network-biology software that determines how cell types generated *in vitro* relate to their naturally occurring counterparts — could improve our ability to produce desirable cells in culture.

FRANZ-JOSEF MÜLLER & JEANNE F. LORING

Over the past few years, websites such as Facebook and Google have attained an uncanny ability to understand us and to predict our behaviour, even before we have consciously decided what to do. This predictive power is achieved through the systematic application of statistical 'inference algorithms' to the vast numbers of connections and links that users establish when browsing the Internet — making up a 'social graph' that can be exploited to characterize distinct groups of Internet users. It would be wonderful to have such a graph to characterize distinct groups of cells. This could then be used in regenerative medicine to overcome the challenge of coercing stem cells to become the cell type needed for a particular therapy. Writing in *Cell*, Cahan *et al.*¹ and Morris *et al.*² describe a network-biology platform, CellNet, that takes a first step in this direction.

The most popular representation of the differentiation of cells from immature precursors to mature cell types was, for many years,

the 'epigenetic landscape' diagram conceived by the biologist Conrad Hal Waddington^{3,4}. This diagram evokes a set of one-way paths down which immature cells roll along defined routes to more-differentiated cellular states. But over the past decade, this simple model has morphed into the concept of a multidirectional cell-identity transfer hub.

In 2007, Yamanaka and colleagues⁵ reprogrammed ordinary human skin cells called dermal fibroblasts into induced pluripotent stem (iPS) cells using transcription factors that are highly expressed in embryonic stem (ES) cells, an equivalent cell type that is derived from early embryos. Both iPS cells and ES cells are pluripotent — they can, given the correct molecular cues, differentiate into almost any cell in the body, forming any one of hundreds of different cell types. Each of these mature cell types is characterized by distinct networks of highly expressed transcription factors, which regulate the expression of large sets of genes. Researchers have used transcription-factor cocktails specific to cell types of interest to try to directly convert one cell type, such as a

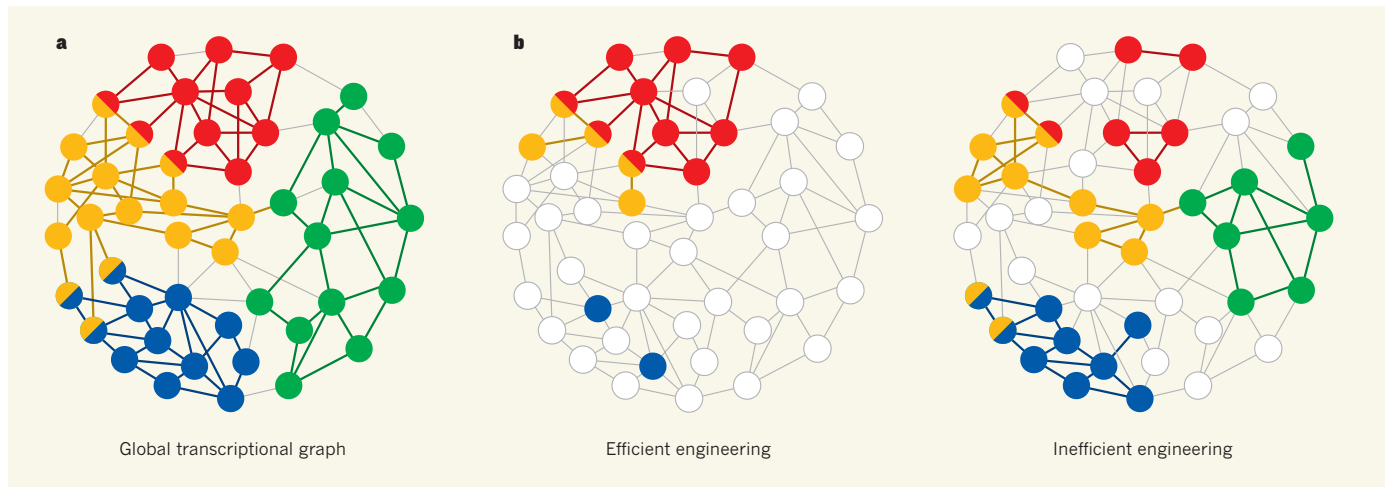


Figure 1 | Improving cellular engineering. Two papers^{1,2} report the development of a network-biology platform called CellNet. **a**, A simplified schematic of the global transcriptional graph generated by CellNet, in which each circle represents a gene and each line links genes that are co-regulated. CellNet defines gene-regulatory networks — groups of highly interconnected and coordinately regulated genes — that are specific to distinct cell types. Gene-regulatory networks that are characteristic

of four cell types are indicated by different colours. **b**, Two examples of gene-expression patterns in engineered cells. CellNet compares the gene-expression networks of these experimentally derived cells with the global transcriptional graph to determine whether the cultured cells resemble a naturally occurring cell type (as in the example on the left) or not (right). Colourless circles indicate genes that are not expressed in the cell type being analysed.

fibroblast, into another, such as a neuron⁶ or a liver cell⁷ (known as a hepatocyte). The abundance of reports suggests that there are almost no limits to the number of possible cellular transformations.

But are these engineered cells genuine copies of cells that exist in the body? There are well-established gene-expression tools for determining whether a stem cell is pluripotent^{8,9}. But remarkably, given the flurry of research into directing stem cells to take on a particular identity, or fate, there is no commonly accepted way to determine whether a differentiating cell is moving towards the right developmental destination. Cahan *et al.* designed the CellNet software to give researchers an idea of how closely matched a cultured cell type is to its presumed counterpart in the body. The program applies a sequence of statistical inference algorithms to create a global transcriptional graph, which resembles the social graphs used by websites such as Facebook (Fig. 1a).

To construct this transcriptional graph, the authors used publicly available gene-expression data from tissues and cells, and information from genome-wide transcription-factor binding studies performed by the ENCODE consortium. The CellNet program identifies gene-regulatory networks (GRNs) for specific cell types in the body, such as neurons and hepatocytes. GRNs are groups of genes that are coordinately regulated in distinct cell types and that are more highly interconnected with one another than with other genes. The program then compares these cell-type-specific GRNs with those from experimentally derived cultured cells to determine how accurately the derived cells mimic the ‘real’ cell type (Fig. 1b). In addition, CellNet suggests transcription factors that could be modulated to shift an

in vitro cell type closer to its *in vivo* correlate.

Cahan and colleagues compared two strategies for producing mature cell types: differentiation from pluripotent stem cells and direct conversion from another cell type. Testing engineered neurons and hepatocytes, CellNet analysis revealed differences between the two approaches. Cell types derived from pluripotent stem cells were similar to the naturally occurring cell types, but directly converted cells could be abnormal. For example, neurons directly converted from fibroblasts retained substantial fibroblastic identity and expressed GRNs that were characteristic of cells from the heart and pancreas.

How can CellNet improve the quality of engineered cells? An inkling of its future utility comes from Morris and colleagues’ study of directly converted hepatocytes, called induced hepatocytes (iHeps). A CellNet comparison of iHeps and actual hepatocytes revealed that iHeps did express GRNs that were characteristic of hepatocytes, but they also activated illicit, developmentally immature transcriptional programs. Following up on this observation, Morris *et al.* found that the iHeps would be better described as induced endoderm progenitors (iEPs). These endodermal precursors can give rise to many cell types that arise from the endoderm (an embryonic cell layer), including cells of the colon, liver and pancreas. Indeed, when the authors used CellNet as a guide to modify the transcription-factor cocktail used for direct conversion, they generated iEPs that could differentiate into mature colon cells when transplanted into mice, and could repair damaged colons.

The major limitation of predictive programs such as CellNet is a shortage of data. In the modern world of ‘big data’, more data always

lead to better predictions. Although Google can profile hundreds of millions of search users and follow their behaviour over several years, the CellNet team were limited to published data generated from a few thousand genome-wide analyses of gene expression. Because of the lack of large data sets from human cells and tissues, the current version of CellNet is practical only for experimental studies of mouse cells.

The lack of large, high-quality genome-wide transcriptional profiles for normal human cell types is a major bottleneck in the development of stem-cell-based therapies and drug screens. We need to learn how to robustly define and mechanistically understand the molecular coordinates for differentiated cell types before we can give human stem cells the directions they need to arrive at the right fate. As the baseball player Yogi Berra once said, “If you don’t know where you’re going, you’ll wind up someplace else”. ■

Franz-Josef Müller is at the Zentrum für Integrative Psychiatrie Kiel, Universitätsklinikum Schleswig-Holstein, 24105 Kiel, Germany. **Jeanne F. Loring** is in the Department of Chemical Physiology, Center for Regenerative Medicine, The Scripps Research Institute, California 92037, USA. e-mails: fj.mueller@zip-kiel.de; jloring@scripps.edu

1. Cahan, P. *et al.* *Cell* **158**, 903–915 (2014).
2. Morris, S. A. *et al.* *Cell* **158**, 889–902 (2014).
3. Slack, J. M. *Nature Rev. Genet.* **3**, 889–895 (2002).
4. Waddington, C. H. *The Strategy of the Genes* (George Allen & Unwin, 1957).
5. Takahashi, K. *et al.* *Cell* **131**, 861–872 (2007).
6. Vierbuchen, T. *et al.* *Nature* **463**, 1035–1041 (2010).
7. Sekiya, S. & Suzuki, A. *Nature* **475**, 390–393 (2011).
8. Müller, F. J. *et al.* *Nature* **455**, 401–405 (2008).
9. Müller, F. J. *et al.* *Nature Methods* **8**, 315–317 (2011).

Asian monsoons in a late Eocene greenhouse world

A. Licht^{1,2,3}, M. van Cappelle^{4,5}, H. A. Abels^{4,6}, J.-B. Ladant⁷, J. Trabucho-Alexandre⁸, C. France-Lanord², Y. Donnadieu⁷, J. Vandenbergh⁹, T. Rigaudier², C. Lécuyer¹⁰, D. Terry Jr¹¹, R. Adriaens⁶, A. Boura¹², Z. Guo¹³, Aung Naing Soe¹⁴, J. Quade³, G. Dupont-Nivet^{4,13,15,16} & J.-J. Jaeger¹

The strong present-day Asian monsoons are thought to have originated between 25 and 22 million years (Myr) ago, driven by Tibetan–Himalayan uplift. However, the existence of older Asian monsoons and their response to enhanced greenhouse conditions such as those in the Eocene period (55–34 Myr ago) are unknown because of the paucity of well-dated records. Here we show late Eocene climate records revealing marked monsoon-like patterns in rainfall and wind south and north of the Tibetan–Himalayan orogen. This is indicated by low oxygen isotope values with strong seasonality in gastropod shells and mammal teeth from Myanmar, and by aeolian dust deposition in northwest China. Our climate simulations support modern-like Eocene monsoonal rainfall and show that a reinforced hydrological cycle responding to enhanced greenhouse conditions counterbalanced the negative effect of lower Tibetan relief on precipitation. These strong monsoons later weakened with the global shift to icehouse conditions 34 Myr ago.

The Asian monsoon system controls precipitation over mainland Asia and is a critical component of modern global atmospheric circulation¹. During summer monsoons, high insolation over continental regions produces a strong land–sea pressure gradient that forces oceanic winds to converge over the East and South Asian continents, bringing oceanic moisture inland and causing abundant rainfall². During winter monsoons, continents cool and winds reverse, causing dry conditions¹ (Fig. 1a). Strong summer monsoonal precipitation, as seen in the present day, is enhanced by the Tibetan, Himalayan and Sino-Burman topographic highs, which favour ascendant convection^{3,4}.

The onset of the modern Asian monsoonal system has been genetically linked to development of high topographic relief associated with the uplift of the Tibetan–Himalayan orogen^{3,5}, although the timing of this uplift and its role in forcing climate dynamics are still a matter of debate^{6–8}. The aeolian dust deposits of the Chinese Loess Plateau, attributed to winter monsoonal storms sweeping clastic material from the deserts of the Asian interior into central China, are reported to be as old as the Late Oligocene–Early Miocene, 25–22 Myr ago^{9,10}. In addition to aeolian sediments, the shift from arid to wet conditions in central China documented by pollen data sets¹¹ and the marked increase in weathering indices and sedimentation rates in Southeast Asian marginal seas⁵ suggest the beginning of strong wind circulation and inland moisture supply at this time.

Although poorly documented, pre-Early Miocene climate in Asia is of particular interest because it is characterized by higher atmospheric CO₂ content (pCO₂), a connection that should improve our understanding of how monsoonal circulation will respond to the forthcoming high-pCO₂ world^{12,13}. Existing climatic models^{3,14–17} suggest that there was significantly weaker, but active, monsoonal circulation during the Eocene, 55–34 Myr ago. However, late Eocene tectonic events, such as the

retreat of the Paratethys Sea from the Tarim Basin (40–37 Myr ago; Fig. 1b, c)^{14–16,18} and the opening of the South China Sea (35–30 Myr ago)¹⁶, would have progressively increased land–sea pressure contrasts and could have set the stage for monsoonal intensification. Moreover, recent simulations¹⁹ suggest that Eocene greenhouse conditions¹² might have globally favoured strong monsoonal precipitation. Palynological and sedimentological evidence has been used to argue both in favour^{20,21} and against¹¹ marked Eocene monsoons on the Asian mainland. These varied interpretations underscore the fact that the existence and intensity of the Asian monsoons during the Eocene have yet to be established by well-dated, comprehensive data sets and tested by climate model experiments.

Eocene monsoons south of the Himalayas

South of the Tibetan–Himalayan orogen, monsoons are primarily expressed by intense summer rainfall in a wide area stretching along the Indian Foreland Basin (Fig. 1a)². In this area, proxies of past isotopic composition of rainwater provide an insight into monsoonal intensity^{22–24}. Monsoonal rainwaters are highly depleted in the oxygen isotope ¹⁸O relative to ¹⁶O during intense rainfall^{25–27}. This ¹⁸O depletion is related to both summer rainfall intensity^{25,27} and the contribution of that rainfall to source water in the Bay of Bengal²⁶, thus producing an intimate correlation between ¹⁸O depletion and summer monsoon intensity²⁵. In contrast, infrequent rains during the winter are strongly enriched in ¹⁸O (refs 26, 27). These seasonal features control surface-water isotopic compositions and are preserved in the isotopic composition of freshwater gastropod shells^{28,29} and of fossil tooth enamel from water-dependent mammals^{22–24,30}. Both biotic proxies have been shown to record past monsoonal precipitation patterns over the past 10 Myr (refs 22, 23).

¹Institut de Paléoprimatologie, Paléontologie Humaine: Evolution et Paléoenvironnements, UMR CNRS 7262, Université de Poitiers, 86000 Poitiers, France. ²Centre de Recherches Pétrographiques et Géochimiques, UMR CNRS 7358, Université de Lorraine 54501 Vandœuvre les Nancy, France. ³Department of Geosciences, University of Arizona, Tucson, Arizona 85721, USA. ⁴Department of Earth Sciences, Universiteit Utrecht, 3584CD, Utrecht, The Netherlands. ⁵Department of Earth Science and Engineering, Imperial College London, London SW7 2AZ, UK. ⁶Department of Earth and Environmental Sciences, Katholieke Universiteit Leuven, 3001 Leuven, Belgium. ⁷Laboratoire des Sciences du Climat et de l'Environnement, UMR CNRS 8212, 91198 Gif-sur-Yvette, France. ⁸Department of Earth Sciences, Durham University, Durham DH1 3LE, UK. ⁹Department of Earth Sciences, Vrije Universiteit, 1081HV Amsterdam, The Netherlands. ¹⁰Laboratoire de Géologie de Lyon, Terre, Planètes, Environnement, UMR CNRS 5276, Université de Lyon, Institut Universitaire de France, 69622 Lyon, France. ¹¹Department of Earth and Environmental Science, Temple University, Philadelphia, Pennsylvania 19122, USA. ¹²Centre de Recherche sur la Paléodiversité et les Paléoenvironnements – UPMC, MNHN, CNRS, 75005 Paris, France. ¹³Key Laboratory of Orogenic Belts and Crustal Evolution, Peking University, 100871 Beijing, China. ¹⁴Department of Geology, Defence Services Academy, Pwint Oo Lwin, Myanmar. ¹⁵Géosciences Rennes, UMR CNRS 6118, Université de Rennes, 35042 Rennes Cedex, France. ¹⁶Universität Potsdam, Institute of Earth and Environmental Science, 14476 Potsdam, Germany.

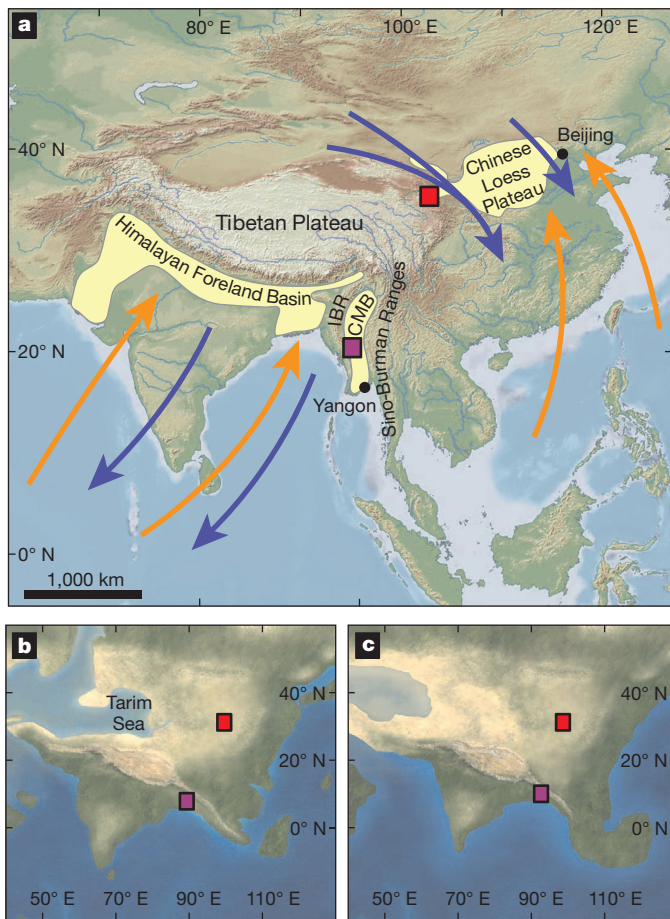


Figure 1 | Location map of study sites and late Eocene palaeogeography of the Asian mainland. **a**, The Xining Basin (red square) and Myanmar (purple square) study sites and the prevailing summer (red arrows) and winter (blue arrows) wind directions of the present-day Asian monsoons. IBR, Indo-Burman Ranges; CMB, Central Myanmar Basin. **b**, Palaeogeographic reconstruction used in the late Eocene (40 Myr ago) climate simulations^{6,45,46} with the Tibetan Plateau maximum height set to 3,500 m and Sino-Burman Ranges to 1,500 m. **c**, Palaeogeographic reconstruction used in the Eocene–Oligocene transition (34 Myr ago) simulations⁴⁹. More detailed topography is given in Extended Data Fig. 1.

Freshwater gastropod shells and fossil teeth of mammals from the Middle Eocene Pondaung and Upper Eocene Yaw Formations (40–34 Myr ago; Fig. 2a) of central Myanmar³¹ show consistently low $\delta^{18}\text{O}$ values (representing the $^{18}\text{O}/^{16}\text{O}$ ratio relative to Vienna standard mean ocean water (V-SMOW) and Vienna Pee Dee Belemnite (V-PDB) international standards), reaching less than -14‰ V-SMOW for gastropod material and 14‰ V-SMOW for fossil teeth (Fig. 2b, c). Eocene fossil enamel and gastropod values are lower than those seen in modern material from the Himalayan Foreland Basin by 4–6‰ and 3.5–4‰, respectively (Extended Data Table 1), but similar to Upper Miocene fossil values^{22–24,29}. The oxygen isotopic composition of tooth enamel is linearly dependent on the ingested water $\delta^{18}\text{O}$ (ref. 30), whereas the composition of gastropod shells is linearly dependent on both the water $\delta^{18}\text{O}$ and temperature²⁸. Warmer late Eocene temperatures $\sim 5^\circ\text{C}$ higher than today^{12,13} would decrease shell $\delta^{18}\text{O}$ values by only 1‰ (refs 22, 28); the low values therefore indicate strong depletion in ^{18}O in late Eocene Burmese surface waters.

Despite the long distance between the comparative sites in the Himalayan Foreland Basin (the Bugti Hills are $\sim 2,500$ km distant from central Myanmar), all sites display a well-established monsoonal cycle in rainwater isotopic composition^{25,27}. Modern and fossil $\delta^{18}\text{O}$ values in the Himalayan Foreland Basin can be lowered by catchments of high-altitude rivers flowing from the Himalayas^{22–24,29}. However, the low values

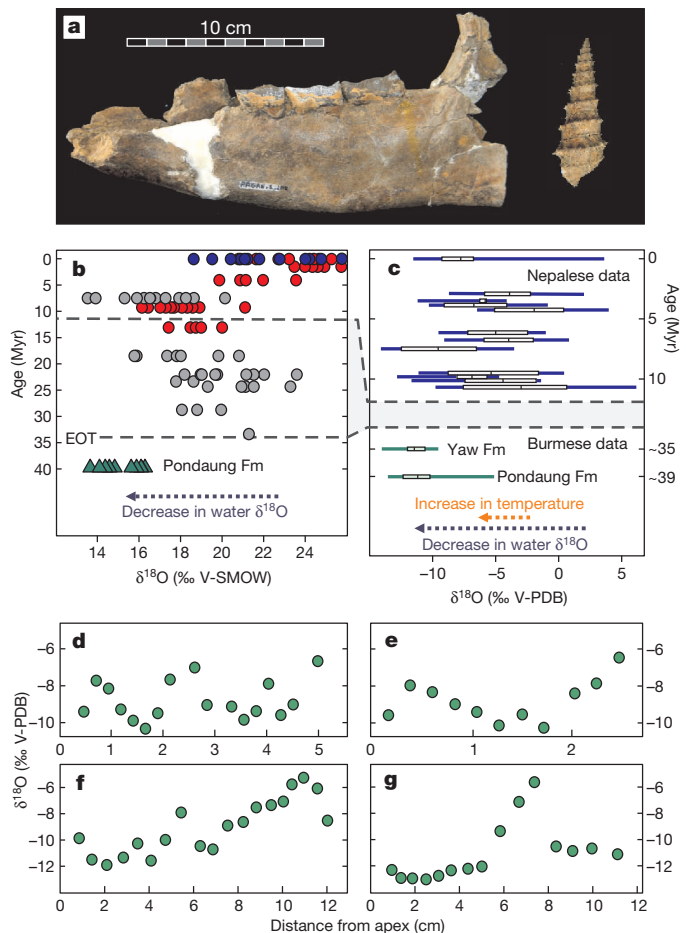


Figure 2 | Low oxygen isotopic values with strong yearly variation in fossils from Myanmar. The values reveal a strong, seasonal depletion in ^{18}O of surface water in the late Eocene. **a**, Fossil material from the Pondaung Formation, including a rhinocerotid jaw and freshwater gastropod. **b**, Comparison of $\delta^{18}\text{O}$ of tooth enamel (phosphate phase) from Burmese fossil mammals (green triangles) with tooth enamel data from the younger Himalayan Foreland Basin (red circles, Pakistan (Siwaliks); grey circles, Pakistan (Bugti Hills); blue circles, central India)^{22–24}. EOT, Eocene–Oligocene transition; Fm, formation. **c**, Comparison of $\delta^{18}\text{O}$ values of Burmese fossil gastropod shells with $\delta^{18}\text{O}$ values from fossil²² and modern²⁹ shells in the Himalayan Foreland Basin (comparison data located at elevations $<1,000$ m). Boxes indicate lower and upper quartiles; inside boxes, solid lines indicate mean; whiskers indicate minimum and maximum values. **d–g**, Examples of $\delta^{18}\text{O}$ cycles from rhinocerotid teeth (enamel carbonate phase, two to four cycles; **d**, incisor; **e**, molar) and gastropod shells (one cycle; two different samples are shown in **f** and **g**). All isotope results are listed in Supplementary Tables 1–3; standard deviations $\leq 0.2\text{‰}$.

for Eocene Burmese fossils cannot be explained by such an altitude effect, considering the limited extent of the Burmese Eocene drainage and the relatively low elevation ($<3,000$ m) of recently uplifted neighbouring mountain ranges³¹. The intense depletion in ^{18}O compared with modern values can be partly explained by the -1‰ shift in late Eocene oceanic $\delta^{18}\text{O}$ (ref. 32). A contribution of East Pacific moisture to precipitation in the proto-Bengal Bay could account for an additional decrease of 2–3‰, considering the isotopic difference between the modern Indian Ocean and the East Pacific seawater and the rainout effects that decrease the isotopic composition of moisture during transport^{27,32}. However, a change in rainfall moisture sources seems unlikely, given that all existing climate models with late Eocene boundary conditions (including our simulations; see below) underscore the persistence of seasonal reversals of Indian oceanic winds and of equatorial moisture sources during the rainy season, similar to the present-day system^{14–17,19}. Regardless of the exact contribution of East Pacific moisture, rainfall $\delta^{18}\text{O}$ values in

the late Eocene were, if all these possible offsets are taken into account, at least similar to, and probably lower than, modern-day $\delta^{18}\text{O}$ values. Thus, they are most probably explained by a strong summer rainfall that was at least as intense as the modern summer monsoon^{22,25}.

Moreover, $\delta^{18}\text{O}$ values within the Burmese fossils have striking cyclic and probably seasonal variations that yield annual growth rate estimates that are consistent with those of modern material^{29,33}. These seasonal variations average 3.8‰ for gastropod shells and 2.2‰ for tooth enamel, with ranges up to twice these values (Fig. 2d–g), similar to those seen in modern tooth enamel and gastropod shells from the Ganga Plain^{23,29}. Like our fossil species, modern gastropods from the Ganga plain rarely have more than one seasonal cycle, because they cannot survive the dry winter²⁹. This interpretation of strong seasonality in the Burmese fossil material is confirmed by growth lines in coeval primate jaws³⁴, pronounced cracking and swelling features in palaeosols³⁵, and fossil wood with marked growth rings^{34,36} similar to modern forests that only grow in environments with strong monsoonal influence³⁶. These combined results reveal that intense summer precipitation was followed by a marked dry season and indicate modern-like monsoonal rainfall south of the proto-Tibetan–Himalayan orogen during the late Eocene, ~40 Myr ago.

Eocene desertification in inner Asia

In addition to our results from Myanmar, we have extended the sedimentary record of the Chinese Loess Plateau at its western margin to include the late Eocene Mahalagou Formation in the Xining Basin, which was deposited between 40 and 33 Myr ago as determined by detailed magnetostratigraphy^{7,37,38}. These strata are dominated by homogeneous red mudstones deposited in dry mudflat environments and are intercalated with gypsum layers (up to 1 m thick) that represent ephemeral to perennial saline lake systems³⁸ (Fig. 3a and Extended Data Fig. 2). These strata can be traced more than 200 km into the Gansu province, which demonstrates their regional palaeoenvironmental significance^{37,38}.

These clastic sediments lack evidence, either in outcrop³⁸ or in thin section, of pedogenesis or sedimentary structures indicative of fluvial transport. The particle size, shape and surface microtexture of quartz grains in the detrital silt and very fine sand fractions of these deposits

were studied under a scanning electron microscope (SEM) and suggest prolonged aeolian transport (Fig. 3b, c). Characteristic textures include dish-shaped concavities, mechanically formed upturned plates, flat cleavage faces and cleavage planes, angular blade-shaped grains and other spalls, and a high abundance of clays adhering to quartz grains and other clay particles³⁹. Grain-size distributions of the clastic component in the red mudstones and gypsum beds show a bimodal distribution strongly indicative of aeolian transport for this clastic material⁴⁰. This bimodal distribution of coarse (16–31 μm) and fine (1.6–2.8 μm) fractions persists throughout our study interval (Fig. 3d). This bimodality is strikingly similar to Miocene–Quaternary deposits of the Chinese Loess Plateau^{10,40–42}, which have a coarse fraction transported by spring-monsoon and winter-monsoon dust storms in near-surface suspension clouds and a fine fraction commonly attributed—although this remains controversial—to year-round, background dust fall from upper-level airflow supplied by westerly winds⁴⁰.

The textural characteristics and grain-size distribution of the late Eocene clastic sediments from the Xining Basin indicate an aeolian origin; this potentially includes partial local reworking of dust by surface water or the settling of dust in shallow lakes, as observed in several aeolian dust deposits in central China⁴³. Despite the reworking, original grain-size properties were retained. Our results from the clastic deposits of the Xining Basin extend the record of aeolian dust in central China back 15 Myr earlier than previously reported^{9,10}.

The onset of aeolian deposition in central China has been related to the onset of desertification and winter monsoonal circulation in inner Asia⁹. Aeolian dust deposits require both a sizeable desert source area to provide aeolian particles and energetic winds to carry the particles to the area of deposition⁹. The prevalence of wet, subtropical conditions in south and coastal China in the late Eocene²⁰ indicates a roughly northwesterly origin for palaeo-winds that is confirmed by our climate simulations (see below), similar to the modern winter monsoonal wind direction, and indicates that the source areas were probably located in inner Asia. The deposits in the Xining Basin suggest that inner Asian desertification was significant in the late Eocene and that spring and winter monsoonal winds were already active.

Gypsum beds intercalated with red mudstone deposits in the Xining Basin provide insight into potential forcing mechanisms of desertification in inner Asia. These gypsum beds represent ephemeral to perennial saline lakes that formed when the water supply from moisture sources was greater³⁸. Potential water sources include the epicontinental Tarim Sea to the west, and the Pacific and Indian Ocean to the east and south^{18,37,38}. A significant decrease in gypsum content relative to mudstone 37 Myr ago³⁸ is synchronous with the last retreat of the Tarim Sea¹⁸, suggesting that this was a significant water source to local rainfall before the sea retreated. However, the persistent, yet much reduced, recurrence of gypsum layers after 37 Myr ago suggests a dominant moisture source from southern and eastern oceans such as that supplied by the modern summer monsoon, although moisture from a remnant of the Paratethys sea further to the west cannot be ruled out. The complete disappearance of gypsum intercalations just after the 34 Myr Eocene–Oligocene transition indicates global climate forcing associated with the coeval shift from greenhouse to icehouse conditions and the onset of large-scale Antarctic ice-sheets^{37,38}. Furthermore, alternating saline lake gypsum and dry mudflat red mudstones layers indicate marked wet and dry periods on orbital timescales³⁸, similar to the warmer and wetter equivalents of the loess–palaeosol alternations of the Chinese Loess Plateau^{10,41,42}, which are attributed to periods of orbitally forced variability in summer monsoonal intensity.

Insights from climate simulations

To test the intensity of the late Eocene monsoons we used climate simulations based on the atmospheric global circulation model LMDz⁴⁴ and a palaeogeographical reconstruction at 40 Myr (refs 45–47) with a Tibetan Plateau of intermediate height (3,500 m)^{6,7}, a wide Tarim Sea¹⁸, Eocene-like pCO_2 levels fourfold pre-industrial atmospheric levels¹²,

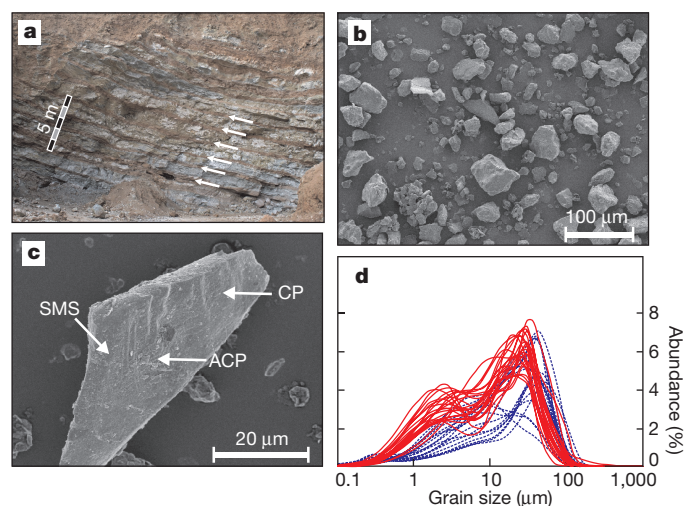


Figure 3 | Sedimentary features of late Eocene clastic deposits in the Xining Basin. **a**, Alternation of red mudstones (white arrows) and metre-thick gypsum layers in the Shuiwan section³⁸. **b**, SEM image of the clastic component showing the different grain sizes and angular grain shapes. **c**, SEM image displaying an angular blade-shaped quartz grain with cleavage planes (CP), adhering clay particles (ACP) and smooth precipitation surfaces (SMS). Additional images are provided in Extended Data Fig. 3. **d**, Comparison of a selection of grain-size distributions of mudstone samples (red lines; $n = 23$) with those for samples from the Chinese Loess Plateau (blue lines; $n = 22$)^{41,42}. All grain-size and mineralogical results are given in Extended Data Fig. 2 and Supplementary Tables 4 and 5.

and two opposite orbital scenarios⁴⁸ (warm austral and warm boreal orbits) representing solar insolation minima and maxima related to orbital cyclicity (Fig. 4 and Methods). Our modelling is distinctly different from existing models using Eocene conditions^{4,14–17,19} in using a more realistic palaeogeography with a higher spatial resolution, and in quantitatively testing the impact of varying greenhouse conditions and orbital parameters on the Eocene Asian mainland. Our modelled atmospheric circulation possesses a well-established winter and summer Asian monsoonal system in both orbital extremes.

South of the proto-Tibetan Plateau, a seasonal, modern-like reversal of Indian oceanic winds is established in our model, as well as the summer emplacement of an intense rainfall belt of more than 12 mm per day (>3,000 mm per year) along the southern flank of the orogen. These model results are in full agreement with a summer monsoonal origin of the low $\delta^{18}\text{O}$ values and marked seasonality in late Eocene fossils from Myanmar. North of the proto-Tibetan Plateau, our model indicates a high-pressure cell in central China that strengthened the northwesterly winds during the winter (Fig. 4a, b) causing monsoonal winds with modern-day velocities¹ of 5–10 m s⁻¹. This is in agreement with a winter monsoonal origin of Xining aeolian dust. In the summer, weak monsoon winds occurred along the flank of the Tibetan highs and along coastal China, while strong westerly surface winds dominated in northern China (Fig. 4c, d). The Xining area intersected the domains of the westerly winds and coastal summer monsoon, suggesting that these westerly summer surface winds may have also contributed to aeolian dust transport⁴².

Our model results show weaker East Asian summer monsoonal winds than in the present day; these were also apparent in previous simulations with a lowered Asian elevation^{3,14–17}. However, the negative impact of lower Tibetan elevation on annual rainfall in our simulations was counterbalanced by enhanced atmospheric pCO₂. The enhanced greenhouse conditions resulted in higher atmospheric water vapour loading and a reinforced hydrological cycle^{3,19}. Despite weaker summer monsoonal winds, the pCO₂ level of fourfold pre-industrial levels is sufficient to generate summer and annual rainfall amounts as high as modern values in Xining and Myanmar (Fig. 4c–f and Extended Data Table 2).

Our simulations further indicate a strong sensitivity of Asian rainfall to orbital parameters that generate precipitation values varying from close to those of the modern day to significantly greater amounts. In the warm austral orbital scenario, a zonal high-pressure band with more arid conditions of commonly 0–400 mm of annual rainfall and insignificant summer precipitation extends from coastal China to the Tarim Sea between 30° and 40° N latitudes (Fig. 4g). In the warm boreal orbital scenario, summer oceanic moisture supply penetrates into central China, causing more abundant rainfall (commonly 500–1,000 mm of annual rainfall), whereas arid conditions are limited to inner China and the Tarim seashores (Fig. 4h).

The repetitive alternation of gypsum and red mudstone in the Xining Basin is driven astronomically, predominantly by obliquity cycles³⁸, indicating an alternation of wetter and drier periods on orbital timescales. In our climate simulations, annual rainfall in the Xining area is more than doubled in the warm boreal scenario compared with the warm austral. Thus, a tentative link can be made between boreal insolation maxima to saline lake expansion causing gypsum precipitation, and austral insolation maxima to lake desiccation phases and red mudstone deposition in the Xining area (Extended Data Fig. 4). It may also explain the seemingly unstable character of arid regions in central China before the Eocene–Oligocene greenhouse–icehouse transition at 34 Myr ago^{11,20,21}.

Under decreasing atmospheric CO₂ pressure and increasing Antarctic ice volume, our climate simulations based on a palaeogeographical reconstruction at 34 Myr ago⁴⁹ reveal a decreasing East Asian moisture supply (Fig. 5a) caused by a decreased pressure gradient from continent to ocean (Fig. 5b). This summer monsoon weakening in East Asia explains the observed disappearance of wet-phase gypsum intercalations from the Xining Basin³⁵ during the greenhouse–icehouse transition across the Eocene–Oligocene boundary¹³.

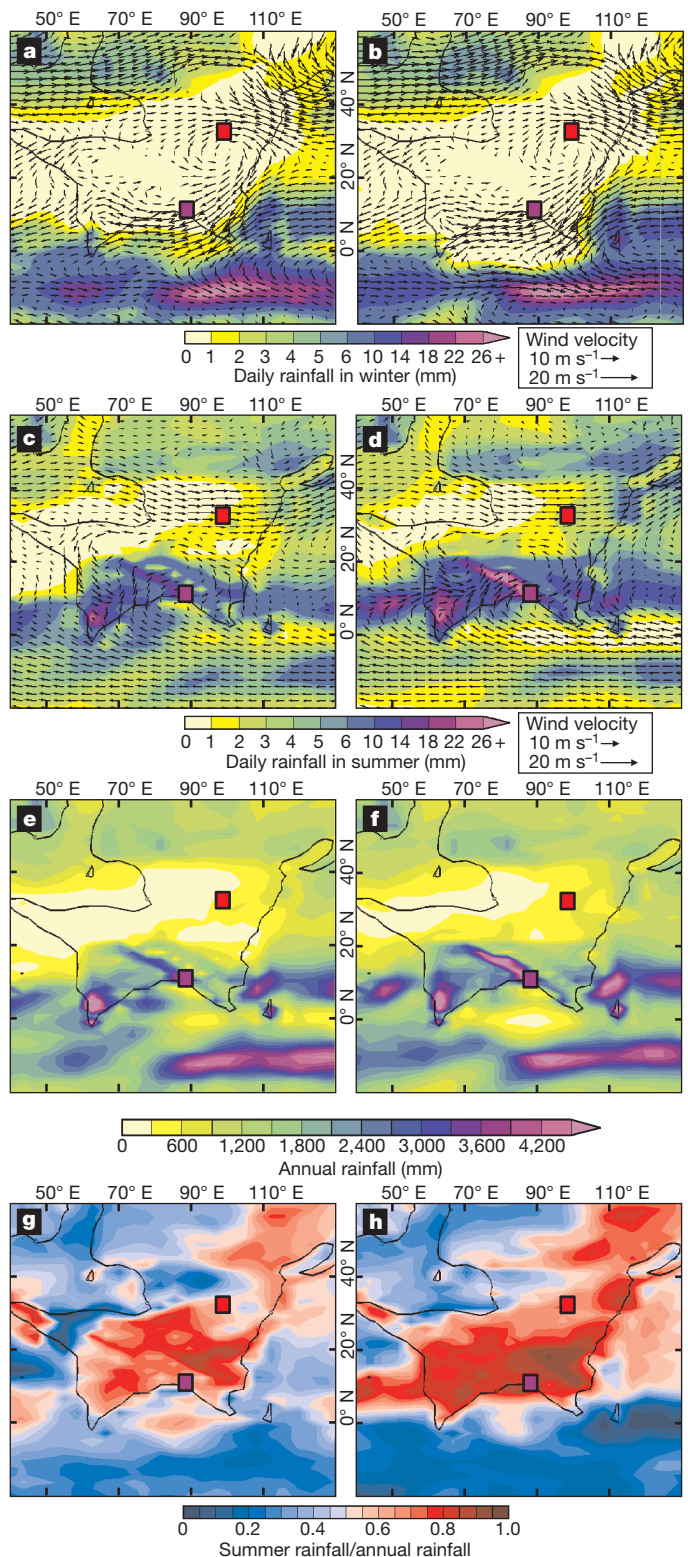


Figure 4 | Climatic simulations at 40 Myr ago, illustrating Eocene monsoonal circulation on the Asian mainland. Simulations were run with interpreted late Eocene palaeogeography (Fig. 1b), pCO₂ level (fourfold pre-industrial atmospheric levels)¹² and with Antarctica set to ice-free conditions⁴⁷. Two orbital scenarios were tested: a ‘warm austral’ extreme⁴⁸ (a, c, e, g) and a ‘warm boreal’ extreme⁴⁸ (b, d, f, h). a, b, Winter rainfall and 850-hPa winds; c, d, summer rainfall and 850-hPa winds (winds are displayed in areas lower than 2,000 m elevation); e, f, annual rainfall; g, h, seasonality index (ratio of rainfall from May to September versus annual rainfall¹⁹).

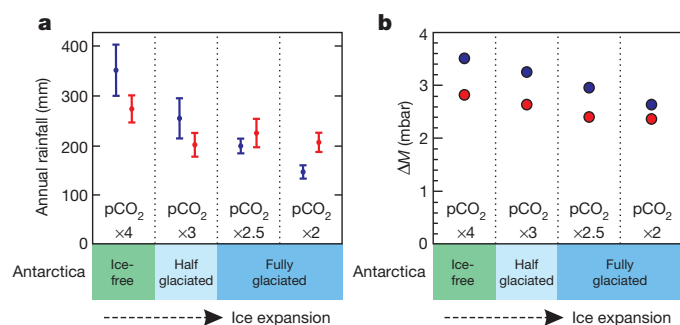


Figure 5 | Climatic simulations at 34 Myr ago. The figure illustrates decreasing monsoon strength in response to ice-sheet expansion and lowering atmospheric CO₂ pressure. Four climate scenarios were run with interpreted Eocene–Oligocene transition palaeogeography (Fig. 1c)¹²: ice-free Antarctica with pCO₂ at fourfold pre-industrial atmospheric levels, half-glaciated Antarctica with pCO₂ at threefold pre-industrial atmospheric levels, and fully glaciated Antarctica with pCO₂ at 2.5-fold and twofold pre-industrial atmospheric levels. **a**, Annual rainfall in the Xining Basin, averaged over the area between 101° E and 105° E and 35° N and 39° N (with standard deviations). Annual rainfall in the ice-free scenario is slightly lower than in the simulations at 40 Myr ago in response to changing palaeogeography (Extended Data Fig. 1). **b**, Differences in the modelled monsoonal index M (ΔM , experiment minus control simulation), quantifying the continent–ocean pressure gradient in Asia and thus monsoonal intensity¹⁵. In both panels, blue represents warm boreal orbital parameters, and red represents warm austral orbital parameters.

Forcing by the Himalayan–Tibetan uplift has a clear impact on monsoon strength in our (and other) studies, but forcing from the global climate, predominantly driven by atmospheric pCO₂, should be equally regarded as one of the governing parameters contributing to the singular strength of the Asian summer and winter monsoons. The decrease in the continent–ocean pressure gradient through the Eocene–Oligocene transition of 0.9 mbar in the warm boreal scenario is the same order of magnitude as the increase of 0.8 mbar induced by the proposed Tibetan uplift during the Miocene in sensitivity test simulations¹⁵. In addition to high pCO₂ in the Eocene, a significant part of the Tibetan–Himalayan orogen was probably already elevated in the Late Eocene, possibly by pre- and/or early-collision orogenesis^{6–8}. As a result, the impact of later uplift events on the stepwise onset of monsoonal circulation may be significantly overestimated.

Online Content Methods, along with any additional Extended Data display items and Source Data, are available in the online version of the paper; references unique to these sections appear only in the online paper.

Received 21 January; accepted 21 July 2014.

Published online 14 September 2014.

- Xu, M. *et al.* Steady decline of east Asian monsoon winds, 1969–2000: evidence from direct ground measurements of wind speed. *J. Geophys. Res.* **111**, D24111 (2006).
- Zhang, S. & Wang, B. Global summer monsoon rainy seasons. *Int. J. Climatol.* **28**, 1563–1578 (2008).
- Prell, W. & Kutzbach, J. Sensitivity of the Indian Monsoon to forcing parameters and implications for its evolution. *Nature* **360**, 647–652 (1992).
- Boos, W. & Kuang, Z. Dominant control of the South Asian monsoon by orographic insulation versus plateau heating. *Nature* **463**, 218–222 (2010).
- Cliff, P. *et al.* Correlation of Himalayan exhumation rates and Asian monsoon intensity. *Nature Geosci.* **351**, 875–881 (2008).
- Rowley, D. & Currie, B. Paleo-altimetry of the late Eocene to Miocene Lunpola basin, central Tibet. *Nature* **439**, 677–681 (2006).
- Dupont-Nivet, G., Hoorn, C. & Konert, M. Tibetan uplift prior to the Eocene–Oligocene climate transition: evidence from pollen analysis of the Xining Basin. *Geology* **36**, 987–990 (2008).
- Molnar, P., Boos, W. & Battisti, D. Orographic controls on climate and paleoclimate of Asia: thermal and mechanical roles for the Tibetan Plateau. *Annu. Rev. Earth Planet. Sci.* **38**, 77–102 (2010).
- Guo, Z. *et al.* Onset of Asian desertification by 22 Myr ago inferred from loess deposits in China. *Nature* **416**, 159–163 (2002).
- Qiang, X. *et al.* New eolian red clay sequence on the western Chinese Loess Plateau linked to onset of Asian desertification about 25 Ma ago. *Sci. China Earth Sci.* **54**, 136–144 (2011).

- Sun, X. & Wang, P. How old is the Asian monsoon system? Paleobotanical records from China. *Palaeogeogr. Palaeoclimatol. Palaeoecol.* **222**, 181–222 (2005).
- Pagani, M., Zachos, J., Freeman, K., Tipler, B. & Bohaty, S. Marked decline in atmospheric carbon dioxide concentrations during the Paleogene. *Science* **309**, 600–603 (2005).
- Zachos, J., Pagani, M., Sloan, L., Thomas, E. & Billups, K. Trends, rhythms, and aberrations in global climate 65 Ma to present. *Science* **292**, 686–693 (2001).
- Ramstein, G., Fluteau, F., Besse, J. & Joussaume, S. Effect of orogeny, plate motion and land–sea distribution on Eurasian climate change over the past 30 million years. *Nature* **386**, 788–795 (1997).
- Fluteau, F., Ramstein, G. & Besse, J. Simulating the evolution of the Asian and African monsoons during the past 30 Myr using an atmospheric general circulation model. *J. Geophys. Res.* **104**, 11995–12018 (1999).
- Zhang, Z., Wang, H., Guo, Z. & Jiang, D. Impacts of tectonic changes on the reorganization of the Cenozoic paleoclimatic patterns in China. *Earth Planet. Sci. Lett.* **257**, 622–634 (2007).
- Zhang, Z. *et al.* Early Eocene Asian climate dominated by desert and steppe with limited monsoons. *J. Asian Earth Sci.* **44**, 24–35 (2012).
- Bosboom, R. *et al.* Late Eocene sea retreat from the Tarim Basin (west China), and concomitant Asian paleoenvironmental change. *Palaeogeogr. Palaeoclimatol. Palaeoecol.* **299**, 385–398 (2011).
- Huber, M. & Goldner, A. Eocene monsoons. *J. Asian Earth Sci.* **44**, 3–23 (2012).
- Quan, C., Liu, Y. & Utescher, T. Eocene monsoon prevalence over China: a paleobotanical perspective. *Palaeogeogr. Palaeoclimatol. Palaeoecol.* **365–366**, 302–311 (2012).
- Wang, D., Lu, S., Han, S., Sun, X. & Quan, C. Eocene prevalence of monsoon-like climate over eastern China reflected by hydrological dynamics. *J. Asian Earth Sci.* **62**, 776–787 (2013).
- Dettman, D. *et al.* Seasonal stable isotope evidence for a strong Asian monsoon throughout the past 10.7 m.y. *Geology* **29**, 31–34 (2001).
- Sharma, S. *et al.* Oxygen isotopes of bovid teeth as archives of paleoclimatic variations in archaeological deposits of the Ganga plain, India. *Quat. Res.* **62**, 19–28 (2004).
- Martin, C., Bentalab, I. & Antoine, P. O. Pakistan mammal tooth stable isotopes show paleoclimatic and paleoenvironmental changes since the early Oligocene. *Palaeogeogr. Palaeoclimatol. Palaeoecol.* **311**, 19–29 (2011).
- Vuille, M., Werner, M., Bradley, R. S. & Keimig, F. Stable isotopes in precipitation in the Asian monsoon region. *J. Geophys. Res.* **110**, D23108 (2005).
- Breitenbach, S. *et al.* Strong influence of water vapor source dynamics on stable isotopes in precipitation observed in Southern Meghalaya, NE India. *Earth Planet. Sci. Lett.* **292**, 212–220 (2010).
- Araguas-Araguas, L., Froehlich, K. & Rozanski, K. Stable isotope composition of precipitation over southeast Asia. *J. Geophys. Res.* **742**, 721–728 (1998).
- Grossman, E. & Ku, T. Oxygen and carbon isotope fractionation in biogenic aragonite: temperature effects. *Chem. Geol.* **59**, 59–74 (1986).
- Gajurel, A., France-Lanord, C., Huyghe, P., Guilmette, C. & Gurung, D. C and O isotope compositions of modern fresh-water mollusc shells and river waters from the Himalaya and Ganga plain. *Chem. Geol.* **233**, 156–183 (2006).
- Kohn, M., Schoeninger, M. & Valley, J. Herbivore tooth oxygen isotope compositions: effects of diet and physiology. *Geochim. Cosmochim. Acta* **60**, 3889–3896 (1996).
- Licht, A. *et al.* A palaeo Tibet–Myanmar connection? Reconstructing the Late Eocene drainage system of central Myanmar using a multi-proxy approach. *J. Geol. Soc. Lond.* **170**, 929–939 (2013).
- Tindall, J. *et al.* Modelling the oxygen isotope distribution of ancient seawater using a coupled ocean–atmosphere GCM: implications for reconstructing early Eocene climate. *Earth Planet. Sci. Lett.* **292**, 265–273 (2010).
- Tafforeau, P., Bentalab, I., Jaeger, J. & Martin, C. Nature of laminations and mineralization in rhinoceros enamel using histology and X-ray synchrotron microtomography: potential implications for palaeoenvironmental isotopic studies. *Palaeogeogr. Palaeoclimatol. Palaeoecol.* **246**, 206–227 (2007).
- Jaeger, J. J. *et al.* Systematics and paleobiology of the anthropoid primate Pondaungia from the late Middle Eocene of Myanmar. *C. R. Palevol* **3**, 243–255 (2004).
- Licht, A. *et al.* Influence of permeability barriers in alluvial hydromorphic palaeosols: the Eocene Pondaung Formation, Myanmar. *Sedimentology* **61**, 362–382 (2014).
- Licht, A. *et al.* Fossil woods from the Late Middle Eocene Pondaung Formation, Myanmar. *Rev. Palaeobot. Palynol.* **202**, 29–46 (2014).
- Dupont-Nivet, G. *et al.* Tibetan plateau aridification linked to global cooling at the Eocene–Oligocene transition. *Nature* **445**, 635–638 (2007).
- Abels, H. A., Dupont-Nivet, G., Xiao, G., Bosboom, R. & Krijgsman, W. Step-wise change of Asian interior climate preceding the Eocene–Oligocene transition (EOT). *Palaeogeogr. Palaeoclimatol. Palaeoecol.* **299**, 399–412 (2011).
- Krinsley, D. & Doornkamp, J. *Atlas of Quartz Sand Surface Textures* (Cambridge Univ. Press, 1973).
- Vandenbergh, J. Grain size of fine-grained windblown sediment: a powerful proxy for process identification. *Earth Sci. Rev.* **121**, 18–30 (2013).
- Lu, H., Vandenbergh, J. & An, Z. Aeolian origin and palaeoclimatic implications of the ‘Red Clay’ (north China) as evidenced by grain-size distribution. *J. Quat. Sci.* **16**, 89–97 (2001).
- Sun, D., Su, R., Bloemendal, J. & Lu, H. Grain-size and accumulation rate records from Late Cenozoic aeolian sequences in northern China: implications for variations in the East Asian winter monsoon and westerly atmospheric circulation. *Palaeogeogr. Palaeoclimatol. Palaeoecol.* **264**, 39–53 (2008).
- Alonso-Zarza, A. *et al.* Mudflat/distal fan and shallow lake sedimentation (upper Vallesian–Turolian) in the Tianshui Basin, Central China: evidence against the late Miocene eolian loess. *Sedim. Geol.* **222**, 42–51 (2009).

44. Hourdin, F. *et al.* The LMDZ4 general circulation model: climate performance and sensitivity to parametrized physics with emphasis on tropical convection. *Clim. Dyn.* **27**, 787–813 (2006).
45. Seton, M. *et al.* Global continental and ocean basin reconstructions since 200 Ma. *Earth-Sci. Rev.* **113**, 212–270 (2012).
46. Hall, R. Late Jurassic–Cenozoic reconstructions of the Indonesian region and the Indian Ocean. *Tectonophysics* **570–571**, 1–41 (2012).
47. Wilson, D. *et al.* Antarctic topography at the Eocene–Oligocene boundary. *Palaeogeogr. Palaeoclimatol. Palaeoecol.* **335–336**, 24–34 (2012).
48. DeConto, R., Pollard, D. & Harwood, D. Sea ice feedback and Cenozoic evolution of Antarctic climate and ice sheets. *Paleoceanography* **22**, PA3214 (2007).
49. Lefebvre, V., Donnadieu, Y., Sepulchre, P., Swingedouw, D. & Zhang, Z. Deciphering the role of southern gateways and carbon dioxide on the onset of the Antarctic Circumpolar Current. *Paleoceanography* **27**, PA4201 (2012).

Supplementary Information is available in the online version of the paper.

Acknowledgements We thank the Commissariat à l’Énergie Atomique/Centre de Calcul Recherche et Technologie for access to computing facilities; V. Barbin for cathodoluminescence microscopy; C. Fontaine for X-ray diffraction; R. Amiot, T. Bouten, M. Konert, M. Lebbink and T. Zalm for laboratory assistance; the many

colleagues of the Franco-Burmese palaeontological team for field assistance; and D. Dettman and F. Fluteau for discussions. This work was supported by the ANR-09-BLAN-0238-02 Program, the University of Poitiers, the Netherlands Organisation for Scientific Research (NWO-ALW) with funding to H.A. and G.D.-N., the Marie Curie CIG 294282, the Ministry of Culture of the Republic of the Union of Myanmar, the French ministries of Foreign Affairs and of Higher Education and Research, the Alexander von Humboldt Foundation, the Chinese Ministry of Education and the National Natural Science Foundation of China (NSFC). A.L. was also funded by a Fyssen Foundation study grant.

Author Contributions A.L., J.-J.J., H.A. and G.D.-N. conceived the project. A.L., A.N.S. and J.-J.J. collected Burmese samples. A.L., T.R., C.F.-L. and C.L. performed isotopic analyses. H.A., G.D.-N., M.v.C., D.T. and Z.G. collected Chinese samples. M.v.C., H.A., J.T.A., D.T., J.V. and R.A. performed petrographic and grain-size analyses of the Xining sediment. J.-B.L. and Y.D. conducted numerical climate modelling. A.L., H.A., M.v.C. and G.D.-N. wrote the manuscript with contributions from all authors.

Author Information Reprints and permissions information is available at www.nature.com/reprints. The authors declare no competing financial interests. Readers are welcome to comment on the online version of the paper. Correspondence and requests for materials should be addressed to A.L. (alicht@email.arizona.edu).

Statin treatment rescues FGFR3 skeletal dysplasia phenotypes

Akihiro Yamashita¹, Miho Morioka¹, Hiromi Kishi¹, Takeshi Kimura^{1,2}, Yasuhito Yahara¹, Minoru Okada¹, Kaori Fujita¹, Hideaki Sawai³, Shiro Ikegawa⁴ & Noriyuki Tsumaki^{1,5}

Gain-of-function mutations in the fibroblast growth factor receptor 3 gene (*FGFR3*) result in skeletal dysplasias, such as thanatophoric dysplasia and achondroplasia (ACH). The lack of disease models using human cells has hampered the identification of a clinically effective treatment for these diseases. Here we show that statin treatment can rescue patient-specific induced pluripotent stem cell (iPSC) models and a mouse model of *FGFR3* skeletal dysplasia. We converted fibroblasts from thanatophoric dysplasia type I (TD1) and ACH patients into iPSCs. The chondrogenic differentiation of TD1 iPSCs and ACH iPSCs resulted in the formation of degraded cartilage. We found that statins could correct the degraded cartilage in both chondrogenically differentiated TD1 and ACH iPSCs. Treatment of ACH model mice with statin led to a significant recovery of bone growth. These results suggest that statins could represent a medical treatment for infants and children with TD1 and ACH.

Achondroplasia (ACH) is the most common skeletal dysplasia, and the condition leads to disproportionate short-limb dwarfism. Mutations in the gene encoding fibroblast growth factor receptor 3 (*FGFR3*) were identified in patients with ACH (refs 1, 2). *FGFR3* mutations were subsequently found in patients with thanatophoric dysplasia, of which there are two types that can be distinguished by the radiographic findings and the results of a molecular analysis: thanatophoric dysplasia type I (TD1) and II (TD2). The phenotype of thanatophoric dysplasia is more severe than that of ACH, and the condition is lethal due to respiratory insufficiency, which is secondary to an abnormal chest wall skeleton. Owing to recent progress in respiratory management, infants with thanatophoric dysplasia can survive for several months to years. *FGFR3* mutations have also been found in some other conditions, which are collectively called *FGFR3* chondrodysplasias³. Mice that are deficient for *FGFR3* show skeletal overgrowth⁴. This mouse phenotype suggests that *FGFR3* is a negative regulator of endochondral bone formation, confirming that the mutations causing *FGFR3* chondrodysplasias are gain-of-function mutations.

FGFR3 functions as a transmembrane receptor tyrosine kinase. Therapeutic strategies aimed at decreasing excessive *FGFR3* signals have been investigated⁵. The application of c-type natriuretic peptide (CNP)⁶, a CNP analogue⁷, parathyroid hormone⁸, a *FGFR3*-binding peptide⁹ and soluble *FGFR3* (ref. 10) led to a recovery of bone growth in a genetically manipulated mouse model of *FGFR3* chondrodysplasia. CNP attenuates the mitogen-activated protein kinase (MAPK) signals which are activated by *FGFR3*. The efficacy of all of these treatments remains to be tested in appropriate human cell models, which have not been available for *FGFR3* chondrodysplasia. In addition, the safety of these treatments needs to be confirmed through additional pre-clinical and clinical tests before wide clinical use can be advocated. The mechanism(s) by which *FGFR3* mutations cause cartilage abnormalities have been investigated by transducing cells with mutant *FGFR3* *in vitro*, and generating a genetically engineered mouse model *in vivo*⁵. The former approach provides information on the impact of *FGFR3* mutations on the receptors, such as receptor stabilization and turnover¹¹. The latter approach has revealed

the impact of *FGFR3* mutations on the growing skeleton and indicated that the endochondral bone formation process is disturbed¹². In addition to these two approaches, recent progress in cell reprogramming technologies is beginning to offer a new disease model: induced pluripotent stem cells (iPSCs). The iPSCs are generated from dermal fibroblasts or blood cells from patients, followed by differentiation into cell types of interest, such as chondrocytes in the case of *FGFR3* chondrodysplasias. This process may provide human cell types and tissues that can allow investigation of the mechanism(s) underlying the onset and progression of disease, and drug screening.

Generation of TD1-specific iPSCs

Human dermal fibroblasts (HDFs) were obtained from three TD1 patients (TD1-714, TD1-10749 and TD1-315H) (Extended Data Fig. 1a). A sequencing analysis of the genomic DNA extracted from the patients' HDFs revealed a heterozygous mutation (R248C) in the *FGFR3* gene in all three TD1 patients (Extended Data Fig. 1a). We established more than three iPSC lines for each TD1 patient and analysed one TD1 iPSC line (TD1-714-3, TD1-10749-1 and TD1-315H-2) derived from the HDFs of each patient. Wild-type iPSC lines (409B2 (ref. 13), KF4009-1 and HDF-11) derived from three control individuals were prepared. We confirmed that all iPSC lines expressed SSEA4 and TRA1-60, and formed teratomas containing all three germ layers (Extended Data Fig. 1a–c).

Abnormal cartilage formation from TD1 iPSCs

We differentiated TD1 and wild-type iPSCs towards chondrocytes. The iPSCs were differentiated into chondrogenic cells in the presence of chondrogenic supplementation on dishes for 14 days, and then were transferred into suspension culture to form cartilaginous particles following the previously described method¹⁴, with modifications. The wild-type iPSCs formed particles composed of cells scattered in a cartilaginous extracellular matrix, as indicated by positive Safranin O staining on day 42. TD1 iPSCs formed particles that did not appear to be stained with Safranin O, indicating that the extracellular matrix contained little glycosaminoglycan (Fig. 1a and Extended Data Fig. 2). The presence of glycosaminoglycan

¹Cell Induction and Regulation Field, Department of Cell Growth and Differentiation, Center for iPS Cell Research and Application, Kyoto University, Kyoto 606-8507, Japan. ²Department of Pediatrics, Osaka University Graduate School of Medicine, Osaka 565-0871, Japan. ³Department of Obstetrics and Gynecology, Hyogo College of Medicine, Hyogo 663-8501, Japan. ⁴Laboratory of Bone and Joint Diseases, Center for Integrated Medical Sciences, RIKEN, Tokyo 108-8639, Japan. ⁵Japan Science and Technology Agency, CREST, Tokyo 102-0075, Japan.

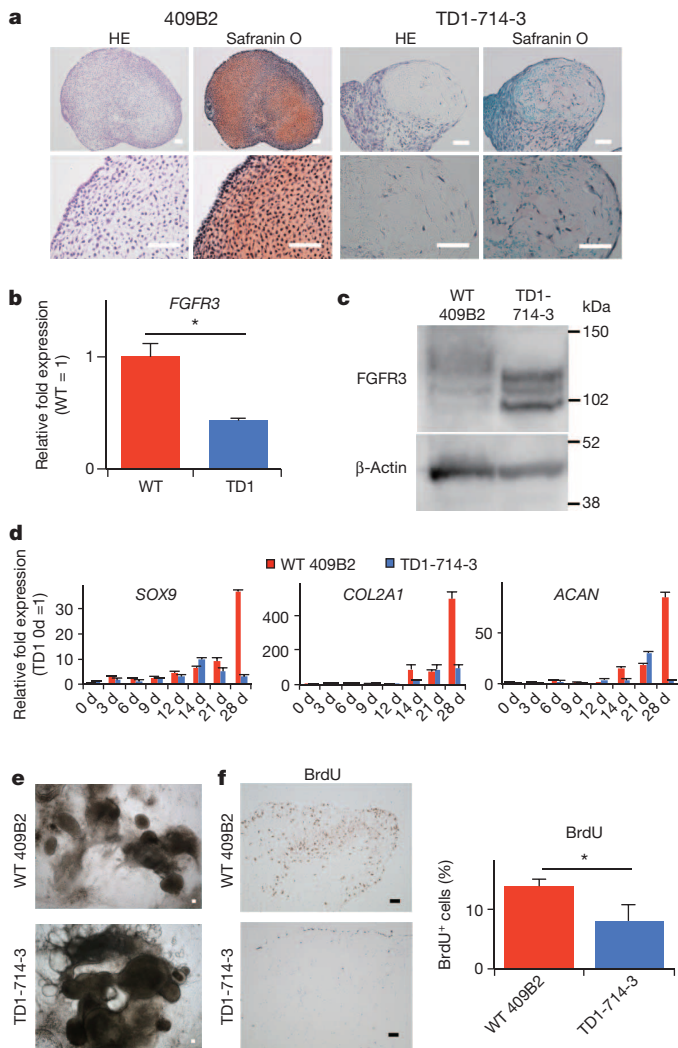


Figure 1 | Chondrogenic differentiation of wild-type iPSCs and TD1 iPSCs.

a, Histology of iPSC-derived cartilaginous particles on day 42. The images are representative of three independent experiments. HE, haematoxylin and eosin staining. **b**, Results of a real-time RT-PCR expression analysis of *FGFR3* mRNA in chondrogenically differentiated iPSC lines on day 28 ($n = 3$ independent iPSC lines). WT, wild type. **c**, Results of an immunoblot analysis of the *FGFR3* protein in chondrogenically differentiated iPSCs on day 28. The images are representative of three independent experiments. **d**, Time course of the changes in the expression of markers in iPSCs subjected to chondrogenic differentiation, as determined by real-time RT-PCR ($n = 3$ technical replicates). **e**, Phase microscopic images of chondrogenically differentiated iPSCs in adhesion culture on day 14. The images are representative of three independent experiments. **f**, iPSC-derived cartilaginous particles on day 28 were treated with BrdU. Left: histological sections were immunostained with anti-BrdU antibodies. Right: the number of BrdU-positive cells were divided by the total number of cells ($n = 3$ particles). The data are representative of two independent experiments. The error bars denote the means \pm s.d. * $P < 0.05$ by the t -test. Scale bars, 50 μ m.

is important for the mechanical properties of cartilage. Messenger RNA expression analysis showed that there were decreased expression levels of chondrocyte markers and increased expression levels of type I collagen genes in chondrogenically differentiated TD1 iPSCs on day 28 (Extended Data Fig. 3a). Immunohistochemical analysis showed that the TD1-iPSC-derived particles expressed more type I collagen and less type II collagen than the wild-type-iPSC-derived particles on day 42 (Extended Data Fig. 3b, c). Focal deposition of type II collagen in the TD1-iPSC-derived particles (Extended Data Fig. 3c, lower panels) suggests that there was limited cartilage formation or remnant cartilage which

was formed in earlier stages that was subsequently degraded. Markers of pluripotency (SSEA4 and TRA1-60) were not detected in either the chondrogenically differentiated wild-type or TD1 iPSCs on day 42 (Extended Data Fig. 3d). The expression level of *FGFR3* mRNA in chondrogenically differentiated TD1 iPSCs was significantly lower than in chondrogenically differentiated wild-type iPSCs (Fig. 1b), probably because of the negative feedback transcriptional regulation due to the gain-of-function mutation of *FGFR3* in the TD1 cells. Immunoblot analysis showed that the amount of *FGFR3* protein in the chondrogenically differentiated TD1 iPSCs was higher than in the chondrogenically differentiated wild-type iPSCs (Fig. 1c), supporting the notion that the mutant *FGFR3* receptor is resistant to degradation, leading to persistent activation of the receptor's signal transduction^{11,15–17}.

To examine how the chondrogenic differentiation of TD1 iPSCs resulted in the formation of abnormal particles, we analysed the time course of the changes in expression of markers in wild-type iPSCs and TD1 iPSCs subjected to chondrogenic differentiation (Fig. 1d and Extended Data Fig. 4a). Expression of *OCT4* (also called *POU5F1*), a marker of pluripotency, decreased rapidly on day 3, and expression of mesodermal/mesodermal markers *T* and *KDR* was transiently increased around days 3–9 in both chondrogenically differentiated wild-type and TD1 iPSCs. Expression of chondrogenic transcription factors *SOX9*, *SOX5* and *SOX6* was activated and increased gradually in both chondrogenically differentiated wild-type and TD1 iPSCs until day 14. Expression levels of *SOX9*, *SOX5* and *SOX6* continued to increase in the chondrogenically differentiated wild-type iPSCs, whereas they decreased gradually after day 14 in the chondrogenically differentiated TD1 iPSCs.

The expression of these chondrogenic transcription factors was followed by expression of their target genes encoding cartilage matrix proteins. Expression of type II collagen gene (*COL2A1*) and aggrecan gene (*ACAN*) was activated on day 14, and increased gradually in both chondrogenically differentiated wild-type and TD1 iPSCs until day 21. The expression levels of *COL2A1* and *ACAN* continued to increase until day 28 in chondrogenically differentiated wild-type iPSCs, whereas they were not changed or were decreased on day 28 in chondrogenically differentiated TD1 iPSCs. These findings suggest that both wild-type iPSCs and TD1 iPSCs were similarly differentiated into chondrocytes until days 14–21. This interpretation was supported by phase microscopic observation, which revealed that the wild-type iPSC and TD1 iPSC cultures similarly produced cell nodules by day 14 (Fig. 1e), because the formation of cell nodules is a typical characteristic of cultured chondrocytes.

Reduced expression of cartilage matrix genes (*COL2A1* and *ACAN*) on day 28, however, indicated that chondrocyte maturation was disturbed in the chondrogenically differentiated TD1 iPSCs after their differentiation into chondrocytes. Previous studies have revealed that chondrocyte proliferation is disturbed in ACH model mice¹² and in chondrocytic cells transduced with *FGFR3* carrying thanatophoric dysplasia and ACH mutations¹⁸, and that chondrocyte apoptosis is increased in thanatophoric dysplasia patients and in chondrogenic cells transduced with *FGFR3* carrying thanatophoric dysplasia and ACH mutations^{16,19,20}. Labelling cells with 5-bromodeoxyuridine (BrdU) revealed that the proliferation rate of the chondrogenically differentiated TD1 iPSCs was decreased compared with that of the chondrogenically differentiated wild-type iPSCs on day 28 (Fig. 1f). The chondrogenically differentiated TD1 iPSCs showed increased numbers of TUNEL-positive cells (Extended Data Figs 4b, c) and increased immunoreactivity for cleaved-caspase 3 (Extended Data Fig. 4d), suggesting that they had increased apoptosis compared with chondrogenically differentiated wild-type iPSCs. Chondrogenically differentiated TD1 iPSCs showed increased expression levels of p21 (Extended Data Fig. 4e). Together these results suggest that the chondrogenically differentiated TD1 iPSC model recapitulates the two primary abnormalities which are found in *FGFR3*-related disease patients and models: decreased proliferation and increased apoptosis of chondrocytes. These two abnormalities might be responsible for the degraded cartilage tissue found in TD1-iPSC-derived particles on day 42.

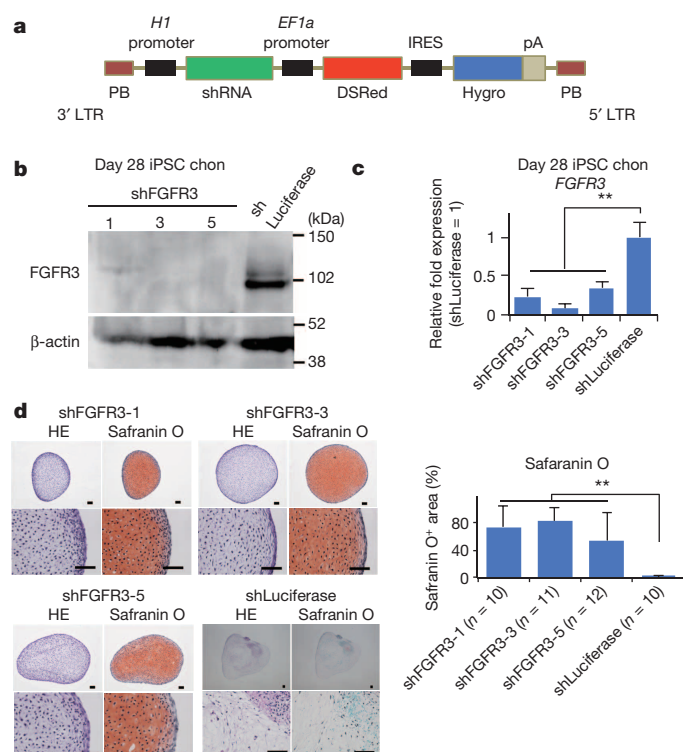


Figure 2 | Results of an analysis of *FGFR3* knockdown in TD1 iPSCs (TD1-714-3) subjected to chondrogenic differentiation. The data were collected from three independent clones respectively bearing three different *FGFR3* shRNAs. **a**, The *FGFR3* shRNA piggyBac (PB) vector. **b**, Results of an immunoblot analysis of *FGFR3* on day 28. iPSC chon, chondrogenically differentiated iPSCs. **c**, The results of a real-time RT-PCR expression analysis of *FGFR3* on day 28 ($n = 3$ technical replicates). **d**, Histological analysis on day 42. Scale bars, 50 μ m. The right panel shows the area of the Safranin-O-positive region in the particles. The number of particles examined is indicated at the bottom. Error bars denote the means \pm s.d. ** $P < 0.01$ by the Tukey-Kramer post-hoc test.

FGFR3 inactivation rescues TD1 iPSC cartilage

To confirm that TD1 iPSCs cannot produce cartilaginous particles due to the gain-of-function mutation of *FGFR3*, we knocked down *FGFR3* in TD1 iPSCs (TD1-714-3) using piggyBac short hairpin RNA (shRNA) vectors (Fig. 2a). Expression of *FGFR3* mRNA and protein was effectively knocked down in the chondrogenically differentiated TD1 iPSCs bearing each of three types of *FGFR3* shRNA (Fig. 2b, c). The TD1 iPSCs transfected with *FGFR3* shRNA formed cartilaginous particles that were positively stained by Safranin O (Fig. 2d). Expression analysis showed that chondrogenically differentiated TD1 iPSCs transduced with *FGFR3* shRNA had increased expression of chondrocyte marker genes and decreased expression of fibroblast marker genes compared with chondrogenically differentiated TD1 iPSCs bearing control shRNA targeting the luciferase gene sequence (Extended Data Fig. 5a).

Furthermore, treatment of chondrogenically differentiated TD1 iPSCs with *FGFR3* neutralizing antibody resulted in partial recovery of cartilage formation (Extended Data Fig. 5b). Expression analysis showed that addition of the *FGFR3* neutralizing antibody increased the expression of chondrocyte marker genes and decreased the expression of fibroblast marker genes in the chondrogenically differentiated TD1 iPSCs (Extended Data Fig. 5c).

These results suggest that the formation of degraded cartilage by TD1 iPSCs is caused by the gain-of-function mutation of *FGFR3*.

Statins rescue TD1-iPSC-derived cartilage

To find effective drugs to treat *FGFR3* chondrodysplasias, we screened molecules for their ability to rescue chondrogenically differentiated TD1 iPSCs from the degraded cartilage phenotype. We selected molecules that had previously been reported to affect *FGFR3* signalling and/or chondrocyte differentiation. Chondrogenically differentiated TD1 iPSCs were rescued by the addition of CNP but not by the addition of an *FGFR* inhibitor or the G-protein antagonist NF449 (Extended Data Fig. 6).

We included statins in the candidate molecules because they have been reported to have anabolic effects on chondrocytes^{21–23}. The statins compose a drug class broadly characterized as lipid-lowering agents. Statins inhibit mevalonic acid synthesis, and as a consequence lead to a decrease in the amount of total cholesterol and decreased levels of low-density lipoproteins. Statins have favourable effects on cardiovascular disease, the nervous system, the immune system, the skeletal system and tumour growth^{24–27}, and there is emerging interest in the pleiotropic

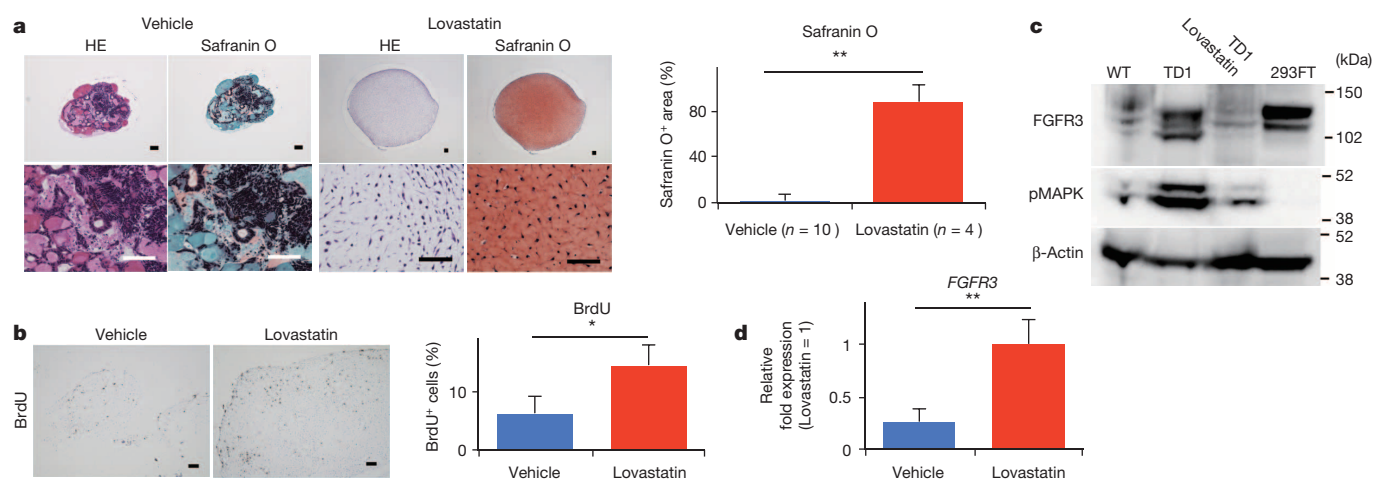


Figure 3 | TD1 (TD1-714-3) iPSCs were chondrogenically differentiated to produce particles in the presence or absence of lovastatin (1 μ M). **a**, Left: histology of the particles on day 42. Right: area of the Safranin-O-positive region in the particles. The number of particles examined is indicated at the bottom. The data are representative of three independent experiments. **b**, Particles on day 28 were treated with BrdU. Left: histological sections were immunostained with anti-BrdU antibodies. Right: number of BrdU-positive cells were divided by the total number of cells ($n = 3$ particles). The data are representative of three independent experiments. Error bars represent the means \pm s.d. * $P < 0.05$ by the t -test.

representative of two independent experiments. **c**, Results of an immunoblot analysis of *FGFR3* and phosphorylated MAPK on day 28. WT, wild-type (409B2)-iPSC-derived particles. 293FT, 293FT cells. The images are representative of three independent experiments. **d**, Results of a real-time RT-PCR expression analysis of *FGFR3* on day 28 ($n = 3$ technical replicates). The data are representative of two independent experiments. Error bars denote the means \pm s.d. * $P < 0.05$; ** $P < 0.01$ by the t -test. Scale bars, 50 μ m.

effects of statins. We found that the addition of lovastatin recovered the cartilage formation of chondrogenically differentiated TD1 iPSCs (Fig. 3a). An expression analysis showed that the addition of lovastatin increased the expression of a chondrogenic transcription factor (SOX9) and cartilage extracellular components (*COL2A1* and *ACAN*) in chondrogenically differentiated TD1 iPSCs (Extended Data Fig. 7a). Labelling TD1-iPSC-derived particles cultured in the presence or absence of lovastatin with BrdU revealed that the addition of lovastatin increased the proliferation rates of chondrogenically differentiated TD1 iPSCs in the particles (Fig. 3b). Furthermore, we confirmed that addition of mevastatin, atorvastatin, pravastatin, rosuvastatin and fluvastatin also recovered the cartilage formation of chondrogenically differentiated TD1 iPSCs (Extended Data Fig. 7b). These results suggest that various statins can rescue chondrogenically differentiated TD1 iPSCs.

To gain insight into the mechanism(s) by which statins rescue the FGFR3 chondrodysplasia models, we examined the expression levels of FGFR3 protein and mRNA. Immunoblot analysis revealed that application of lovastatin rescued chondrogenically differentiated TD1 iPSCs from the increased amount of FGFR3 protein (Fig. 3c). Accordingly, application of lovastatin rescued chondrogenically differentiated TD1 iPSCs from an increased amount of phosphorylated MAPK, a downstream target of FGFR3 signalling. The changes in the amount of FGFR3 protein were not regulated at the mRNA expression level, because the *FGFR3* mRNA expression levels were increased by lovastatin application in chondrogenically differentiated TD1 iPSCs (Fig. 3d), suggesting that statin treatment may accelerate the degradation of FGFR3 protein in chondrogenically differentiated TD1 iPSCs.

Statin exposure rescues ACH iPSC cartilage

We next investigated whether lovastatin could rescue another FGFR3 chondrodysplasia: ACH. We generated iPSCs from HDFs obtained from two individuals with ACH and one individual who was homozygous for an ACH mutation (ACHhomo). The chondrogenic differentiation of ACH iPSCs and ACHhomo iPSCs resulted in the formation of particles that lacked the cartilaginous element, as indicated by negative Safranin O staining. Addition of lovastatin to the culture media recovered the cartilage formation of chondrogenically differentiated ACH iPSCs and ACHhomo iPSCs (Extended Data Fig. 8).

Statins cause bone elongation in ACH mice

We examined whether statin treatment could rescue *Fgfr3^{Ach}* transgenic mice from the FGFR3 chondrodysplasia phenotype *in vivo*. The *Fgfr3^{Ach}* transgenic mice¹² express *Fgfr3* with an ACH mutation in chondrocytes under the control of the *Col2a1* promoter/enhancer sequences. *Fgfr3^{Ach}* transgenic mice show dwarfism, short limb bones and a short snout. Daily intraperitoneal injections of rosuvastatin significantly increased the anteroposterior lengths of the skulls and the lengths of the ulnas, femurs and tibiae in the *Fgfr3^{Ach}* mice when they were 15 days old (Fig. 4 and Extended Data Fig. 9). There were no significant differences in the lengths of the ulnas and tibiae between *Fgfr3^{Ach}* mice receiving rosuvastatin and wild-type mice receiving vehicle.

The lengths of primordial cartilage in *Fgfr3^{Ach}* mice increased more in organ culture in the presence of lovastatin than in the absence of lovastatin (Extended Data Fig. 10a), indicating that lovastatin acts on the cartilage directly to induce its elongation. Labelling the primordial cartilage with BrdU revealed that lovastatin increased the proliferation rate of chondrocytes in the *Fgfr3^{Ach}* primordial cartilage (Extended Data Fig. 10b).

The pellets of *Fgfr3^{Ach}* primary chondrocytes cultured in the presence of lovastatin showed more intense Safranin O staining than did the pellets of *Fgfr3^{Ach}* primary chondrocytes in the absence of lovastatin (Extended Data Fig. 10c). *Fgfr3^{Ach}* pellets cultured in the presence of lovastatin showed increased expression levels of *Sox9*, *Col2a1* and *Acan* at 2 weeks after the start of pellet culture, as well as increased expression levels of *Runx2* and *Col10a1* at 4 weeks after the start of pellet culture, compared with those cultured in the absence of lovastatin (Extended

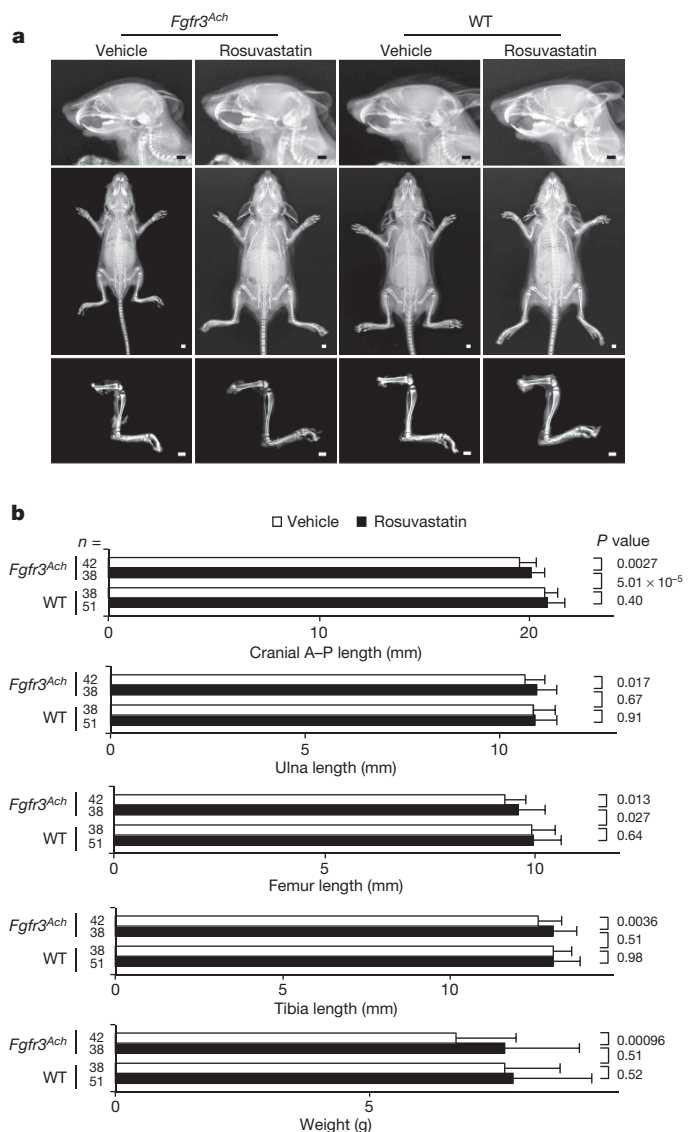


Figure 4 | Rescuing ACH model (*Fgfr3^{Ach}*) mice from reduced bone growth by intraperitoneal injection of rosuvastatin. **a**, Top: X-ray images of heads. Lateral views. Middle: X-ray images of bodies. Anterior-posterior view. Bottom: X-ray images of the hindlimb skeletons. Scale bars, 2 mm. **b**, Measurements of the anteroposterior (A-P) length of the heads and the length of the ulnas, femurs and tibiae in X-ray images and weights. The numbers of mice for each group were: *Fgfr3^{Ach}* mice treated with vehicle, *n* = 42; *Fgfr3^{Ach}* mice treated with statin, *n* = 38; wild-type mice treated with vehicle, *n* = 38; wild-type mice treated with statin, *n* = 51. The error bars denote the means ± s.d. *t*-test *P* values are indicated.

Data Fig. 10d). These results suggest that statin treatment stimulated both chondrocytic differentiation and maturation towards hypertrophy by increasing the expression of *Sox9* and *Runx2*, respectively.

Immunoblot analysis of primary chondrocytes showed that a larger amount of FGFR3 was detected in the *Fgfr3^{Ach}* chondrocytes than in the wild-type chondrocytes (Extended Data Fig. 10e), probably due to overexpression of the *Fgfr3^{Ach}* transgene and inhibited degradation of the mutant FGFR3. Addition of lovastatin to the culture decreased the amount of FGFR3 in the *Fgfr3^{Ach}* chondrocytes, and addition of MG132 increased the amount of FGFR3 in *Fgfr3^{Ach}* chondrocytes which were cultured in the presence of lovastatin. The expression of FGFR3 was slightly increased in *Fgfr3^{Ach}* chondrocytes by the addition of bafilomycin A1 in the presence of lovastatin in the cultures. These results suggest that statin treatment induced the degradation of mutant FGFR3, mainly through a proteasomal pathway.

Discussion

The degree of abnormality in the histology of the resultant TD1-iPSC- and ACH-iPSC-derived cartilaginous particles on day 42 appeared to be more severe than that observed in the cartilage of patients with TD1 and ACH, respectively. One of the reasons for this discrepancy may be that the *in vitro* culture environment lacks any compensatory machinery to adapt skeletal tissues to the malfunction of chondrocytes caused by FGFR3 mutations. The exaggeration of phenotypes has been recognized in iPSC models of other diseases, including Alzheimer's disease²⁸. This exaggeration of the phenotype exhibited by TD1-iPSC-derived chondrocytes may be advantageous for screening drugs, because it may decrease the occurrence of false-negative events.

We injected ACH model mice with 1.0 mg kg⁻¹ rosuvastatin, which is equivalent to 70 mg per day in a 70 kg human. A dose of 80 mg per day of rosuvastatin was studied in a clinical trial and found to be associated with an increased risk of muscle toxicity and renal toxicity compared with a dose of 40 mg per day²⁹. However, a dose of 1.0 mg per kg rosuvastatin is not always intolerable. It is important to note that when rosuvastatin was administered at this dose it was able to elongate the skeletal elements of the ACH model mice, because a considerable proportion of the statin administered was removed by the liver. It remains to be determined which statin is the most effective and what dose is needed. The precise mechanism(s) by which statin treatment can rescue the chondrocyte abnormalities associated with FGFR3 diseases remain to be elucidated, although we have obtained some insights into the statin-induced promotion of FGFR3 degradation, which is inhibited in cases with mutant FGFR3 (see Supplementary Discussion for further information).

Because statins have been administered to large numbers of human patients for many years, there is abundant information available on their safety, although their effects on infants and juvenile patients are still largely unknown. The fact that the treatment rescued both human iPSC disease models and mouse disease models suggests that statins might be effective and applicable for patients with TD1 and ACH.

Online Content Methods, along with any additional Extended Data display items and Source Data, are available in the online version of the paper; references unique to these sections appear only in the online paper.

Received 1 February; accepted 19 August 2014.

Published online 17 September 2014.

- Rousseau, F. *et al.* Mutations in the gene encoding fibroblast growth factor receptor-3 in achondroplasia. *Nature* **371**, 252–254 (1994).
- Shiang, R. *et al.* Mutations in the transmembrane domain of FGFR3 cause the most common genetic form of dwarfism, achondroplasia. *Cell* **78**, 335–342 (1994).
- Warman, M. L. *et al.* Nosology and classification of genetic skeletal disorders: 2010 revision. *Am. J. Med. Genet. A* **155**, 943–968 (2011).
- Deng, C., Wynshaw-Boris, A., Zhou, F., Kuo, A. & Leder, P. Fibroblast growth factor receptor 3 is a negative regulator of bone growth. *Cell* **84**, 911–921 (1996).
- Laederich, M. B. & Horton, W. A. Achondroplasia: pathogenesis and implications for future treatment. *Curr. Opin. Pediatr.* **22**, 516–523 (2010).
- Yasoda, A. *et al.* Systemic administration of C-type natriuretic peptide as a novel therapeutic strategy for skeletal dysplasias. *Endocrinology* **150**, 3138–3144 (2009).
- Lorget, F. *et al.* Evaluation of the therapeutic potential of a CNP analog in a Fgfr3 mouse model recapitulating achondroplasia. *Am. J. Hum. Genet.* **91**, 1108–1114 (2012).
- Xie, Y. *et al.* Intermittent PTH (1–34) injection rescues the retarded skeletal development and postnatal lethality of mice mimicking human achondroplasia and thanatophoric dysplasia. *Hum. Mol. Genet.* **21**, 3941–3955 (2012).
- Jin, M. *et al.* A novel FGFR3-binding peptide inhibits FGFR3 signaling and reverses the lethal phenotype of mice mimicking human thanatophoric dysplasia. *Hum. Mol. Genet.* **21**, 5443–5455 (2012).

- Garcia, S. *et al.* Postnatal soluble FGFR3 therapy rescues achondroplasia symptoms and restores bone growth in mice. *Sci. Transl. Med.* **5**, 203ra124 (2013).
- Monsonego-Ornan, E., Adar, R., Feferman, T., Segev, O. & Yayon, A. The transmembrane mutation G380R in fibroblast growth factor receptor 3 uncouples ligand-mediated receptor activation from down-regulation. *Mol. Cell. Biol.* **20**, 516–522 (2000).
- Naski, M. C., Colvin, J. S., Coffin, J. D. & Ornitz, D. M. Repression of hedgehog signaling and BMP4 expression in growth plate cartilage by fibroblast growth factor receptor 3. *Development* **125**, 4977–4988 (1998).
- Okita, K. *et al.* A more efficient method to generate integration-free human iPSCs. *Nature Methods* **8**, 409–412 (2011).
- Oldershaw, R. A. *et al.* Directed differentiation of human embryonic stem cells toward chondrocytes. *Nature Biotechnol.* **28**, 1187–1194 (2010).
- Cho, J. Y. *et al.* Defective lysosomal targeting of activated fibroblast growth factor receptor 3 in achondroplasia. *Proc. Natl Acad. Sci. USA* **101**, 609–614 (2004).
- Harada, D. *et al.* Sustained phosphorylation of mutated FGFR3 is a crucial feature of genetic dwarfism and induces apoptosis in the ATDC5 chondrogenic cell line via PLCγ-activated STAT1. *Bone* **41**, 273–281 (2007).
- Guo, C. *et al.* Sprouty 2 disturbs FGFR3 degradation in thanatophoric dysplasia type II: a severe form of human achondroplasia. *Cell. Signal.* **20**, 1471–1477 (2008).
- Krejci, P. *et al.* Analysis of STAT1 activation by six FGFR3 mutants associated with skeletal dysplasia undermines dominant role of STAT1 in FGFR3 signaling in cartilage. *PLoS ONE* **3**, e3961 (2008).
- Legeai-Mallet, L., Benoist-Lasselin, C., Delezoide, A. L., Munnich, A. & Bonaventure, J. Fibroblast growth factor receptor 3 mutations promote apoptosis but do not alter chondrocyte proliferation in thanatophoric dysplasia. *J. Biol. Chem.* **273**, 13007–13014 (1998).
- Yamanaka, Y., Tanaka, H., Koike, M., Nishimura, R. & Seino, Y. PTHrP rescues ATDC5 cells from apoptosis induced by FGF receptor 3 mutation. *J. Bone Miner. Res.* **18**, 1395–1403 (2003).
- Yudoh, K. & Karasawa, R. Statin prevents chondrocyte aging and degeneration of articular cartilage in osteoarthritis (OA). *Aging* **2**, 990–998 (2010).
- Simopoulou, T., Malizos, K. N., Poultsides, L. & Tsezou, A. Protective effect of atorvastatin in cultured osteoarthritic chondrocytes. *J. Orthop. Res.* **28**, 110–115 (2010).
- Baker, J. F., Walsh, P. M., Byrne, D. P. & Mulholland, K. J. Pravastatin suppresses matrix metalloproteinase expression and activity in human articular chondrocytes stimulated by interleukin-1β. *J. Orthopaed. Traumatol.* **13**, 119–123 (2012).
- Mundy, G. *et al.* Stimulation of bone formation *in vitro* and in rodents by statins. *Science* **286**, 1946–1949 (1999).
- Millar, P. J. & Floras, J. S. Statins and the autonomic nervous system. *Clinical Sci.* **126**, 401–415 (2014).
- Olivieri, F. *et al.* Telomere/telomerase system: a new target of statins pleiotropic effect? *Curr. Vasc. Pharmacol.* **10**, 216–224 (2012).
- Zhang, J. *et al.* Statins, autophagy and cancer metastasis. *Int. J. Biochem. Cell Biol.* **45**, 745–752 (2013).
- Israel, M. A. *et al.* Probing sporadic and familial Alzheimer's disease using induced pluripotent stem cells. *Nature* **482**, 216–220 (2012).
- Wolfe, S. M. Dangers of rosuvastatin identified before and after FDA approval. *Lancet* **363**, 2189–2190 (2004).

Supplementary Information is available in the online version of the paper.

Acknowledgements We thank H. Ohashi, J. Murotsuki, T. Yamada and K. Ozono for preparation of the dermal fibroblasts from a patient and discussion. We thank D. Ornitz and A. Yasoda for the *Fgfr3^{Ach}* mice. We thank K. Okita and S. Yamanaka for providing the hiPSC line 409B2, and A. Hotta for transducing the piggyBac vectors. We thank A. Motomura, X. Chen, Y. Minegishi, M. Nishino, T. Kobayashi, N. Oda, E. Ikeda and Y. Makita for their assistance. This study was supported in part by the Japan Science Technology Agency (JST), CREST (to N.T.) and Research Center Network for Realization of Regenerative Medicine (to N.T.), and Scientific Research Grant No. 24890101 (to A.Y.) and 26861716 (to A.Y.) and No. 24390354 (to N.T.) from MEXT.

Author Contributions A.Y. was involved in most of the experiments. M.M. performed the immunohistological and immunoblot analyses, as well as the DNA construction. H.K., T.K. and Y.Y. performed the mouse experiments. M.O. contributed to the generation of iPSCs. H.S. and S.I. were involved in the study design. K.F. performed the immunoblot analyses. N.T. designed the study. A.Y. and N.T. wrote the paper.

Author Information Reprints and permissions information is available at www.nature.com/reprints. The authors declare no competing financial interests. Readers are welcome to comment on the online version of the paper. Correspondence and requests for materials should be addressed to N.T. (ntsumaki@cira.kyoto-u.ac.jp).

Loss of oncogenic Notch1 with resistance to a PI3K inhibitor in T-cell leukaemia

Monique Dail¹, Jason Wong¹, Jessica Lawrence¹, Daniel O'Connor¹, Joy Nakitandwe², Shann-Ching Chen², Jin Xu¹, Leslie B. Lee³, Keiko Akagi⁴, Qing Li⁵, Jon C. Aster⁶, Warren S. Pear⁷, James R. Downing², Deepak Sampath³ & Kevin Shannon¹

Mutations that deregulate Notch1 and Ras/phosphoinositide 3 kinase (PI3K)/Akt signalling are prevalent in T-cell acute lymphoblastic leukaemia (T-ALL), and often coexist. Here we show that the PI3K inhibitor GDC-0941 is active against primary T-ALLs from wild-type and *Kras*^{G12D} mice, and addition of the MEK inhibitor PD0325901 increases its efficacy. Mice invariably relapsed after treatment with drug-resistant clones, most of which unexpectedly had reduced levels of activated Notch1 protein, downregulated many Notch1 target genes, and exhibited cross-resistance to γ -secretase inhibitors. Multiple resistant primary T-ALLs that emerged *in vivo* did not contain somatic *Notch1* mutations present in the parental leukaemia. Importantly, resistant clones upregulated PI3K signalling. Consistent with these data, inhibiting Notch1 activated the PI3K pathway, providing a likely mechanism for selection against oncogenic Notch1 signalling. These studies validate PI3K as a therapeutic target in T-ALL and raise the unexpected possibility that dual inhibition of PI3K and Notch1 signalling could promote drug resistance in T-ALL.

Targeted anticancer therapies exploit genetic and biochemical alterations unique to malignant cells, and administering combinations of targeted drugs based on the constellation of specific mutations present in an individual tumour is a rational strategy for treating advanced cancers. In T-ALL, mutations that deregulate Notch1 and Ras/PI3K signalling occur in 60% and 55% of patients, respectively^{1–3}. Recent data indicate that PI3K pathway activation is associated with aggressive biological features, drug resistance and poor prognosis in T-ALL^{4–9}. GDC-0941 is a potent PI3K inhibitor that is rapidly advancing in clinical development¹⁰. We observed downregulation of activated Notch1 signalling and reduced Myc expression in T-ALL cell lines and primary leukaemias that became resistant to GDC-0941 *in vitro* and *in vivo*. These data implicate PI3K as a dominant oncogenic driver pathway in T-ALL, and indicate that combining targeted anticancer drugs may have unanticipated effects on clonal dynamics and inadvertently promote the outgrowth of resistant cells.

Loss of Notch1 with PI3K inhibitor resistance

T-ALLs were generated by performing retroviral insertional mutagenesis (RIM) in wild-type (*Kras*^{WT}) and *Mx1-cre*, *Kras*^{LSL-G12D} (*Kras*^{G12D}) mice¹¹, and by expressing mutant *Kras* in a transduction/transplantation system¹². These primary T-ALLs are characterized by diverse retroviral integrations, heterogeneous biochemical activation of the Raf/MEK/ERK and PI3K/Akt effector pathways, and secondary acquisition of somatic *Notch1* mutations (Extended Data Fig. 1a). Cell lines generated from murine T-ALLs are uniformly sensitive to PI3K inhibition^{11,12}. To uncover potential mechanisms of acquired resistance, we exposed T-ALL cell line E2 (ref. 12) to increasing concentrations of GDC-0941 (ref. 10). In comparison to the parental E2 cell line, all three resistant lines (E2-R3, E2-R5 and E2-R6) proliferated in a tenfold higher concentration of GDC-0941 as assessed by cell numbers (Fig. 1a) and 5-bromodeoxyuridine (BrdU) labelling (Fig. 1b and Extended Data Fig. 2a). Resistant E2 cells also required higher drug concentrations to efficiently induce cleaved caspase 3 and inhibit higher levels of phosphorylated Akt (pAkt) (Fig. 1c, d).

Unexpectedly, resistant E2 clones downregulated the expression of activated Notch intracellular domain (NICD) proteins and were insensitive to compound E, a potent γ -secretase inhibitor (GSI) that blocks an essential enzymatic cleavage step for generating NICD³ (Fig. 1e, f).

Efficacy of PI3K and MEK inhibitors *in vivo*

Leukaemias generated by RIM recapitulate the genetic heterogeneity seen in advanced human cancers, and transplantation into recipient mice provides a flexible system for investigating therapeutic responses and elucidating mechanisms of drug resistance (Extended Data Fig. 1b). Advantages of this approach include: (1) primary cancers are treated in immunocompetent mice; (2) retroviral integration patterns can be used to track the emergence of drug-resistant clones; and (3) relapsed leukaemia cells can be re-transplanted to verify intrinsic resistance and test alternative therapies¹³. We transplanted 6 *Kras*^{WT} and 15 *Kras*^{G12D} T-ALLs (Extended Data Table 1) into 168 recipients (8 per leukaemia) and randomly assigned these mice to receive GDC-0941 or control vehicle ($n = 5$ and 3, respectively). Mice were treated for 8 weeks or until they required euthanasia due to progressive leukaemia. The maximally tolerated dose (MTD) of GDC-0941 is 125 mg kg⁻¹ day⁻¹ in sublethally irradiated mice and results in drug exposures sufficient to effectively inhibit PI3K for >8 h (Extended Data Fig. 3). Overall, treatment at this dose significantly extended the survival of recipients transplanted with *Kras*^{WT}, but not *Kras*^{G12D}, leukaemias (Fig. 2a, b). An analysis of individual primary leukaemias showed that 3 of 6 *Kras*^{WT} and 4 of 15 *Kras*^{G12D} T-ALLs responded to GDC-0941 (Extended Data Table 1). Importantly, these heterogeneous and transient *in vivo* responses contrast with the uniform *in vitro* sensitivity of T-ALL cell lines to PI3K inhibition^{11,12}.

The Raf/MEK/ERK pathway is a major effector of oncogenic Ras signalling, and combining MEK and PI3K inhibitors is efficacious in murine *Kras*-driven tumours¹⁴. We previously administered PD0325901 (PD901), a potent and selective MEK inhibitor¹⁵, to mice transplanted with *Kras*^{WT} or *Kras*^{G12D} T-ALLs¹¹. PD901 marginally increased the survival of recipients

¹Department of Pediatrics and Beniof Children's Hospital, University of California, San Francisco, California 94143, USA. ²Department of Pathology, St Jude Children's Research Hospital, Memphis, Tennessee 38105, USA. ³Department of Translational Oncology, Genentech Inc., South San Francisco, California 94080, USA. ⁴Department of Molecular Virology, Immunology and Medical Genetics, Ohio State University, Columbus, Ohio 43210, USA. ⁵Division of Haematology/Oncology, Department of Medicine, University of Michigan, Ann Arbor, Michigan 48109, USA. ⁶Department of Pathology, Brigham & Women's Hospital, Harvard Medical School, Boston, Massachusetts 02115, USA. ⁷Abramson Family Cancer Research Institute and the Department of Pathology and Laboratory Medicine, Perelman School of Medicine, University of Pennsylvania, Philadelphia, Pennsylvania 19104, USA.

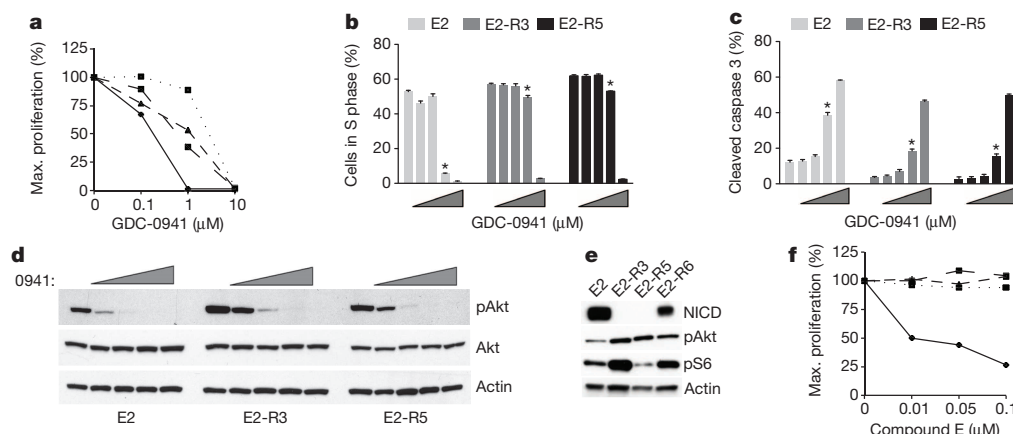


Figure 1 | GDC-0941-resistant T-ALL lines downregulate NICD and increase pAkt. **a**, GDC-0941 dose escalation yielded three resistant lines (dotted lines) from T-ALL cell line E2 (solid line). **b–d**, Resistant T-ALL cells were exposed to GDC-0941 (triangles, 0.01–1 μ M). **b**, **c**, Resistant cells require a tenfold higher dose of GDC-0941 to inhibit BrdU incorporation (**b**) and have impaired cleaved caspase 3 induction (**c**). Error bars show standard error of the mean (s.e.m.) of three technical replicates with differences between parental

and resistant cells at 1 μ M marked with an asterisk (two-sided *t*-test; **b**, R3, R5, $P < 0.0001$; **c**, R3, R5, $P = 0.0004$). **d**, Western blotting 20 min after GDC-0941 (0941) exposure shows that elevated pAkt S473 levels are suppressed in resistant lines by higher drug concentrations. **e**, **f**, Activated Notch1 (NICD) is reduced in resistant T-ALL cells (**e**), which are also resistant to compound E (**f**; dotted lines). The experiments in **a–e** were performed three times, and in **f** in duplicate.

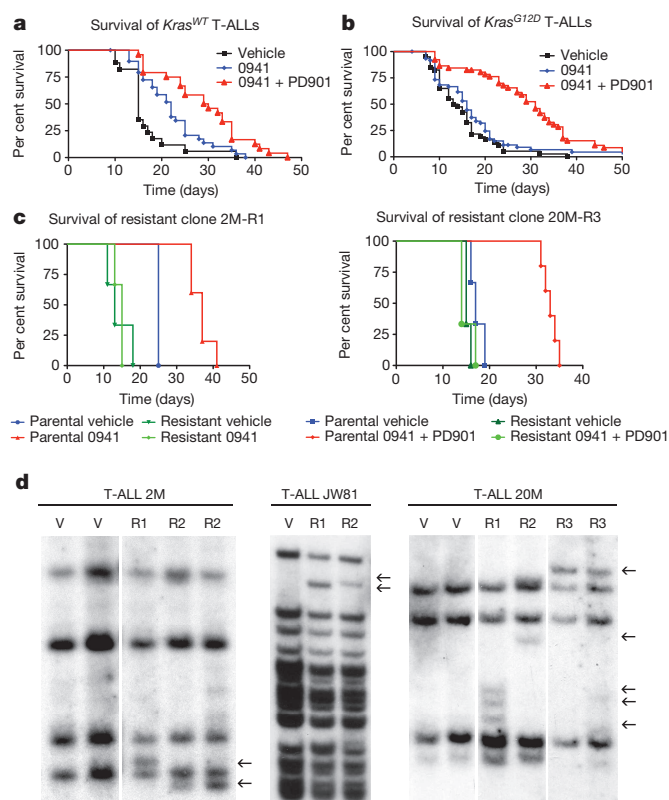


Figure 2 | Responses to targeted agents and clonal evolution. **a**, Kaplan-Meier analysis of *Kras*^{WT} T-ALLs treated with vehicle ($n = 17$), GDC-0941 (0941; $n = 29$) or GDC-0941 plus PD901 ($n = 24$). Treatment with GDC-0941 or the combination extended survival (log-rank, $P = 0.013$ and $P < 0.0001$). **b**, *Kras*^{G12D} T-ALLs treated with vehicle ($n = 39$), GDC-0941 ($n = 55$) or GDC-0941 plus PD901 ($n = 47$) only responded to the combination (log-rank, $P < 0.0001$). **c**, Refractory leukaemias have intrinsic drug resistance. Each relapsed T-ALL was transplanted into secondary recipients and retreated with GDC-0941 (2M R1) or GDC-0941 plus PD901 (20M-R3). Relapsed leukaemias (green lines) are unresponsive to treatment that was efficacious in parental T-ALLs (compare blue and red lines). **d**, Southern blot analysis detects novel retroviral integrations (arrows) in resistant leukaemias that are absent in vehicle-treated mice (V). Genetically distinct subclones are designated R1, R2, and so on.

of *Kras*^{G12D} leukaemias (median 3 days), but was not efficacious in *Kras*^{WT} T-ALLs¹¹. Treating mice with the same dose of PD901 (5 mg kg⁻¹ day⁻¹) and GDC-0941 at the MTD of 125 mg kg⁻¹ day⁻¹ caused weight loss and severe anaemia (data not shown). To reduce toxicity, we devised a protocol whereby mice received daily GDC-0941 (100 mg kg⁻¹ day⁻¹) as a 'backbone' in combination with intermittent PD901 (5 mg kg⁻¹ given 4 days per week; see Extended Data Fig. 1c). This new regimen was evaluated in a second randomized trial that included 136 recipients of 12 *Kras*^{G12D} and 5 *Kras*^{WT} T-ALLs investigated in the previous single agent trial of GDC-0941 (Extended Data Table 1). Treatment with the GDC-0941/PD901 combination dramatically extended the survival of mice transplanted with either *Kras*^{WT} or *Kras*^{G12D} T-ALLs compared to the control vehicle (Fig. 2a, b). Examining the individual *Kras*^{G12D} leukaemias showed that the GDC-0941/PD901 combination markedly extended the survival of recipients transplanted with T-ALLs that were initially sensitive to GDC-0941, and was also efficacious in seven leukaemias that were unresponsive to GDC-0941 alone (Extended Data Table 1).

Drug-resistant clones downregulate NICD

Despite continuous treatment, recipient mice invariably died of refractory T-ALL, which showed similar morphological and immunophenotypic features to the respective parental leukaemia (Extended Data Fig. 4). We transplanted leukaemia cells from mice that succumbed after initially responding to either GDC-0941 ($n = 5$) or to the GDC-0941/PD901 combination ($n = 5$) into secondary recipients, retreated them, and found that none responded to treatment *in vivo* (Fig. 2c). On the basis of these functional data, we hereafter refer to leukaemias that emerged after an initial response to targeted agents as 'resistant'. We analysed retroviral integrations to determine whether resistant T-ALLs exhibit clonal evolution. Southern blotting with a virus-specific probe revealed shared restriction fragments as well as one or more novel bands in many resistant leukaemias (Fig. 2d), and shotgun cloning of viral integration sites demonstrated insertions that were unique to or highly enriched in different resistant subclones (Extended Data Table 2). Clonal evolution was observed in 10 of 14 responsive T-ALLs, but not in the 7 primary T-ALLs that displayed *de novo* drug resistance (Extended Data Table 1).

Reduced NICD expression in GDC-0941-resistant cell lines (Fig. 1e) led us to examine Notch1 signalling in resistant T-ALLs that emerge *in vivo*. Indeed, western blot analysis revealed greatly reduced NICD expression in 19 of 31 (61%) independent resistant clones derived from 8 parental T-ALLs (Fig. 3a and Extended Data Fig. 5a). Resistant T-ALLs

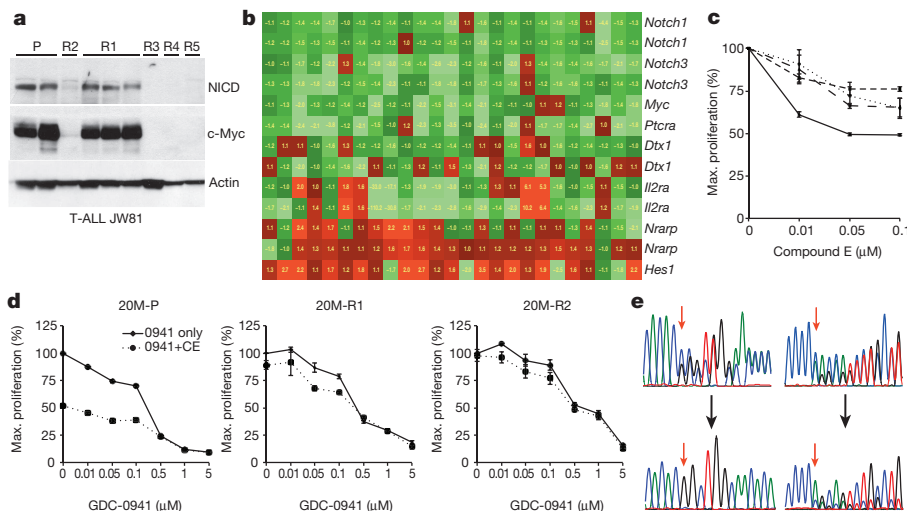


Figure 3 | Resistant T-ALLs have impaired Notch1 signalling and are resistant to compound E. **a**, Biochemical analysis of resistant clones (R1–R5) compared to parental JW81 (P). Each lane represents an independent sample ($n = 2$ for JW81, $n = 3$ for JW81 R1). **b**, Expression profiling of Notch1 target genes in 17 parental/resistant leukaemia pairs (8 in duplicate). **c**, **d**, T-ALL 20M parental (20M-P) and resistant clones were exposed to compound E (**c**) or to 0.1 μM compound E and different GDC-0941 concentrations (**d**) for 48 h. Error bars show s.e.m. of three technical replicates. **e**, *Notch1* mutations (red arrows) in parental leukaemias (top) are absent or dramatically reduced in resistant leukaemias (bottom).

also showed markedly reduced levels of Myc, a downstream effector of activated Notch signalling strongly implicated in leukaemogenesis (Fig. 3a and Extended Data Fig. 5a)¹. Expression profiling of 17 'NICD/Myc off' resistant T-ALLs demonstrated downregulation of multiple Notch1 transcriptional target genes including *Notch1*, *Notch3*, *Myc*, *Ptcr*, *Dtx1* and *Il2ra* compared with the corresponding parental leukaemia (Fig. 3b). Interestingly, *Nrarp* and *Hes1* transcript levels were stable or higher in resistant T-ALLs, a finding independently verified by quantitative real-time PCR (Fig. 3b and data not shown). This observation suggests that *Nrarp* and *Hes1* expression is uncoupled from Notch1 pathway activation in resistant T-ALLs.

To determine whether resistant leukaemias are less dependent on Notch1 signalling, we exposed primary T-ALL cells to compound E *ex vivo*. Multiple resistant clones isolated from two parental T-ALLs showed reduced sensitivity to GSI treatment than the corresponding parental leukaemia (Fig. 3c and Extended Data Fig. 5b). We also cultured parental and resistant leukaemia cells in a range of GDC-0941 concentrations with or without 0.1 μM of compound E. Whereas compound E cooperated with GDC-0941 to reduce the growth of parental T-ALLs, GSI treatment had no additive effects in the resistant clones (Fig. 3d and Extended Data Fig. 5c).

We sequenced *Notch1* and found that mutations identified in the parental T-ALLs were unexpectedly absent or detected at greatly reduced levels in six independent resistant leukaemias derived from four parental T-ALLs (Fig. 3e). In addition, retroviral integrations within the Notch pathway genes *Notch1*, *Aph1* (also known as *Alph1*) and *Dtx1* were highly enriched in three resistant leukaemias with reduced NICD/Myc expression, strongly implicating insertional mutagenesis as an alternative mechanism of reduced Notch1 signalling (Extended Data Fig. 5d and Extended Data Table 2). Importantly, resistant leukaemias with decreased or absent NICD and Myc expression were recovered from recipients treated with either GDC-0941 or with the GDC-0941/PD901 combination, suggesting that PI3K inhibition imposes selective pressure to downregulated oncogenic Notch1 signalling.

Activated Notch1 suppresses PI3K signalling

To address why *Notch1* mutations that confer a clonal growth advantage during leukaemogenesis might unexpectedly 'switch' to become deleterious when PI3K is inhibited therapeutically, we examined PI3K signalling in resistant T-ALLs with loss of NICD expression. Each parental and resistant T-ALL displayed a consistent pattern of protein phosphorylation in independent recipient mice (Fig. 4a). Resistant leukaemias generally had reduced PTEN expression and biochemical evidence of PI3K pathway activation—characterized by elevated pAkt and pS6 levels—relative to the respective parental T-ALL (Fig. 4a). Some resistant leukaemias also showed increased pERK (Fig. 4a). Whereas GDC-0941

treatment markedly reduced BrdU incorporation by parental T-ALLs *in vivo*, resistant leukaemias continued to proliferate (Fig. 4b and Extended Data Fig. 2b). Parental T-ALL cells isolated from recipient mice expressed high levels of cleaved caspase 3 after overnight culture, which were further induced by exposure to GDC-0941 (Fig. 4c). Basal cleaved caspase 3 levels were remarkably lower in resistant T-ALLs, but were induced by GDC-0941 exposure (Fig. 4c). Importantly, induction of cleaved caspase 3 in resistant T-ALLs correlated with the 5–50-fold higher concentrations of GDC-0941 required to suppress pAkt (Fig. 4d and Extended Data Fig. 6).

In T-ALL and during thymic development Notch1 upregulates *Hes1*, which enhances PI3K signalling by inhibiting *Pten* expression^{6,16}. These data support the existence of selective pressure for resistant T-ALLs to retain *Hes1* expression, even as they downregulated other Notch1 target genes (Fig. 3b). We reasoned that outgrowth of leukaemic clones lacking NICD might reflect additional inhibitory crosstalk between these two oncogenic pathways. To address this question, we first investigated whether reducing Notch1 activity modulates PI3K signalling in cell lines without PTEN expression. Indeed, exposing PTEN-deficient cell lines to compound E induced Akt phosphorylation (Fig. 4e). This response was not observed in BW, a T-ALL cell line lacking NICD expression (Fig. 4e), and was variable in T-ALL cell lines with intact PTEN expression (Extended Data Fig. 7a, b). The reciprocal experiment of pharmacologically inhibiting PI3K signalling did not alter NICD expression (Extended Data Fig. 7c).

We next modulated Notch pathway activation in Jurkat T-ALL cells to assess the effects on GDC-0941 responses. Enforced expression of NICD enhanced sensitivity to GDC-0941 (Fig. 4f), which was also true in several other T-ALL cell lines (Extended Data Fig. 7d). By contrast, expressing a dominant-negative Mastermind protein (dnMAML) that blocks Notch1 transcriptional activity conferred resistance to GDC-0941 and increased pAkt levels (Fig. 4f, g). Consistent with these data, exposing Jurkat cells to 0.1 μM of compound E, which inhibits NICD but does not alter proliferation, antagonized GDC-0941-mediated growth inhibition (Extended Data Fig. 7e, f). Importantly, exogenous NICD expression abrogated the ability of compound E to induce resistance to GDC-0941 (Extended Data Fig. 7g).

Discussion

To our knowledge, this is the first example in which *in vivo* treatment with a targeted anticancer agent selected for resistant clones lacking activation of a major oncogenic pathway involved in tumorigenesis (Fig. 4h). Parental leukaemias expressing NICD activate Myc and other Notch1 target genes (Fig. 4h, left). Many of these aggressive cancers respond to GDC-0941—either as a single agent or in combination with a MEK inhibitor. However, all ultimately develop drug resistance, which is frequently

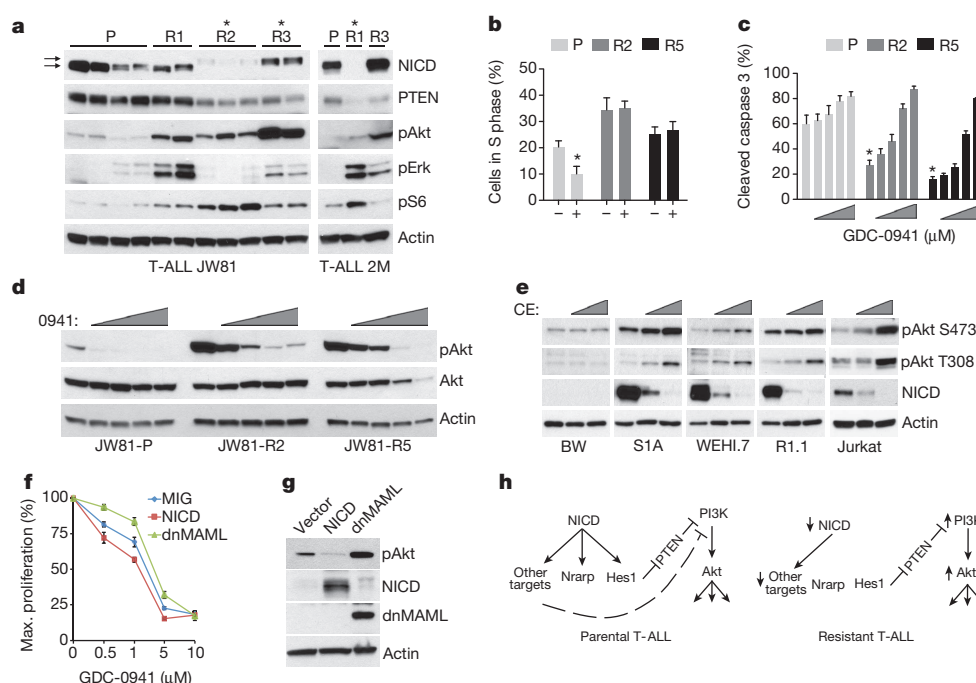


Figure 4 | Notch1 modulates PI3K signalling and GDC-0941 sensitivity. **a**, Western blot of JW81 and 2M and drug-resistant clones. Asterisks mark resistant T-ALLs with altered Notch1 signalling. Resistant T-ALLs JW81-R2 and -R3 lack the *Notch1* mutation in JW81 and thus express a larger Notch1 protein (top arrow) whereas mutant Notch1 is smaller (bottom arrow). Resistant T-ALLs have increased pAkt S473 levels and four of five show reduced PTEN expression. **b**, BrdU incorporation is reduced in parental T-ALL cells upon *in vivo* treatment ($*P = 0.004$, two-sided *t*-test). **c**, Basal apoptosis levels are higher in parental T-ALLs exposed to GDC-0941 *ex vivo* ($*P = 0.003$, two-sided *t*-test) and are induced after drug exposure in resistant leukaemias.

b, c, Error bars show s.e.m. of ≥ 3 mice. **d**, pAkt S473 levels in T-ALL cells 20 min after *ex vivo* GDC-0941 (0941) exposure. **e**, Dose-dependent decrease in NICD levels in T-ALL lines cultured with compound E (CE) for 72 h correlates with increased pAkt (three independent experiments). **f**, NICD expression enhances GDC-0941 sensitivity in Jurkat cells, while dnMAML reduces sensitivity compared to control vector (MIG). Error bars show s.e.m. of three experiments. **g**, Western blot showing NICD, dnMAML and pAkt S473 in Jurkat cells from **f**. **h**, Model of Notch1-PI3K crosstalk in sensitive and resistant T-ALLs.

characterized by loss of NICD expression and enhanced activation of the PI3K/Akt/S6 signalling pathway (Fig. 4h, right). Biochemical and transcriptional downregulation of Notch1 signalling occurred in over 60% of resistant T-ALLs. The late acquisition of *Notch1* mutations in murine T-ALLs^{11,12} is consistent with human studies showing that *NOTCH1* mutations are frequently cooperating events that may be absent at relapse¹⁷. Similarly, this RIM model accurately recapitulates the branched clonal architecture observed in relapsed human leukaemia¹⁸, as resistant T-ALLs isolated after *in vivo* drug treatment invariably shared multiple retroviral insertions with the corresponding parental T-ALL (Fig. 2d). In some instances, isolating the same resistant T-ALL from multiple independent recipient mice provided compelling evidence for treatment-induced selection of a pre-existing clone (Fig. 2d). However, MOL4070LTR is a replication competent retrovirus and new integrations might also contribute to resistance.

We show that resistant T-ALLs restore activated PI3K/Akt signalling, but remain sensitive to high concentrations of GDC-0941. This paradigm of 'on pathway' but 'off target' resistance has been observed in advanced human cancers that recurred after treatment with tyrosine kinase inhibitors. For example, melanomas treated with Braf kinase inhibitors deploy multiple genetic mechanisms to reactivate Raf/MEK/ERK signalling (reviewed in ref. 19). It is therefore theoretically possible that more potent or selective PI3K inhibitors could overcome acquired resistance in T-ALL. However, we administered GDC-0941 at the MTD, and deeper target inhibition might not be feasible owing to toxicity to normal tissues.

Resistant T-ALL cells downregulated Myc expression. As Myc directly binds and positively regulates the *PTEN* promoter in T-ALL⁶, loss of Myc expression might facilitate the outgrowth of GDC-0941-resistant cells through this mechanism. However, *PTEN*/*Pten*-negative T-ALL cell lines increased pAkt levels in response to compound E, which

infers the existence of PTEN-independent inhibitory crosstalk between the Notch1 and PI3K/Akt pathways. This idea is consistent with a recent report showing that Notch1 inhibits Akt activation by enhancing association with the PP2A phosphatase in Jurkat cells²⁰. Furthermore, enforced expression of Myc did not recapitulate the enhanced sensitivity to GDC-0941 induced by NICD (Fig. 4f and Extended Data Fig. 7d; data not shown). While it is unclear how resistant T-ALL cells compensate for loss of Myc expression, *Pten* loss or Akt activation overcomes the adverse effects of Myc withdrawal in a zebrafish model of T-ALL²¹. The unexpected observation that elevated NICD and Myc expression is dispensable for T-ALL growth *in vivo* might partially underlie the disappointing clinical efficacy of GSIs observed to date²².

GDC-0941 prolongs the survival of recipient mice transplanted with primary T-ALL cells and drives clonal evolution *in vivo*, thereby validating PI3K as a therapeutic target in this aggressive cancer. Together with a recent study implicating PI3K signalling in resistance to glucocorticoids⁵, our data strongly support evaluating PI3K inhibition in T-ALL in combination with other anti-leukaemia agents. *RAS* mutations are commonly detected in early T-cell precursor ALL, an aggressive paediatric leukaemia with a high rate of treatment failure²³, and a recent study implicated *NRAS* mutations in T-ALL relapse²⁴. We identified oncogenic *Kras* mutations as a biomarker of resistance to GDC-0941 mono-therapy, and provide evidence that combining PI3K and MEK inhibitors might be beneficial in these challenging patients. Simultaneously targeting the NOTCH1 and PI3K/AKT pathways is a rational therapeutic approach in T-ALL^{6,25}. Importantly, however, our data suggest that combination regimens might inadvertently undermine the efficacy of PI3K inhibitors by facilitating the survival and outgrowth of drug resistant clones. Given this, sequential treatment with a NOTCH1 pathway inhibitor to suppress *NOTCH1* mutant clones found at diagnosis followed by PI3K/AKT inhibition is an appealing approach. Finally,

whereas the *NOTCH1* mutations found in T-ALL constitutively increase NOTCH1 signalling, inactivating mutations are implicated as 'drivers' in other human cancers²⁶. Our studies therefore raise the provocative possibility that these loss-of-function *NOTCH1* mutations contribute to tumorigenesis by aberrantly activating PI3K signalling.

METHODS SUMMARY

GDC-0941 was provided by Genentech and synthesized as previously described¹⁴. Compound E was purchased from Calbiochem. The PD0325901 used in these studies was synthesized by Shanghai Chempartner. All drugs were diluted in dimethylsulphoxide (DMSO) for *in vitro* studies. To generate resistant cell lines, the E2 line was plated in 0.5 μ M GDC-0941 in six individual wells. As the cells became confluent, they were passaged and the GDC-0941 dose was increased to generate resistant clones E2-R3, E2-R5 and E2-R6, all of which grow in lymphocyte growth medium (LGM) containing 60 μ M GDC-0941. The *Notch1* gene was amplified using primers 5'-A TAGCATGATGGGGCCACTA-3' and 5'-CTCTGGAATGTGGGTGATCTGG-3' as previously described¹¹. Southern blotting and cloning of retroviral insertions were performed as described elsewhere¹¹. PCR products were sequenced by Quintara, and retroviral sequence tags were aligned against the University of California, Santa Cruz (UCSC) mm9 mouse reference genome assembly. All animal experiments conformed to national regulatory standards and were approved by the UCSF Committee on Animal Research. For T-ALL transplantation, 2×10^6 cells were injected retro-orbitally into male 8–12-week-old sublethally irradiated congenic recipient mice. For pharmacokinetic and pharmacodynamic studies, plasma was isolated from blood and the concentrations of GDC-0941 in each plasma sample were determined by a non-validated liquid chromatography/mass spectrometry/mass spectrometry (LC/MS/MS) assay as previously described¹⁴. Total Akt and pAkt S473 were measured by the Multi-Spot Detection System (Meso Scale Discovery). For preclinical testing, recipient mice were randomly assigned to receive control vehicle (0.5% hydroxypropyl methylcellulose and 0.2% Tween 80), GDC-0941 as a single agent, or GDC-0941 combined with PD0325901. We performed gene expression profiling on 28 independent parental and resistant mouse T-ALL tumours (Extended Data Table 3) using Affymetrix GeneChip HT MG-430 PM Affymetrix microarrays according to the manufacturer's instructions.

Online Content Methods, along with any additional Extended Data display items and Source Data, are available in the online version of the paper; references unique to these sections appear only in the online paper.

Received 26 July 2013; accepted 20 May 2014.

Published online 20 July 2014.

1. Aster, J. C., Blacklow, S. C. & Pear, W. S. Notch signalling in T-cell lymphoblastic leukaemia/lymphoma and other haematological malignancies. *J. Pathol.* **223**, 263–274 (2011).
2. Gutierrez, A. *et al.* High frequency of PTEN, PI3K, and AKT abnormalities in T-cell acute lymphoblastic leukemia. *Blood* **114**, 647–650 (2009).
3. Tosello, V. & Ferrando, A. A. The NOTCH signaling pathway: role in the pathogenesis of T-cell acute lymphoblastic leukemia and implication for therapy. *Ther. Adv. Hematol.* **4**, 199–210 (2013).
4. Blackburn, J. S. *et al.* Clonal evolution enhances leukemia-propagating cell frequency in T cell acute lymphoblastic leukemia through Akt/mTORC1 pathway activation. *Cancer Cell* **25**, 366–378 (2014).
5. Piovon, E. *et al.* Direct reversal of glucocorticoid resistance by AKT inhibition in acute lymphoblastic leukemia. *Cancer Cell* **24**, 766–776 (2013).
6. Palomero, T. *et al.* Mutational loss of PTEN induces resistance to NOTCH1 inhibition in T-cell leukemia. *Nature Med.* **13**, 1203–1210 (2007).
7. Trinquand, A. *et al.* Toward a NOTCH1/FBXW7/RAS/PTEN-based oncogenetic risk classification of adult T-cell acute lymphoblastic leukemia: a Group for Research in Adult Acute Lymphoblastic Leukemia study. *J. Clin. Oncol.* **31**, 4333–4342 (2013).
8. Jotta, P. Y. *et al.* Negative prognostic impact of PTEN mutation in pediatric T-cell acute lymphoblastic leukemia. *Leukemia* **24**, 239–242 (2010).
9. Clappier, E. *et al.* Clonal selection in xenografted human T cell acute lymphoblastic leukemia recapitulates gain of malignancy at relapse. *J. Exp. Med.* **208**, 653–661 (2011).

10. Folkes, A. J. *et al.* The identification of 2-(1H-indazol-4-yl)-6-(4-methanesulfonyl-piperazin-1-ylmethyl)-4-morpholin-4-yl-t hieno[3,2-d]pyrimidine (GDC-0941) as a potent, selective, orally bioavailable inhibitor of class I PI3 kinase for the treatment of cancer. *J. Med. Chem.* **51**, 5522–5532 (2008).
11. Dail, M. *et al.* Mutant *Ikzf1*, *Kras*^{G12D}, and *Notch1* cooperate in T lineage leukemogenesis and modulate responses to targeted agents. *Proc. Natl Acad. Sci. USA* **107**, 5106–5111 (2010).
12. Shieh, A. *et al.* Defective K-Ras oncoproteins overcome impaired effector activation to initiate leukemia *in vivo*. *Blood* (2013).
13. Lauchle, J. O. *et al.* Response and resistance to MEK inhibition in leukaemias initiated by hyperactive Ras. *Nature* **461**, 411–414 (2009).
14. Sos, M. L. *et al.* Identifying genotype-dependent efficacy of single and combined PI3K- and MAPK-pathway inhibition in cancer. *Proc. Natl Acad. Sci. USA* **106**, 18351–18356 (2009).
15. Brown, A. P., Carlson, T. C., Loi, C. M. & Graziano, M. J. Pharmacodynamic and toxicokinetic evaluation of the novel MEK inhibitor, PD0325901, in the rat following oral and intravenous administration. *Cancer Chemother. Pharmacol.* **59**, 671–679 (2007).
16. Wendorff, A. A. *et al.* Hes1 is a critical but context-dependent mediator of canonical Notch signaling in lymphocyte development and transformation. *Immunity* **33**, 671–684 (2010).
17. Mansour, M. R. *et al.* Notch-1 mutations are secondary events in some patients with T-cell acute lymphoblastic leukemia. *Clin. Cancer Res.* **13**, 6964–6969 (2007).
18. Mullighan, C. G. *et al.* Genomic analysis of the clonal origins of relapsed acute lymphoblastic leukemia. *Science* **322**, 1377–1380 (2008).
19. Corcoran, R. B., Settleman, J. & Engelman, J. A. Potential therapeutic strategies to overcome acquired resistance to BRAF or MEK inhibitors in BRAF mutant cancers. *Oncotarget* **2**, 336–346 (2011).
20. Hales, E. C., Orr, S. M., Larson Gedman, A., Taub, J. W. & Matherly, L. H. Notch1 regulates AKT activation loop (Thr³⁰⁸) dephosphorylation through modulation of the PP2A phosphatase in PTEN-null T-cell acute lymphoblastic leukemia cells. *J. Biol. Chem.* **288**, 22836–22848 (2013).
21. Gutierrez, A. *et al.* Pten mediates Myc oncogene dependence in a conditional zebrafish model of T cell acute lymphoblastic leukemia. *J. Exp. Med.* **208**, 1595–1603 (2011).
22. Aster, J. C. & Blacklow, S. C. Targeting the Notch pathway: twists and turns on the road to rational therapeutics. *J. Clin. Oncol.* **30**, 2418–2420 (2012).
23. Zhang, J. *et al.* The genetic basis of early T-cell precursor acute lymphoblastic leukaemia. *Nature* **481**, 157–163 (2012).
24. Tzoneva, G. *et al.* Activating mutations in the *NT5C2* nucleotidase gene drive chemotherapy resistance in relapsed ALL. *Nature Med.* **19**, 368–371 (2013).
25. Gutierrez, A. & Look, A. T. NOTCH and PI3K-AKT pathways intertwined. *Cancer Cell* **12**, 411–413 (2007).
26. Lobry, C., Oh, P. & Aifantis, I. Oncogenic and tumor suppressor functions of Notch in cancer: it's NOTCH what you think. *J. Exp. Med.* **208**, 1931–1935 (2011).

Acknowledgements This work was supported by grants from the William Lawrence and Blanche Hughes Foundation to J.C.A. and K.S.; by Specialized Center of Research (SCOR) awards 7019 and 7703 from the Leukaemia and Lymphoma Society of America; by National Institutes of Health grants R37 CA72614 and R01 CA180037 (to K.S.), K99 CA157950 (to M.D.), K08 CA134649 (to Q.L.) and P01 CA119070 (to J.C.A. and W.S.P.), and by the ALSAC of St. Jude Children's Research Hospital (J.R.D.). K.A. is supported by the Ohio Supercomputer Center (#PAS0425) and is an Ohio Cancer Research Associate (#GRT00024299); and J.X. received a Research Fellowship from the American Cancer Society (ACS). K.S. is an ACS Research Professor. We are grateful to T. Jacks and D. Tuveson for *Kras*^{G12D} mice; to L. Wolff for the MOL4070 virus; and to D. Largaespada and G. Narla for sharing their advice and expertise.

Author Contributions M.D., J.R.D., D.S. and K.S. designed experiments and analysed the data. M.D., J.W., J.L., D.O'C., J.N. and L.B.L. performed experiments. S.-C.C. and K.A. provided bioinformatics analysis. J.X., J.C.A., W.S.P., Q.L. and D.S. provided reagents. J.C.A., W.S.P., J.R.D. and D.S. provided conceptual advice. M.D. and K.S. wrote the manuscript.

Author Information Expression profiling data have been deposited in the Gene Expression Omnibus under accession number GSE48260. Reprints and permissions information is available at www.nature.com/reprints. The authors declare competing financial interests: details are available in the online version of the paper. Readers are welcome to comment on the online version of the paper. Correspondence and requests for materials should be addressed to K.S. (shannonk@peds.ucsf.edu).

Structural basis for the inhibition of the eukaryotic ribosome

Nicolas Garreau de Loubresse¹, Irina Prokhorova¹, Wolf Holtkamp², Marina V. Rodnina², Gulnara Yusupova¹ & Marat Yusupov¹

The ribosome is a molecular machine responsible for protein synthesis and a major target for small-molecule inhibitors. Compared to the wealth of structural information available on ribosome-targeting antibiotics in bacteria, our understanding of the binding mode of ribosome inhibitors in eukaryotes is currently limited. Here we used X-ray crystallography to determine 16 high-resolution structures of 80S ribosomes from *Saccharomyces cerevisiae* in complexes with 12 eukaryote-specific and 4 broad-spectrum inhibitors. All inhibitors were found associated with messenger RNA and transfer RNA binding sites. In combination with kinetic experiments, the structures suggest a model for the action of cycloheximide and lactimidomycin, which explains why lactimidomycin, the larger compound, specifically targets the first elongation cycle. The study defines common principles of targeting and resistance, provides insights into translation inhibitor mode of action and reveals the structural determinants responsible for species selectivity which could guide future drug development.

In all living cells, ribosomes are large ribonucleoprotein assemblies responsible for the accurate conversion of the genetic information encoded within mRNA into a corresponding protein. Although core functions of the ribosome are conserved in all kingdoms of life, eukaryotic ribosomes are at least 40% larger than their bacterial counterparts with a total mass ranging from ~3.3 MDa (yeasts and plants) up to ~4.5 MDa (mammals)^{1–3}. The additional complexity of the eukaryotic ribosome structure is reflected in differences in terms of functions and aspects of translation and its regulation⁴.

Given the central role of the ribosome in the cell, living organisms have elaborated defence strategies using small-molecule inhibitors to impair ribosomal functions. Decades of studies have revealed the great diversity of molecular mechanisms used by a multitude of antibacterial agents (antibiotics)^{5,6}. Atomic structures of prokaryotic ribosomes provided the basis for the development of novel antibiotics and in turn ribosome inhibitors served as tools to study protein synthesis in bacteria⁷. Similarly, the eukaryotic ribosome is a major target for broad-spectrum and eukaryote-specific small-molecule inhibitors isolated from natural sources. Despite limited understanding of their molecular mechanism, eukaryote-specific ribosomal inhibitors are increasingly used in research and hold potential for new therapeutics against a wide range of infectious diseases, cancers and genetic disorders^{8–12}.

To date, no structural data are available for small-molecule inhibitors in complexes with either the complete eukaryotic ribosome or its subunits. Some eukaryote-specific inhibitors were investigated using crystals of the 50S subunit of the archaea *Haloarcula marismortui* given its similarity with some parts of the eukaryotic ribosome^{13,14}. A previous X-ray study of the large subunit of *Tetrahymena thermophila* did not succeed to unambiguously place cycloheximide in its density due to limited resolution¹⁵. To gain insight into the mode of action of ribosome inhibitors in eukaryotes and to identify principles for drug development, we determined 16 crystal structures at high resolution, up to 2.9 Å, of the *S. cerevisiae* 80S ribosome in complexes with 12 eukaryote-specific and 4 broad-spectrum inhibitors (Fig. 1, Extended Data Figs 1–3 and Extended Data Table 1). The broad-spectrum inhibitors target the peptidyl transferase centre on the large subunit (blasticidin S), the

decoding centre (geneticin G418) and the mRNA–tRNA binding site on the small subunit (pactamycin, edeine). Eukaryotic-specific inhibitors were chosen on the basis of their capacity to alter cell proliferation and/or protein synthesis and their selectivity restricted to eukaryotes. The list comprises cycloheximide, lactimidomycin, phyllanthoside, T-2 toxin, deoxynivalenol, verrucaric acid, narciclasine, lycorine, nagilactone C, anisomycin, homoharringtonine and cryptopleurine.

The present study illustrates the chemical diversity of the small-molecule inhibitors targeting the eukaryotic ribosome. All of them were systematically found in a clash with or in a close proximity to mRNA or transfer RNA (tRNA) binding sites on both subunits (Fig. 2a, b). In contrast to bacterial antibiotics, none were located in the peptide exit tunnel, which correlates with the increased number of rRNA modifications in this region of the eukaryotic ribosomes¹⁶. Although the 80S ribosome contains 1.4 MDa of additional features absent in bacteria, it is noteworthy that all eukaryote-specific inhibitors target primary functional sites. This observation highlights the role of nucleotide substitutions in the formation of eukaryotic-specific pockets in the core of the machinery. Remarkably, the structures also explain the predominance of resistance mutations found in ribosomal proteins in or near the inhibitor binding sites (Extended Data Table 2). In contrast to bacteria, the high-copy number of rDNA in eukaryotic genomes limits the appearance of point mutations in rRNA. Instead, resistance mutations emerge exclusively within ribosomal proteins, encoded by one or two genes, sometimes located further away and separated by a layer of rRNA nucleotides like in the case of protein uL3. Consequently, development of drugs targeting the eukaryotic ribosome can be facilitated to prevent drug resistance by focusing on regions with the smallest number of proteins.

The 60S tRNA E-site

Among all three tRNA binding sites on the large subunit, the E-site is the most diverse across species, showing different nucleotide and protein content in bacteria, archaea and eukaryotes. Following peptide bond formation, this site accommodates deacylated tRNAs before their release in the cytoplasm.

¹Institut de Génétique et de Biologie Moléculaire et Cellulaire (IGBMC), INSERM U964, CNRS UMR7104, Université de Strasbourg, 67404, Illkirch, France. ²Department of Physical Biochemistry, Max Planck Institute for Biophysical Chemistry, Am Fassberg 11, 37077 Göttingen, Germany.

Eukaryote-specific

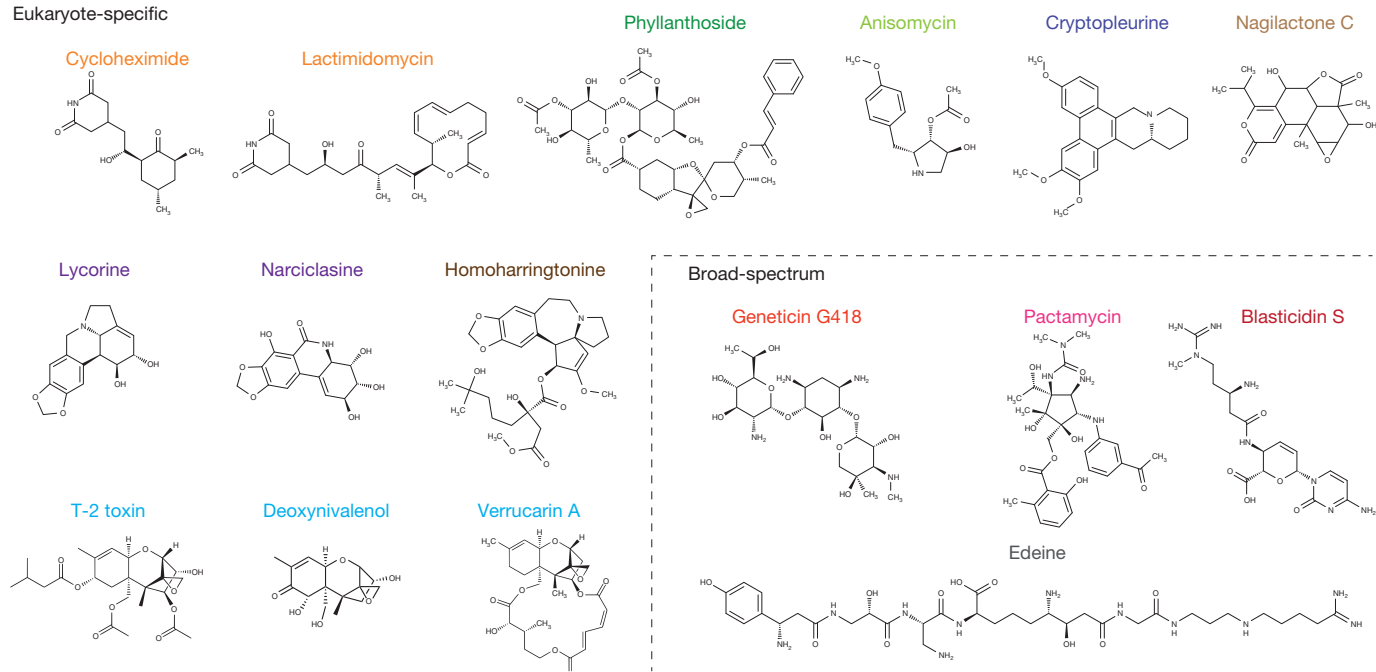


Figure 1 | Chemical structures of the 16 small-molecule inhibitors.

a, Chemical structures of small-molecule inhibitors analysed in the study. Cycloheximide and lactimidomycin have an instrumental role in ribosome profiling experiments^{18,20}. Homoharringtonine is a marketed drug for the treatment of chronic myeloid leukaemia³⁷. Lycorine and narciclasine are

The glutarimide inhibitors, cycloheximide and lactimidomycin, were located in the E-site on the large subunit in a pocket formed by universally conserved nucleotides of the 25S rRNA and a stretch of the eukaryote-specific protein eL42 (Fig. 3a). Lactimidomycin

alkaloids known for their medicinal and toxic properties³⁸. T-2 toxin, deoxynivalenol and verrucaric A are widespread mycotoxins representatives of the three major trichothecenes subclasses³⁹. The aminoglycoside geneticin (G418) promotes the read-through of premature termination codons¹¹.

bears an additional lactone ring that is positioned on top of eL42 and directed towards the subunit interface. Although chemically unrelated to glutarimides, phyllanthoside makes contact with the same rRNA nucleotides and interacts with eL42 in a manner resembling the tRNA

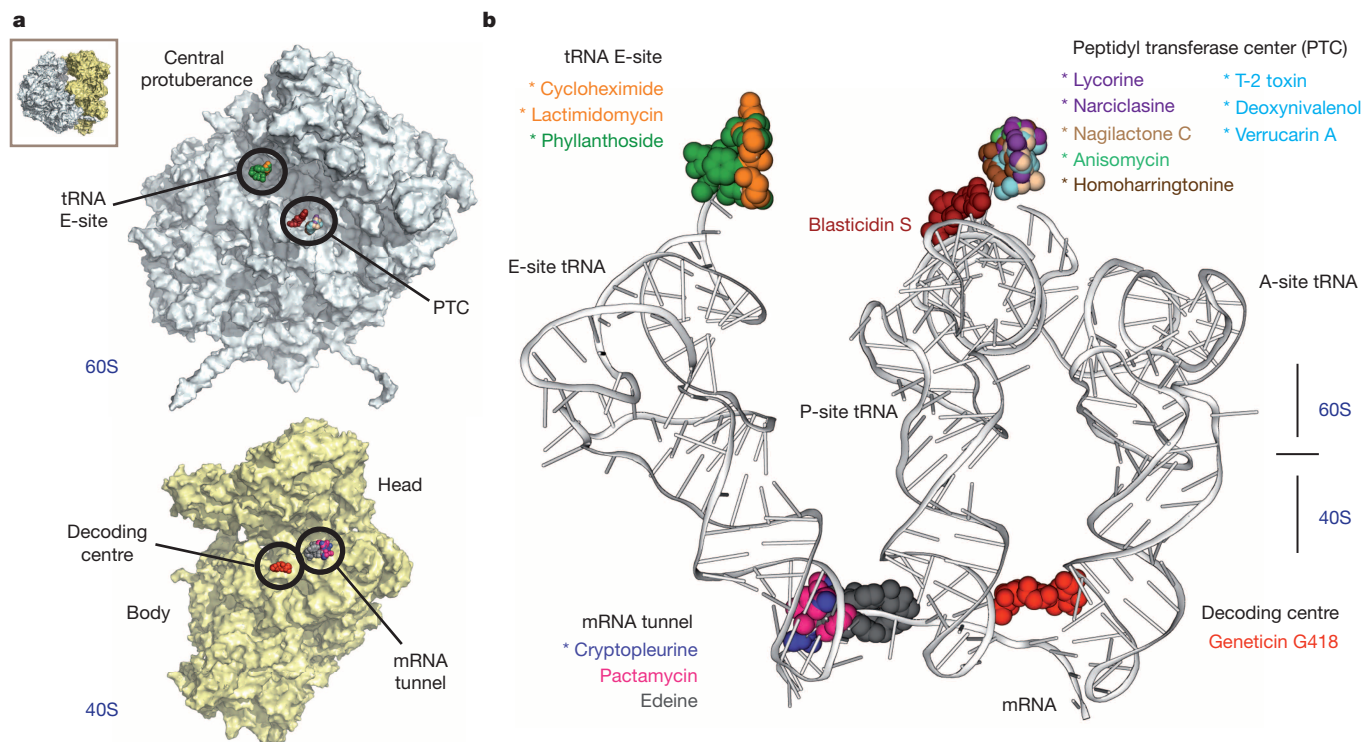


Figure 2 | Binding sites of inhibitors on the yeast ribosome. **a**, The binding sites can be grouped in four functional regions: the tRNA E-site and the peptidyl transferase centre (PTC) on the large subunit (60S) and the decoding centre (DC) and the mRNA channel on the small subunit (40S). View from

the subunit interface. **b**, All inhibitors target mRNA and tRNA binding sites. The tRNAs and mRNA (white) structures were taken from the PDB (Protein Data Bank) entries 3I8I and 3I8H. Eukaryotic-specific inhibitors are marked with an asterisk.

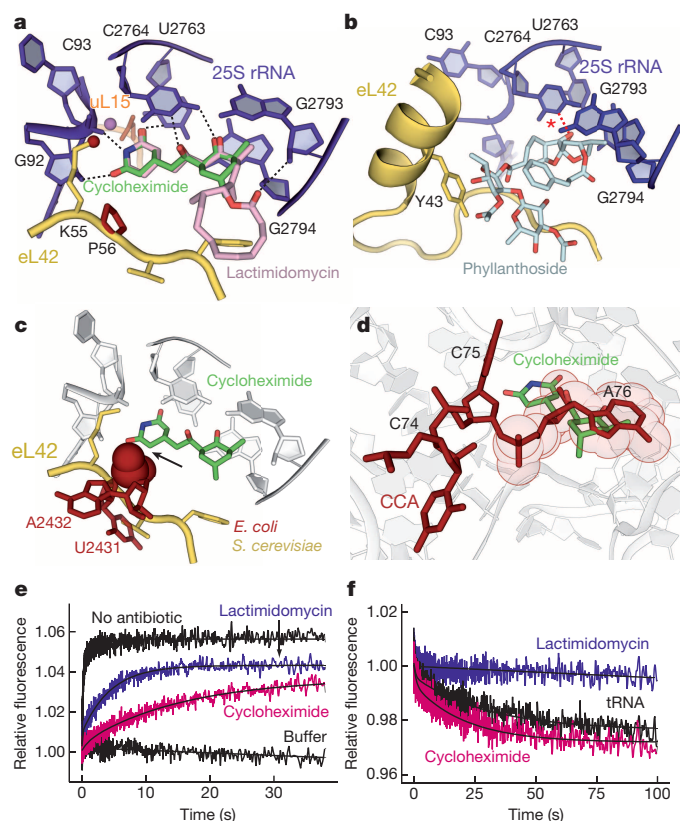


Figure 3 | Structure and function of 60S tRNA E-site inhibitors.

a, Cycloheximide (green) and lactimidomycin (pink) share the same binding site. Both structures are in agreement with resistance mutations in proteins eL42 (Pro 56) and uL15 (Gln 38) (red) and with the role of eL42 Lys 55 monomethylation (red sphere)^{40–42}. **b**, Binding site of phyllanthoside (light blue). The asterisk indicates a putative covalent bond. **c**, Two bacterial-specific nucleotides, U2431 and A2432, prevent the binding of E-site inhibitors to the bacterial ribosome (PDB accession codes: 2AVY, 2AW7). **d**, E-site inhibitors prevent the binding of deacylated tRNA. The CCA tri-nucleotide (red) mimics the acceptor end of the deacylated tRNA. **e**, Inhibition of tRNA binding to the 80S E-site by lactimidomycin (blue) and cycloheximide (magenta). Controls without inhibitors (upper trace) and in the absence of 80S ribosomes (lower trace) are also shown. **f**, Dissociation of tRNA^{Phe}(Prf) from 80S E-site as induced by addition of excess of non-labelled tRNA^{Phe} (black), cycloheximide (magenta) or lactimidomycin (blue).

CCA-end (Fig. 3b). The electron density suggests the presence of a covalent bond between C2764 (C2394, *Escherichia coli* numbering) and phyllanthoside epoxide group. This observation is consistent with the described irreversible effect of the inhibitor on protein synthesis¹⁷.

The strict selectivity of E-site inhibitors towards eukaryotes is explained by the presence of two bacterial-specific rRNA residues that occlude the binding pocket (Fig. 3c). In archaea, the orientation of the protein eL42 on the large subunit of *H. marismotui* would most probably preclude the binding of lactimidomycin and phyllanthoside (Extended Data Fig. 4). To localize the position of the E-site tRNA on the large subunit, we solved the structure of the yeast ribosome in complex with the tri-nucleotide CCA that mimics the acceptor end of the deacylated tRNA (Extended Data Fig. 5). The structures explain previous biochemical data showing that cycloheximide and lactimidomycin compete with the binding of the tRNA CCA-end in the E-site of the large subunit¹⁸ (Fig. 3d). Phyllanthoside probably has a similar mode of inhibition¹⁷.

60S E-site accessibility for inhibitors

Although cycloheximide and lactimidomycin bind to the same site and probably compete with the E-site tRNA, they affect translation in a different way. Lactimidomycin preferentially arrests ribosomes at

the first peptide bond, whereas cycloheximide stalls ribosomes during ongoing translation^{18–20}.

To better understand this difference, we used a rapid kinetic approach to study the effects of both inhibitors on tRNA binding to the E-site with a fluorescently labelled tRNA (proflavin (Prf) tRNA^{Phe})²¹. Binding of tRNA^{Phe}(Prf) to the 80S or 70S ribosomes resulted in an almost identical rapid fluorescence change, reflecting the recruitment of the tRNA to the E-site, whereas transition from the E-site to the P-site was slow and not monitored (Extended Data Fig. 6a)²². When the ribosomes were pre-treated with lactimidomycin or cycloheximide, the rate of tRNA binding decreased, as expected for competitive inhibition (Fig. 3e). The apparent rates of tRNA binding decreased with the inhibitor concentration with a dose response curves, yielding $K_i = 2.7 \pm 0.7 \mu\text{M}$ for lactimidomycin and $K_i = 0.1 \pm 0.05 \mu\text{M}$ for cycloheximide (Extended Data Fig. 6b). Although the value for lactimidomycin was in agreement with the published data, cycloheximide appeared to have a much higher efficacy than reported for mammalian ribosomes using a footprinting technique¹⁸. Direct measurements of the binding affinity of cycloheximide to yeast ribosomes using isothermal titration calorimetry yielded a $K_d = 0.14 \pm 0.05 \mu\text{M}$, in agreement with the result of our competition studies (Extended Data Fig. 6c).

Next, we tested whether the accessibility of the E-site plays a role. We followed the dissociation of tRNA^{Phe}(Prf) from 80S ribosomes upon addition of cycloheximide or lactimidomycin (Fig. 3f). Upon addition of cycloheximide, tRNA^{Phe}(Prf) was rapidly removed from the E-site, indicating that the inhibitor can rapidly exchange with tRNA. In contrast, lactimidomycin did not induce tRNA dissociation, suggesting that its binding to 80S ribosomes is inhibited when the E-site is occupied by deacylated tRNA. Clearly, tRNA^{Phe}(Prf) can un-bind from the E-site within the observation time; however, its re-binding appears to be faster than the accommodation of lactimidomycin in the E-site. The structure of lactimidomycin with its additional lactone ring may obstruct the binding of the inhibitor to the E-site, making lactimidomycin a 'slow' inhibitor that can efficiently bind only in the absence of the physiological competitor, that is, during the first elongation cycle. Our data demonstrate that the size of the glutarimide compounds dictates their accessibility to the ribosome and consequently their mode of action.

The peptidyl transferase centre

Targeted by the majority of antibiotics, the catalytic centre of the ribosome located on the large subunit is exclusively composed of highly conserved rRNA nucleotides. The reaction of peptide bond formation requires the two substrates, that is, aminoacyl-tRNA and peptidyl-tRNA, to be properly aligned in the A-site and P-site of the peptidyl transferase centre, respectively.

In contrast to blasticidin S which binds in the P-site of the large subunit in the same way in bacteria and archaea, numerous eukaryote-specific inhibitors were found associated with the A-site of the peptidyl transferase centre (Fig. 4a and Extended Data Fig. 7)²³. Remarkably, chemically diverse inhibitors share a similar mode of binding within the pocket. Upon binding, all A-site inhibitors induce a similar pattern of structural rearrangements in their direct vicinity that propagate up to 15 Å away from the peptidyl transferase centre (Extended Data Fig. 8a). The common structural scaffold of trichothecenes inhibitors, represented by T-2 toxin, deoxynivalenol and verrucaric acid, mediates all major contacts with rRNA residues in the binding pocket (Fig. 4b). The acetate-based substituents of T-2 toxin are pointing towards the peptide tunnel entrance, whereas the verrucaric acid large macrocycle extends further towards the macrolide binding site in bacteria. Lycorine, narcilasin and homoharringtonine are plant alkaloids sharing similarities, including a dioxol-pyrroline group (Fig. 4c). In contrast to trichothecenes, the three alkaloids adopt a distinct conformation in the pocket where the dioxol-pyrroline group is positioned differently. These findings suggest that the dioxol-pyrroline group might play a specific role such as being a recognition motif for enzymes in the alkaloid

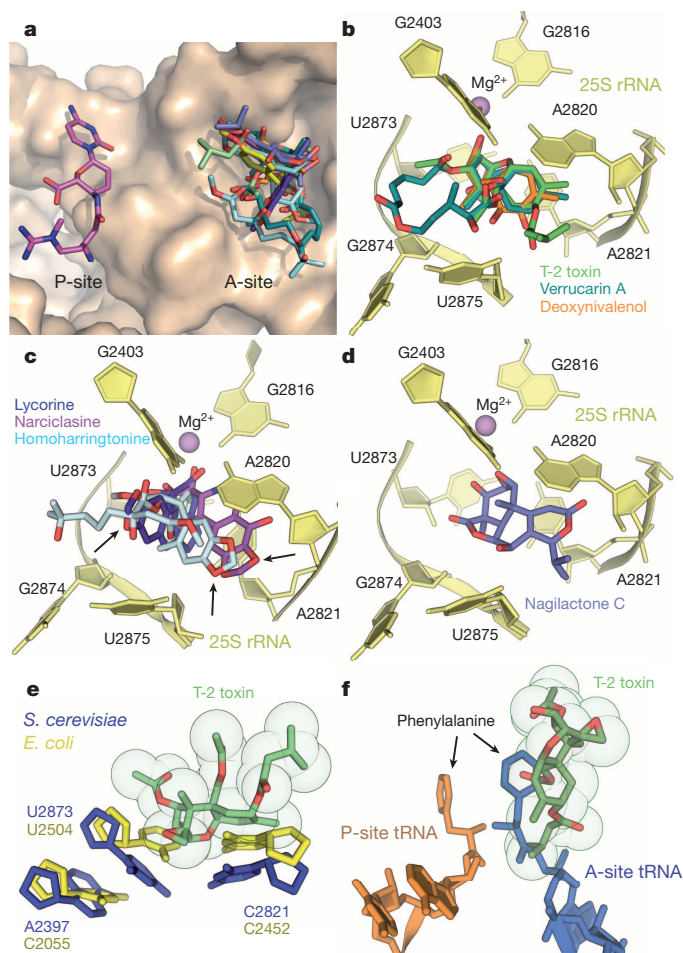


Figure 4 | Structures of 60S peptidyl transferase centre inhibitors.

a, Blasticidin S binds to the 60S tRNA P-site, whereas T-2 toxin, deoxynivalenol, verrucarins A, lycorine, narciclasine, homoharringtonine, nagilactone C and anisomycin are clustered in the 60S tRNA A-site. **b**, Binding site of T-2 toxin (green), deoxynivalenol (orange) and verrucarins A (cyan). **c**, Binding site of narciclasine (purple), lycorine (blue), homoharringtonine (pale cyan). The arrows highlight the location of the dioxol-pyrroline group. **d**, Binding site of nagilactone C (blue). **e**, The conformation of U2504 in bacteria (PDB accession codes: 2AVY, 2AW7) closes the binding site to the eukaryotic-specific A-site inhibitors. **f**, A-site inhibitors hinder aminoacyl-tRNA positioning in the peptidyl transferase centre. The Phe-tRNA structures were taken from PDB accession codes 2WDG, 2WDL.

biosynthetic pathway. Nagilactone C shares all the features of A-site inhibitors (Fig. 4d). Finally, homoharringtonine and anisomycin binding is conserved between archaea and eukaryotes; however, some variations were found in the anisomycin vicinity (Extended Data Fig. 8b).

Consistent with structural data obtained from the archaeal 50S subunit, the identity of 25S rRNA residue 2397 (2055) is suggested to influence the conformation of U2873 (U2504) that dictates the binding of either bacterial-specific or eukaryotic-specific inhibitors (Fig. 4e)¹⁴. In bacteria, the residue 2397 (2055) is a cytosine, whereas an adenine is found in 96% of eukaryotes. Of therapeutic interest, the remaining 4% of eukaryotes might be sensitive to antibacterial drugs instead of eukaryotic inhibitors, such as *Giardia* species²⁴. Most A-site inhibitors were found to impair peptide bond formation during translation elongation (Extended Data Table 1). Superimposition of aminoacyl-tRNA structures shows that the entrance of the amino acid moiety in the peptidyl transferase centre is hindered by the presence of A-site inhibitors (Fig. 4f).

The decoding centre

The decoding centre of the ribosome forms a geometrically restricted pocket that accurately selects aminoacyl-tRNA in accordance with

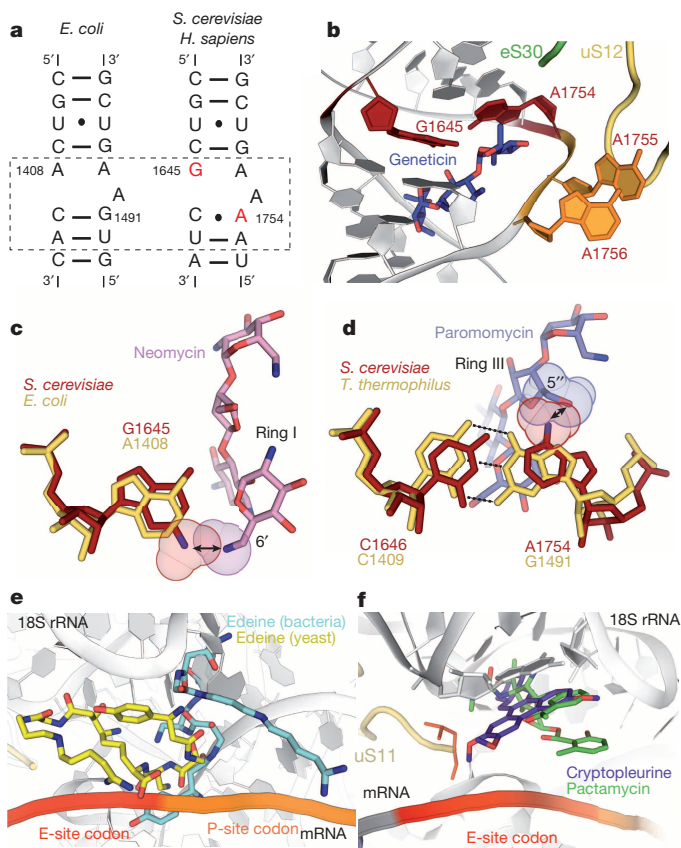


Figure 5 | Structures of 40S mRNA and tRNA inhibitors. **a**, The aminoglycosides binding site is different in eukaryotes. Secondary structure diagrams of helix 44 from bacteria (16S rRNA, left) and from yeast and human (18S rRNA, right). **b**, Geneticin (blue) binds to helix 44 and induces the flipping out of A1755 and A1756 (orange). **c**, The conformation of G1645 in yeast 18S rRNA restricts the binding of aminoglycosides bearing a 6' amino group in ring I, as shown for neomycin (pink, PDB accession code: 3QAN). **d**, The conformation of A1754 in yeast restricts the binding of aminoglycosides bearing a 5' hydroxyl group in ring III, as shown for paromomycin (blue, PDB 3UZ3). **e**, Edeine adopts a different conformation on the bacterial (blue, PDB 1195) and eukaryotic ribosome (yellow). **f**, Pactamycin (green) and cryptopleurine (purple) share the same binding site in the 40S E-site. Natural mutations in the C-terminal part of protein uS11 (red) confer resistance to cryptopleurine⁴³. The mRNA structure was taken from PDB accession code 4KZZ.

mRNA codons positioned in the A-site^{25,26}. In bacteria, aminoglycosides antibiotics alter translation accuracy and inhibit tRNA translocation by perturbing the conformation of the decoding centre nucleotides. Besides their potent activity against Gram-negative bacteria, the aminoglycoside-induced suppression of premature termination holds potential for the treatment of inherited disorders caused by nonsense mutations^{11,27}.

The canonical aminoglycoside binding site is located within the internal loop of helix 44 of 18S rRNA, which is part of the decoding centre that contains the essential and universally conserved nucleotides A1755 (A1492) and A1756 (A1493). In close vicinity, two nucleotides differ between bacteria and eukaryotes, but are identical in yeast and humans: G1645 (A1408) and A1754 (G1491) (Fig. 5a)^{28,29}.

The large class of aminoglycosides can be divided in three subgroups according to their chemical structures: kanamycins, neomycins and gentamicins³⁰. We chose geneticin (G418) as a representative of kanamycins with high affinity for the eukaryotic ribosome. Geneticin binds into the aminoglycoside pocket and induces the flipping out of A1755 and A1756 (Fig. 5b). The structure highlights direct interactions between geneticin ring I and the eukaryote-specific residues G1645 and A1754.

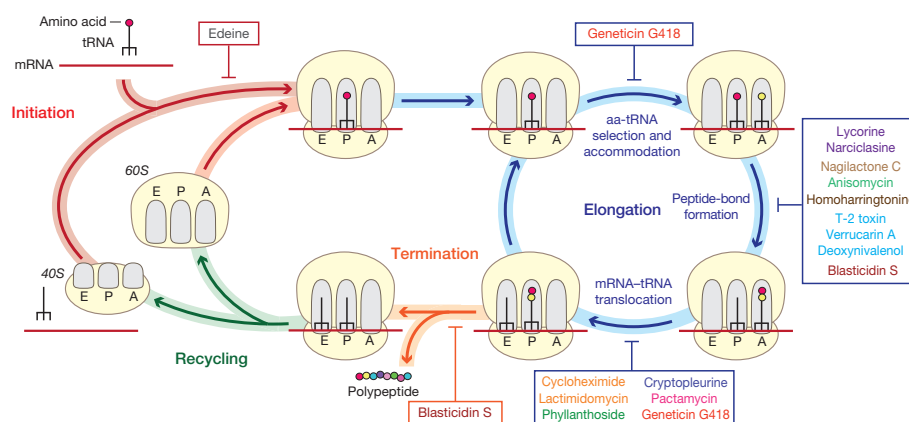


Figure 6 | Inhibitors action during protein synthesis in eukaryotes. Schematic showing the steps of protein synthesis in eukaryotes impaired by the small-molecule inhibitors.

Although some aminoglycosides exhibit broad-spectrum activity against both bacteria and eukaryotes, most of them remain poorly or not active on eukaryotic cytosolic ribosomes. This resistance mechanism observed within the class is attributed to the aforementioned structural differences present in eukaryotes. We demonstrate that the conformation of G1645, which is different from the conformation of A1408 in bacteria, acts as a barrier on the eukaryotic ribosome by preventing the accommodation of aminoglycosides with a 6'-substituent in ring I different from hydroxyl (Fig. 5c). This finding confirms previous results on low inhibitory activity of aminoglycosides in eukaryotes³¹. In line with this, most kanamycins and all gentamicins contain an amino group or a carbon side chain at this position responsible for their limited effect on the eukaryotic ribosome. However, some members of the neomycin family, such as paromomycin, contain a 6'-hydroxyl substituent and yet remain poorly active on the cytosolic eukaryotic ribosomes. We identified a second structural barrier to neomycin binding: in comparison to bacteria, A1754 is shifted in eukaryotes due to a non-canonical interaction with C1646. Consequently, A1754 prevents the accommodation of the 5'-hydroxyl group in ring III sometimes present in neomycins, which provides an explanation for the biochemical data (Fig. 5d)²⁸.

The mRNA and tRNA binding sites

Additional rRNA elements and proteins have led to important remodelling of the small subunit structure in eukaryotes, which serves as a platform for numerous protein factors and participates actively in translation initiation. During initiation, the subunit binds to and moves along the mRNA 5' untranslated region to search for the proper start codon.

In bacteria, edeine binds between the P-site and the E-site of the small subunit and impairs the binding of initiator tRNA to the P-site during initiation^{32,33}. In the yeast ribosome, edeine binds to the same region but adopts a markedly different conformation than on the bacterial 30S subunit (Fig. 5e). Located almost exclusively in the E-site, the binding pocket is formed by 18S rRNA nucleotides positioned in the mRNA path. Edeine affects translation differently in prokaryotes and eukaryotes in keeping with the fact that the mechanism of initiation is markedly distinct. Indeed, edeine interferes with start codon recognition by promoting continuous scanning of the 40S subunit and preventing subunit joining³⁴. Thus, mRNA and edeine may simultaneously bind to the 40S subunit to promote scanning and prevent initiator tRNA interaction with the start codon.

Pactamycin and cryptopleurine are located exclusively in the 40S E-site and share the same binding pocket that overlaps in part with the edeine binding site. Both inhibitors are found in the mRNA channel in the E-site and interact with the ribosome by stacking with the residue G904 of 18S rRNA (Fig. 5f). Pactamycin is a broad-spectrum inhibitor

with binding mode conserved in bacteria and eukaryotes. On the other hand, cryptopleurine was described as a eukaryote-specific inhibitor³⁵. The structure of cryptopleurine bound to yeast ribosome in the present functional state does not provide the basis for its specificity. The location of pactamycin and cryptopleurine imply that they act on the step of translocation from the P-site to the E-site and may also affect initiation in eukaryotes. It remains to be shown whether the translocation inhibition is promoted by hindering mRNA and/or tRNA movement.

Conclusions

This study provides a complete atomic description of 16 inhibitors bound to the yeast ribosome, highlighting common principles of targeting and shedding light on their binding sites, modes of action, determinants of species selectivity and resistance. By targeting exclusively mRNA and tRNA binding sites on both subunits, small-molecule inhibitors impair several ribosome functions mainly, but not exclusively, during the elongation cycle (Fig. 6).

In conjunction with kinetic experiments, we demonstrate that the size of glutarimide inhibitors dictates their binding to the ribosome at specific stages of elongation, resulting in different effects on translation. This model may have direct implications for other ribosome inhibitors in eukaryotes and in bacteria. For example, in the peptidyl transferase centre A-site, a similar mechanism may explain why anisomycin (small) and homoharringtonine (large) share the same binding site but block different stages of elongation³⁶.

Similarly to antibiotics acting against the bacterial ribosome, 80S ribosome inhibitors are sophisticated tools to study protein synthesis in eukaryotes²⁰. Our study highlights general principles for drug targeting and provides foundations for structure-based drug design. These structures will facilitate the development of next-generation antibiotics with reduced adverse effects and new therapeutics against infectious diseases, cancers and genetic disorders caused by premature termination codons^{8–12}. High-resolution X-ray crystallography of the 80S ribosome opens a new area of investigation—a large number of ribosome inhibitors certainly remain to be discovered and analysed.

Online Content Methods, along with any additional Extended Data display items and Source Data, are available in the online version of the paper; references unique to these sections appear only in the online paper.

Received 7 May; accepted 6 August 2014.

Published online 10 September 2014.

1. Ben-Shem, A. *et al.* The structure of the eukaryotic ribosome at 3.0 Å resolution. *Science* **334**, 1524–1529 (2011).
2. Melnikov, S. *et al.* One core, two shells: bacterial and eukaryotic ribosomes. *Nature Struct. Mol. Biol.* **19**, 560–567 (2012).
3. Jenner, L. *et al.* Crystal structure of the 80S yeast ribosome. *Curr. Opin. Struct. Biol.* **22**, 759–767 (2012).

4. Sonenberg, N. & Hinnebusch, A. G. Regulation of translation initiation in eukaryotes: mechanisms and biological targets. *Cell* **136**, 731–745 (2009).
5. Wilson, D. N. Ribosome-targeting antibiotics and mechanisms of bacterial resistance. *Nature Rev. Microbiol.* **12**, 35–48 (2014).
6. Blaha, G. M., Polikanov, Y. S. & Steitz, T. A. Elements of ribosomal drug resistance and specificity. *Curr. Opin. Struct. Biol.* **22**, 750–758 (2012).
7. Zhou, J. *et al.* Design at the atomic level: generation of novel hybrid biarylloxazolidinones as promising new antibiotics. *Bioorg. Med. Chem. Lett.* **18**, 6179–6183 (2008).
8. Hobbie, S. N. *et al.* Genetic reconstruction of protozoan rRNA decoding sites provides a rationale for paromomycin activity against *Leishmania* and *Trypanosoma*. *PLoS Negl. Trop. Dis.* **5**, e1161 (2011).
9. Lu, W., Roongsawang, N. & Mahmud, T. Biosynthetic studies and genetic engineering of pactamycin analogs with improved selectivity toward malarial parasites. *Chem. Biol.* **18**, 425–431 (2011).
10. Santagata, S. *et al.* Tight coordination of protein translation and HSF1 activation supports the anabolic malignant state. *Science* **341**, 1238303 (2013).
11. Bidou, L., Allamand, V., Rousset, J. P. & Namy, O. Sense from nonsense: therapies for premature stop codon diseases. *Trends Mol. Med.* **18**, 679–688 (2012).
12. Darnell, J. C. & Klann, E. The translation of translational control by FMRP: therapeutic targets for FXS. *Nature Neurosci.* **16**, 1530–1536 (2013).
13. Gürel, G., Blaha, G., Steitz, T. A. & Moore, P. B. Structures of triacetyloleandomycin and mycalamide A bind to the large ribosomal subunit of *Haloarcula marismortui*. *Antimicrob. Agents Chemother.* **53**, 5010–5014 (2009).
14. Gürel, G., Blaha, G., Moore, P. B. & Steitz, T. A. U2504 determines the species specificity of the A-site cleft antibiotics: the structures of tiamulin, homoharringtonine, and bruceantin bound to the ribosome. *J. Mol. Biol.* **389**, 146–156 (2009).
15. Klinge, S., Voigts-Hoffmann, F., Leibundgut, M., Arpagaus, S. & Ban, N. Crystal structure of the eukaryotic 60S ribosomal subunit in complex with initiation factor 6. *Science* **334**, 941–948 (2011).
16. Decatur, W. A. & Fournier, M. J. rRNA modifications and ribosome function. *Trends Biochem. Sci.* **27**, 344–351 (2002).
17. Chan, J., Khan, S. N., Harvey, I., Merrick, W. & Pelletier, J. Eukaryotic protein synthesis inhibitors identified by comparison of cytotoxicity profiles. *RNA* **10**, 528–543 (2004).
18. Schneider-Poetsch, T. *et al.* Inhibition of eukaryotic translation elongation by cycloheximide and lactimidomycin. *Nature Chem. Biol.* **6**, 209–217 (2010).
19. Lee, S., Liu, B., Huang, S. X., Shen, B. & Qian, S. B. Global mapping of translation initiation sites in mammalian cells at single-nucleotide resolution. *Proc. Natl Acad. Sci. USA* **109**, E2424–E2432 (2012).
20. Ingolia, N. T., Ghaemmamghami, S., Newman, J. R. & Weissman, J. S. Genome-wide analysis *in vivo* of translation with nucleotide resolution using ribosome profiling. *Science* **324**, 218–223 (2009).
21. Wintermeyer, W. & Zachau, H. G. Fluorescent derivatives of yeast tRNA^{Phe}. *Eur. J. Biochem.* **98**, 465–475 (1979).
22. Lill, R., Robertson, J. M. & Wintermeyer, W. Affinities of tRNA binding sites of ribosomes from *Escherichia coli*. *Biochemistry* **25**, 3245–3255 (1986).
23. Svidritskiy, E., Ling, C., Ermolenko, D. N. & Korostelev, A. A. Blastocidin S inhibits translation by trapping deformed tRNA on the ribosome. *Proc. Natl Acad. Sci. USA* **110**, 12283–12288 (2013).
24. Cannone, J. J. *et al.* The comparative RNA web (CRW) site: an online database of comparative sequence and structure information for ribosomal, intron, and other RNAs. *BMC Bioinformatics* **3**, 2 (2002).
25. Demeshkina, N., Jenner, L., Westhof, E., Yusupov, M. & Yusupova, G. A new understanding of the decoding principle on the ribosome. *Nature* **484**, 256–259 (2012).
26. Ogle, J. M., Murphy, F. V., Tarry, M. J. & Ramakrishnan, V. Selection of tRNA by the ribosome requires a transition from an open to a closed form. *Cell* **111**, 721–732 (2002).
27. Shulman, E. *et al.* Designer aminoglycosides that selectively inhibit cytoplasmic rather than mitochondrial ribosomes show decreased ototoxicity: a strategy for the treatment of genetic diseases. *J. Biol. Chem.* **289**, 2318–2330 (2014).
28. Fan-Minogue, H. & Bedwell, D. M. Eukaryotic ribosomal RNA determinants of aminoglycoside resistance and their role in translational fidelity. *RNA* **14**, 148–157 (2008).
29. Recht, M. I., Douthwaite, S. & Puglisi, J. D. Basis for prokaryotic specificity of action of aminoglycoside antibiotics. *EMBO J.* **18**, 3133–3138 (1999).
30. Becker, B. & Cooper, M. A. Aminoglycoside antibiotics in the 21st century. *ACS Chem. Biol.* **8**, 105–115 (2013).
31. Perez-Fernandez, D. *et al.* 4'-O-substitutions determine selectivity of aminoglycoside antibiotics. *Nature Commun.* **5**, 3112 (2014).
32. Dinou, G. *et al.* Dissecting the ribosomal inhibition mechanisms of edeine and pactamycin: the universally conserved residues G693 and C795 regulate P-site RNA binding. *Mol. Cell* **13**, 113–124 (2004).
33. Pioletti, M. *et al.* Crystal structures of complexes of the small ribosomal subunit with tetracycline, edeine and IF3. *EMBO J.* **20**, 1829–1839 (2001).
34. Kozak, M. & Shatkin, A. J. Migration of 40S ribosomal subunits on messenger RNA in the presence of edeine. *J. Biol. Chem.* **253**, 6568–6577 (1978).
35. Dölz, H., Vazquez, D. & Jimenez, A. Quantitation of the specific interaction of [14a-3H]cryptopleurine with 80S and 40S ribosomal species from the yeast *Saccharomyces cerevisiae*. *Biochemistry* **21**, 3181–3187 (1982).
36. Ingolia, N. T., Lareau, L. F. & Weissman, J. S. Ribosome profiling of mouse embryonic stem cells reveals the complexity and dynamics of mammalian proteomes. *Cell* **147**, 789–802 (2011).
37. Chen, Y. & Li, S. Omacetaxine mepesuccinate in the treatment of intractable chronic myeloid leukemia. *Onco Targets Ther.* **7**, 177–186 (2014).
38. Evidente, A. *et al.* Biological evaluation of structurally diverse amarylidae alkaloids and their synthetic derivatives: discovery of novel leads for anticancer drug design. *Planta Med.* **75**, 501–507 (2009).
39. McCormick, S. P., Stanley, A. M., Stover, N. A. & Alexander, N. J. Trichothecenes: from simple to complex mycotoxins. *Toxins* **3**, 802–814 (2011).
40. Shirai, A., Sadaie, M., Shinmyozu, K. & Nakayama, J. Methylation of ribosomal protein L42 regulates ribosomal function and stress-adapted cell growth. *J. Biol. Chem.* **285**, 22448–22460 (2010).
41. Kawai, S. *et al.* Drastic alteration of cycloheximide sensitivity by substitution of one amino acid in the L41 ribosomal protein of yeasts. *J. Bacteriol.* **174**, 254–262 (1992).
42. Kaäuffer, N. F., Fried, H. M., Schwindinger, W. F., Jasin, M. & Warner, J. R. Cycloheximide resistance in yeast: the gene and its protein. *Nucleic Acids Res.* **11**, 3123–3135 (1983).
43. Sánchez, L., Vázquez, D. & Jiménez, A. Genetics and biochemistry of cryptopleurine resistance in the yeast *Saccharomyces cerevisiae*. *Mol. Gen. Genet.* **156**, 319–326 (1977).

Supplementary Information is available in the online version of the paper.

Acknowledgements We thank J. Liu (Johns Hopkins Medical Institute), D. Wilson (Gene Center Munich), P. Hazendonk (Agriculture and Agri-Food Canada) and the NIH/NCI Developmental Therapeutics Program for providing materials. We acknowledge SOLEIL synchrotron (France), all staff members of PROXIMA1 beamline, especially A. Thompson and P. Legrand for their assistance during data collection. We thank A. Perez Lara, MPI Göttingen, for the help with the ITC experiments and S. Melnikov, IGBMC, for reading the manuscript. I.P. acknowledges support from AFM-Telethon post-doctoral fellowship. This work was supported by the SATT Conectus Technology Maturation grant I12-042 (to N.G.D.L.), the ERC Advanced grant 294312, the Human Frontier Science Program grant RGP0062/2012 and the Russian Government Program of Competitive Growth of Kazan Federal University (to M.Y.), the French National Research Agency grant ANR-11-BSV8-006 01 (to G.Y.) and the Deutsche Forschungsgemeinschaft grant (to M.V.R.).

Author Contributions M.Y. supervised the study. N.G.D.L. designed the experiments. N.G.D.L. and I.P. conducted purification, crystallization and post-crystallization treatment experiments, collected X-ray diffraction data and carried out the structure determination. N.G.D.L., I.P., G.Y. and M.Y. analysed the crystal structures. M.V.R. and W.H. designed, performed and interpreted rapid kinetic experiments. N.G.D.L. wrote the initial manuscript to which M.V.R., G.Y. and M.Y. contributed specialist insights. All authors helped with refining the manuscript and approved the final version.

Author Information Atomic coordinates and structure factors for the reported crystal structures have been deposited in the Protein Data Bank (<http://www.pdb.org/pdb/home/home.do>) under accession codes 4U3M (anisomycin), 4U56 (blastocidin S), 4U3N (CCA), 4U55 (cryptopleurine), 4U3U (cycloheximide), 4U53 (deoxynivalenol), 4U4N (edeine), 4U4O (geneticin G418), 4U4Q (homoharringtonine), 4U4R (lactimidomycin), 4U4U (lycorine), 4U52 (nagilactone C), 4U51 (narcilasin), 4U4Y (pactamycin), 4U4Z (phyllanthoside), 4U6F (T-2 toxin) and 4U50 (verrucarin). Reprints and permissions information is available at www.nature.com/reprints. The authors declare no competing financial interests. Readers are welcome to comment on the online version of the paper. Correspondence and requests for materials should be addressed to M.Y. (marat@igbmc.fr).

Early turbulent mixing as the origin of chemical homogeneity in open star clusters

Yi Feng¹ & Mark R. Krumholz¹

The abundances of elements in stars are critical clues to stars' origins. Observed star-to-star variations in logarithmic abundance within an open star cluster—a gravitationally bound ensemble of stars in the Galactic plane—are typically only about 0.01 to 0.05 over many elements^{1–9}, which is noticeably smaller than the variation of about 0.06 to 0.3 seen in the interstellar medium from which the stars form^{10–14}. It is unknown why star clusters are so homogenous, and whether homogeneity should also prevail in regions of lower star formation efficiency that do not produce bound clusters. Here we report simulations that trace the mixing of chemical elements as star-forming clouds assemble and collapse. We show that turbulent mixing during cloud assembly naturally produces a stellar abundance scatter at least five times smaller than that in the gas, which is sufficient to explain the observed chemical homogeneity of stars. Moreover, mixing occurs very early, so that regions with star formation efficiencies of about 10 per cent are nearly as well mixed as those with formation efficiencies of about 50 per cent. This implies that even regions that do not form bound clusters are likely to be well mixed, and improves the prospects of using 'chemical tagging' to reconstruct (via their unique chemical signatures, or tags) star clusters whose constituent stars have become unbound from one another and spread across the Galactic disk.

The question of how star clusters become chemically well mixed has received relatively little attention. With a few exceptions¹⁵, work to date has been limited to simple analytic estimates¹⁶, or to calculations omitting star formation and self-gravity^{17,18}. To improve this situation, we have performed a series of simulations of star cluster formation including hydrodynamics, gravity, and optically thin radiative heating and cooling. Our simulations use the ORION code^{19–21}, with a new implementation of particle-mesh gravity (Methods, Extended Data Figs 1 and 2). We use initial conditions based on the 'colliding flow' model²². We consider a region containing gas of number density $n_0 = 1 \text{ cm}^{-3}$ (mass density $\rho_0 = 2.1 \times 10^{-24} \text{ g cm}^{-3}$) with initial temperature $T = 5,000 \text{ K}$. The gas has a random turbulent velocity v_{rms} , for which we consider two values: 0.17 and 1.7 km s^{-1} ; we refer to runs with these values as S and L, for small and large turbulence, respectively. In addition to the turbulent velocity, we set up two cylindrical regions 32 pc long and 32 pc in radius, centred on the x axis, with their closer ends separated by 64 pc, within which the gas has a uniform velocity $v_0 = 9.2 \text{ km s}^{-1}$, directed towards the other cylinder. To trace chemical mixing, the simulation includes two passive scalars Q_L and Q_R , which have initial abundances of 1 within the left and right cylinders, respectively, and 0 elsewhere. In addition to these two simulations with smooth initial conditions, we also run a simulation C (for clumpy)¹⁵, in which we randomly add cold clumps one coarse cell in radius with a filling fraction of 0.05 and a number density $n_c = 132.5 \text{ cm}^{-3}$; at this density the equilibrium temperature is such that the pressure is in equilibrium with that of the warm low-density background. Full details of the simulations are given in Methods.

The overall evolution of our simulations is very similar to previous colliding flow simulations^{15,22,23} (Fig. 1). The two streams of gas converge rapidly, and compression of material at the heads of the two cylinders leads to thermal instability and the formation of a cold phase even before the two flows collide. For runs S and L, the two streams collide just before

10 Myr of evolution, and this produces a dense, cold, turbulent layer that is gravitationally unstable. The layer begins to form stars at ~ 19 Myr in run S, and approximately 50% of the gas in the two streams has been converted to stars by ~ 25 Myr of evolution (Extended Data Fig. 3). In run L, star formation begins at ~ 25 Myr, and follows a similar time evolution to run S thereafter. In run C, the two streams collide at ~ 6 Myr because the dense cold phase is less decelerated by the warm phase. Star formation begins immediately after collision, and $\sim 40\%$ of the gas in the two streams has been converted to stars by ~ 13 Myr of evolution. We note that all our simulations have star formation rates that exceed observationally inferred values^{24,25}, but we select this scenario for examination precisely because its rapidity minimizes the time available to fully mix out chemical inhomogeneities. Our results should therefore represent lower limits on the true amount of mixing.

By the onset of star formation, the interaction region where the flows have collided is reasonably well mixed by the turbulence (Fig. 1). The ratio of passive scalar concentrations $R = Q_L/Q_R$ is very broad for material at densities up to $\sim 10^{-22} \text{ g cm}^{-3}$, reflecting the broad range of abundances in low-density gas. However, in gas with densities of $\sim 10^{-21} \text{ g cm}^{-3}$ or higher, the range of compositions is dramatically reduced (Fig. 2). For the densest gas, the full range in R is at most a decade, and the vast majority of the mass is spread over an even smaller range. This densest gas is produced in regions where the two flows are converging and mixing efficiently, and it is these regions that produce stars.

To assess how this affects stellar abundances, we note that the abundance scatter for some element in a collection of stars is formally defined as $S_* = \left[\sum (\log a_{*,i} - \overline{\log a_*})^2 / N \right]^{1/2}$, where the sum runs over all N stars present at any time, $a_{*,i}$ is the abundance of that element in star i , and $\overline{\log a_*} = 1/N \sum_i \log a_{*,i}$ is the mean of the logarithmic abundance over all stars. To compute this quantity from our simulations, let a_L and a_R be the abundances of some element of interest in the left and right streams, respectively. Without loss of generality, we can choose $a_L < a_R$. For each star i formed in the simulations, we know the masses $M_{L,i}$ and $M_{R,i}$ contributed by each stream. The abundance $a_{*,i}$ of that star is therefore $a_{*,i} = (a_L M_{L,i} + a_R M_{R,i}) / (M_{L,i} + M_{R,i})$. Note that the actual values of a_L and a_R need not be chosen before the simulations are run, since the only quantities actually measured from the simulations are $M_{L,i}$ and $M_{R,i}$. We can therefore use a single simulation to compute S_* for an arbitrary value of the gas abundance ratio, a_R/a_L (see Extended Data Fig. 4).

We show in Methods that the dependence of S_* on a_R/a_L is characterized by two limiting cases: when $a_R/a_L \approx 1$, we have $S_* \approx 2\sigma_Y S_g \equiv S_{\text{slope}} S_g$. Here $Y_i = M_{R,i} / (M_{L,i} + M_{R,i})$ is the mass fraction in star i provided by

the right stream, $\sigma_Y = \sqrt{\sum (Y_i - \bar{Y})^2 / N}$ is the dispersion of the Y_i values, and we have defined the gas scatter as $S_g = \left\{ \left[(\log a_L - \overline{\log a_g})^2 + (\log a_R - \overline{\log a_g})^2 \right] / 2 \right\}^{1/2}$, where $\overline{\log a_g} = (\log a_L + \log a_R) / 2$ is the mean logarithmic abundance in the two streams. In the opposite limit, when $a_R/a_L \gg 1$, we have $S_* \approx \sigma_{\log Y} \equiv S_{\text{limit}}$ where $\sigma_{\log Y}$ is the dispersion of $\log Y_i$. Intuitively, the reduction in abundance scatter is at its minimum when the gas is close to homogenous already, and S_{slope} characterizes the factor by which the gas abundance scatter is reduced in this

¹Department of Astronomy and Astrophysics, University of California, Santa Cruz, California 95064, USA.

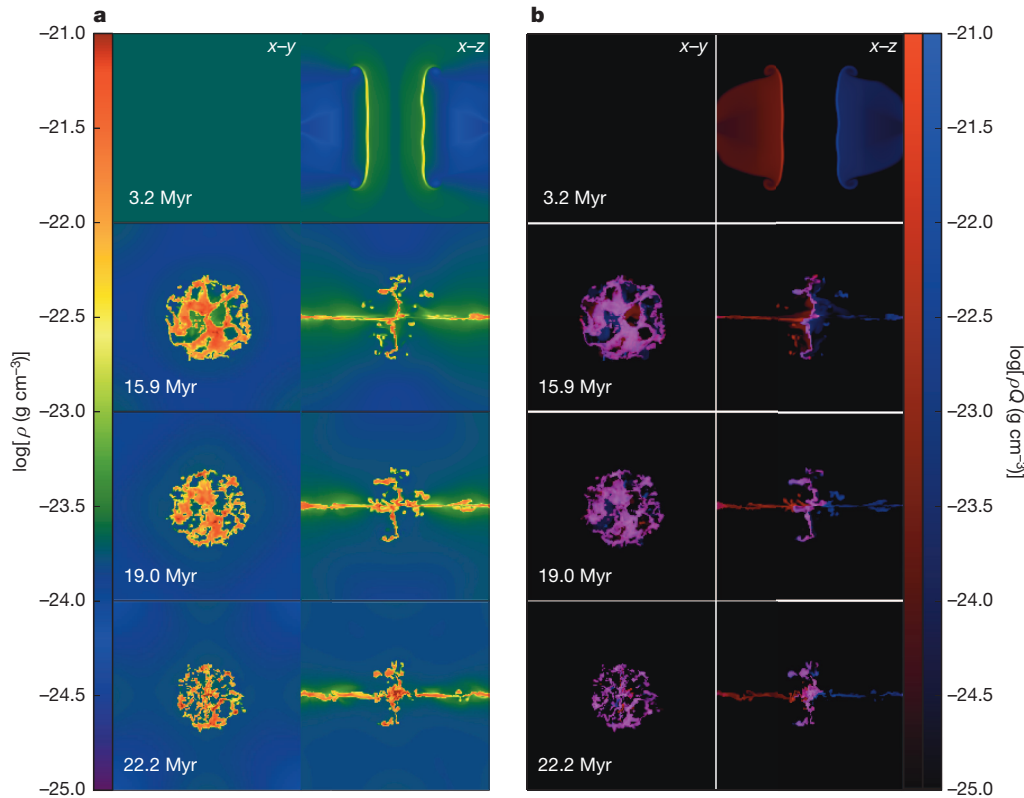


Figure 1 | Slices through simulation S at a variety of times, showing the total density and the densities of the passive scalar fields. **a**, Gas density ρ in run S on slices in the x - y (left column) and y - z (right column) planes. The rows show increasing times in the simulation, as indicated in each row. **b**, Density of passive scalars ρQ_L (red) and ρQ_R (blue) at the same times and in the same planes as in **a**. The densities of the two tracers have been mapped to the red and blue channels of the image, so that cells containing equal contributions from the two streams appear as purple, with the intensity of the purple colour proportional to the logarithm of the total density. In contrast, cells dominated by one passive scalar or the other appear as red or blue in colour.

limit. The quantity S_{limit} is the maximum possible stellar abundance scatter no matter how inhomogeneous the gas is.

We define the star formation efficiency $\varepsilon = M_*/2M_{\text{inf}}$, where M_* is the total stellar mass and M_{inf} is the mass in one of the streams; $M_{\text{inf}} = 6.5 \times 10^3 M_\odot$ in runs S and L, and $4.9 \times 10^4 M_\odot$ in run C (M_\odot is the solar mass). The general evolution of both S_{limit} and S_{slope} with ε in run S is a rapid rise from 0 as the first stars form (Fig. 3), followed by a rapid fall by the time ε reaches ~ 0.02 . At values of $\varepsilon > 0.1$, we have $S_{\text{limit}} \lesssim 0.4$ and $S_{\text{slope}} \lesssim 0.3$, indicating that a relatively small abundance inhomogeneity will be reduced by a factor of at least 3 in the star formation process, and that even a very large inhomogeneity will produce at most ~ 0.4 dex of scatter in the resulting stars. By the time the star formation efficiency reaches $\sim 30\%$, the reduction in scatter is close to a factor of 5, and the absolute upper limit on the scatter is ~ 0.2 dex. In run L, the stronger turbulence delays the onset of star formation and allows more rapid mixing at early times, so the stellar scatter starts small and very gradually increases with time. However, it is always smaller than at the corresponding value of ε in run S. Similarly, S_{limit} is smaller in run C

than in run S, probably due to the stronger global collapse in the clumpy run¹⁵. However, S_{slope} is nearly identical in runs S and C. This suggests that clumpiness does not alter the amount of mixing much where $S_g \ll 1$. We have also conducted convergence studies to verify that our results for mixing are robust against changes in numerical resolution (Methods, Extended Data Figs 5 and 6).

Figure 3 indicates that the process of star formation leads to a great deal of chemical homogenization as soon as even very modest star formation efficiencies are achieved. For realistic efficiencies, which are probably in range ~ 10 – 50% on the scale of star clusters²⁶, we should expect the abundance scatter to be reduced by at least a factor of ~ 4 – 6 compared to that in the gas from which the stars are formed, and even in the most chemically inhomogeneous environments the scatter will be no more than a few tenths of a dex. Since observed gas abundance scatters are $S_g \approx 0.06$ – 0.3 dex over size scales of ~ 0.1 – 1 kpc (refs 10–14), a factor of ~ 5 reduction in the stellar abundance scatter compared to this is sufficient to fully explain the observed scatter $S_* \approx 0.01$ – 0.05 dex seen in open clusters and moving groups.

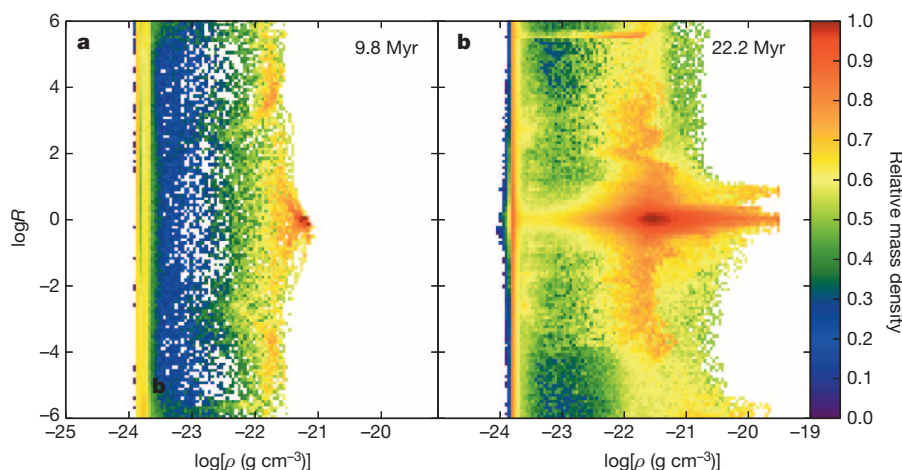


Figure 2 | Distribution of gas in simulation S in density and mixing ratio at two different times. The colour in each two-dimensional pixel indicates the relative fraction of mass in the corresponding bin of (ρ, R) , where $R = Q_L/Q_R$ is the ratio of the two passive scalars. Panel **a** shows the result at $t = 9.8$ Myr, just as the two streams are beginning to collide, and panel **b** shows the result at $t = 22.2$ Myr, just after the onset of rapid star formation. Note that some of the features seen in **b**, including the streaks near $R \approx 3 \times 10^{-6}$ and $R \approx 10^{-1}$, are transients due to the chaotic nature of the mixing process. Similar features appear at other times and for different simulation resolutions, but they come and go essentially randomly. Only the most more prominent structure near $R = 0$ is persistent.

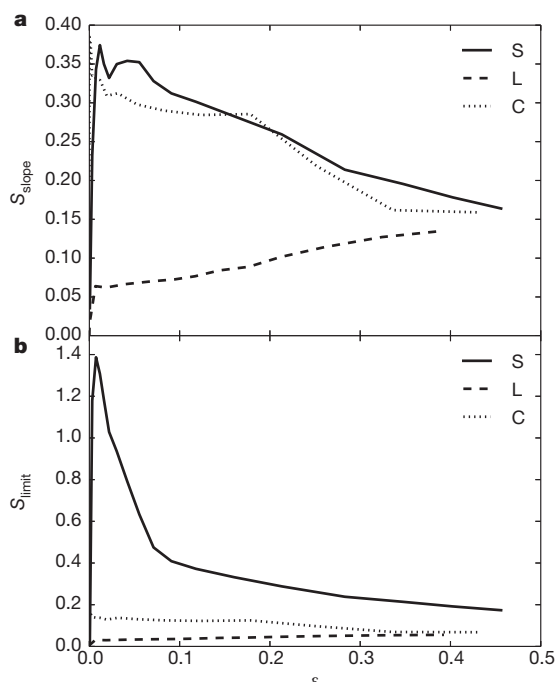


Figure 3 | Two measures of the stellar abundance scatter as a function of star formation efficiency in simulations S, L and C. **a**, S_{slope} versus star formation efficiency ϵ , where S_{slope} indicates the factor by which the gas abundance scatter S_g is reduced by star formation in the limit where $S_g \ll 1$. **b**, S_{limit} versus star formation efficiency ϵ , where S_{limit} is the maximum possible stellar abundance scatter in the gas where $S_g \gg 1$.

Moreover, our results are also very encouraging for the prospects of chemical tagging as a method of reconstructing the star formation history of the Milky Way, and for identifying potential ‘solar siblings’—stars born in the same cluster as the Sun^{27,28}. We find that both S_{limit} and S_{slope} reach values of ~ 0.1 – 0.3 even at low star formation efficiencies of ~ 0.1 , and that the degree of mixing increases only modestly as ϵ rises from ~ 0.1 to ~ 0.5 . Since star formation sites with $\epsilon \approx 0.1$ – 0.3 are probably the progenitors of the majority of field stars, while those with $\epsilon \approx 0.5$ probably represent the sites of bound cluster formation, our results imply that the clusters and moving groups that have been studied for chemical homogeneity thus far are not atypical in their degree of chemical mixing. They are at most marginally better mixed. Thus it is likely that even those stars that did not form in bound clusters will be chemically similar to their neighbours formed at the same point in space and time, and that these unique chemical signatures can serve as a fingerprint to identify these common formation sites even as stars disperse throughout the Galaxy. Indeed, with a group finding technique²⁹ and high resolution data, recent work³⁰ shows evidence that chemical tagging of field stars does identify coeval groups of stars. We discuss the implications and broader context of our work in more detail in Methods.

Online Content Methods, along with any additional Extended Data display items and Source Data, are available in the online version of the paper; references unique to these sections appear only in the online paper.

Received 28 February; accepted 1 July 2014.

Published online 31 August 2014.

- De Silva, G. M., Freeman, K. C., Bland-Hawthorn, J., Asplund, M. & Bessell, M. S. Chemically tagging the HR 1614 moving group. *Astron. J.* **133**, 694–704 (2007).
- De Silva, G. M. *et al.* Chemical homogeneity in Collinder 261 and implications for chemical tagging. *Astron. J.* **133**, 1161–1175 (2007).
- Pancino, E., Carrera, R., Rossetti, E. & Gallart, C. Chemical abundance analysis of the open clusters Cr 110, NGC 2099 (M 37), NGC 2420, NGC 7789, and M 67 (NGC 2682). *Astron. Astrophys.* **511**, A56 (2010).

- Bubar, E. J. & King, J. R. Spectroscopic abundances and membership in the Wolf 630 moving group. *Astron. J.* **140**, 293–318 (2010).
- De Silva, G. M. *et al.* High-resolution elemental abundance analysis of the Hyades supercluster. *Mon. Not. R. Astron. Soc.* **415**, 563–575 (2011).
- Ting, Y.-S., De Silva, G. M., Freeman, K. C. & Parker, S. J. High-resolution elemental abundance analysis of the open cluster IC 4756. *Mon. Not. R. Astron. Soc.* **427**, 882–892 (2012).
- Reddy, A. B. S., Giridhar, S. & Lambert, D. L. Comprehensive abundance analysis of red giants in the open clusters NGC 752, 1817, 2360 and 2506. *Mon. Not. R. Astron. Soc.* **419**, 1350–1361 (2012).
- De Silva, G. M. *et al.* Search for associations containing young stars: chemical tagging IC 2391 and the Argus association. *Mon. Not. R. Astron. Soc.* **431**, 1005–1018 (2013).
- Reddy, A. B. S., Giridhar, S. & Lambert, D. L. Comprehensive abundance analysis of red giants in the open clusters NGC 2527, 2682, 2482, 2539, 2335, 2251 and 2266. *Mon. Not. R. Astron. Soc.* **431**, 3338–3348 (2013).
- Rosolowsky, E. & Simon, J. D. The M33 metallicity project: resolving the abundance gradient discrepancies in M33. *Astrophys. J.* **675**, 1213–1222 (2008).
- Sanders, N. E., Caldwell, N., McDowell, J. & Harding, P. The metallicity profile of M31 from spectroscopy of hundreds of H II regions and PNe. *Astrophys. J.* **758**, 133 (2012).
- Berg, D. A. *et al.* New radial abundance gradients for NGC 628 and NGC 2403. *Astrophys. J.* **775**, 128 (2013).
- Bresolin, F. The abundance scatter in M33 from H II regions: is there any evidence for azimuthal metallicity variations? *Astrophys. J.* **730**, 129 (2011).
- Li, Y., Bresolin, F. & Kennicutt, R. C. Jr Testing for azimuthal abundance gradients in M101. *Astrophys. J.* **766**, 17 (2013).
- Carroll-Nellenback, J., Frank, A. & Heitsch, F. The effects of inhomogeneities within colliding flows on the formation and evolution of molecular clouds. *Astrophys. J.* (submitted); preprint available at <http://arXiv.org/abs/1304.1367> (2013).
- Murray, S. D. & Lin, D. N. C. On the origin of metal homogeneities in globular clusters. *Astrophys. J.* **357**, 105–112 (1990).
- de Avillez, M. A. & Mac Low, M.-M. Mixing timescales in a supernova-driven interstellar medium. *Astrophys. J.* **581**, 1047–1060 (2002).
- Yang, C.-C. & Krumholz, M. Thermal-instability-driven turbulent mixing in galactic disks. I. Effective mixing of metals. *Astrophys. J.* **758**, 48 (2012).
- Truelove, J. K. *et al.* Self-gravitational hydrodynamics with three-dimensional adaptive mesh refinement: methodology and applications to molecular cloud collapse and fragmentation. *Astrophys. J.* **495**, 821–852 (1998).
- Klein, R. I. Star formation with 3-D adaptive mesh refinement: the collapse and fragmentation of molecular clouds. *J. Comput. Appl. Math.* **109**, 123–152 (1999).
- Krumholz, M. R., McKee, C. F. & Klein, R. I. Embedding Lagrangian sink particles in Eulerian grids. *Astrophys. J.* **611**, 399–412 (2004).
- Vázquez-Semadeni, E. *et al.* Molecular cloud evolution. II. From cloud formation to the early stages of star formation in decaying conditions. *Astrophys. J.* **657**, 870–883 (2007).
- Heitsch, F., Hartmann, L. W., Slyz, A. D., Devriendt, J. E. G. & Burkert, A. Cooling, gravity, and geometry: flow-driven massive core formation. *Astrophys. J.* **674**, 316–328 (2008).
- Tan, J. C., Krumholz, M. R. & McKee, C. F. Equilibrium star cluster formation. *Astrophys. J.* **641**, L121–L124 (2006).
- Krumholz, M. R. & Tan, J. C. Slow star formation in dense gas: evidence and implications. *Astrophys. J.* **654**, 304–315 (2007).
- Krumholz, M. R. The big problems in star formation: the star formation rate, stellar clustering, and the initial mass function. *Phys. Rep.* **539**, 49–134 (2014).
- Portegies Zwart, S. F. The lost siblings of the Sun. *Astrophys. J.* **696**, L13–L16 (2009).
- Bland-Hawthorn, J., Krumholz, M. R. & Freeman, K. The long-term evolution of the galactic disk traced by dissolving star clusters. *Astrophys. J.* **713**, 166–179 (2010).
- Mitschang, A. W., De Silva, G., Sharma, S. & Zucker, D. B. Quantifying chemical tagging: towards robust group finding in the Galaxy. *Mon. Not. R. Astron. Soc.* **428**, 2321–2332 (2013).
- Mitschang, A. W. *et al.* Quantitative chemical tagging, stellar ages and the chemodynamical evolution of the Galactic disc. *Mon. Not. R. Astron. Soc.* **438**, 2753–2764 (2014).

Acknowledgements This work was funded by NSF grants AST-0955300 and AST-1405962, NASA ATP grant NNX13AB84G, NASA TCAN grant NNX14AB52G, and NASA through Hubble Award number 13256 issued by the Space Telescope Science Institute, which is operated by the Association of Universities for Research in Astronomy, Inc., under NASA contract NAS 5-26555. The simulations reported in this research were carried out on the UCSC supercomputer Hyades, which is supported by the NSF (award number AST-1229745).

Author Contributions Y.F. ran the simulations, produced all the figures, and wrote parts of the text. M.R.K. aided in the interpretation and wrote the other parts of the text.

Author Information Reprints and permissions information is available at www.nature.com/reprints. The authors declare no competing financial interests. Readers are welcome to comment on the online version of the paper. Correspondence and requests for materials should be addressed to M.R.K. (mkrumhol@ucsc.edu).

Water vapour absorption in the clear atmosphere of a Neptune-sized exoplanet

Jonathan Fraine^{1,2,3}, Drake Deming^{1,4}, Bjorn Benneke³, Heather Knutson³, Andrés Jordán², Néstor Espinoza², Nikku Madhusudhan⁵, Ashlee Wilkins¹ & Kamen Todorov⁶

Transmission spectroscopy has so far detected atomic and molecular absorption in Jupiter-sized exoplanets, but intense efforts to measure molecular absorption in the atmospheres of smaller (Neptune-sized) planets during transits have revealed only featureless spectra^{1–4}. From this it was concluded that the majority of small, warm planets evolve to sustain atmospheres with high mean molecular weights (little hydrogen), opaque clouds or scattering hazes, reducing our ability to observe the composition of these atmospheres^{1–5}. Here we report observations of the transmission spectrum of the exoplanet HAT-P-11b (which has a radius about four times that of Earth) from the optical wavelength range to the infrared. We detected water vapour absorption at a wavelength of 1.4 micrometres. The amplitude of the water absorption (approximately 250 parts per million) indicates that the planetary atmosphere is predominantly clear down to an altitude corresponding to about 1 millibar, and sufficiently rich in hydrogen to have a large scale height (over which the atmospheric pressure varies by a factor of *e*). The spectrum is indicative of a planetary atmosphere in which the abundance of heavy elements is no greater than about 700 times the solar value. This is in good agreement with the core-accretion theory of planet formation, in which a gas giant planet acquires its atmosphere by accreting hydrogen-rich gas directly from the protoplanetary nebula onto a large rocky or icy core⁶.

We observed transits of HAT-P-11b⁷ (mass, $M_p = (25.8 \pm 2.9)M_\oplus$ (M_\oplus , Earth mass); radius, $R_p = (4.37 \pm 0.08)R_\oplus$ (R_\oplus , Earth radius); equilibrium temperature, $T_{eq} = (878 \pm 50)$ K) in a joint programme involving NASA's Hubble and Spitzer space telescopes. Our Hubble observations comprised 1.1–1.7 μm grism spectroscopy using the Wide Field Camera 3 (WFC3) in spatial scanning mode. We also integrated these data over wavelength to produce WFC3 photometry^{1–4,8}. Our Spitzer observations comprised photometry during two transits in each of the 3.6 and 4.5 μm bands of the Infrared Array Camera⁹ (IRAC). Because the planet lies in the field of view of NASA's Kepler spacecraft¹⁰, precision optical photometry (~ 642 nm) was obtained simultaneously with our Spitzer observations, although not simultaneously with our Hubble observations. Table 1 summarizes specific details of our observations, and Fig. 1a shows our transit photometry and model fits. Because HAT-P-11 is an active planet-hosting star^{11–13}, we show that starspots on the stellar surface are not sufficiently cool, nor sufficiently prevalent, to mimic the effect of water vapour absorption in the planet¹⁴. Our simultaneous Spitzer and Kepler photometry was critical to defining the temperature of the starspots that could otherwise, potentially mimic the effect of water vapour absorption in the planetary atmosphere.

HAT-P-11b crosses starspots on virtually every transit^{12,13}, as seen prominently Fig. 1a. Our WFC3 photometry has the sensitivity to detect starspot crossings², but none were observed when Hubble observed the system. Our WFC3 observations contain large temporal gaps because Hubble passes behind the Earth^{1–4,15}, but not during the transit. Therefore, unocculted starspots, rather than occulted ones, potentially affect our transmission spectrum^{16,17}. When the planet blocks unspotted portions

of the stellar photosphere, the absorption lines in cool unocculted spots become relatively more prominent^{12,13}.

Figure 1a shows the binned and normalized light curves of our four simultaneous Kepler–Spitzer transits and our WFC3 band-integrated light curve. We fitted analytic transit light curves to all of time series with PyMC¹⁸ to generate Markov chain Monte Carlo (MCMC) distributions to estimate the planetary parameters^{19,20}. We reanalysed the phased and binned Kepler data using improved limb-darkening coefficients derived from stellar model atmospheres²¹. To fit the Spitzer and WFC3 transits, we held the orbital distance and inclination constant at our Kepler-derived values. Although the uncertainties in the Kepler-derived parameters were smaller than in previous studies^{12,13}, our purpose was to implement the updated limb-darkening law and derive orbital parameters for all of our observations.

Each of the Kepler light curves obtained concurrently with our Spitzer observations shows starspot crossings as deviations in the light curves between ~ 0.3 and 0.7 h after mid-transit. The amplitude of these deviations is a function of both the area and the temperature of the occulted spots^{12,13}. Because the Kepler and Spitzer photometries were concurrent, the relative intensity is independent of the starspots' areas. However, because the contrast between starspot temperature and the photosphere is a chromatic effect, the amplitude of these deviations varied with wavelength^{16,17}. The spot crossings are not obvious in the Spitzer data because thermal radiation produces a much smaller contrast between the stellar photosphere and spot fluxes in the infrared than in the optical. The ratio between the Spitzer and Kepler spot crossing amplitudes constrained lower limits on the starspot temperatures for the crossed starspots.

We included the relative shape of the spot crossings, sliced from each residual Kepler light curve, and scaled their amplitudes as free parameters in our MCMC analysis with our Spitzer transits. The distributions of the Spitzer/Kepler spot crossing amplitude ratios are shown in Fig. 1b. The dashed black lines represent the predicted spot crossing amplitude ratios for given spot temperature contrasts. We calculated these temperatures by representing the spots using model stellar atmospheres at various temperatures²². Using χ^2 difference ($\delta\chi^2$) tests, we indirectly detected spot crossings only at 3.6 μm because only these Spitzer observations resulted in positive, bounded photosphere-to-spot temperature contrasts. The 4.5 μm Spitzer observations are consistent with zero, or a non-detection at infrared wavelengths. These measurements, especially the non-detections, imply that the starspots crossed during each transit are too hot to mimic water vapour absorption features in the planetary spectrum^{12,14}. Our starspot analysis is described in Methods along with the distribution of Kepler spot crossing amplitudes, for comparison with those observed concurrently with Spitzer.

The activity of HAT-P-11^{7,11–13} produces variations in the total brightness of the star owing to the rotation of spots in and out of view, which will change the band-integrated transit depth measured at different epochs. If the relative stellar brightness at the epoch of each observation is known, then the transit depths can be corrected to a common

¹Department of Astronomy, University of Maryland, College Park, Maryland 20742-2421, USA. ²Instituto de Astrofísica, Pontificia Universidad Católica de Chile, 7820436 Macul, Santiago, Chile. ³Division of Geological and Planetary Sciences, California Institute of Technology, Pasadena, California 91125, USA. ⁴NASA Astrobiology Institute's Virtual Planetary Laboratory, Seattle, Washington 98195, USA.

⁵Institute of Astronomy, University of Cambridge, Madingley Road, Cambridge CB3 0HA, UK. ⁶Department of Physics, ETH Zürich, 8049 Zürich, Switzerland.

Table 1 | Summary of observations

Date (UT)	Start time	End time	Observatory (instrument)	Band pass (μm)	Spectral resolution	Cadence (s)	Number of observations
7 Jul. 2011	23:11:42	06:37:52	Warm Spitzer (IRAC Channel 1)	3.6	~ 4	0.4	62,592
5 Aug. 2011	07:02:48	14:28:58	Warm Spitzer (IRAC Channel 2)	4.5	~ 4	0.4	58,112
15 Aug. 2011	01:49:20	09:15:30	Warm Spitzer (IRAC Channel 1)	3.6	~ 4	0.4	52,633
29 Aug. 2011	17:37:18	01:03:28	Warm Spitzer (IRAC Channel 2)	4.5	~ 4	0.4	62,592
18 Oct. 2012	17:37:18	01:03:28	Hubble (WFC3 G141)	1.13–1.64	~ 60 –89	123	113
24 Dec. 2012	23:56:56	03:05:58	Hubble (WFC3 G141)	1.13–1.64	~ 60 –89	123	99

We observed HAT-P-11b during four warm Spitzer observations, two transits at both 3.6 and 4.5 μm with the IRAC instrument⁹, and two observations using the Hubble WFC3 G141 grism spectrometer, spanning 1.1–1.7 μm . Concurrent Kepler observations were retrieved for comparison with our warm Spitzer observations, but were unavailable for our Hubble spectroscopic observations.

value. Kepler measured HAT-P-11's relative brightness during all four Spitzer observations, but not during our WFC3 observation. The unknown stellar brightness during this observation introduced an additional uncertainty in our estimate of the WFC3 transit depth, relative to the Spitzer and Kepler observations, of ± 51 p.p.m. In Fig. 2, the offset between the WFC3 spectrum and the best-fit model is ~ 93 p.p.m. on average.

Figure 2 shows our HAT-P-11b transmission spectrum with Kepler, WFC3 and Spitzer transits combined. We constrain the atmospheric composition using the SCARLET tool, which is a new version of the Bayesian retrieval framework described in previous studies^{23,24}. Our primary results are a robust 5.1σ detection of water absorption in the WFC3 data and a 3σ upper limit on HAT-P-11b's atmospheric metallicity (the proportion by mass of elements heavier than hydrogen and helium) of ~ 700 times the solar metallicity⁵, corresponding to a mean molecular weight of ~ 10.2 g mol⁻¹ at the 10 mbar level (Fig. 3). Transmission spectra of selected atmospheric models^{23–26} are plotted for a comparison with the observations in Fig. 2, with colour-matched symbols in Fig. 3. Although the significance of the water vapour detection is unaffected by uncertainties in the stellar activity because all wavelengths in the water band are measured simultaneously, this uncertainty made it prohibitively difficult to place robust constraints on the

methane and carbon dioxide abundances and, therefore, the C/O ratio of HAT-P-11b's atmosphere²⁶.

Figure 3 shows that constraints on the atmospheric metallicity and cloud-top pressure are correlated. Atmospheric compositional scenarios along a curved distribution agree with the data at 3σ , spanning a range of atmospheric metallicities from 1 to 700 times the solar metallicity. Figure 2 shows that a representative 10,000-times-solar (water-dominated) spectrum is robustly excluded by the data. The high mean molecular weight of this atmosphere would not allow the significant water absorption feature observed in the WFC3 band pass.

We found that models with atmospheric metallicities corresponding to solar metallicity require the presence of small-particle hazes to match the HST and Kepler data points simultaneously. The fit to the data improves towards higher metallicities, reaching the best-fit value at 190 times solar metallicity. The presence of the water absorption feature in the WFC3 spectrum requires that any cloud deck must be at an altitude higher than the 10 mbar pressure level (Fig. 3), and the Kepler and Spitzer transit depths impose a similar lower limit on the cloud top pressure.

The atmospheric and bulk compositions of exoplanets provide important clues to their formation and evolution. Mass and radius alone do not provide unique constraints on the bulk compositions of these planets,

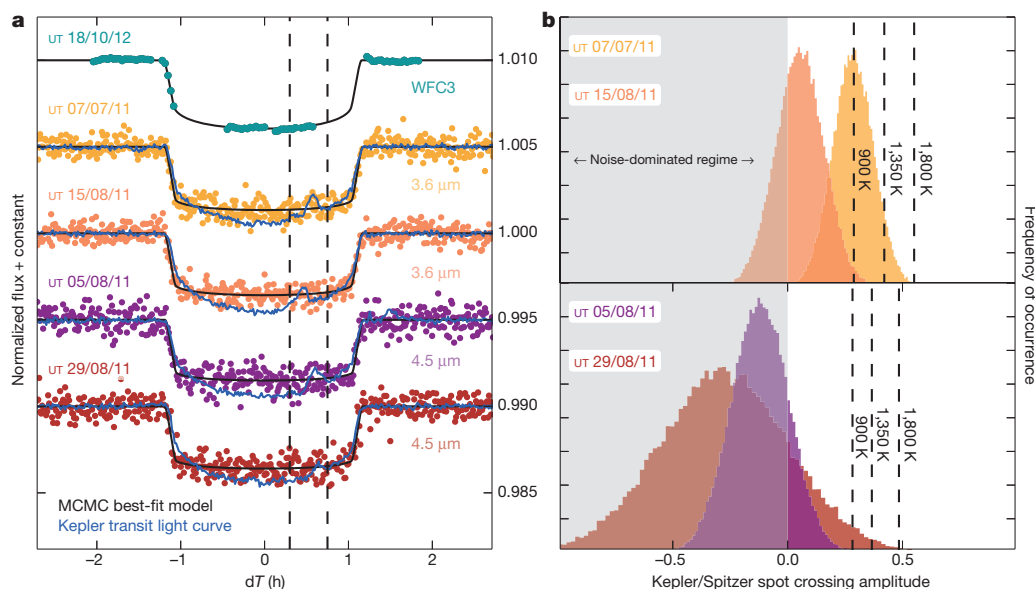


Figure 1 | White-light transit curves and starspot crossing temperature estimates. **a**, Transit curves from the Hubble WFC3 and warm Spitzer, aligned in phase and shifted in flux for clarity. The four warm Spitzer transits at both 3.6 and 4.5 μm (ref. 9) are binned for illustration. Starspot crossings are seen as deviations near +0.5 h in the Kepler photometry (blue). **b**, We estimated the starspot temperatures by dividing the Spitzer transit residuals by the Kepler

transit residuals (colours as in **a**). The dashed lines represent the photosphere-to-starspot temperatures for three stellar model atmospheres²². Water vapour has been detected in sunspots as cool as 3,000 K, corresponding to a contrast of $\sim 1,800$ K here¹⁴. There is essentially no starspot temperature that can produce sufficiently strong water absorption to mimic our result.

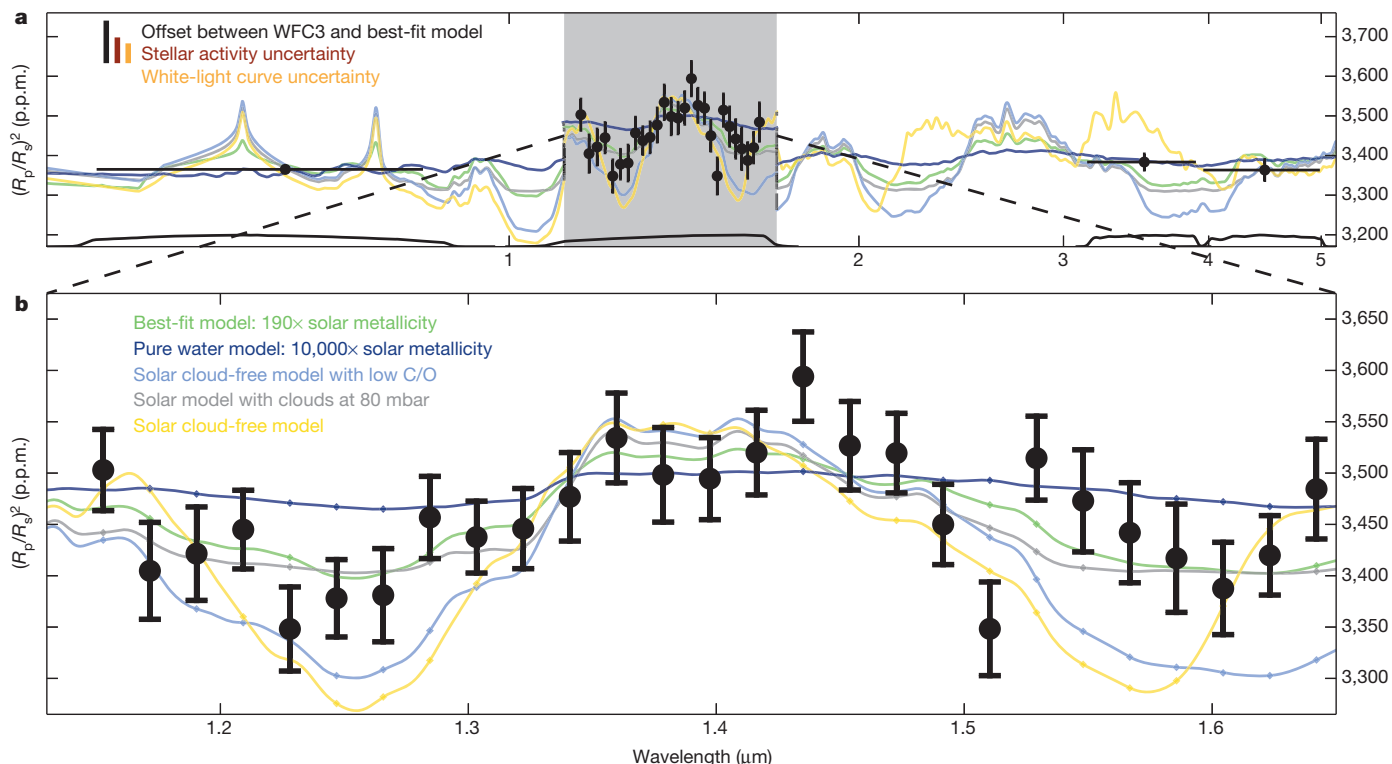


Figure 2 | The transmission spectrum of HAT-P-11b. **a**, Our WFC3 observations show transit depth variations in agreement with a hydrogen-dominated atmosphere. The coloured, solid lines^{23,24} correspond to matching markers displayed in Fig. 3. The error bars represent the standard deviations over the uncertainty distributions. An atmosphere with a high mean molecular

mass (dark blue line) is ruled out by our observations by $>3\sigma$. The WFC3 spectrum was allowed to shift, as a unit, over these uncertainties. R_s , stellar radius. **b**, Detailed view of our WFC3 spectrum. For the purposes of visually comparing the spectral significance, we shifted all of the models by 93 p.p.m. in the grey region in **a** and in **b**.

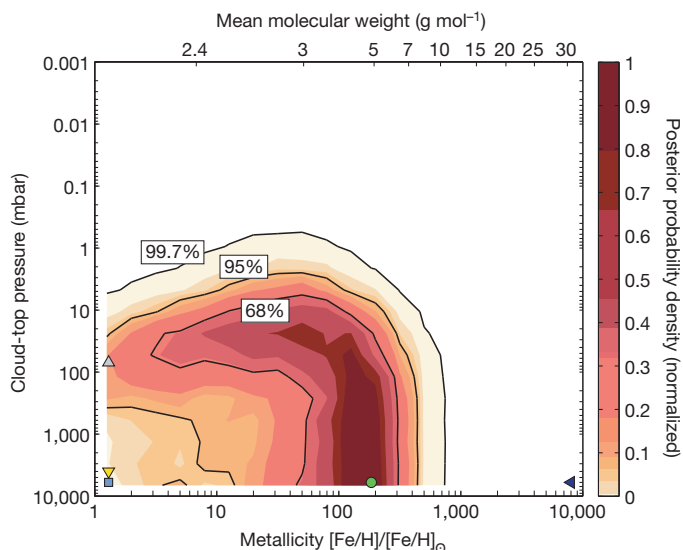


Figure 3 | Spectral retrieval results of our transmission spectrum. The coloured regions indicate the probability density as a function of metallicity (relative to solar) and cloud-top pressure derived using our Bayesian atmospheric retrieval framework^{23,24}. Mean molecular weight was derived for a solar C/O ratio at 10 mbar. Black contours mark the 68%, 95% and 99.7% Bayesian credible regions. The depth of the observed water feature in the WFC3 spectrum required the presence of a large atmospheric scale height that can only be self-consistently obtained for an atmospheric metallicity below 700 times solar at 3σ (99.7%) confidence. The atmosphere is probably predominately cloud-free at least down to the 1 mbar level. We indicate the matching models plotted in Fig. 2 with coloured markers.

which are degenerate for various combinations of rock, ice and hydrogen gas²⁷. By measuring the mean molecular weight of the atmosphere using transmission spectroscopy, we can resolve these degeneracies and provide stronger constraints on the interior compositions of these planets^{5,24,27,28}. Observations of water vapour dominate the shape of the infrared spectral features for warm (planetary temperature, $T_p \approx 1,000$ K) exoplanets. In contrast, the featureless transmission spectra observed for several similarly small planets^{1-4,16} ($R_p \approx 3R_{\oplus}$ – $4R_{\oplus}$) imply that scattering hazes, clouds or high mean molecular weights exist in those atmospheres, obscuring absorption features^{5,23,24} and limiting our ability to understand their interiors directly^{5,24,27}. HAT-P-11b is the smallest and coldest planet with an absorption signature measured by transmission; this allows the estimation of its atmosphere's mean molecular weight, providing new insights into the formation history of this Neptune-mass planet^{5,24,27-30}.

Online Content Methods, along with any additional Extended Data display items and Source Data, are available in the online version of the paper; references unique to these sections appear only in the online paper.

Received 4 April; accepted 7 August 2014.

1. Knutson, H. *et al.* A featureless transmission spectrum for the Neptune-mass exoplanet GJ 436b. *Nature* **505**, 66–68 (2014).
2. Kreidberg, L. *et al.* Clouds in the atmosphere of the super-Earth exoplanet GJ 1214b. *Nature* **505**, 69–72 (2014).
3. Knutson, H. *et al.* Hubble Space Telescope near-IR transmission spectroscopy of the super-Earth HD 97658b. Preprint at <http://arxiv.org/abs/1403.4602> (2014).
4. Ehrenreich, D. *et al.* Near-infrared transmission spectrum of the warm-Uranus GJ 3470b with the Wide Field Camera-3 on the Hubble Space Telescope. Preprint at <http://arxiv.org/abs/1405.1056v3> (2014).
5. Moses, J. *et al.* Compositional diversity in the atmospheres of hot Neptunes, with application to GJ 436b. *Astrophys. J.* **777**, 34 (2013).
6. D'Angelo, G., Durisen, R. H. & Lissauer, J. J. in *Exoplanets* (ed. Seager, S.) 319–346 (Univ. Arizona Press, 2010).

7. Bakos, G. *et al.* HAT-P-11b: a super-Neptune planet transiting a bright K star in the Kepler field. *Astrophys. J.* **710**, 1724–1745 (2010).
8. Deming, D. *et al.* Infrared transmission spectroscopy of the exoplanets HD 209458b and XO-1b using the Wide Field Camera-3 on the Hubble Space Telescope. *Astrophys. J.* **774**, 95 (2013).
9. Fazio, G. *et al.* The Infrared Array Camera (IRAC) for the Spitzer Space Telescope. *Astrophys. J.* **154**, 10 (2004).
10. Borucki, W. *et al.* Kepler Planet-Detection Mission: introduction and first results. *Science* **327**, 977–980 (2010).
11. Knutson, H., Howard, A. & Isaacson, H. A correlation between stellar activity and hot Jupiter emission spectra. *Astrophys. J.* **720**, 1569–1576 (2010).
12. Deming, D. *et al.* Kepler and ground-based transits of the exo-Neptune HAT-P-11b. *Astrophys. J.* **740**, 33 (2011).
13. Sanchis-Ojeda, R. & Winn, J. Starspots, spin-orbit misalignment, and active latitudes in the HAT-P-11 exoplanetary system. *Astrophys. J.* **743**, 61 (2011).
14. Bernath, P. Water in sunspots and stars. *Int. Astron. Union Symp.* **12**, 70 (2002).
15. Berta, Z. *et al.* The GJ1214 super-Earth System: stellar variability, new transits, and a search for additional planets. *Astrophys. J.* **736**, 12 (2011).
16. Fraine, J. D. *et al.* Spitzer transits of the super-Earth GJ1214b and implications for its atmosphere. *Astrophys. J.* **765**, 127 (2013).
17. Sing, D. *et al.* Hubble Space Telescope transmission spectroscopy of the exoplanet HD 189733b: high-altitude atmospheric haze in the optical and near-ultraviolet with STIS. *Mon. Not. R. Astron. Soc.* **416**, 1443–1455 (2011).
18. Patil, A., Huard, D. & Fonnesbeck, C. PyMC: Bayesian stochastic modelling in Python. *J. Stat. Softw.* **35**, 4–85 (2010).
19. Ford, E. Quantifying the uncertainty in the orbits of extrasolar planets. *Astron. J.* **129**, 1706–1717 (2005).
20. Ford, E. Improving the efficiency of Markov chain Monte Carlo for analyzing the orbits of extrasolar planets. *Astrophys. J.* **642**, 505–522 (2006).
21. Castelli, F. & Kurucz, R. New grids of ATLAS9 model atmospheres. Preprint at <http://arxiv.org/abs/astro-ph/0405087> (2004).
22. Husser, T.-O. *et al.* A new extensive library of PHOENIX stellar atmospheres and synthetic spectra. *Astron. Astrophys.* **553**, A6 (2013).
23. Benneke, B. & Seager, S. Atmospheric retrieval for super-Earths: uniquely constraining the atmospheric composition with transmission spectroscopy. *Astrophys. J.* **753**, 100 (2012).
24. Benneke, B. & Seager, S. How to distinguish between cloudy mini-Neptunes and water/volatile-dominated super-Earths. *Astrophys. J.* **778**, 153 (2013).
25. Madhusudhan, N. *et al.* A high C/O ratio and weak thermal inversion in the atmosphere of exoplanet WASP-12b. *Nature* **469**, 64–67 (2011).
26. Madhusudhan, N. C/O ratio as a dimension for characterizing exoplanetary atmospheres. *Astrophys. J.* **758**, 36 (2012).
27. Rogers, L. & Seager, S. A framework for quantifying the degeneracies of exoplanet interior compositions. *Astrophys. J.* **712**, 974–991 (2010).
28. Fortney, J. *et al.* A framework for characterizing the atmospheres of low-mass low-density transiting planets. *Astrophys. J.* **775**, 80 (2013).
29. Chiang, E. & Laughlin, G. The minimum-mass extrasolar nebula: in situ formation of close-in super-Earths. *Mon. Not. R. Astron. Soc.* **431**, 3444–3455 (2013).
30. Hu, R. & Seager, S. Photochemistry in terrestrial exoplanet atmospheres. III. Photochemistry and thermochemistry in thick atmospheres on super Earths and mini Neptunes. *Astrophys. J.* **784**, 63 (2014).

Acknowledgements J.F., A.J. and N.E. acknowledge support from project IC120009 ‘Millennium Institute of Astrophysics (MAS)’ of the Millennium Science Initiative, Chilean Ministry of Economy; FONDECYT project 1130857; and BASAL CATA PFB-06. N.E. is supported by CONICYT-PCHA/Doctorado Nacional. We thank P. McCullough for his assistance in the planning and execution of our observations. We are grateful to I. Crossfield, L. Kreidberg and E. Agol for providing their open-source, Python code banks on their individual websites. We are also grateful for discussions with M. Line, J. Fortney and J. Moses about the nature of photochemistry and interior structures. We thank the ATLAS and PHOENIX teams for providing stellar models. We also thank the SciPy and NumPy associations for providing extensive and rigorous numerical routines for an assortment of mathematical and computational techniques.

Author Contributions J.F. led the data analysis for this project with contributions from D.D., H.K., N.E., A.J. and A.W. A.W. supplied Hubble spectral fitting routines and interpretations. N.E. and A.J. supplied Python routines for MCMC, wavelet and transit curve analyses specific to transiting exoplanets. D.D., H.K., N.E. and A.J. provided computational equipment and administration. D.D., N.M., H.K. and K.T. successfully applied for and provided data from Hubble. B.B. and N.M. provided atmospheric models and accompanying fits. B.B. performed atmospheric retrieval analysis and provided figures and interpretations. N.E. supplied stellar limb-darkening coefficients calculated from both ATLAS and PHOENIX models.

Author Information Reprints and permissions information is available at www.nature.com/reprints. The authors declare no competing financial interests. Readers are welcome to comment on the online version of the paper. Correspondence and requests for materials should be addressed to J.F. (jfraine@astro.umd.edu).

Placing an upper limit on cryptic marine sulphur cycling

D. T. Johnston¹, B. C. Gill², A. Masterson¹, E. Beirne¹, K. L. Casciotti³, A. N. Knapp⁴ & W. Berelson⁵

A quantitative understanding of sources and sinks of fixed nitrogen in low-oxygen waters is required to explain the role of oxygen-minimum zones (OMZs) in controlling the fixed nitrogen inventory of the global ocean. Apparent imbalances in geochemical nitrogen budgets¹ have spurred numerous studies to measure the contributions of heterotrophic and autotrophic N₂-producing metabolisms (denitrification and anaerobic ammonia oxidation, respectively)^{2,3}. Recently, 'cryptic' sulphur cycling was proposed as a partial solution to the fundamental biogeochemical problem of closing marine fixed-nitrogen budgets in intensely oxygen-deficient regions⁴. The degree to which the cryptic sulphur cycle can fuel a loss of fixed nitrogen in the modern ocean requires the quantification of sulphur recycling in OMZ settings. Here we provide a new constraint for OMZ sulphate reduction based on isotopic profiles of oxygen (¹⁸O/¹⁶O) and sulphur (³³S/³²S, ³⁴S/³²S) in seawater sulphate through oxygenated open-ocean and OMZ-bearing water columns. When coupled with observations and models of sulphate isotope dynamics and data-constrained model estimates of OMZ water-mass residence time, we find that previous estimates for sulphur-driven remineralization and loss of fixed nitrogen from the oceans are near the upper limit for what is possible given *in situ* sulphate isotope data.

The ocean's budget of fixed nitrogen (primarily nitrate [NO₃⁻], nitrite [NO₂⁻] and ammonium [NH₄⁺]) is predominantly controlled by the rates of biological dinitrogen (N₂) fixation and N₂ production by denitrification and anaerobic ammonia oxidation (anammox). Rates of anammox (converting NH₄⁺ and NO₂⁻ to N₂) arguably compete with denitrification (reducing NO₃⁻ to N₂) for the NO₂⁻ used in N₂ production^{2,3}, although the flux of NH₄⁺ supplied from the remineralization of organic matter by denitrification is in areas insufficient to fuel anammox². The role of the sulphur cycle was championed as a partial solution to the fundamental biogeochemical problem of closing marine fixed-nitrogen budgets in intensely oxygen-deficient regions, such as the Chilean OMZ⁴. The proposed involvement of sulphur cycling was aptly termed 'cryptic' for two reasons: first, the oxygen-deficient waters off the Chilean coast are devoid of free sulphide, H₂S—the terminal metabolic product of sulphate (SO₄²⁻) reduction—and, second, thermodynamic calculations favour respiration with oxidants such as NO₃⁻ over that of sulphate reduction. Evidence for cryptic sulphur cycling has come from microbial community analyses and shipboard incubations. Community-level pyrosequencing of DNA from waters within the Chilean OMZ indicated the presence of core sulphate reduction and sulphide oxidation genes⁴. In addition, an array of sulphide-amended shipboard incubations demonstrated active sulphate reduction and sulphide oxidation in waters retrieved from the OMZ. Shipboard incubation experiments are a classic method of evaluating metabolic rates, and they underpin constraints on the nitrogen cycle as well^{2,3}. However, in nitrogen cycling, the rates measured by shipboard incubations have been substantiated by geochemical measurements and modelling⁵. The corrected sulphate reduction rates derived from *ex situ* incubation experiments (after accounting for sulphide oxidation) suggested that the cryptic sulphur cycle is responsible

for up to ~30% of the carbon remineralization within the Chilean OMZ and is therefore a substantial new source of NH₄⁺ for anammox. If correct, these rates would be globally significant for marine elemental budgets.

The impact of sulphur cycling can be directly tested through evaluating the stable isotope systematics of seawater sulphate. The O and S isotopic compositions of SO₄²⁻ are time-integrated recorders of biogeochemical processing. These isotope records preserve complementary, yet unique, information. Sulphate S isotopes primarily preserve the metabolic fingerprint of dissimilatory sulphate reduction, which commonly occurs in marine sediments and where the metabolite sulphide is depleted in heavy isotopes, leaving the residual sulphate enriched⁶. Further, the examination of ³³S provides additional leverage on biogeochemical activity, permitting differentiation between contributions from oxidative and reductive metabolisms⁷. Conversely, sulphate O isotopes are primarily controlled by equilibration between water and a redox intermediate, sulphite⁸. Sulphite has a central role in oxidation reactions but is also a requisite intermediate in reductive reactions. Microbial cycling therefore results in the enrichment of ¹⁸O in residual sulphate (that is, seawater sulphate). This O-isotope enrichment accompanies cycling even in the absence of net sulphate reduction (that is, intracellular recycling). Thus, the potential exists for a cryptic sulphur cycle to be recorded in the oxygen isotopic composition of sulphate within OMZs.

To investigate the significance of sulphur cycling in OMZs, we provide an isotopic characterization of modern seawater sulphate ($\delta^{18}\text{O}_{\text{sulphate}}$, $\delta^{34}\text{S}_{\text{sulphate}}$ and $\Delta^{33}\text{S}_{\text{sulphate}}$, where $\Delta^{33}\text{S} = \delta^{33}\text{S}_{\text{meas}} - 1,000((1 + \delta^{34}\text{S}_{\text{meas}}/1000)^{0.515} - 1)$ and $\delta^{33}\text{S}_{\text{meas}}$ is a measured value; Fig. 1). An accumulation of work dating back half a century (standardized herein) provides a context for evaluating these signals. Here we conducted a new, comprehensive characterization of S and O isotopes, including ³³S, in seawater sulphate from nearly 200 samples collected from ten different water-column profiles in the modern ocean. Taken together, we establish a strongly constrained average composition for seawater sulphate: $\delta^{18}\text{O}_{\text{sulphate}} = +8.67\text{‰} (\pm 0.21, 1\sigma)$, $\delta^{34}\text{S}_{\text{sulphate}} = +21.15\text{‰} (\pm 0.15, 1\sigma)$, and $\Delta^{33}\text{S}_{\text{sulphate}} = +0.048 (\pm 0.006, 1\sigma)$. These samples range in dissolved oxygen and oxidized nitrogen concentrations ([NO₃⁻] + [NO₂⁻]) from essentially zero up to 250 and 45 μM , respectively. Two of these water columns (Eastern Tropical South Pacific (ETSP) stations 11 and 25) intersect regions experiencing significant oxygen depletion (as evident through the accumulation of nitrite, expression of a N deficit, and elevated $\delta^{15}\text{N}_{\text{NO}_3}$ values; Extended Data Fig. 3).

Studies of the marine sulphur cycle illustrate the long residence time and slow turnover of S and O in sulphate (~10⁷ and 10⁶ years, respectively^{9,10}), especially when placed in the context of much shorter oceanic mixing times (~1,000 years). It is therefore expected that both the S and O compositions of marine sulphate will be well mixed except in regions where biological cycling overcomes water mass circulation and mixing. Statistical analyses of our data show that OMZ samples are isotopically indistinguishable in $\delta^{18}\text{O}_{\text{sulphate}}$, $\delta^{34}\text{S}_{\text{sulphate}}$ and $\Delta^{33}\text{S}_{\text{sulphate}}$ from the global mean composition (95% confidence level; Fig. 1 and Extended Data Fig. 4). This homogeneity remains true whether comparing different depths and

¹Department of Earth and Planetary Sciences, Harvard University, Cambridge, Massachusetts 02138, USA. ²Department of Geosciences, Virginia Tech University, Blacksburg, Virginia 24061, USA.

³Department of Environmental Earth System Science, Stanford University, Stanford, California 94305, USA. ⁴Department of Earth, Ocean and Atmospheric Sciences, Florida State University, Tallahassee, Florida 32306, USA. ⁵Department of Earth Sciences, University of Southern California, Los Angeles, California 90089, USA.

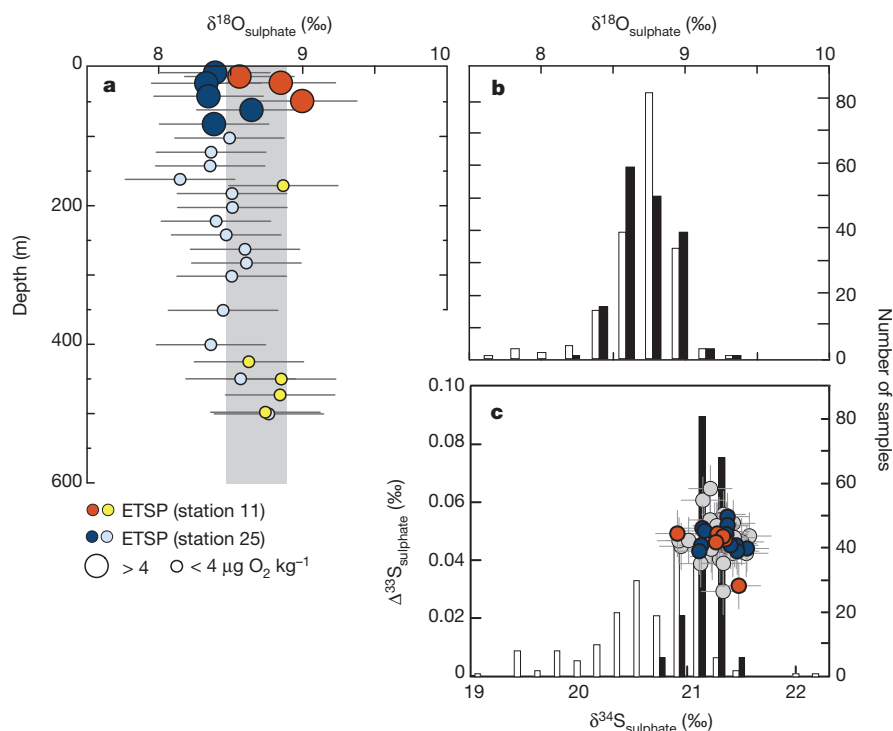


Figure 1 | Establishing the isotopic composition of seawater sulphate.

a, Water-column profiles of $\delta^{18}\text{O}_{\text{sulphate}}$ through two OMZ settings (ETSP stations 11 and 25) as a function of oxygen concentrations. Samples for this study are from the Bermuda Atlantic Time-series Study site, the Sampling and Analysis of Fe (SAFE) site, Eastern Tropical South Pacific stations 5, 6, 11 and 25, GEOTRACES stations 3-SS and 11, Angola upwelling station 18, and tropical South Atlantic station 1. Results are shown as means $\pm 1\sigma$. **b, c**, Histograms of new (black) and published (white) $\delta^{18}\text{O}_{\text{sulphate}}$ data

(b, c) and $\Delta^{33}\text{S}$ values **(c)** for a larger suite of water-column profiles; this study further serves to establish the isotopic composition of seawater sulphate. Colours in **c** are same as in **a** (with grey samples from oxygenated water columns), all included with 1σ errors. Note that published data sets did not sample OMZ environments. The histogram in **c** is from $\text{SO}_2\text{-SO}_2$ -based analyses, whereas data points plotted are from SF_6 -based analyses (this study amends between SO_2 and SF_6 scales).

water masses within a single water-column profile or comparing similar water depths from multiple profiles including OMZ-bearing and well-ventilated water masses.

The lack of a clear $\delta^{18}\text{O}_{\text{sulphate}}$ signal places direct constraints on the significance of a water-column sulphur cycle. A quantitative context derived from microbial (pure and mixed) culture experiments^{11,12} and marine sediments^{13–17} defines the expected isotopic change in $\delta^{18}\text{O}_{\text{sulphate}}$ as sulphate is cycled. Of the two, marine sedimentary pore waters may provide the most closely analogous system to an open-ocean water column and define a range of responses in $\delta^{18}\text{O}_{\text{sulphate}}$ as sulphate is consumed. However, both approaches (culture experiments and pore waters) yield essentially the same result. The reduction and cycling of sulphate always results in an enrichment in $\delta^{18}\text{O}_{\text{sulphate}}$, most often approaching +25‰ (water = 0‰ versus Vienna Standard Mean Ocean Water (VSMOW); Fig. 2). This holds true in the presence and absence of sulphide oxidation reactions^{18,19}. Thus, even in the absence of net sulphate reduction (that is, when reduction equals oxidation—the postulated cryptic sulphur cycle), sulphur cycling by sulphate-reducing bacteria in the water column should drive an increase in $\delta^{18}\text{O}_{\text{sulphate}}$ (ref. 8). This characteristic $\delta^{18}\text{O}_{\text{sulphate}}$ response has been documented in nearly 200 pore-water measurements in which both O isotopes and sulphate concentrations are available. In environments where sulphate reduction rates are low, such as those expected in the water column of an OMZ and commonly preserved in sediment pore waters, a strong nonlinear increase in $\delta^{18}\text{O}_{\text{sulphate}}$ accompanies sulphate consumption²⁰. The best example of this behaviour is from diatomaceous sediments underlying the Angola–Benguela current (Fig. 2)¹⁵. Conversely, an almost linear increase in $\delta^{18}\text{O}_{\text{sulphate}}$ is associated with relatively high sulphate reduction rates, such as those captured in organic-rich sediments from the Gulf of Mexico (Fig. 2)¹³. In this study we present these data as end-member responses and explore a variety of different forms of the fit (such as exponential, power and

Michaelis–Menten) between $\delta^{18}\text{O}_{\text{sulphate}}$ and sulphate concentrations for the different sulphate reduction rates. We conservatively choose a simple one-phase decay model (least-squares ordinary fit) to describe the data.

We posit that quantifying the $\delta^{18}\text{O}_{\text{sulphate}}$ response to sulphate reduction permits the development of an *in situ* prediction for the integrated consequences of cryptic sulphur cycling. This prediction is a function of the vigour with which sulphate is processed, and if one considers that any parcel of water has a finite residence time within the OMZ (τ , in days), this ‘vigour’ can be translated to a rate of sulphate reduction. Here we perform a set of simple calculations based on two features: first, the expected $\delta^{18}\text{O}_{\text{sulphate}}$ response (in per mille) to sulphate consumption (in millimolar; Fig. 2), and second, the published residence times of water in the ETSP OMZ relative to mixing and advection (1–10 years^{21,22}). The sharpness of this approach is primarily then limited by the precision of the isotopic measurement and estimates of τ . Because no significant change in $\delta^{18}\text{O}_{\text{sulphate}}$ was observed in the OMZ relative to well-ventilated water masses, we ask the question: how large an isotopic excursion in $\delta^{18}\text{O}_{\text{sulphate}}$ could have been produced while remaining statistically unresolvable, and what rate of sulphate reduction does that correspond to? The capacity to identify a $\delta^{18}\text{O}_{\text{sulphate}}$ anomaly will be related to the average analytical uncertainty for any single measurement (better than 0.2‰) and the sample density (n) through the interval of interest. Further, each water column carries a unique mean, a normally distributed variance (of $\sim 0.13\text{‰}$ (1σ)), and a standard error of $\sim 0.03\text{‰}$ (Extended Data Fig. 4). Because we are interested in an intra-water-column $\delta^{18}\text{O}_{\text{sulphate}}$ signal, we assign a value of 0.13‰ to the resolvable $\delta^{18}\text{O}_{\text{sulphate}}$ threshold signal, but note that our conclusions do not qualitatively change with the choice of a slightly larger or smaller value (see the sensitivity test in Extended Data Fig. 5). Given the expected low overall rates of sulphate reduction in a water column and the rarity with which even marine-sediment pore-water

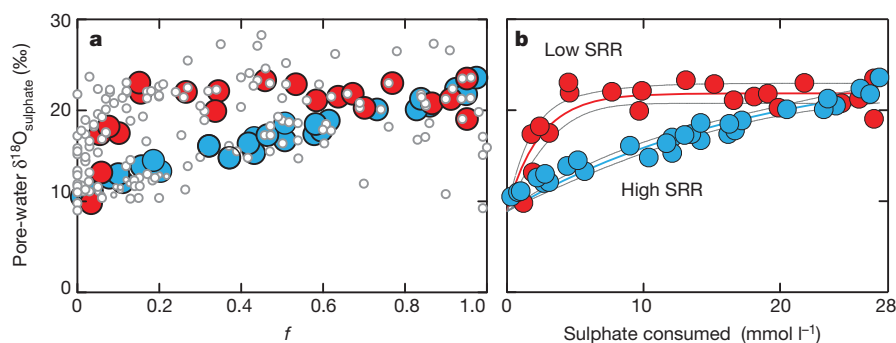


Figure 2 | Pore-water $\delta^{18}\text{O}$ profiles. Two models were developed to quantify the isotopic response of sulphate reduction. They are derived from the compilation of 199 measurements of pore-water sulphate concentration and $\delta^{18}\text{O}_{\text{sulphate}}$ profiles (small white circles in **a**). To normalize the data to various bottom-water sulphate concentrations, we first plot them as a relative fraction of sulphate reduced (f). At the individual pore-water profile level, two types of down-core behaviour are present. A majority of the data show a strong

$\delta^{18}\text{O}_{\text{sulphate}}$ data follow the 'high sulphate reduction rates (SRR)' trajectory, we take the 'low SRR' model from Fig. 2 as a guide (note that using the 'high SRR' model increases predictions of sulphate reduction rates about fivefold). Thus, our prediction for the maximum sulphate reduction rates possible in the ETSP OMZs is between 6.4×10^{-2} and $6.4 \times 10^{-3} \text{ mmol m}^{-3} \text{ d}^{-1}$ at water mass residence times of 1 and 10 years, respectively (Fig. 3). These limits on *in situ* sulphate reduction rates overlap those experimentally extracted from the Chilean upwelling⁴ (Fig. 3).

The cryptic nature of the sulphur cycle—that is, the absence of detectable water-column sulphide—requires that rates of chemoautotrophic sulphide oxidation match those of sulphate reduction in space and time. The putative rates of sulphate reduction in OMZ settings therefore carry important implications for our understanding of OMZ biogeochemistry⁴. For example, the amount of nitrate consumption required to balance a sulphide oxidation rate of $1 \text{ mmol S m}^{-2} \text{ d}^{-1}$ could account for a large fraction of the estimated N loss from the ETSP⁵. If sulphide oxidation were coupled to complete denitrification (NO_3^- to N_2), the oxidation of $1 \text{ mmol S m}^{-2} \text{ d}^{-1}$ would produce a flux of $0.8 \text{ mmol N}_2 \text{ m}^{-2} \text{ d}^{-1}$, or up to $\sim 30\%$ of estimates of total nitrate loss². In parallel, chemoautotrophic sulphide oxidation is indeed prevalent where free sulphide (from sedimentary sources) accumulates within coastal ETSP waters; however, in these settings sulphate reduction is spatially decoupled from the point of subsequent sulphur oxidation. Unlike conditions found in the ETSP

OMZ, the location of chemoautotrophic sulphide oxidation in coastal waters generally occurs at the interface between nitrate-reducing and sulphate-reducing waters^{23,24}. The occurrence of active sulphate reduction in the presence of nitrate and nitrite thus remains an intriguing puzzle. This puzzle may be in fact rectified through further work targeting the role of microenvironments within sinking particulate matter.

Although the predicted $\delta^{18}\text{O}_{\text{sulphate}}$ signal in the ETSP OMZ was at or just below detection with our current approach, the $\delta^{18}\text{O}$ effect predicted here is captured in other saline environments (for instance, Framvaren Fjord²⁵ and Blood Falls, Antarctica²⁶) and serves as an independent geochemical tool with which to track key biogeochemical processes in OMZ settings. Other direct tests, such as those for the N and O isotopes of nitrate and nitrite, provide independent estimates of the relative rates of nitrate and nitrite reduction²⁷ and detail the capacity of the nitrogen cycle to accommodate an oxidative sulphur cycle. If nitrate reduction is largely coupled to sulphide oxidation, then the isotope effect of nitrate reductase in those organisms (note that periplasmic nitrate reductase and respiratory nitrate reductase are present in many sulphur oxidizers and SUP05 (ref. 28)) will dictate the expressed slope of the $\delta^{15}\text{N}_{\text{NO}_3}$ versus $\delta^{18}\text{O}_{\text{NO}_3}$ signal that defines OMZ environments²⁹. Finally, sulphide production in the ETSP OMZ, even if transient, might also be expected to serve as a sink for chalcophile trace elements; however, studies on elements such as cobalt and nickel show nutrient-like behaviour rather than inorganic scavenging³⁰. OMZ environments thus remain a biogeochemical conundrum in terms of closing mass-balance on key nutrient and major element cycles, especially fixed nitrogen. Solving this conundrum remains a critical challenge, given the importance of these settings in the overall chemical budget of the ocean; this is a role that only stands to increase as the climate of our planet warms.

Online Content Methods, along with any additional Extended Data display items and Source Data, are available in the online version of the paper; references unique to these sections appear only in the online paper.

Received 5 November 2013; accepted 16 July 2014.

Published online 7 September 2014.

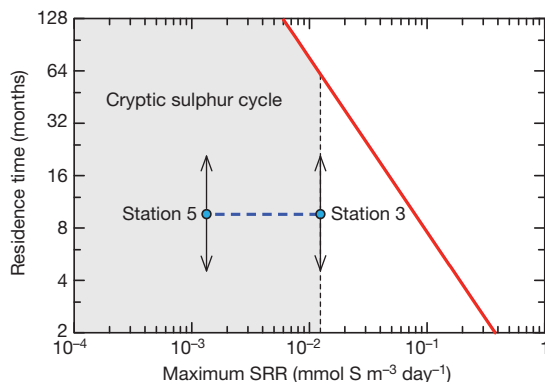


Figure 3 | Model predictions for the maximum allowable rate of sulphate reduction. Predicted SRRs as a function of water mass residence time based on $\delta^{18}\text{O}_{\text{sulphate}}$ constraints. The line represents the minimum detectable SRR for a given τ (using the low-SRR model from Fig. 2), or a maximum possible rate that would not carry a resolvable $\delta^{18}\text{O}_{\text{sulphate}}$ effect. Also included are the rate estimates from shipboard experiments at the Chilean upwelling⁴, stations 3 and 5, without a prescribed residence time.

- Codispoti, L. A. Is the ocean losing nitrate? *Nature* **376**, 724 (1995).
- Lam, P. *et al.* Revising the nitrogen cycle in the Peruvian oxygen minimum zone. *Proc. Natl Acad. Sci. USA* **106**, 4752–4757 (2009).
- Ward, B. B. *et al.* Denitrification as the dominant nitrogen loss process in the Arabian Sea. *Nature* **461**, 78–81 (2009).
- Canfield, D. E. *et al.* A cryptic sulfur cycle in oxygen-minimum-zone waters off the Chilean coast. *Science* **330**, 1375–1378 (2010).
- DeVries, T., Deutsch, C., Rafter, P. A. & Primeau, F. Marine denitrification rates determined from a global 3-D inverse model. *Biogeochemistry* **10**, 2481–2496 (2013).
- Jorgensen, B. B. Theoretical model of the stable isotope distribution in marine sediments. *Geochim. Cosmochim. Acta* **43**, 363–374 (1979).
- Johnston, D. T. Multiple sulfur isotopes and the evolution of Earth's surface sulfur cycle. *Earth Sci. Rev.* **106**, 161–183 (2011).

8. Wankel, S. D., Bradley, A. S., Eldridge, D. L. & Johnston, D. T. Determination and application of the equilibrium oxygen isotope effect between water and sulfite. *Geochim. Cosmochim. Acta* **125**, 694–711 (2014).
9. Turchyn, A. V. & Schrag, D. P. Oxygen isotope constraints on the sulfur cycle over the past 10 million years. *Science* **303**, 2004–2007 (2004).
10. Paytan, A., Kastner, M., Campbell, D. & Thiemens, M. H. Sulfur isotopic composition of Cenozoic seawater sulfate. *Science* **282**, 1459–1462 (1998).
11. Mizutani, Y. & Rafter, T. A. Oxygen isotopic composition of sulphates. 4. Bacterial fractionation of oxygen isotopes in reduction of sulphate and in oxidation of sulphur. *N. Z. J. Sci.* **12**, 60–68 (1969).
12. Fritz, P., Basharmal, G. M., Drimmie, R. J., Ibsen, J. & Qureshi, R. M. Oxygen isotope exchange between sulfate and water during bacterial reduction of sulfate. *Chem. Geol.* **79**, 99–105 (1989).
13. Aharon, P. & Fu, B. S. Microbial sulfate reduction rates and sulfur and oxygen isotope fractionations at oil and gas seeps in deepwater Gulf of Mexico. *Geochim. Cosmochim. Acta* **64**, 233–246 (2000).
14. Aharon, P. & Fu, B. S. Sulfur and oxygen isotopes of coeval sulfate-sulfide in pore fluids of cold seep sediments with sharp redox gradients. *Chem. Geol.* **195**, 201–218 (2003).
15. Turchyn, A. V., Sivan, O. & Schrag, D. P. Oxygen isotopic composition of sulfate in deep sea pore fluid: evidence for rapid sulfur cycling. *Geobiology* **4**, 191–201 (2006).
16. Wortmann, U. G., Bernasconi, S. M. & Bottcher, M. E. Hypersulfidic deep biosphere indicates extreme sulfur isotope fractionation during single-step microbial sulfate reduction. *Geology* **29**, 647–650 (2001).
17. Wortmann, U. G. *et al.* Oxygen isotope biogeochemistry of pore water sulfate in the deep biosphere: dominance of isotope exchange reactions with ambient water during microbial sulfate reduction (ODP Site 1130). *Geochim. Cosmochim. Acta* **71**, 4221–4232 (2007).
18. Farquhar, J., Canfield, D. E., Masterson, A., Bao, H. & Johnston, D. Sulfur and oxygen isotope study of sulfate reduction in experiments with natural populations from Faellestrand, Denmark. *Geochim. Cosmochim. Acta* **72**, 2805–2821 (2008).
19. Mangalo, M., Meckenstock, R. U., Stichler, W. & Einsiedl, F. Stable isotope fractionation during bacterial sulfate reduction is controlled by reoxidation of intermediates. *Geochim. Cosmochim. Acta* **71**, 4161–4171 (2007).
20. Antler, G., Turchyn, A. V., Rennie, V., Herut, B. & Sivan, O. Coupled sulfur and oxygen isotope insight into bacterial sulfate reduction in the natural environment. *Geochim. Cosmochim. Acta* **118**, 98–117 (2013).
21. DeVries, T., Deutsch, C., Primeau, F., Chang, B. & Devol, A. Global rates of water-column denitrification derived from nitrogen gas measurements. *Nature Geosci.* **5**, 547–550 (2012).
22. Kalvelage, T. *et al.* Nitrogen cycling driven by organic matter export in the South Pacific oxygen minimum zone. *Nature Geosci.* **6**, 228–234 (2013).
23. Lavik, G. *et al.* Detoxification of sulphidic African shelf waters by blooming chemolithotrophs. *Nature* **457**, 581–584 (2009).
24. Schunck, H. *et al.* Giant hydrogen sulfide plume in the oxygen minimum zone off Peru supports chemolithoautotrophy. *PLoS ONE* **8**, <http://dx.doi.org/10.1371/journal.pone.0068661> (2013).
25. Mandernack, K. W., Krouse, H. R. & Skei, J. M. A stable sulfur and oxygen isotopic investigation of sulfur cycling in an anoxic marine basin, Framvaren Fjord, Norway. *Chem. Geol.* **195**, 181–200 (2003).
26. Mikucki, J. A. *et al.* A contemporary microbially maintained subglacial ferrous ‘ocean’. *Science* **324**, 397–400 (2009).
27. Casciotti, K. L., Buchwald, C. & McIlvin, M. Implications of nitrate and nitrite isotopic measurements for the mechanisms of nitrogen cycling in the Peru oxygen deficient zone. *Deep Sea Res. Part I Oceanogr. Res. Pap.* **80**, 78–93 (2013).
28. Walsh, D. A. *et al.* Metagenome of a versatile chemolithoautotroph from expanding oceanic dead zones. *Science* **326**, 578–582 (2009).
29. Sigman, D. M. *et al.* Coupled nitrogen and oxygen isotope measurements of nitrate along the eastern North Pacific margin. *Glob. Biogeochem. Cycles* **19**, (2005).
30. Saito, M. A., Moffett, J. W. & DiTullio, G. R. Cobalt and nickel in the Peru upwelling region: a major flux of labile cobalt utilized as a micronutrient. *Glob. Biogeochem. Cycles* **18**, GB4030 (2004).

Acknowledgements We thank the Johnston laboratory, B. Chang, S. Wankel, D. Canfield and J. Granger for discussions and comments; D. Capone and M. Prokopenko for sample collection (all supported by National Science Foundation (NSF) Division of Ocean Sciences); and G. Henderson, W. Homoky and GEOTRACES. Funding was provided by Harvard University (D.T.J., A.M.), the Agouron Institute (D.T.J., B.C.G.) and the NSF EAR-I/F (D.T.J., E.B.) and NSF/OCE grant nos 1140404 (K.L.C.) and 0850905 (A.N.K.).

Author Contributions D.T.J. and B.C.G. developed the project. W.B. and K.L.C. provided samples with the help of W. Homoky and G. Henderson (GEOTRACES). B.C.G., A.M. and E.B. performed the analyses. K.C. and A.N. performed nitrogen measurements with assistance from M. Forbes. D.T.J. and A.M. performed all modelling. All authors contributed to the writing of the manuscript.

Author Information Reprints and permissions information is available at www.nature.com/reprints. The authors declare no competing financial interests. Readers are welcome to comment on the online version of the paper. Correspondence and requests for materials should be addressed to D.T.J. (johnston@eps.harvard.edu).

METHODS

Sample source and handling. The details for each site are provided in Extended Data Table 1. Once seawater samples arrived at Harvard, a concentrated (1 M) BaCl₂ solution was added to water samples to remove the sulphate as BaSO₄. This barite precipitate was then filtered out of the water, briefly acidified (to remove potentially co-precipitated BaCO₃), dried and weighed. The original volume of seawater and the final mass of BaSO₄ precipitate were used to calculate sulphate concentration. Analysis of standards and replicates suggests a 2σ uncertainty of 4% for sulphate concentration estimates, which is 1.12 mM at a seawater concentration of 28 mM.

As the purpose of this work was to evaluate the potential for sulphate reduction, we performed a simple analysis to examine whether a change in sulphate concentrations is present in these data. This would be a signal for net sulphate reduction (second only to the observation of sulphide in the water column). Where metadata were available, we normalized sulphate concentrations to chloride concentrations (Extended Data Fig. 1). On most cruises, practical salinity was reported. We converted these data to an estimate of chloride content in the following manner. The average Cl[−] concentration of the ocean is 19.353 (g/kg), with a Practical Salinity (PSU) of 35.159 (g kg^{−1}). This yielded a ratio of 1.817, which we used to convert PSU measured on the ship back to Cl[−]. We then converted sulphate concentrations to g kg^{−1} to maintain consistency with units. Our average SO₄^{2−} (g kg^{−1})/Cl[−] (g kg^{−1}) was ~0.148. Given the error for sulphate contents, a 1 mM change in sulphate concentration would result in a 0.005 change in the sulphate/chloride ratio (within 2σ of the mean). There was a weak yet significant correlation between sulphate and chloride ($P = 0.0075$), largely controlled by samples from deeper water within ETSP station 6, which carried slightly elevated sulphate/chloride. This suggested a sulphate excess (or freshening), and so was the opposite of that predicted by cryptic sulphur cycling. Without these data included, there was no statistical relationship ($P = 0.8968$).

Isotope methods. Sulphate precipitates (BaSO₄) were subjected to three different isotope measurements, which are described in sequence. Because we are presenting a rigorous calibration of the isotopic composition of seawater, we are explicit and thorough in describing all necessary corrections and calibrations. Normal δ notation is used throughout, with the ³³S data captured by Δ³³S.

Measurement 1. For δ¹⁸O_{sulphate}, we directly loaded barite into silver cups for analysis on a high-temperature conversion elemental analyser mated to a Thermo Scientific Delta V Plus configured in continuous-flow mode. A constant mass of ground glassy carbon was added to each of the samples and standards to promote complete flash pyrolysis. The analyte gas in this case was CO. Given the challenges associated with ionizing CO (often resulting in noisy data or artificially enriched values), we measured each of our samples five times. In association with these samples, we also analysed three different sulphate standards, whose statistics are compiled in Extended Data Table 2a. Values in parentheses are 1σ (standard deviation) errors. The different errors on each standard may reflect the analysis of that particular material and its given crystallinity. This also resulted in a combined weighted error estimate of 0.17‰ and a standard error of 0.01‰ for the 151 standard analyses. For seawater samples, we present the mean value of the five unique analyses on each sample. Thus, the 178 samples represent 890 unique analyses. The mean value derived from these data are 8.67‰, with a 1σ of 0.21‰ (standard error of 0.01‰). Aided by the large number of analyses, the uncertainty on our seawater sulphate sample set is well within that established by our standards. However, each water column demonstrates significantly less variability, with an error of 0.13‰. This number is discussed below in the context of δ¹⁸O_{s.c.}

Measurement 2. For standard sulphur isotope measurements (³⁴S/³²S), we again directly analysed barite powders. We loaded sample plus vanadium pentoxide into tin capsules and analysed these with an Elemental Analyzer mated to a Thermo Scientific Delta V Plus configured in continuous-flow mode. The analyte gas was SO₂ and we simultaneously measured primary SO₂ and secondary SO ion beams. We measured all samples ($n = 180$) presented here in duplicate (360 unique analyses), which resulted in a reproducibility of 0.15‰. Determination of the accuracy (as opposed to precision) of these measurements, and thus the actual δ³⁴S of seawater sulphate, is described below, and was only possible after considering SF₆ measurements.

Measurement 3. In parallel with continuous-flow measurements, we also measured a subset of seawater sulphate samples ($n = 52$) by means of SF₆ on a MAT 253. This approach required numerous additional steps. Barite powders were first reduced to Ag₂S by chemical processing with a 'Thode' solution³¹. Once as sulphide, the sample was introduced into a custom-built fluorination vacuum line, where the headspace was charged with a tenfold excess of F₂ gas. After heating, the product SF₆ was purified by gas chromatography and through a series of cryogenic focusing steps. The SF₆ gas was then introduced into the MAT 253, resulting in analytical precisions (accounting for full reproducibility of wet chemistry, fluorination and mass spectrometry) of 0.28‰ and 0.006‰ for δ³⁴S and Δ³³S, respectively. Our ³³S value is based on a Vienna Cañon Diablo troilite composition of Δ³³S = 0.107‰ versus Cañon Diablo troilite.

Comparing all these data required an evaluation of the standards being used throughout both instrumental methods. Key to this was the following observation: International Atomic Energy Agency (IAEA) standards S1, S2 and S3 are provided as Ag₂S (sulphide), whereas NBS-127, SO-5 and SO-6 are provided as BaSO₄ (sulphate). As sulphates cannot be directly run by SF₆, published values are on different scales. That is, sulphate standards are on a SO₂ scale, whereas sulphide standards are on a SF₆ scale. This distinction is not new to this study; however, the instrumentation in the Johnston laboratory facility permits a direct calibration of this system. We performed this in the following way:

We calibrated the δ³⁴S for the IAEA standards as SF₆. These values (see below) were then used as the calibrated values to correct the measurement of IAEA S1, S2 and S3 as SO₂, effectively placing SO₂ sulphide data on a SF₆ scale. Thus, mean values were the same (see Extended Data Table 2b) and listed with a 1σ error. Next, we chemically reduced the sulphate standards to sulphide, using methods outlined above. This permitted the sulphate standards (measured as sulphides) to be placed on the SF₆ scale. We then calibrated the measurement of sulphate standards run as BaSO₄ by means of SO₂ back to the SF₆ scale. Each sulphate standard was thus measured in three different ways, each of which (post-process) are listed in Extended Data Table 2c. All the 'unknowns' for this study are BaSO₄. Thus, all the standards placed in-run with these samples are the sulphate form of NBS-127, SO-5 and SO-6. All of our data were handled in the same fashion as the standards and are presented on a SF₆ scale. This leads to a composition of seawater sulphate of 21.15‰ (0.15‰, 1σ, $n = 180$) on a δ³⁴S_{Ag₂S-SO₂} scale and 21.35‰ (0.28‰, 1σ, $n = 52$) on a δ³⁴S_{Ag₂S-SF₆} scale. The larger variability in the SF₆ measurements (and possibly the slightly enriched value) is probably a consequence of more complex sample handling. That is, these samples all went through Thode reductions. That process is thought to carry a large fractionation, such that even a small deviation from a perfect chemical yield could induce an effect. Notably, the direct test on the expression of this fractionation yielded no isotopic offset (see above), and the two values are statistically unresolvable at the 1σ level. However, in an effort at full disclosure, we indicate our chemistry as the most variable step.

Nitrate isotopes and nutrients. Samples from station 11 (ETSP 2011) were analysed at sea for [NO₂[−]] and [PO₄^{3−}] using standard methods³², and for [NO₃[−] + NO₂[−]] by chemiluminescence³³. [NO₃[−]] was determined by difference. Frozen samples from station 25 (ETSP 2005) were analysed for [NO₂[−]] and [PO₄^{3−}] by standard methods³². Nitrate isotopes (δ¹⁵N and δ¹⁸O) for both stations were determined with the denitrifier method^{34,35} at Stanford University after treatment with sulphamic acid to remove NO₂[−] (ref. 36). Nitrate isotope analyses were referenced to US Geological Survey 32, 34 and 35 as described previously³⁷. The values for these standards are listed in the next section and are available from IAEA (see Extended Data Table 2d and Extended Data Fig. 3). Station 25 [NO₃[−]] measurements were derived from the $m/z = 44$ peak area from the nitrate isotope analyses, normalized to peak areas of standard reference materials run in 5 and 20 nmol amounts.

Data handling and published values. Here we present a compilation of δ¹⁸O_{sulphate} values from the literature to compare with our seawater sulphate data set^{13–15,25,38–40}. Our data has been set to the VSMOW scale using a recent calibration⁴¹ of the available reference sulphate materials: NBS-127, IAEA SO-5 and IAEA-SO-6. This new calibration was needed because previous calibrations had used materials that were poorly suited for the high-temperature conversion techniques used to analyse δ¹⁸O_{sulphate}. This poor calibration is probably one of the main factors for the poor inter-laboratory comparability of δ¹⁸O_{sulphate} data generated with this technique observed in past studies; other factors include differences in treatment of the BaSO₄ before high-temperature conversion⁴² and the aforementioned challenges associated with ionizing the CO generated from the sample.

To compare the published data directly with our data, the former had to be normalized to account for the new calibration⁴¹. In some cases, the authors reported the values for the sulphate oxygen isotope standards that were used to place their data on the VSMOW scale^{14,25,39}. For these data, normalization of the reported data was straightforward: the published data were simply normalized by using the difference between the reported and newly calibrated δ¹⁸O values of the standards. However, for most of the published data, the methods for the calibration were not given^{38,40,42–44}. The bulk of these data could be brought into line with the distribution of our data and the other normalized published data simply by subtracting the 0.7‰ from the reported isotope values, namely the difference between the previous and new³² δ¹⁸O values of the NBS 127 reference standard: 9.3‰ and 8.59‰, respectively. Data from one source did not receive this normalization; these were distributed about an average δ¹⁸O_{sulphate} of +8.7‰, similar to the mean found in our data. Presumably the calibration used in that study was close to one generated by the recent inter-laboratory calibration⁴¹.

Model construction. The model presented in the text of the paper carries two components: the first is derived from sediment pore-water observations (Fig. 2) and the second is the water-column OMZ model.

Pore-water models. The isotopic composition of sulphate (both O and S) is known to evolve towards enriched values as sulphate is cycled or consumed^{13–15,20,25,45,46}. This is recorded by a range of different behaviours in pore-water sulphate²⁰. One end-member response is a strongly nonlinear change in $\delta^{18}\text{O}$ versus sulphate as sulphate is consumed. This response accompanies low rates of sulphate reduction, much like that predicted for the cryptic sulphur cycle⁴. The other extreme, which describes elevated rates of sulphate reduction, is a shallow and almost linear slope on the same Cartesian plane. As noted, these differing behaviours are postulated to be in response to differential sulphate reduction rates²⁰. To capture the full range of possible responses (what we deem a conservative approach), data were fitted from two end-member systems: Sites 1081 and 1086 from Ocean Drilling Program leg 175 along the west African margin¹⁵ and sediments underlying the Gulf of Mexico¹³. Leg 175 samples are from sediment pore waters where organic rich, largely diatomaceous sediments underlie the Angola–Benguela current. These pore waters capture non-linear behaviour and low sulphate reduction rates. The pore waters from hydrocarbon seeps on the northern Gulf of Mexico continental slope define almost linear behaviour, characteristic of high sulphate reduction rates. See ref. 20 for a treatment of these data²⁰. Nearly all published pore-water $\delta^{18}\text{O}_{\text{sulphate}}$ data fall between these two arrays (Fig. 2). Similarly, experimental data from batch culture experiments (all liquid cultures) largely fit indistinguishably within the bounds set by the pore-water examples noted above. That is, in experiments containing only sulphate-reducing bacteria, the $\delta^{18}\text{O}$ of residual sulphate becomes isotopically enriched as sulphate is consumed. At the microbe scale, this response has been modelled extensively^{20,47–50}.

The pore-water relationship noted above can be quantified. We use a simple least-squares fit to a one-phase decay equation on both data sets, to maintain consistency. As noted in the text, a variety of different fits were considered. A one-phase decay assumes the least about the mechanisms underlying the behaviour (for instance, a Michaelis–Menten relationship, which invokes a particular biochemical response). The full equations and fits for those two exercises are as follows: for high sulphate reduction rates,

$$\delta^{18}\text{O}_{\text{s.c.}} = (8.67\text{‰} - 24.92\text{‰}) \times e^{-0.05926 \times (\text{sulphate consumed})} + 24.92\text{‰} \quad (1)$$

and for low sulphate reduction rates,

$$\delta^{18}\text{O}_{\text{s.c.}} = (8.67\text{‰} - 21.86\text{‰}) \times e^{-0.4224 \times (\text{sulphate consumed})} + 21.86\text{‰} \quad (2)$$

Included here was the adoption of the mean background composition of seawater sulphate as the boundary condition at high sulphate concentrations (8.67‰ above). The other isotopic values listed (24.92‰ and 21.86‰) in these equations are the limits approached as sulphate concentrations approach zero. In essence, they define the response in $\delta^{18}\text{O}_{\text{sulphate}}$ associated with sulphate loss. The only unknown variable in this equation is the ‘sulphate consumed’ term in the exponent. The sulphate consumption term is where we can bridge to a model of the modern ocean water column, as described below.

The same exercise could be performed with sulphur isotopes. However, the intrinsic fractionations are understood to be much more variable⁵¹, and the result is therefore less meaningful. For these reasons, and given the much shorter residence time of oxygen in sulphate and greater likelihood of capturing the cryptic sulphur cycle (as opposed to S), we target oxygen isotopes for the time being.

Choice of $\delta^{18}\text{O}_{\text{s.c.}}$ A critical decision in the quantitative treatment presented in the paper is deciding how large an isotopic excursion in $\delta^{18}\text{O}_{\text{sulphate}}$ is possible without being statistically resolvable. This is represented by the $\delta^{18}\text{O}_{\text{s.c.}}$ term (left-hand side of equations (1) and (2)). In the text, we chose a value of 0.13‰, the average standard deviation (66% confidence) within any single water column (see Extended Data Fig. 4), including those sampling oxygen-deficient waters. This is discussed below, but first, and for context, here we first present the data in rank order, as a function of the median for any given one-dimensional water column and with the error (95% confidence interval) associated with that particular water column (Extended Data Figure 4). At the far right is the total data set, with those outside the 95% confidence interval noted as circles.

The data are colour-coded by ocean basin, with the OMZ sites in open boxes. The sites and their respective intra-water-column median $\delta^{18}\text{O}_{\text{sulphate}}$ and error (95% confidence interval) are presented in Extended Data Figure 4 in the following order (here listed as means and 1 σ): Eastern Tropical South Pacific station 25 (8.46‰, 0.14‰), Angola upwelling station 25 (8.51‰, 0.12‰), the SAFE station (8.54‰, 0.14‰), tropical South Atlantic station 1 (8.57‰, 0.10‰), Bermuda Atlantic Time-series station (8.57‰, 0.13‰), Eastern Tropical South Pacific station 5 (8.76‰, 0.12‰), Eastern Tropical South Pacific station 11 (8.78‰, 0.11‰), South Atlantic—GEOTRACES stations 3-SS (8.80‰, 0.15‰) and 11 (8.93‰, 0.16‰), Eastern Tropical South Pacific station 6 (8.86‰, 0.15‰), and finally a box and whisker of all the data from this study (open circles are those that fall outside the 95% confidence interval). There is no statistically significant variability at the 2 σ or 95% level when evaluating the data set as a whole. The overall mean and standard deviation on the entire global database are 8.67‰ and 0.21‰ (1 σ). Using both a D’Agostino &

Pearson and Shapiro–Wilk normality test, the distribution of data for each water column is normal (except for station 6), as is the entire data set. As is clear from Extended Data Figure 4, each water-column profile carries a unique mean, although the error envelopes all overlap. One consequence of this distribution is that the error for a given water column (represented as a standard deviation) is actually smaller than the entire data set, meaning that some of the variance may later be shown to be real. Improved analytical precisions could prove or disprove this hypothesis. Although this study greatly improved on previously published precisions, that later story remains beyond the scope of this work. However, given this, in the main paper we take a value of 0.13‰ as the chosen level of resolvable variance for any given water column—this is similar to the error associated with any given standard material. As a sensitivity analysis we also calculate the consequences for constraining sulphur cycling if $\delta^{18}\text{O}_{\text{s.c.}}$ is 0.21‰ (1 σ on the whole data set) rather than 0.13‰ (Extended Data Fig. 5). This would be the most conservative approach; however, it does not take full advantage of the statistical leverage provided by increased sampling density. In contrast, our given sampling density for any given water column also allows a standard error of the mean (s.e.m.) to be calculated, which yields a s.e.m. of 0.03‰. This value is approaching the calculated shot noise, or the instrumental limit of machine precision. If we consider the implication of a $\delta^{18}\text{O}_{\text{s.c.}}$ at 0.03‰, this would require shorter residence times to accommodate previous rate estimates (Extended Data Fig. 5). Our choice of 0.13‰ in the main paper is taken from this overall logic.

Translation to OMZ. To translate the quantitative relationship between $\delta^{18}\text{O}_{\text{sulphate}}$ and sulphate consumed (the variables in the pore-water fit presented in Fig. 2 and in equations (1) and (2)) into an OMZ environment, we can introduce a new term. The term ‘sulphate consumed’ is equivalent to a volumetric sulphate reduction rate multiplied by the residence time of sulphate in that water:

$$\text{sulphate consumed (mmol m}^{-3}\text{)} = \text{SRR (mmol m}^{-3}\text{d}^{-1}\text{)} \times \tau \text{ (days)} \quad (3)$$

The right-hand side of equation (3) is then substituted into equations (1) and (2). The solution can be reorganized to then solve for SRR as a function of residence time (Fig. 3). This requires that $\delta^{18}\text{O}_{\text{s.c.}}$ be assigned (see above). To constrain residence times for OMZ water masses, we compiled published estimates for lateral transport of water through the OMZ (below) and built a simplistic one-dimensional water-column model (also outlined below) having the same range of residence times. Published residence times for the ETSP range from 3 to 12 months^{52,53}, with most dating back to work by Codispoti in the 1980s. More recent estimates based on either chlorofluorocarbons or biogeochemical modelling (N deficits) suggest a range from 1 to 10 years for the residence times in ETSP waters^{51,22}. (A single estimate for the Arabian Sea upwelling suggests that the residence times may be much longer (greater than 10 years)⁵⁴, and thus would be more likely to preserve a $\delta^{18}\text{O}_{\text{sulphate}}$ anomaly.) We use this range as a guide in our interpretation (see Fig. 3) and set the stage for further, more refined, water-column residence time estimates to better constrain possible cryptic sulphur cycle behaviour. Given that the estimates of OMZ water-column sulphate reduction rates are low compared with those observed and measured in marine sediments⁵⁵, we use the ‘low SRR’ model from Fig. 2 as the preferred constraint on the maximum sulphate reduction rate. Using the above listed residence times and previous estimates of reduction rates for the cryptic sulphur cycle from ETSP stations 3 and 5 (ref. 4), we can define the molar quantity of sulphate reduced. Our approach gives a maximum estimate of the integrated rate, whereas the previous shipboard work gave an estimate of the instantaneous rate.

Restricted basins and fjords would offer an opportunity to test our hypothesis. In fact, one study²⁶ of the Framvaren fjord confirmed the presence of a $\delta^{18}\text{O}_{\text{sulphate}}$ excursion when sulphur cycling was present in an anoxic water column. The 5‰ effect started to grow into the residual sulphate pool just beneath the oxic–anoxic interface. This was not cryptic cycling, simply sulphur cycling in the most classic sense. Sulphate reduction rates and water mass residence times were unclear in that fjord, as was the overall sulphur budget; however, that study certainly confirmed that $\delta^{18}\text{O}_{\text{sulphate}}$ signals can be generated and preserved in water-column environments.

Although we present our model results in terms of residence times and a volumetric rate of sulphate reduction, it is most common to provide a depth-integrated microbial rate (mmol m^{−2} d^{−1}). This can be done simply by augmenting our volumetric rates by the length scale over which sulphate reduction may be active. For simplicity and using estimates from the ETSP stations 3 and 5 as a guide, we use generic length scales of 100 m in the one-dimensional upwelling model (Extended Data Fig. 6), representing the thickness of the OMZ (or that portion of the OMZ that hosts sulphate reduction). Pinpointing the exact distribution of sulphate reduction is challenging at this stage for the following reasons. The fact that it is ‘cryptic’ means that it is not expressed in classical geochemical measurements (that is, it is not traceable with sulphide concentration data), nor could it be predicted with thermodynamic calculations (that is, it reportedly occurs in areas containing more energetic electron acceptors). One might assume one of the following: first, that sulphate reduction is evenly distributed throughout the OMZ; second, that it carries a Gaussian distribution throughout the whole region of anoxia; third, that it is strongly

asymmetric towards the older water, which would have had more time to consume competing oxidants; or fourth, that it is very heterogeneous or localized to micro-zones (imagine sulphate reduction at the centre of marine snow). Here we assume that sulphate reduction has a Gaussian distribution within an OMZ 100 m thick. **Other water-column predictions.** One major reason that the cryptic sulphur cycle is putatively important is for its consequences for coupled geochemical cycles, notably C and N (see Extended Data Fig. 7). Although exact predictions are provided in the text, below we provide a model of how the different predictions for OMZ sulphur cycling are manifested in these other element systems (and $\delta^{18}\text{O}$) as a guide for evaluating this model and for carrying this sort of approach forward. To do so, we assume a unidirectional flow path for water through an OMZ. This approach assumes vertical advective fluxes, with the 'oldest' OMZ water occurring at the top of the OMZ. We arbitrarily take a path length (z) of 200 m and allow the residence time to range from 1 to 10 years (ref. 4).

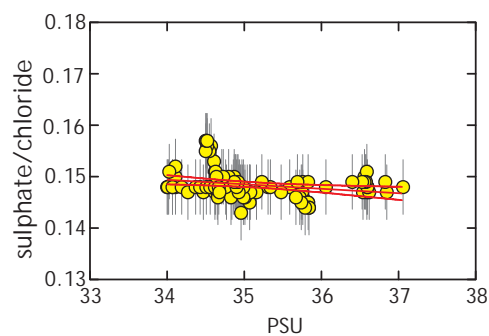
In what follows we provide an example to demonstrate the coupling of element cycles. These are based on the sulphate reduction rate from the reported 'cryptic' sulphur cycle in the Chilean upwelling zone ($1 \text{ mmol m}^{-2} \text{ d}^{-1}$). We can then cast this prediction into isotope space if sulphate reduction is distributed normally. As noted above, this is not the only possible distribution of sulphate reduction; however, this assumption allows us to illustrate some important consequences. Regardless of the distribution, we also present the integrated sulphate reduced (Extended Data Fig. 7) over the entire OMZ—the net sum of this measure is dependent on the average rate and residence time of water in the zone of active sulphate reduction, and is independent of how sulphate reduction is distributed. We also call attention to the observation that no measurable change in sulphate concentrations is noted in our data, with a 2σ tolerance of 1.12 mM, which sets an independent measure of the allowable net sulphate reduction. Together, these first predictions permit the consequences in $\delta^{18}\text{O}_{\text{sulphate}}$ to be estimated as a function of the residence time of the water transiting the OMZ (Extended Data Fig. 5).

Paired with these consequences for the sulphur cycle is the requirement that the nitrogen cycle should accommodate complete sulphide oxidation, so as to circumvent the in-growth of sulphidic waters. That is, for every mole of sulphide generated, that quantity must be oxidized back to sulphate, here by means of nitrate reduction (probably to N_2 ; however, reduction to other intermediates such as NH_4 or NO_2^- is possible). There are well-established chemoautotrophic microbial pathways that set this stoichiometry. Thus, we can cast quantitative predictions for the nitrate budget required to mask the apparent sulphate reduction, with either a 5:8 or a 1:1 sulphur:nitrogen stoichiometry (reduction to N_2 and ammonium, respectively). This is cast as a rate of nitrate consumption (Extended Data Fig. 7). In evaluating these figures, note that the maximum nitrate concentrations observed within our OMZ settings is 45 μM , which essentially sets the maximum amount of sulphide that can be oxidized in any given water parcel. A final consideration, especially as it relates to future geochemical investigations of the OMZ water column, is the net stoichiometry of sulphate reduction and sulphide oxidation. For the two different forms of chemoautotrophy noted above, the reactions essentially mimic those of heterotrophic denitrification and of dissimilatory nitrate reduction to ammonium, respectively⁵⁵.

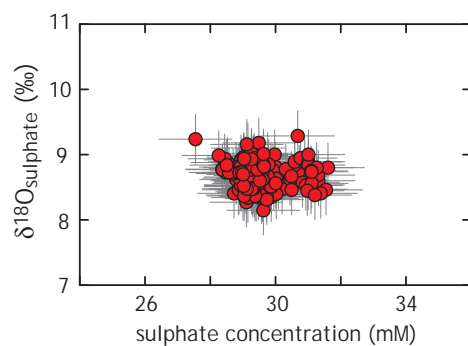
All original data generated for this study are in Source Data files 1 (isotopes) and 2 (nutrients).

31. Forrest, J. & Newman, L. Ag 110 microgram sulfate analysis for short time resolution of ambient levels of sulfur aerosols. *Anal. Chem.* **49**, 1579–1584 (1977).
32. Strickland, J. D. H. & Parsons, T. R. A practical handbook of seawater analysis. *Bull. Fish. Res. Bd Can.* **2**, 1–310 (1972).

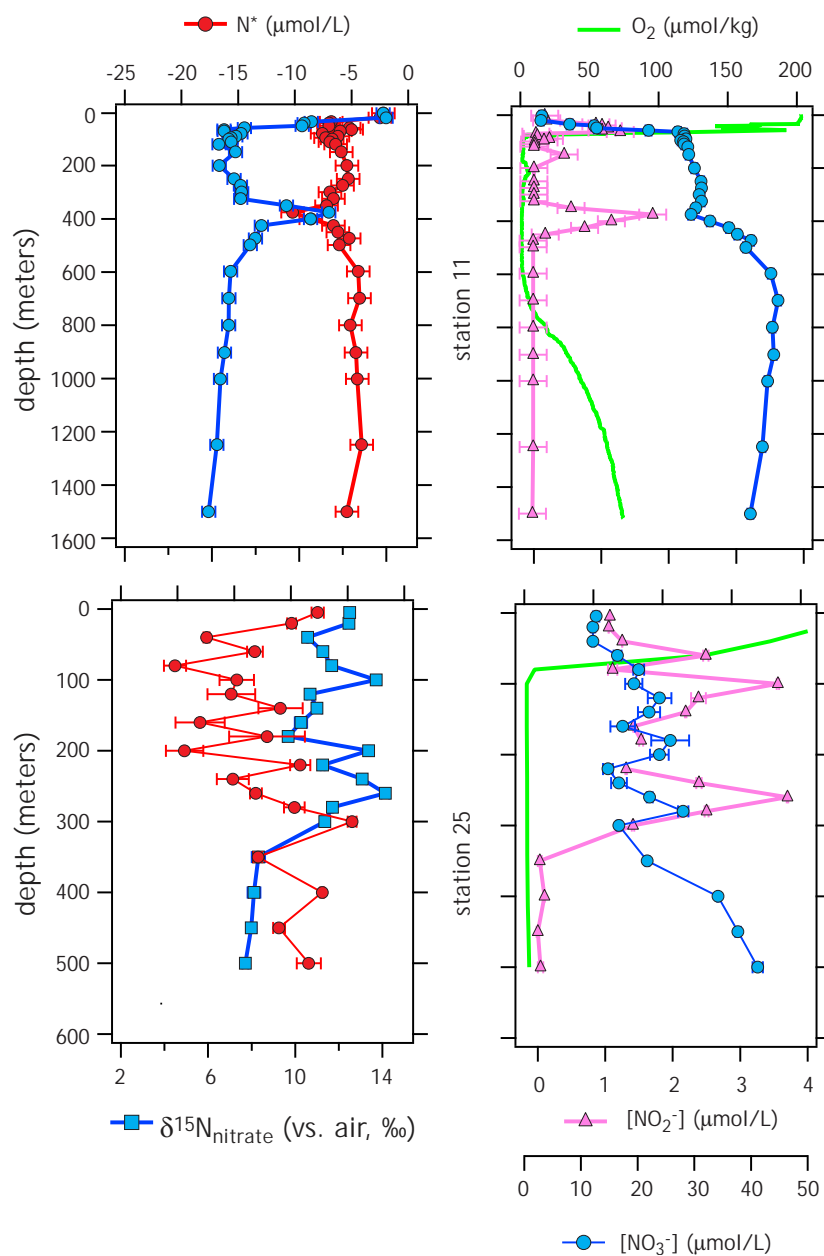
33. Garside, C. A chemi-luminescent technique for the determination of nanomolar concentrations of nitrate and nitrite in sea-water. *Mar. Chem.* **11**, 159–167 (1982).
34. Casciotti, K. L., Sigman, D. M., Hastings, M. G., Bohlke, J. K. & Hilkert, A. Measurement of the oxygen isotopic composition of nitrate in seawater and freshwater using the denitrifier method. *Anal. Chem.* **74**, 4905–4912 (2002).
35. Sigman, D. M. *et al.* A bacterial method for the nitrogen isotopic analysis of nitrate in seawater and freshwater. *Anal. Chem.* **73**, 4145–4153 (2001).
36. Granger, J. & Sigman, D. M. Removal of nitrite with sulfamic acid for nitrate N and O isotope analysis with the denitrifier method. *Rapid Commun. Mass Spectrom.* **23**, 3753–3762 (2009).
37. McIlvin, M. R. & Casciotti, K. L. Technical updates to the bacterial method for nitrate isotopic analyses. *Anal. Chem.* **83**, 1850–1856 (2011).
38. Bottcher, M. E. The stable isotopic geochemistry of the sulfur and carbon cycles in a modern karst environment. *Isotopes Environ. Health Stud.* **35**, 39–61 (1999).
39. Bottcher, M. E., Oelschlager, B., Hopner, T., Brumsack, H. J. & Rullkötter, J. Sulfate reduction related to the early diagenetic degradation of organic matter and 'black spot' formation in tidal sandflats of the German Wadden Sea (southern North Sea): stable isotope (C-13, S-34, O-18) and other geochemical results. *Org. Geochem.* **29**, 1517–1530 (1998).
40. Knoller, M. R. Sulfur cycling and biodegradation in contaminated aquifers: insights from stable isotope investigations. *Environ. Sci. Technol.* **42**, 7807–7812 (2008).
41. Brand, W. A. *et al.* Comprehensive inter-laboratory calibration of reference materials for delta O-18 versus VSMOW using various on-line high-temperature conversion techniques. *Rapid Commun. Mass Spectrom.* **23**, 999–1019 (2009).
42. Ku, T. C. W., Walter, L. M., Coleman, M. L., Blake, R. E. & Martini, A. M. Coupling between sulfur recycling and syndepositional carbonate dissolution: Evidence from oxygen and sulfur isotope composition of pore water sulfate, South Florida Platform, USA. *Geochim. Cosmochim. Acta* **63**, 2529–2546 (1999).
43. Longinelli, A. in *Handbook of Environmental Isotope Geochemistry* Vol. 3 (ed. Fritz, P. & Fontes, J. C.), 219–256 (Elsevier, 1989).
44. Aller, R. C., Madrid, V., Chistoserdov, A., Aller, J. Y. & Heilbrun, C. Unsteady diagenetic processes and sulfur biogeochemistry in tropical deltaic muds: implications for oceanic isotope cycles and the sedimentary record. *Geochim. Cosmochim. Acta* **74**, 4671–4692 (2010).
45. Lloyd, R. M. Oxygen-18 composition of oceanic sulfate. *Science* **156**, 1228–1231 (1967).
46. Longinelli, A. & Craig, H. Oxygen-18 variations in sulfate ions in sea water and saline lakes. *Science* **156**, 56–59 (1967).
47. Cortecci, G., Molcard, R. & Noto, P. Isotopic analysis of deep structure in Tyrrhenian Sea. *Nature* **250**, 134–136 (1974).
48. Zak, I., Sakai, H. & Kaplan, I. R. In *Isotope Marine Chemistry* (eds Goldberg, E. D., Horibe, Y. & Saruhashi, K.) 339–373 (Rokakuho, 1980).
49. Brunner, B., Bernasconi, S. M., Kleikemper, J. & Schroth, M. H. A model for oxygen and sulfur isotope fractionation in sulfate during bacterial sulfate reduction processes. *Geochim. Cosmochim. Acta* **69**, 4773–4785 (2005).
50. Muller, I. A., Brunner, B., Breuer, C., Coleman, M. A. & Bach, W. The oxygen isotope equilibrium fractionation between sulfite species and water. *Geochim. Cosmochim. Acta* **120**, 562–581 (2013).
51. Leavitt, W. D., Bradley, A. S., Halevy, I. & Johnston, D. T. Influence of sulfate reduction rates on the Phanerozoic sulfur isotope record. *Proc. Natl Acad. Sci. USA* **110**, 11244–11249 (2013).
52. Codispoti, L. A. & Christensen, J. P. Nitrification, denitrification and nitrous-oxide cycling in the eastern tropical South-Pacific Ocean. *Mar. Chem.* **16**, 277–300 (1985).
53. Zamora, L. M. *et al.* Nitrous oxide dynamics in low oxygen regions of the Pacific: insights from the MEMENTO database. *Biogeosciences* **9**, 5007–5022 (2012).
54. Olson, D. B., Hitchcock, G. L., Fine, R. A. & Warren, B. A. Maintenance of the low-oxygen layer in the central Arabian Sea. *Deep Sea Res. Part II Top. Stud. Oceanogr.* **40**, 673–685 (1993).
55. Canfield, D. E., Thamdrup, B. & Kristensen, E. *Aquatic Geomicrobiology* 640 (Elsevier, 2005).



Extended Data Figure 1 | Test of whether changes in sulphate concentrations (although small) are related to salinity (here in practical salinity units). A significant but weak correlation exists ($P = 0.0075$): see the text for discussion.

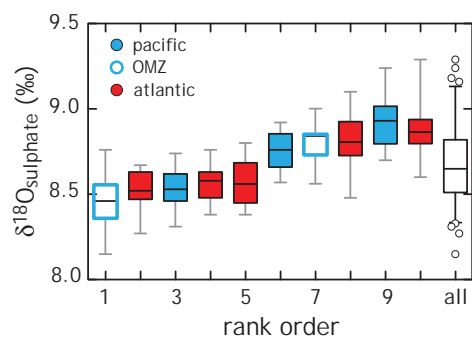


Extended Data Figure 2 | Plot of sulphate concentrations against isotopic composition of sulphate. The lack of a correlation is consistent with no overall heterogeneity in the ocean, especially as a function of sulphate reduction or sulphide oxidation, which would impart the characteristic ^{18}O effect.

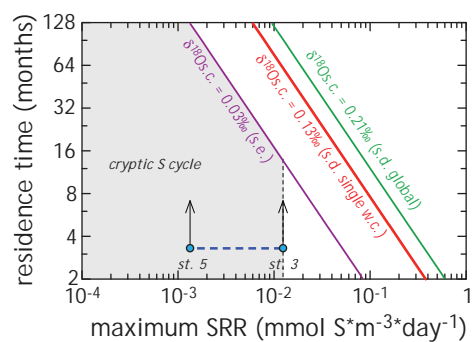


Extended Data Figure 3 | Series of figures demonstrating the severity of oxygen deficiency at stations 11 and 25. This is reflected both in nutrient

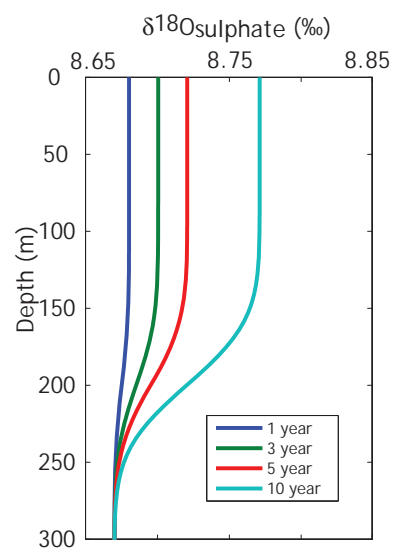
budgets, tracked with N^* , and in isotopes (in $\delta^{15}N$). Data are presented for both stations 11 and 25.



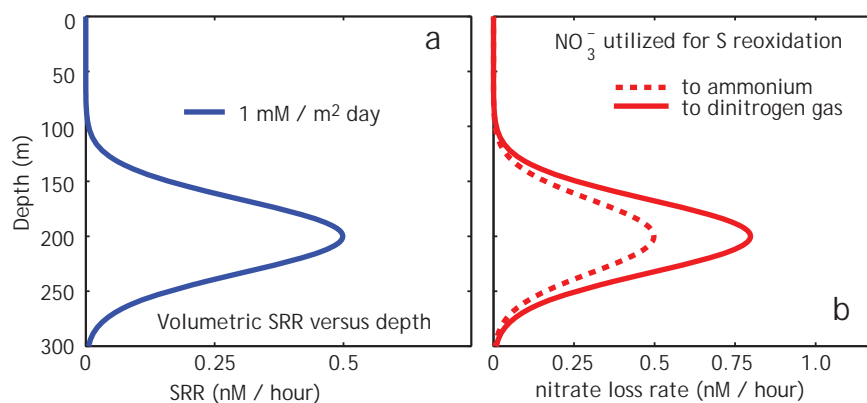
Extended Data Figure 4 | Rank order box-and-whisker presentation of $\delta^{18}\text{O}_{\text{sulphate}}$ data for the ten water columns studied. Data are discussed in the text. At the far right is a representation of all the data. Whiskers are 95% confidence intervals around a given median value (black bars at the centre of the boxes).



Extended Data Figure 5 | Replotting of Fig. 3 with two different choices for $\delta^{18}\text{O}_{\text{s.c.}}$. One estimate is based on s.e.m.; the other is based on the uncertainty over the entire global data set.



Extended Data Figure 6 | Isotopic predictions for sulphate cycling as a function of water mass transit time. The contour key shows various residence times of water within oxygen-deficient waters.



Extended Data Figure 7 | The link between nitrogen and sulphur.

a, Prediction for sulphate reduction rates for a cryptic sulphur cycle containing 1 mmol m⁻² d⁻¹ sulphate reduction. **b**, Prediction for nitrate consumption

rate. All biogeochemistry is arbitrarily distributed over a path length of 200 m. Units were chosen to be directly comparable to those in Table 1 of ref. 4.

Extended Data Table 1 | Site locations

<u>Common Name</u>	<u>Lat, Long</u>	<u>PI</u>	<u>OMZ Bearing</u>
Tropical S. Atl (station 1)	-11°N, 330°E	K.C.	no
Angola upwelling (station18)	-14.75°N, 11.5°E	K.C.	no
ETSP (station 6)	-15°N, 260°E	K.C.	no
ETSP (station 25)	-12.13°N, 281.03°E	K.C.	yes
BATS	31.67°N, 295.83°E	K.C.	no
SAFE	30°N, 220°E	K.C.	no
ETSP (station 11)	-10°N, 277.5°E	A.K.	yes
ETSP (station 5)	-20°N, 280°E	A.K.	no
GEOTRACES st. 3-SS	-36.5°N, 13.1°E	W.H.	no
GEOTRACES st.11	-39.2°N, 7.8°E	W.H.	no

Extended Data Table 2 | Sulphur and oxygen isotope standards

Standard	n	Mean $\delta^{18}\text{O}_{\text{suflate}}$	literature value ³³ (‰, VSMOW)
NBS-127	46	8.66‰ (0.14)	8.59‰ (0.26)
SO-5	47	12.07‰ (0.18)	12.13‰ (0.33)
SO-6	58	-11.36‰ (0.17)	-11.35‰ (0.31)

Flow in bedrock canyons

Jeremy G. Venditti¹, Colin D. Rennie², James Bomhof², Ryan W. Bradley¹, Malcolm Little¹ & Michael Church³

Bedrock erosion in rivers sets the pace of landscape evolution, influences the evolution of orogens and determines the size, shape and relief of mountains^{1,2}. A variety of models link fluid flow and sediment transport processes to bedrock incision in canyons. The model components that represent sediment transport processes are increasingly well developed^{3–5}. In contrast, the model components being used to represent fluid flow are largely untested because there are no observations of the flow structure in bedrock canyons. Here we present a 524-kilometre, continuous centreline, acoustic Doppler current profiler survey of the Fraser Canyon in western Canada, which includes 42 individual bedrock canyons. Our observations of three-dimensional flow structure reveal that, as water enters the canyons, a high-velocity core follows the bed surface, causing a velocity inversion (high velocities near the bed and low velocities at the surface). The plunging water then upwells along the canyon walls, resulting in counter-rotating, along-stream coherent flow structures that diverge near the bed. The resulting flow structure promotes deep scour in the bedrock channel floor and undercutting of the canyon walls. This provides a mechanism for channel widening and ensures that the base of the walls is swept clear of the debris that is often deposited there, keeping the walls nearly vertical. These observations reveal that the flow structure in bedrock canyons is more complex than assumed in the models presently used. Fluid flow models that capture the essence of the three-dimensional flow field, using simple phenomenological rules that are computationally tractable, are required to capture the dynamic coupling between flow, bedrock erosion and solid-Earth dynamics.

The linkages between the uplift of mountains, tectonics and climate are critical for understanding how surface processes affect solid-Earth dynamics and remain one of the primary open questions in Earth science. To understand these linkages we must examine the large-scale drivers of bedrock incision by rivers^{2,6–8}. Large-scale bedrock canyons in actively uplifting terrain link tectonics, climate and topography. Bedrock incision in canyons at the local scale happens through a combination of plucking (removal of blocks of rock from the river bed or banks) and various types of abrasion by sediment particles. Although there is some uncertainty about their relative importance², there are models for abrasion by bedload³, suspended load⁴ and plucking⁵. The flow parameterization most often used in bedrock erosion models is based on stream power^{6,8–12}. Although this approach allows for computationally tractable landscape-scale modelling over long periods and at large scales^{6,8}, flow and sediment transport dynamics are not considered, making the approach of limited value for the prediction of bedrock channel morphology and dynamics. Moreover, the stream power approach masks the fluid processes that drive the sediment movements that cause bedrock erosion. Mechanistic parameterizations of the flow use simplifying assumptions of steady, uniform flow^{13–16} and empirical frictional relations^{17,18}, because full representations of coupled fluid and sediment dynamics are not currently computationally tractable at large scale. More advanced models of boundary shear stress in channel cross-sections have recently been incorporated into bedrock river models that allow modelling of channel shape^{16,19,20}. However, none of these flow models has been tested because there are no field observations of the flow structure in bedrock canyons. Access to these rivers is difficult and

the instrumentation necessary for observations has only relatively recently been adapted from oceanographic research for use in rivers.

To address this gap in our understanding of bedrock rivers, we undertook a 524-km-long continuous centerline acoustic Doppler current profiler (ADCP) survey of the Fraser Canyon, British Columbia, Canada (see Methods). An ADCP provides profiles of three-dimensional velocity measured in Earth coordinates (Easting, Northing, vertical) and bed elevation at discrete intervals. From this we calculate the downstream horizontal velocity magnitude ($U_e^2 + U_n^2$)^{0.5} (where U_e and U_n are the Easting and Northing velocities) and the vertical velocity, which is orthogonal to the horizontal plane. The Fraser Canyon is a geographical region along the Fraser River characterized by a series of 42 individual canyons where the river crosses the Interior Plateau of British Columbia and flows along a fault between the Coast and Cascade mountain ranges (Extended Data Fig. 1). The channel alternates between alluvial and bedrock-bound reaches, the latter of which comprise about 18% of the river length. About 10% of the total length is ‘canyons’—that is, rock-bound, conspicuously narrow reaches. The along-stream profiles of the canyons all show a drop in bed elevation, forming a deeply scoured pool as the channel is constricted (Fig. 1a), with deeper pools formed where the channel constriction is greater. The channel width to mean depth ratios (w/h) of the canyons vary between 2.3 and 17.3 (mean of 6.9; ratios of >20 are common for alluvial channels²¹; in unconfined reaches of Fraser River the average is 52). Canyon width to maximum depth ratios (w/h_{\max}) varied from 1.5 to 10.1 during our surveys (at higher flows, these values will decline because the channel is laterally constricted).

As flow is confined in a canyon, the cross-sectional area decreases and mass-balance dictates that the flow must accelerate. But if canyon floor elevation declines rapidly downstream, increasing the depth, the flow will decelerate. The deceleration should be more pronounced in narrow bedrock canyons where additional drag from the walls may be of the same magnitude as the drag exerted from the channel bed¹⁶. In the widest canyons of the Fraser, flow decelerates uniformly with depth as flow enters the canyons and accelerates as flow exits the canyons. In the narrower canyons, a high-velocity core appears to plunge below the water surface and follow the bed topography down into the pool (Fig. 1a). The high-velocity core dissipates with distance downstream, but with each narrowing of the canyons, the plunging velocity core reappears. The pattern of multiple plunging high-velocity cores observed in Iron Canyon (Fig. 1a) is typical of the narrow bedrock canyons of the Fraser River.

What could cause a plunging high-velocity core? The structure of flow along the centreline is a manifestation of the three-dimensional flow field. Cross-sections through three-dimensional grids of measured spatially distributed velocity fields in the canyons (Fig. 2 and Supplementary Videos 1 and 2; see Methods for details of data processing) show there is a clear velocity inversion (low-velocity fluid at the top of the water column and high-velocity fluid at the bottom; Fig. 1b) that corresponds to negative vertical velocities along the channel centreline. To compensate for this downward flow, upwelling along the canyon walls brings highly turbulent, low-velocity fluid up from near the bed, causing the inversion. Our observations suggest that these upwellings take the form of large and powerful, intermittent coherent flow structures that form boils at the water surface²². These structures represent deviations

¹Department of Geography, Simon Fraser University, Burnaby, British Columbia V5A 1S6, Canada. ²Department of Civil Engineering, University of Ottawa, Ottawa, Ontario K1N 6N5, Canada. ³Department of Geography, The University of British Columbia, Vancouver, British Columbia V6T 1Z2, Canada.

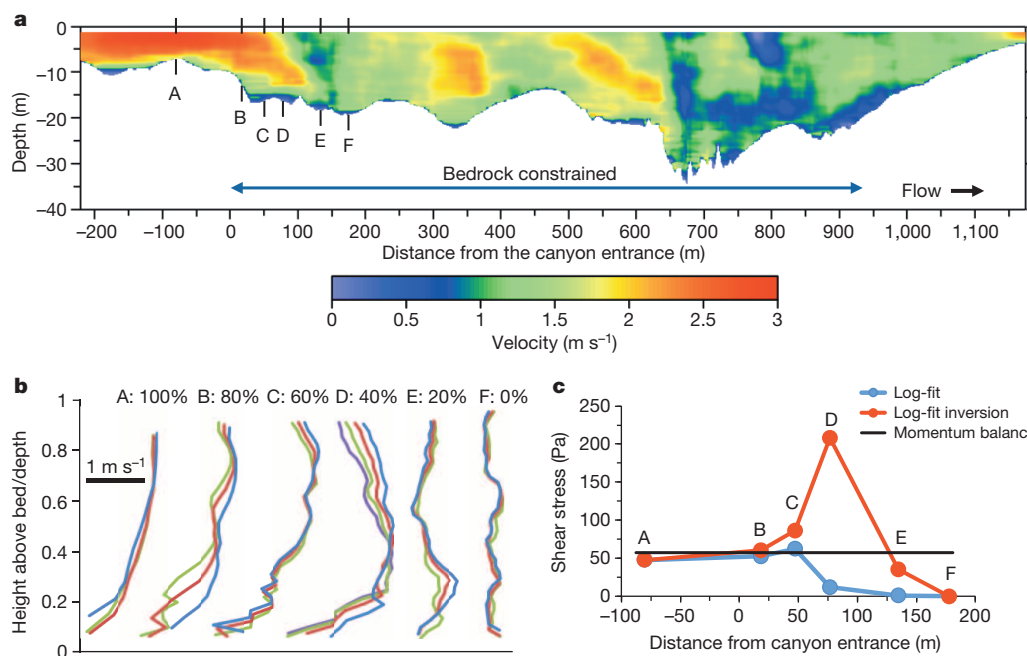


Figure 1 | Centreline transects of flow through a narrow bedrock canyon of the Fraser River. **a**, Primary downstream velocity (colour scale) in Iron Canyon ($w/h = 4.2$, $w/h_{\max} = 1.7$), the second narrowest of the Fraser canyons. Primary downstream velocity is the horizontal velocity magnitude calculated from Easting and Northing velocity components, rotated to minimize the depth-averaged, cross-channel velocity of each profile. **b**, Velocity profiles

along the entrance to the canyon at locations corresponding to the letters A to F in **a**. The approximate height of the velocity inversion is given as a percentage of flow depth. **c**, Shear stresses calculated from reach-averaged momentum balance, velocity profiles through the whole water column (log-fit) and the lower linear portion of the velocity profile below the inversion (log-fit inversion).

from the mean flow, and are advected towards the channel centre, dissipating into the mean flow as the channel expands downstream.

We hypothesize that the observed flow structure is caused by convective deceleration as flow exits the channel constriction and enters the scour hole. Experiments on flow into pools²³ with a morphology similar to our bedrock canyons revealed downward-directed mean velocity as flow expanded into the pool. Furthermore, the same pattern of secondary circulation was observed. This included lateral convergence at the water surface during deceleration in the pool. In pool experiments, downwelling in the centre of the channel and upwelling along the channel walls also occurred, which has been demonstrated to take the form of

intermittent coherent flow structures in similar experiments²⁴. This pattern of secondary flow is typical in narrow channels²⁵ and has been attributed to anisotropy of turbulence at channel boundaries and the free surface. We suspect that a similar process occurs in the bedrock canyons of the Fraser River, whereby upwelling along the channel walls and flow convergence at the surface leads to relatively low-speed, highly turbulent fluid at the water surface in the channel centre downstream of the constriction. The upwelling reduces near-bed dynamic pressure²⁶, which will encourage the higher-speed flow entering the canyons to advect along the floor, and a positive feedback whereby the high-speed fluid near the bed contributes to intense upwelling along the walls. The initiation of this flow structure in a bedrock channel is probably caused by the lateral constriction, forcing a canyon to deepen until it reaches morphodynamic equilibrium with the near-bed flow (and the sediment transport responsible for incision).

We expect the three-dimensional flow processes observed in the canyons of the Fraser River to be applicable to many canyon-bound rivers worldwide. This is because significant changes in channel width, which we argue here drive convective deceleration and flow inversion, are common. This suggests a model of flow in narrow bedrock canyons (Fig. 3) that is very different from what is currently accepted. Velocity inversions and the associated plunging high-velocity cores (Fig. 3a) cause steeper near-bed velocity gradients than would occur if the flow decelerated uniformly into canyons. This would tend to increase vertical incision and formation of scour holes because shear stress, which drives the sediment transport processes responsible for incision, scales as $\tau \propto (du/dz)^2$ (where u is the velocity at height z above the bed).

For example, reach-averaged shear stress in Iron Canyon, calculated from the one-dimensional momentum balance for steady, uniform flow (see Methods), was 115 Pa, roughly half of which is applied to the walls because it is narrow relative to its depth¹⁶. Velocity profiles through the whole water column predict shear stress to increase slightly and then decline moving into Iron Canyon (Fig. 1c), but this also requires steady, uniform flow. On the other hand, using the linear portion of near-bed velocity gradients, below the inversion inflection point, produces the most

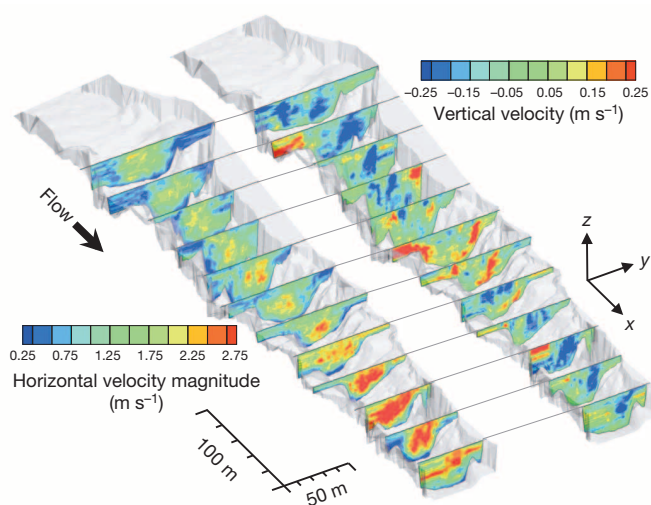


Figure 2 | Cross-sections of horizontal velocity magnitude and vertical velocity in Black Canyon downstream of a constriction. See Supplementary Video 1 of the horizontal velocity magnitude and Supplementary Video 2 of vertical velocity fields through the whole measurement section.

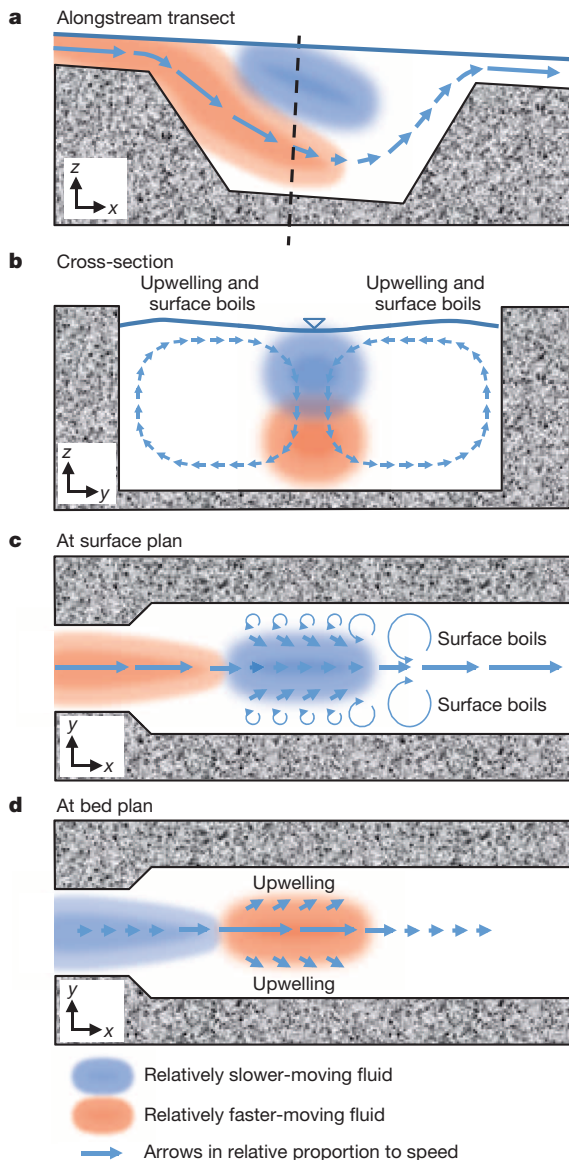


Figure 3 | Conceptual model of flow in a bedrock canyon. **a**, Alongstream section through the flow field showing the apparent plunging velocity core. **b**, Cross-section at dashed line in panel **a** showing velocity inversion and the observed water surface profile caused by flow paths. **c**, Flow pattern at the water surface showing accelerated, then convergent decelerated flow in the alongstream direction and intermittent surface boils produced by large-scale coherent flow structures. **d**, Flow pattern at the bed showing decelerated, then divergent accelerated flow and zones of upwelling, which take the form of large-scale coherent flow structures. x , y and z are the streamwise, cross-stream and vertical velocity directions, respectively. The diagrams are vertically and horizontally exaggerated.

accurate representations of local shear stress (see Methods). This approximation indicates that shear stress was 47 Pa at the canyon entrance, rose to 208 Pa along the entrance slope, and then declined to nearly zero in the bottom of the scour hole where the flow changes from convectively decelerating to accelerating (Fig. 1c).

The larger shear stress along the entrance slope to a canyon would tend to focus erosion there, resulting in an upstream migrating scour hole that resembles a submerged knickpoint. Where the plunging high-velocity core extends beyond the entrance slope, a canyon will deepen until it reaches morphodynamic equilibrium. The counter-rotating secondary flow structure (Fig. 3b) causes decelerated surface flow along a channel centreline (Fig. 3c). The vertical upwelling along canyon walls (Fig. 3b) and divergent flow at the bed (Fig. 3d) can cause centreline ridges along

a canyon floor, which we observed in some of the Fraser canyons. Divergent flow at the bed also provides a mechanism for undercutting canyon walls (as has been observed experimentally^{27,28}). Failure of undercut rock could promote channel widening over long timescales if upstream knickpoint migration occurred over a lesser time frame. The general pattern of fluid motion would also tend to keep the base of canyon walls swept clean of wasted debris, maintaining near-vertical walls.

The observed patterns of flow in the Fraser canyons suggest that modelling canyon morphodynamics and evolution requires more detailed understanding of the flow dynamics that drive sediment transport in canyons. The steep near-bed velocity gradients along plunging velocity cores cause correspondingly higher and lower local shear stresses than would be predicted from reach-averaged shear stress for steady uniform flow, calculated using mean velocity and a flow resistance equation, or log-normal velocity profiles that extend from the bed to the water surface. These locally higher and lower shear stresses may average out over the length of canyons, but the morphology of a canyon and patterns of incision are driven by the spatial variations in the shear stress. Erosion rates tend to scale with bed shear stress to a power greater than unity^{3–5}, so even if local bed shear stresses average out over the length of a canyon, local erosion rates will not average out, leading to larger canyon erosion rates even when averaged over long timescales. Further observations, along with hydrodynamic modelling that captures both the secondary circulation and the dynamics of the upwelling coherent flow structures, are required to determine how best to abstract these insights on the complexity of flow in bedrock canyons over the temporal and spatial scales of drainage basin organization⁸ and orogen development¹.

Online Content Methods, along with any additional Extended Data display items and Source Data, are available in the online version of the paper; references unique to these sections appear only in the online paper.

Received 29 March; accepted 13 August 2014.

- Whipple, K. X. The influence of climate on the tectonic evolution of mountain belts. *Nature Geosci.* **2**, 97–104 (2009).
- Whipple, K. X., DiBiase, R. A. & Crosby, B. T. in *Treatise on Geomorphology* (eds Shroder, J. & Wohl, E.) Vol. 9 *Fluvial Geomorphology* 550–573 (Academic Press, 2013).
- Sklar, L. S. & Dietrich, W. E. A mechanistic model for river incision into bedrock by saltating bed load. *Wat. Resour. Res.* **40**, W06301 (2004).
- Lamb, M. P., Dietrich, W. E. & Sklar, L. S. A model for fluvial bedrock incision by impacting suspended and bed load sediment. *J. Geophys. Res.* **113**, F03025 (2008).
- Chatanantavet, P. & Parker, G. Physically based modeling of bedrock incision by abrasion, plucking, and macroabrasion. *J. Geophys. Res.* **114**, F04018 (2009).
- Ferrier, K. L., Huppert, K. L. & Perron, J. T. Climatic control of bedrock incision. *Nature* **496**, 206–209 (2013).
- Finnegan, N. J., Schum, R. & Finnegan, S. A signature of transience in bedrock river incision rates over timescales of 10^4 – 10^7 years. *Nature* **505**, 391–394 (2014).
- Willett, S. D. et al. Dynamic reorganization of river basins. *Science* **343**, <http://dx.doi.org/10.1126/science.1248765> (2014).
- Howard, A. D. & Kerby, G. Channel changes in badlands. *Geol. Soc. Am. Bull.* **94**, 739–752 (1983).
- Seidl, M. A. & Dietrich, W. E. The problem of channel erosion into bedrock. *Catena* (Suppl.) **23**, 101–124 (1992).
- Howard, A. D., Dietrich, W. E. & Seidl, M. A. Modeling fluvial erosion on regional and continental scales. *J. Geophys. Res.* **99**, 13971–13986 (1994).
- Seidl, M. A., Dietrich, W. E. & Kirchner, J. W. Longitudinal profile development into bedrock: an analysis of Hawaiian channels. *J. Geol.* **102**, 457–474 (1994).
- Stark, C. P. A self-regulating model of bedrock river channel geometry. *Geophys. Res. Lett.* **33**, L04402 (2006).
- Barbour, J. R. et al. Magnitude-frequency distributions of boundary shear stress along a rapidly eroding bedrock river. *Geophys. Res. Lett.* **36**, L04401 (2009).
- Turowski, J. M., Lague, D. & Hovius, N. Response of bedrock channel width to tectonic forcing: insights from a numerical model, theoretical considerations, and comparison with field data. *J. Geophys. Res.* **114**, F03016 (2009).
- DiBiase, R. A. & Whipple, K. X. The influence of erosion thresholds and runoff variability on the relationships among topography, climate, and erosion rate. *J. Geophys. Res.* **116**, F04036 (2011).
- Tucker, G. E. & Hancock, G. R. Modelling landscape evolution. *Earth Surf. Process. Landf.* **35**, 28–50 (2010).
- Howard, A. D. A detachment-limited model of drainage basin evolution. *Wat. Resour. Res.* **30**, 2261–2285 (1994).
- Nelson, P. A. & Seminara, G. Modeling the evolution of bedrock channel shape with erosion from saltating bed load. *Geophys. Res. Lett.* **38**, L17406 (2011).

20. Wobus, C. W., Tucker, G. E. & Anderson, R. S. Self-formed bedrock channels. *Geophys. Res. Lett.* **33**, L18408 (2006).
21. Leopold, L. B., Wolman, M. G. & Miller, J. P. *Fluvial Processes in Geomorphology* (Freeman, 1964).
22. Venditti, J. G. *et al.* (eds) in *Coherent Flow Structures at Earth's Surface* 1–16 (Wiley, 2013).
23. MacVicar, B. J. & Rennie, C. D. Flow and turbulence redistribution in a straight artificial pool. *Wat. Resour. Res.* **48**, W02503 (2012).
24. MacVicar, B. J., Obach, L. & Best, J. L. in *Coherent Flow Structures at Earth's Surface* (eds Venditti, J. G. *et al.*) 243–259 (Wiley, 2013).
25. Nezu, I. & Nakagawa, H. *Turbulence in Open-Channel Flows* 96–110 (A. A. Balkema, 1993).
26. Yang, S.-Q. Velocity distribution and wake-law in gradually decelerating flows. *J. Hydraul. Res.* **47**, 177–184 (2009).
27. Finnegan, N. J., Sklar, L. S. & Fuller, T. K. Interplay of sediment supply, river incision, and channel morphology revealed by the transient evolution of an experimental bedrock channel. *J. Geophys. Res.* **112**, F03S11 (2007).
28. Fuller, T. K. *Field, Experimental and Numerical Investigations into the Mechanisms and Drivers of Lateral Erosion in Bedrock Rivers*. PhD thesis, Univ. Minnesota (2013).

Supplementary Information is available in the online version of the paper.

Acknowledgements This study was supported by Natural Science and Engineering Research Council grants to M.C., J.G.V. and C.D.R. We thank D. Baerg and his crew at Fraser River Raft Expeditions for undertaking the logistics of the river traverse, R. DiBiase for reviewing an early draft of the manuscript, and M. Lin and C. Adderley for assistance with data processing.

Author Contributions M.C. planned and organized the field campaign and provided guidance through the analysis. J.G.V., C.D.R. and M.C. performed the survey and supervised data processing and analysis by J.B., R.W.B. and M.L. J.G.V. analysed the data and wrote the manuscript with input from C.D.R. and M.C.

Author Information Reprints and permissions information is available at www.nature.com/reprints. The authors declare no competing financial interests. Readers are welcome to comment on the online version of the paper. Correspondence and requests for materials should be addressed to J.G.V. (jeremy_venditti@sfu.ca).

Brain structure resolves the segmental affinity of anomalocaridid appendages

Peiyun Cong¹, Xiaoya Ma^{1,2}, Xianguang Hou¹, Gregory D. Edgecombe² & Nicholas J. Strausfeld^{3,4}

Despite being among the most celebrated taxa from Cambrian biotas, anomalocaridids (order Radiodonta) have provoked intense debate about their affinities within the moulting-animal clade that includes Arthropoda. Current alternatives identify anomalocaridids as either stem-group euarthropods^{1–3}, crown-group euarthropods near the ancestry of chelicerates⁴, or a segmented ecdysozoan lineage with convergent similarity to arthropods in appendage construction⁵. Determining unambiguous affinities has been impeded by uncertainties about the segmental affiliation of anomalocaridid frontal appendages. These structures are variably homologized with jointed appendages of the second (deutocerebral) head segment, including antennae and ‘great appendages’ of Cambrian arthropods, or with the paired antenniform frontal appendages of living Onychophora and some Cambrian lobopodians. Here we describe *Lyrarapax unguispinus*, a new anomalocaridid from the early Cambrian Chengjiang biota, southwest China, nearly complete specimens of which preserve traces of muscles, digestive tract and brain. The traces of brain provide the first direct evidence for the segmental composition of the anomalocaridid head and its appendicular organization. Carbon-rich areas in the head resolve paired pre-protocerebral ganglia at the

origin of paired frontal appendages. The ganglia connect to areas indicative of a bilateral pre-oral brain that receives projections from the eyestalk neuropils and compound retina. The dorsal, segmented brain of *L. unguispinus* reinforces an alliance between anomalocaridids and arthropods rather than cycloneuralians. Correspondences in brain organization between anomalocaridids and Onychophora resolve pre-protocerebral ganglia, associated with pre-ocular frontal appendages, as characters of the last common ancestor of euarthropods and onychophorans. A position of Radiodonta on the euarthropod stem-lineage implies the transformation of frontal appendages to another structure in crown-group euarthropods, with gene expression and neuroanatomy providing strong evidence that the paired, pre-oral labrum is the remnant of paired frontal appendages¹.

Arthropoda von Siebold, 1848

Radiodonta Collins, 1996

Amplectobeluidae Vinther *et al.*, 2014

Lyrarapax unguispinus gen. et sp. nov.

Life Science Identifier (LSID). urn:lsid:zoobank.org:act:BFE89E0E-CEB2-406A-B516-FEC5EC5A7C2A

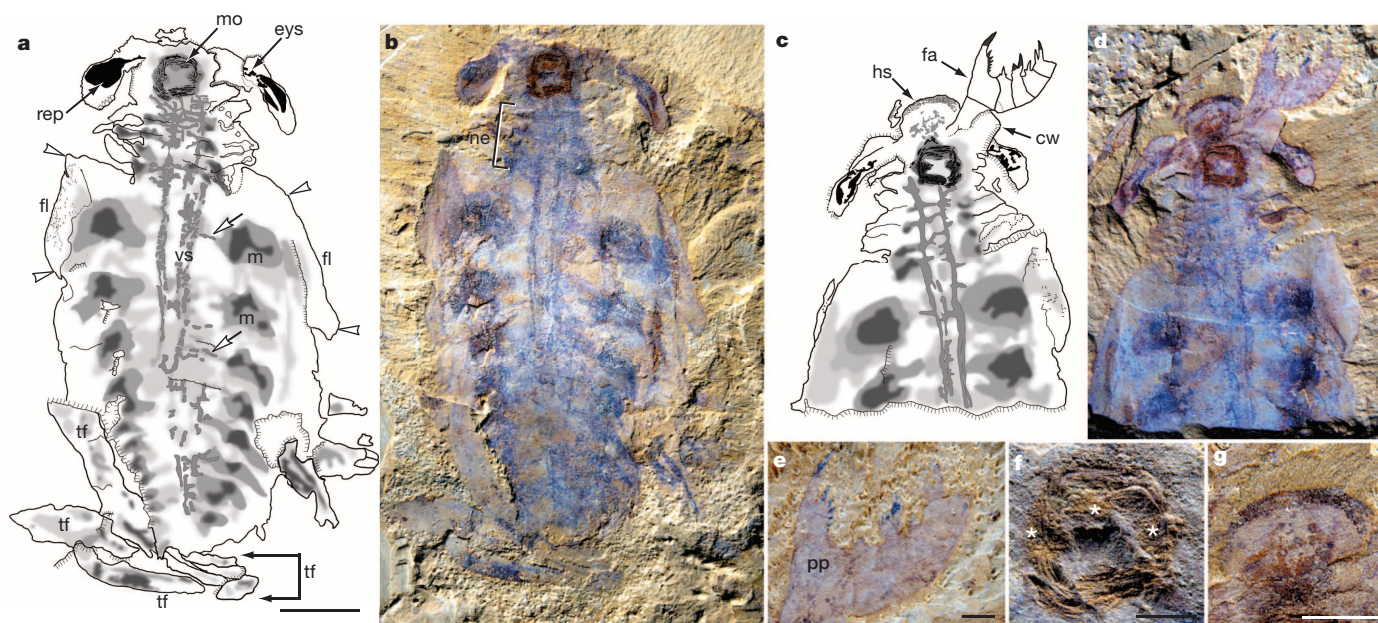


Figure 1 | *L. unguispinus* from the Chengjiang Lagerstätte. **a, b**, Ventral view of YKLP 13304b (counterpart) showing mouth cone (arrowed mo), eye stalks (eyes), retinal pigmentation (rep), four neck segments (ne), traces of putative vascular system (vs) and its branches (open arrows) leading to metamerite muscle blocks (m) aligned with lateral flaps, including oar-like first pair (fl, between arrowheads), and partly overlapping blades of tail fan (tf). **c, d**, Ventral view of YKLP 13304a (part) showing one frontal appendage (fa),

part of the dorsal cowl (cw) and pigmented head shield anterior rim (hs). **e**, Frontal appendage: large proximal podomere (pp) equipped with serial spines allowing apposition against inner teeth of more distal podomeres. **f**, Enlarged oral cone showing concentric ridges and triangular areas (stars) suggestive of denticles. **g**, Pigmented rim of head shield. Scale bars: **a**, also for **b–d**, 5 mm; **e, f**, 1 mm; **g**, 3 mm.

¹Yunnan Key Laboratory for Palaeobiology, Yunnan University, Kunming 650091, China. ²Department of Earth Sciences, The Natural History Museum, Cromwell Road, London SW7 5BD, UK. ³Department of Neuroscience, University of Arizona, Tucson, Arizona 85721, USA. ⁴Center for Insect Science, University of Arizona, Tucson, Arizona 85721, USA.

Etymology. *lyra* (Latin): referring to an overall lyre-like body shape; *rapax* (Latin): predator; *unguis* (Latin): claw; *spinus* (Latin): thorn, alluding to the spinose, claw-like frontal appendages.

Holotype. Holotype YKLP 13304a, b (Fig. 1 and Extended Data Figs 1a and 2a–d), part and counterpart.

Referred material. Paratypes YKLP 13305 (part only, Figs 2 and 3b, c), YKLP 13306 (part and counterpart, Extended Data Fig. 3).

Locality. Ercaicun (YKLP 13304, 13306) and Mafang (YKLP 13305) in Haikou, Yunnan Province, China.

Horizon. Heilinpu Formation, Cambrian Series 2, Stage 3, Yu'an-shan Member (*Eoredlichia*–*Wutingaspis* assemblage zone).

Diagnosis. Small anomalocaridid, body length to 8 cm, with a pronounced, four-segmented neck; frontal appendage short, one proximal podomere

bearing a stout, blade-shaped endite with pectinate, sclerotized spines that gradually become larger distally, the successive podomeres with alternating small and larger endites; body flap of first trunk segment hypertrophied, paddle-shaped, succeeding body flaps narrowing relatively strongly; tail fan composed of three pairs of blades.

L. unguispinus is known from three largely complete specimens (Supplementary Information). It is assigned to Radiodonta based upon the following diagnostic characters⁶: large, club-shaped, compound eyes, having the same relative size, shape and position as in *Anomalocaris canadensis*⁷; frontal appendages, the only appendages in the head or trunk, arthropodized and bearing serially repeated ventral spines on each podomere (Fig. 1e and Extended Data Fig. 1a); a large mouth cone opening ventrally in the head (Fig. 1a–d, f), its size being typical

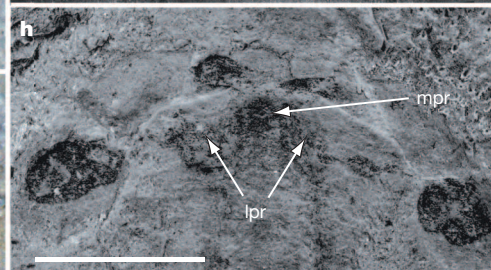
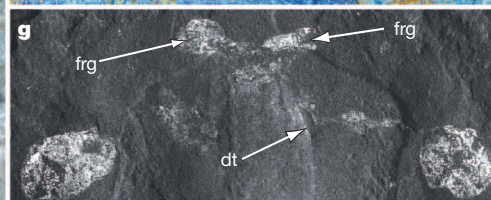
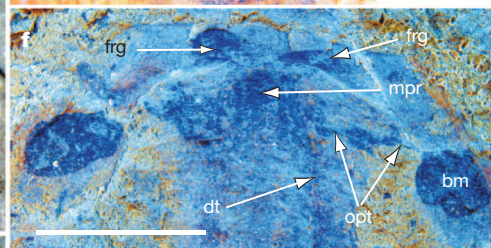
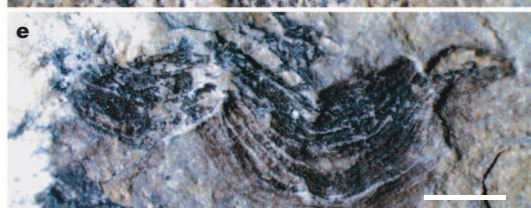
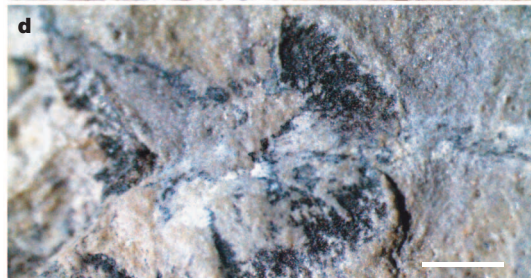
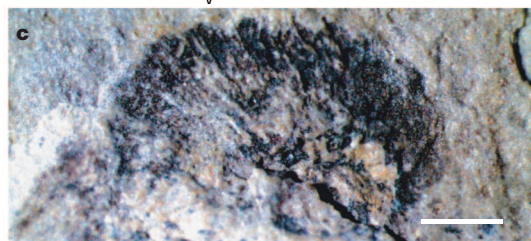
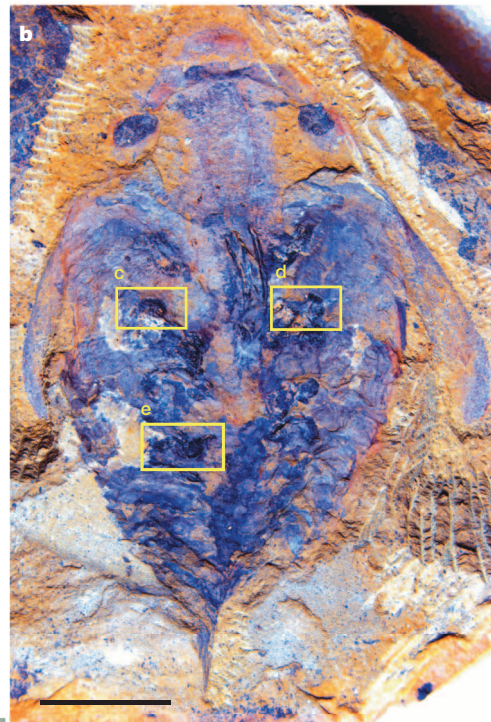
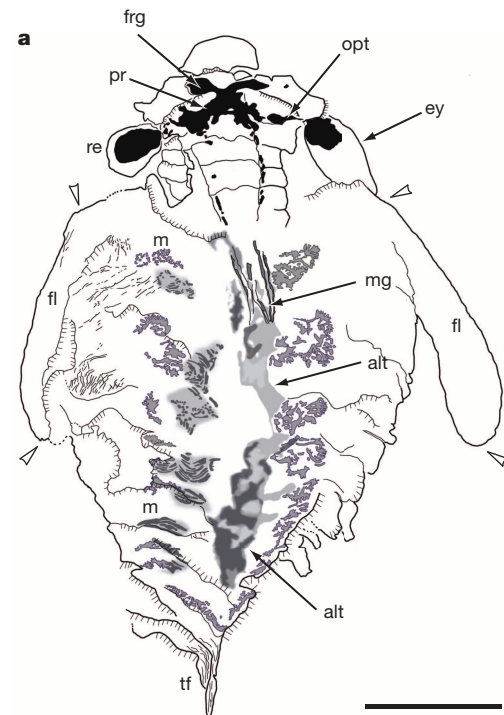


Figure 2 | *L. unguispinus*.

a, b, Dorsal view of YKLP13305 (left side slightly tilted downwards) resolving straight midgut (mg) and sinusoidal alimentary tract (alt). Four neck and eleven trunk segments, the first providing paired oar-like flaps (fl between arrowheads), the last providing the tail fan (tf). Dark areas in the head indicate paired frontal appendage ganglia (frg), optic tract (opt) linking retinas (re) in eyes (ey) to flattened lateral protocerebral lobes (lpr in **h**) flanking an approximately bilaterally symmetric protocerebrum (pr). Metameric striate areas indicate muscle (m). **c–e**, Raised and indented grooves of muscle blocks (enlargements of boxed areas in **b**). **f–h**, Neural traces: blue digital filter (**f**) cancels colours in fossil except dark neural regions (for example, medial protocerebrum, mpr) that are resolved by scanning electron microscopy and energy-dispersive X-ray spectroscopy (**g**), as carbon-rich domains, and shown by oblique illumination relative to eye and head margins (**h**); bm, basement membrane and first optic neuropil. Raised neck segments gradually obscure caudally directed descending tracts (dt). Scale bars: **a, b**, 1 cm; **c–e**, 0.5 mm; **f** (also for **g**) and **h**, 5 mm.

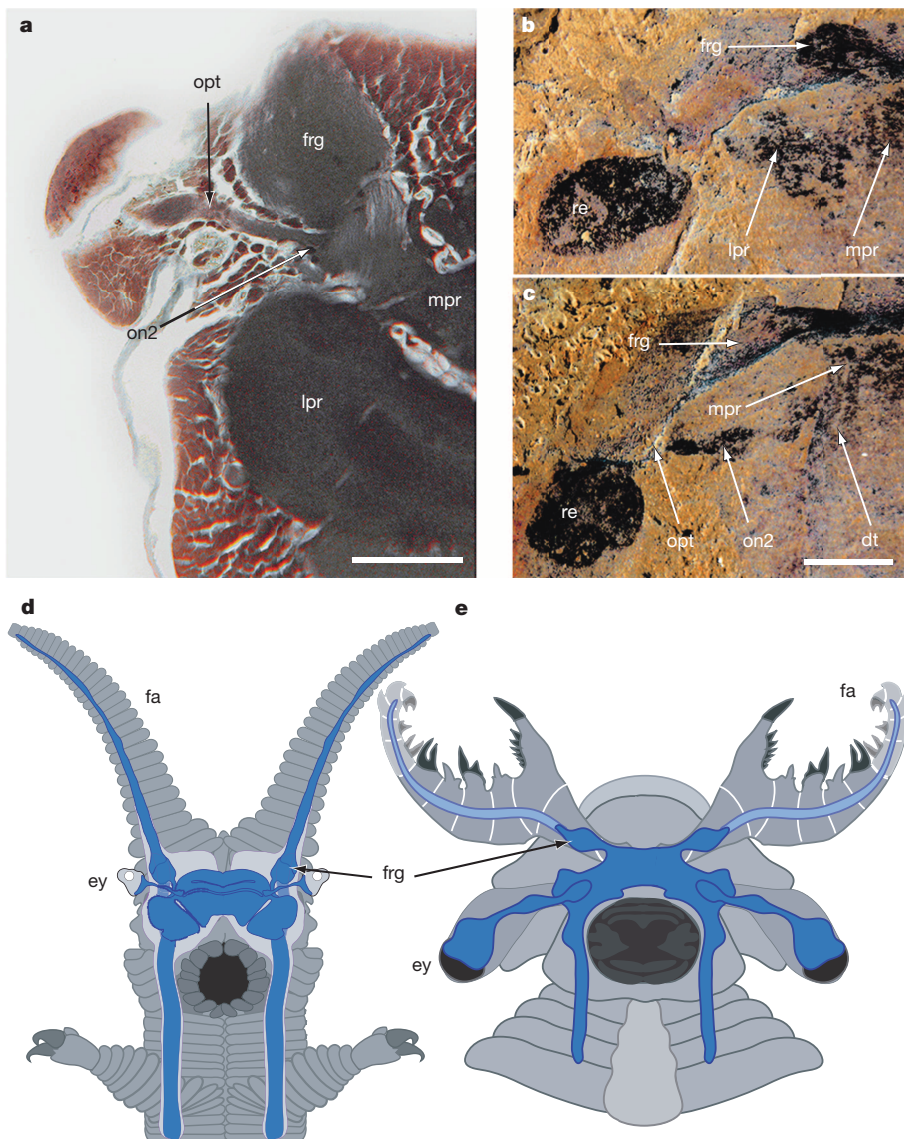


Figure 3 | Comparison of onychophoran and *L. unguispinus* brain. **a**, Horizontal section of hemibrain of *E. rowelli* stained with osmium-ethyl gallate, showing frontal appendage ganglion (frg) anterior to optic tract (opt) and second optic neuropil (on2) connected to medial protocerebral neuropil (mpr; lateral protocerebrum, lpr). **b, c**, Both sides of brain of *L. unguispinus* YKLP 13305 aligned to match orientation of **a**. Corresponding areas (and retinas, re) indicated, as is one root of descending tracts (dt). **d, e**, Comparison of *E. rowelli* and *L. unguispinus* brains. Nervous extensions into the frontal appendages (fa; on subsequent sections of *E. rowelli*; Extended Data Fig. 2e), not visible in the fossil, are added (paler blue). Incomplete distal part of frontal appendage of *L. unguispinus* reconstructed (paler grey). Eye, ey. Scale bars: **a**, 100 μ m; **c** (also for **b**), 2 mm.

for a radiodontan⁸; short, narrow segments defining a neck region (as in *A. canadensis* and *Peytoia nathorsti*); segmental body flaps, a tripartite tail fan (Fig. 1a, b) and dorsal bands of setal blades ('gills') (Extended Data Fig. 3e) having the usual proportions for the group. A pigmented rim at the anterior margin of the head (best seen in YKLP 13304a; Fig. 1d, g) is interpreted as the margin of a dorsal carapace, as known from other radiodontans⁷. Phylogenetic analysis resolves *L. unguispinus* within Radiodonta⁶ as the closest relative of *Amplectobelua* (Extended Data Fig. 4) based on shared derived characters of the pincer-like frontal appendages (Supplementary Information).

In all three specimens (Figs 1, 2 and Extended Data Fig. 3) the eye-stalks contain terminal areas that are black, sometimes surmounted by dark blue colouration. Ommatidia (Extended Data Fig. 2a, b) are indicated as long, slightly curved troughs that extend through pale blue-pigmented areas in the right eye of YKLP 13304b, terminating in a darker zone lying distal to a roughly oval area of black pigmentation that further extends as a broken tract directed towards the head (Extended Data Fig. 2a–c). A similar trace is observed in the left eye of YKLP 13304b where there is evidence for faceted organization (Extended Data Fig. 2d). The observed relationship between photoreceptor terminals and underlying structure is typical of euarthropod eyes equipped with compound facets, which have been demonstrated as the eye structure typifying anomalocaridids⁹. The black domains in YKLP 13304 are thus interpreted as the first optic neuropil of the eye. Corresponding black

domains in YKLP 13305 are connected via black tracts to further broadened pigmented areas disposed centrally, lateral to and confluent with an approximately symmetric domain extending across the head in front of the mouth, compared with YKLP 13304 (Fig. 2a). Anterior to this dark area, and attached to each side of it anteriorly, are two approximately almond-shaped areas located at a position corresponding to the point of origin of the frontal appendages. Employment of a digital blue filter accentuates these dark structures as well as contiguous fragments comprising cord-like traces that extend a short distance caudally, indicative of two parallel tracts from the main pre-oral mass (Fig. 2f). Energy-dispersive X-ray spectroscopy resolves the dark areas as carbon concentrations (Fig. 2g). Allowing for some distortions probably due to compression, bilateral symmetry demonstrates that these structures represent an organ system. Comparison of YKLP 13304 and 13305 suggests these structures are not contiguous with the mouth cone, or any regions caudal to it (Fig. 2h), and the confluence of these carbon-rich areas with tracts leading from the compound eyes identifies the observed areas as flattened brain and cerebral ganglia (Fig. 2f–h). These structures correspond to the profile of a flattened horizontal view of a compressed onychophoran brain (Fig. 3a and Extended Data Fig. 2e, both compared with Fig. 3b, c). The trunk of YKLP 13305 resolves other carbon-rich organ systems that are structurally distinct from those in the head. These other systems are indicative of a large convoluted gut, gut-associative muscle and variously oriented lamellate body-wall muscle

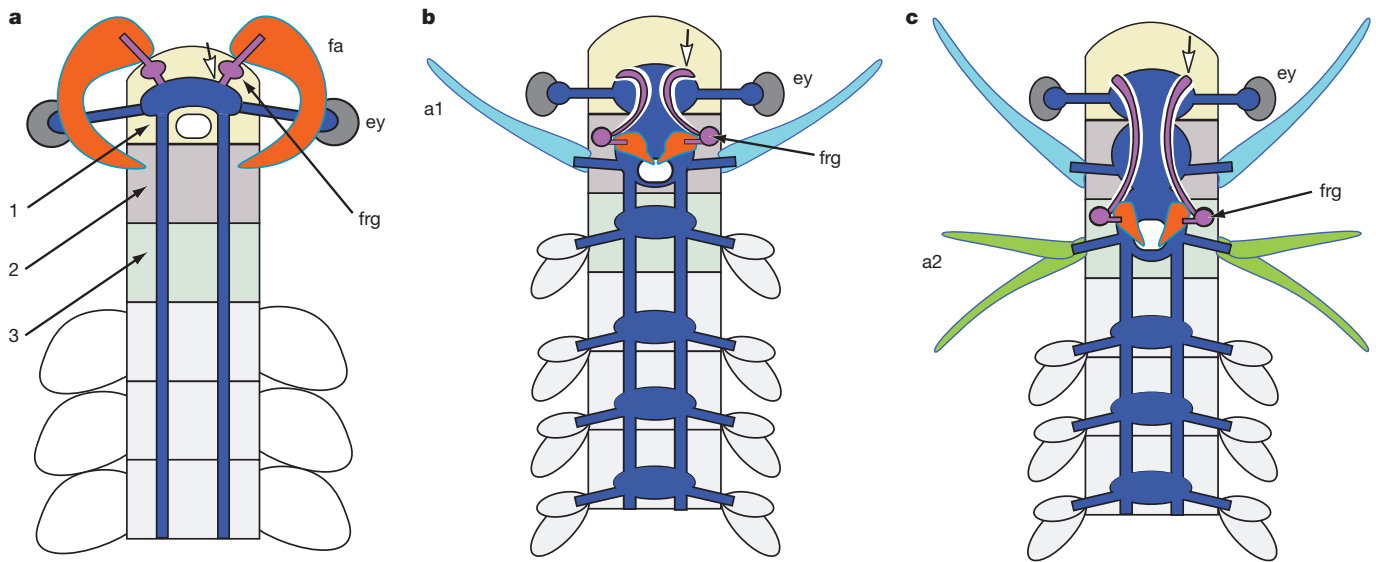


Figure 4 | Evolutionary shift of frontal appendage and its ganglia.

a–c, Proposed transformation of frontal appendages (fa, orange) and cognate ganglia (frg, purple) in Radiodonta (**a**) to labrum (orange) and cognate ganglia (frg) in a crustacean (**c**), via a hypothetical stem euarthropod (**b**) where the

mouth has migrated from the first to second cephalic segment (in **a** segments coloured 1–3; correspondingly in **b** and **c**). Axon tracts linking frg and roof of protocerebrum (open arrow) shown in purple. a1, a2: crustacean first and second antennae.

blocks (Fig. 2c–e). These are similar, respectively, to gut muscle and striated muscle traces described from *Pambdelurion whittingtoni*¹⁰ and *A. canadensis*⁷.

Carbon-rich cephalic structures of YKLP 13305 (Fig. 2g) resolve the disposition of brain centres that substantially differ from ground pattern organization expected of a euarthropod brain, but resolve specific correspondences with the cerebral ground pattern of Onychophora. Mandibulates and chelicerates (=Euarthropoda) possess segmental ganglia connected by paired nerve cords to tripartite brains, the latter a consequence of developmental fusion of three neuromeres rostral to or flanking the gut. This ground pattern has existed at least since the Lower Cambrian, as exemplified by the mandibulate-like brain of *Fuxianhuia protensa*¹¹ and the chelicerate-like central nervous system of the mega-cheiran *Alalcomenaeus* sp.¹².

Such segmental arrangements contrast to the organization of the central nervous system in Onychophora¹³, where nerve cords from paired pre-ocular frontal appendages supply a brain that lies in front of the mouth and which provides paired lateral cords comprising continuous synaptic neuropil connected by orthogonal connections down its length¹⁴. No segmental ganglia are resolved¹³, an absence interpreted as an ancestral trait of Arthropoda¹⁵. In Onychophora, localization of engrailed protein in the brain resolves only a single posterior segmental boundary¹⁶, thereby refuting its proposed tri- or bipartite segmental organization^{17,18}. Resolving the brain and nerve cords of the onychophoran *Euperipatoides rowelli* with osmium–ethyl gallate staining¹⁹ demonstrates that bundled axons from the frontal appendages supply a large ganglion-like neuropil that lies anterior to the optic tract, the latter supplying neuropil of a heterolateral brain lying anterior to and above the mouth (Fig. 3a). Carbon deposits in the head of *L. unguispinus* likewise resolve paired, approximately almond-shaped, pre-ocular domains situated above the origin of the frontal appendages (Figs 2f–h and 3b, c). These structures are here interpreted as frontal appendage ganglia that are contiguous with the anterior brain and, as in Onychophora, are anterior to optic tracts extending into the brain from the eyes. The absence of any suboesophageal neuropil mass, but the origin of paired tracts directed caudally (Fig. 3b, c), offers further evidence for the correspondence of brain organization in onychophorans and anomalocaridids (Fig. 3d, e), whereas none of the putative brain regions of *L. unguispinus* correspond to either of the two ground patterns of euarthropod brains. Enlargements at two points along the anomalocaridid optic nerve suggest two successive optic

neuropils (Fig. 3c), one distal within the eyecup, as would be expected of a highly visual predator. Onychophora also possess two neuropils, albeit smaller, one distal beneath the photoreceptor layer, the other central²⁰.

As inferred from their position on the head¹, the association of anomalocaridid frontal appendages with ganglia anterior to the eye and optic nerves identifies frontal appendages as pre-protocerebral and thus unambiguously distinct from postocular euarthropod appendages such as chelicerae, chelifores or first antennae (crustacean antennules) that originate at the deutocerebrum^{21,22}. The assignment of frontal appendages to the deutocerebrum by forcing their homology with euarthropod antennae²³ or a transformation series that proposes anomalocaridid frontal appendages as homologues of megacheiran great appendages and chelicerae⁴ are thus contradicted.

A pre-protocerebral appendage in *L. unguispinus* with an associated ganglion that is connected to the anterior surface of the protocerebrum (Figs 2f–h and 3e) is shared with Onychophora but not Euarthropoda. Although the stem-group euarthropod *Isoxys* has been interpreted as possessing an anomalocaridid-like appendage²⁴, this is likely to originate posterior to the eyestalks and, if so, implies that similarities are convergent. Accommodating Radiodonta on the euarthropod stem lineage demands a transformation of the ancestral pre-protocerebral frontal appendages into another structure. The labrum has been suggested as the most logical candidate for the euarthropod homologue of the anomalocaridid frontal appendages¹. Support for this hypothesis is provided by studies of labral development, particularly in the amphipod *Parhyale hawaiiensis*²⁵ where appendicular gene expression is resolved during the embryonic differentiation of the labrum in front of the eyes, followed by a subsequent migration to a tritocerebral location during the development and caudal migration of the stomodeum. Molecular evidence from *Tribolium* shows the labrum composed of appendicular endites²⁶. Expression of appendage gap genes in mandibulates and chelicerates demonstrates homologous morphogenetic expression in the labrum across all Euarthropoda²². Tracing sensory neurons from the odonate labrum demonstrates a sensory organization typical of jointed limbs²⁷. A pre-protocerebral appendicular ancestry of the labrum¹ is reflected across extant Euarthropoda by the presence of discrete paired neuropils that receive its afferents and which are directly connected to the anterior roof of the protocerebrum via an ascending axon tract²⁸. This organization supports an evolutionary shift of the placement of the frontal appendages accompanied by a corresponding shift of their cognate

ganglia, which, throughout, have retained their ancestral connection to the most anterior surface of the brain (Fig. 4).

METHODS SUMMARY

All studied specimens of *L. unguispinus* (YKLP 11304–11306) are deposited at the Yunnan Key Laboratory for Palaeobiology, Yunnan University, Kunming, China. Digital images of the specimens were captured with Nikon D3X or Leica DFC5000 cameras attached to a Leica M205C photomicroscope and were processed in Adobe Photoshop CS5 using, where appropriate, digital filter functions to absorb specific colours. High-resolution images and geochemical maps were obtained using a LEO 1455VP scanning electron microscope and energy-dispersive X-ray spectroscopy, at 12 kV accelerating voltage and 12 Pa chamber pressure. The final carbon maps were montaged from individual maps with Adobe Photoshop CS5.

Online Content Methods, along with any additional Extended Data display items and Source Data, are available in the online version of the paper; references unique to these sections appear only in the online paper.

Received 3 April; accepted 16 May 2014.

Published online 16 July 2014.

- Budd, G. E. A palaeontological solution to the arthropod head problem. *Nature* **417**, 271–275 (2002).
- Daley, A. C., Budd, G. E., Caron, J.-B., Edgecombe, G. D. & Collins, D. The Burgess Shale anomalocaridid *Hurdia* and its significance for early euarthropod evolution. *Science* **323**, 1597–1600 (2009).
- Legg, D. A., Sutton, M. D. & Edgecombe, G. D. Arthropod fossil data increase congruence of morphological and molecular phylogenies. *Nature Commun.* **4**, 2485 (2013).
- Haug, J. T., Waloszek, D., Maas, A., Liu, Y. & Haug, C. Functional morphology, ontogeny and evolution of mantis shrimp-like predators in the Cambrian. *Palaeontology* **55**, 369–399 (2012).
- Hou, X. & Bergström, J. in *Originations, Radiations and Biodiversity Changes: Evidences from the Chinese Fossil Record* (eds Rong, J. et al.) 139–158, 847–850 (Science Press, 2006).
- Vinther, J., Stein, M., Longrich, N. R. & Harper, D. A. T. A suspension-feeding anomalocarid from the Early Cambrian. *Nature* **507**, 496–499 (2014).
- Daley, A. C. & Edgecombe, G. D. Morphology of *Anomalocaris canadensis* from the Burgess Shale. *J. Paleontol.* **88**, 68–91 (2014).
- Daley, A. C. & Bergström, J. The oral cone of *Anomalocaris* is not a classic “peytoia”. *Naturwissenschaften* **99**, 501–504 (2012).
- Paterson, J. R. et al. Acute vision in the giant Cambrian predator *Anomalocaris* and the origin of compound eyes. *Nature* **480**, 237–240 (2011).
- Budd, G. E. Arthropod body-plan evolution in the Cambrian with an example from anomalocaridid muscle. *Lethaia* **31**, 197–210 (1998).
- Ma, X., Hou, X., Edgecombe, G. D. & Strausfeld, N. J. Complex brain and optic lobes in an early Cambrian arthropod. *Nature* **490**, 258–261 (2012).
- Tanaka, G., Hou, X., Ma, X., Edgecombe, G. D. & Strausfeld, N. J. Chelicerate neural ground pattern in a Cambrian great appendage arthropod. *Nature* **17**, 364–367 (2013).
- Schürmann, F.-W. in *Arthropod Brain: Its Evolution, Development, Structure and Function* (ed. Gupta A. P.) 159–180 (John Wiley, 1987).
- Mayer, G. & Whittington, P. M. Neural development in Onychophora (velvet worms) suggests a step-wise evolution of segmentation in the nervous system of Panarthropoda. *Dev. Biol.* **335**, 263–275 (2009).
- Mayer, G. & Harzsch, S. Distribution of serotonin in the trunk of *Metaperipatus blainvillei* (Onychophora, Peripatopsidae): implications for the evolution of the nervous system in Arthropoda. *J. Comp. Neurol.* **507**, 1196–1208 (2008).
- Eriksson, B. J., Tait, N. N., Budd, G. E. & Akam, M. The involvement of *engrailed* and *wingless* during segmentation in the onychophoran *Euperipatoides kanangrensis* (Peripatopsidae: Onychophora) (Reid 1996). *Dev. Genes Evol.* **219**, 249–264 (2009).
- Strausfeld, N. J., Strausfeld, C. M., Stowe, S., Rowell, D. & Loesel, R. The organization and evolutionary implications of neuropils and their neurons in the brain of the onychophoran *Euperipatoides rowelli*. *Arthropod Struct. Dev.* **35**, 169–196 (2006).
- Mayer, G., Whittington, P. M., Sunnucks, P. & Pflüger, H. J. A revision of brain composition in Onychophora (velvet worms) suggests that the tritocerebrum evolved in arthropods. *BMC Evol. Biol.* **10**, 255 (2010).
- Wigglesworth, V. B. The use of osmium in the fixation and staining of tissue. *Proc. R. Soc. Lond. B* **147**, 185–199 (1957).
- Strausfeld, N. J., Strausfeld, C. M., Loesel, R., Rowell, D. & Stowe, S. Arthropod phylogeny: onychophoran brain organization suggests an archaic relationship with a chelicerate stem lineage. *Proc. R. Soc. B* **273**, 1857–1866 (2006).
- Boxshall, G. A. The evolution of arthropod limbs. *Biol. Rev. Camb. Philos. Soc.* **79**, 253–300 (2004).
- Scholtz, G. & Edgecombe, G. D. The evolution of arthropod heads: reconciling morphological, developmental and palaeontological evidence. *Dev. Genes Evol.* **216**, 395–415 (2006).
- Stein, M. A new arthropod from the Early Cambrian of north Greenland, with a ‘great appendage’-like antennula. *Zool. J. Linn. Soc.* **158**, 477–500 (2010).
- Legg, D. A. & Vannier, J. The affinities of the cosmopolitan arthropod *Isoxys* and its implications for the origin of arthropods. *Lethaia* **46**, 540–550 (2013).
- Browne, W. E., Price, A. L., Gerberding, M. & Patel, N. H. Stages of embryonic development in the amphipod crustacean, *Parhyale hawaiiensis*. *Genesis* **42**, 124–149 (2005).
- Haas, M. S., Brown, S. J. & Beeman, R. W. Homeotic evidence for the appendicular origin of the labrum in *Tribolium castaneum*. *Dev. Genes Evol.* **211**, 96–102 (2001).
- Boyan, G. S., Williams, J. L. D., Posser, S. & Brauning, P. Morphological and molecular data argue for the labrum being non-apical, articulated, and the appendage of the intercalary segment in the locust. *Arthropod Struct. Dev.* **31**, 65–76 (2002).
- Strausfeld, N. J. *Arthropod Brains: Evolution, Functional Elegance, and Historical Significance* Ch 9, 427–446 (Belknap, 2012).

Supplementary Information is available in the online version of the paper.

Acknowledgements This work was supported by the National Natural Science Foundation of China (U1302232, 41372031 and 40962001), a Leverhulme Trust Research Project Grant (F/00 696/T), by the Center for Insect Science, University of Arizona, and by a grant from the Air Force Research Laboratory (FA86511010001) to N.J.S. We thank T. Goral for assistance with energy dispersive X-ray spectroscopy. We acknowledge A. Daley’s advice about anomalocaridid anatomy.

Author Contributions Fossil data were analysed by all authors, all of whom contributed to the text.

Author Information This published work and the nomenclatural acts it contains have been deposited in ZooBank under accession number <http://zoobank.org/urn:lsid:zoobank.org:pub:189DCAFF-0DD6-49C2-BE80-E999DDF059C1>. Reprints and permissions information is available at www.nature.com/reprints. The authors declare no competing financial interests. Readers are welcome to comment on the online version of the paper. Correspondence and requests for materials should be addressed to X.H. (xghou@ynu.edu.cn) or N.J.S. (flybrain@neurobio.arizona.edu).

Island biogeography of the Anthropocene

Matthew R. Helmus¹, D. Luke Mahler² & Jonathan B. Losos³

For centuries, biogeographers have examined the factors that produce patterns of biodiversity across regions. The study of islands has proved particularly fruitful and has led to the theory that geographic area and isolation influence species colonization, extinction and speciation such that larger islands have more species and isolated islands have fewer species (that is, positive species–area and negative species–isolation relationships)^{1–4}. However, experimental tests of this theory have been limited, owing to the difficulty in experimental manipulation of islands at the scales at which speciation and long-distance colonization are relevant⁵. Here we have used the human-aided transport of exotic anole lizards among Caribbean islands as such a test at an appropriate scale. In accord with theory, as anole colonizations have increased, islands impoverished in native species have gained the most exotic species, the past influence of speciation on island biogeography has been obscured, and the species–area relationship has strengthened while the species–isolation relationship has weakened. Moreover, anole biogeography increasingly reflects anthropogenic rather than geographic processes. Unlike the island biogeography of the past that was determined by geographic area and isolation, in the Anthropocene—an epoch proposed for the present time interval— island biogeography is dominated by the economic isolation of human populations.

The number of species (that is, richness) on islands is theorized to be a function of colonization and *in situ* speciation that add species, and extinction that subtracts them^{1–6}. Larger and less-isolated islands have lower extinction and higher colonization compared to smaller and more-isolated islands. Larger islands have more *in situ* speciation than smaller islands because they have a greater diversity of habitat types and offer more opportunities for allopatric divergence^{7,8}, while isolated islands have fewer and more closely related species because they are infrequently colonized^{9,10}. Island area is thought to set the maximum richness islands can contain (that is, equilibrium saturation points¹), while isolation and *in situ* speciation influence how close islands are to saturation. Together, these processes are presumed to cause the positive species–area and negative species–isolation relationships (SARs and SIRs) ubiquitous across islands.

Tests of this theory are lacking owing to limits in the scale at which experimental manipulation is possible⁵. For example, the most comprehensive experiment was an arthropod defaunation and recovery manipulation of six small, un-isolated islands (maximum area <0.003 ha; maximum interisland distance <1.2 km)¹¹. Other tests have monitored diversity recoveries from natural catastrophes that wiped out existing species (for example, volcanic eruptions¹²). These studies demonstrated that colonization and extinction can balance each other to determine species richness—although this equilibrium may take a long time, if ever, to achieve^{4,13}—and that area and extinction rate are negatively correlated¹⁴. Other predicted relationships have not been experimentally investigated because all previous tests were on few islands of small size and limited isolation where the effects of speciation and long-distance colonization could not be assessed.

Here, we illustrate how the spread of exotic species experimentally tests island biogeography theory^{15–17}. In the past, changes to the species richness of major islands (that is, those large and isolated enough to have

speciation and infrequent colonizations) have occurred on timescales precluding direct human observation and testing of theoretical predictions. This is no longer the case today. For many insular groups, island richness is increasing as the number of exotic species establishing surpasses the number of native species lost¹⁸.

Caribbean *Anolis* lizards are one such group. Until recently, each Caribbean island bank—shallow areas that connect islands—hosted endemic clades of anoles (Fig. 1, Extended Data Fig. 1)¹⁹. This high endemism resulted because over-water dispersal is naturally perilous for anoles, making natural long-distance colonization rare and allopatric speciation common even among neighbouring banks. No anole has gone extinct except possibly one (*Anolis roosevelti*)²⁰. In contrast, 34 populations comprising 18 species have established on a Caribbean island far from their native bank, increasing mean bank richness from 4.72 (2.06 s.e.m.) to 5.41 (1.91; $P \ll 0.001$, Fig. 1, Extended Data Table 1). If the tenets of island biogeography theory are valid, then this human-mediated increased colonization will predictably alter anole biogeography and richness relationships. Here we test three predictions: exotic anoles have mostly established on impoverished banks, increased anole colonizations have diminished the past signal of speciation on bank richness, and the anole SAR has strengthened while the anole SIR has weakened.

Have exotic anoles established on banks furthest from their area-set saturation points? Banks impoverished in native anoles should provide the most opportunity for new species establishment. We estimated bank saturation as the residuals from a log-linear regression of native richness on area (that is, lower residuals suggest impoverished banks, Extended Data Fig. 2). As predicted, exotic anoles have established on the most impoverished banks (coefficient of exotic richness on saturation: -0.422 ± 0.126 , $P = 0.002$)—a result also robust to an alternative metric based on a direct estimate of the anole saturation curve (-0.409 ± 0.126 , $P = 0.003$, Extended Data Table 2).

Has increased colonization obscured the past effect of speciation on anole biogeography? Speciation is responsible for two main biogeographic patterns in anoles. First, because an isolated island is more likely to contain species descended from speciation of a few colonists from the same source area rather than multiple colonists from multiple source areas, which is more likely for proximate islands¹⁰, negative phylogenetic diversity–isolation relationships (PDIRs) are expected where the most isolated islands contain small numbers of closely related species. Such a relationship previously existed for Caribbean anoles. Anoles found on the same bank were more closely related to each other than expected if species randomly colonized banks regardless of isolation (Fig. 1; mean standardized effect: -8.08 , $P \ll 0.001$, indicating strong phylogenetic underdispersion)²¹, and as a result of this non-random colonization, the PDIR was strongly negative (past PDIR coefficient: -0.734 ± 0.196 , $P = 0.002$, Extended Data Fig. 3). In the present day, anole assemblages are more phylogenetically random (increase in mean standardized effect: 3.02 , $P \ll 0.001$) because exotic species can colonize isolated banks from across the Caribbean (compare native and exotic distributions in Fig. 1)²²; consequently the anole PDIR has been eliminated (present PDIR coefficient: -0.520 ± 0.245 , $P > 0.05$; Extended Data Fig. 3).

Second, *in situ* speciation is expected to be a nonlinear function of area, stemming from a threshold area below which speciation does not

¹Amsterdam Global Change Institute, Department of Animal Ecology, Vrije Universiteit, 1081 HV Amsterdam, The Netherlands. ²Center for Population Biology, University of California, Davis, California 95616, USA. ³Department of Organismic and Evolutionary Biology and Museum of Comparative Zoology, Harvard University, Cambridge, Massachusetts 02138, USA.

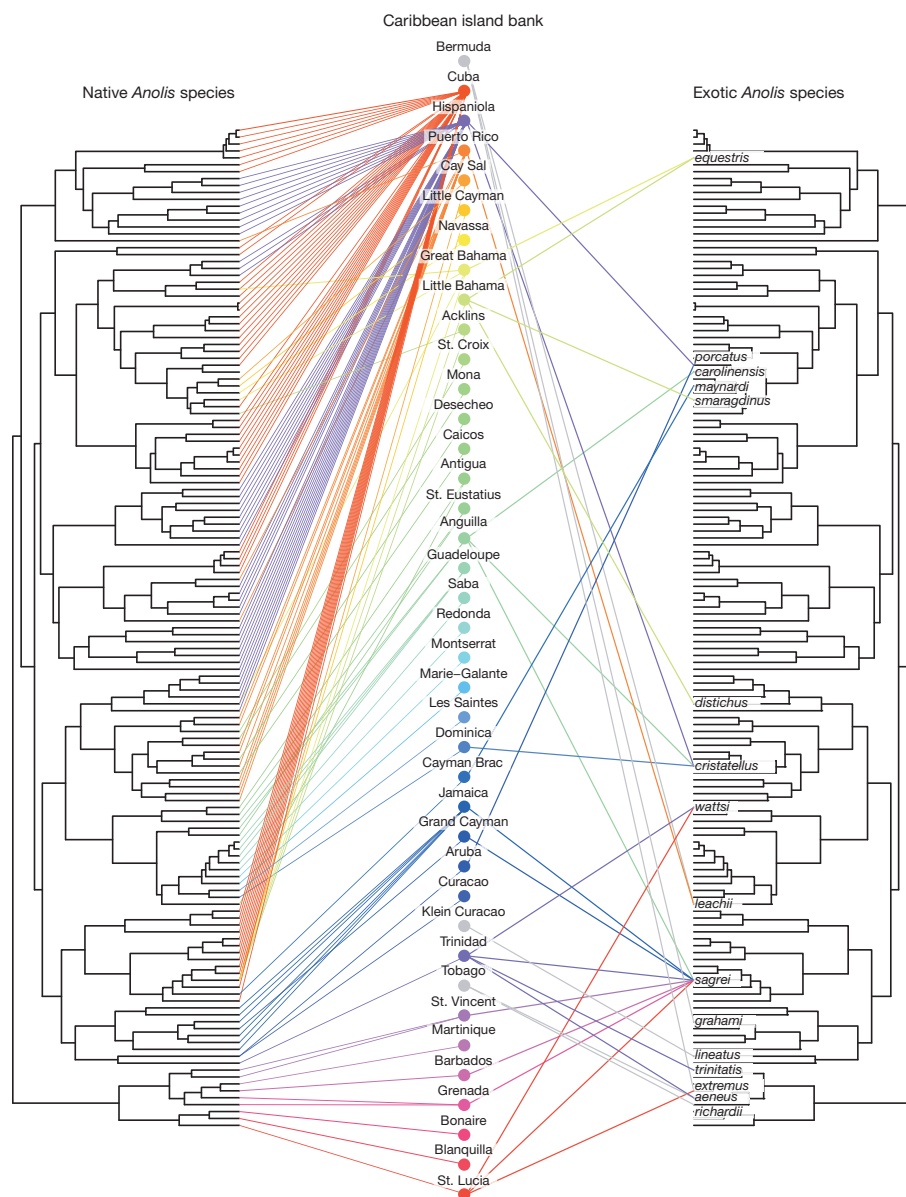


Figure 1 | The biogeographic distributions of Caribbean anole lizards in the Anthropocene. Lines link species to the banks where they are found; the mirrored tree^{21,29} is ordered to minimize the crossing of native-to-bank links. Bermuda, Klein Curaçao and Tobago have no native anoles.

occur^{6–8}. This effect causes two-part SARs in which species richness rises modestly with area up to the threshold, and then increases dramatically. In the past, the anole SAR exhibited this nonlinearity (Fig. 2a), but the pattern is now gone. The present-day SAR is linear ($P < 0.001$) because the area relationship of banks without *in situ* speciation has become similar to the area relationship of banks with *in situ* speciation (Fig. 2b). This homogenization of relationships is expected because banks that lacked *in situ* speciation (Extended Data Fig. 1) were impoverished in

species, especially banks just below the breakpoint in Fig. 2a ($P = 0.007$, Extended Data Table 3).

Does area now explain more, and isolation less, of the variation in anole richness? By adding species to impoverished islands, increased colonization should move islands towards their area-set saturation points, strengthening the SAR; and because isolated islands, especially those too small for *in situ* speciation, should be impoverished, the SIR should weaken. In the past, a strong, negative SIR existed (Table 1, Fig. 2c) with

Table 1 | The shifting importance of area and isolation to Caribbean anole biogeography

	Sum of squares					Explained variation		Past to present change	
	Area	Geographic isolation			Residual	Area	Total isolation	Area	Total isolation
Past	(+) 13.73	(–) 2.11	(–) 3.53	(–) 4.23	10.27	41%	29%		
Exotic	(+) 4.69	0.04	(+) 7.43	(+) 6.57	20.13	12%	36%		
Present	(+) 17.88	(–) 2.16	0.14	0.28	13.76	52%	7%	29%	–74%

'Past' is native richness. 'Exotic' is exotic richness. 'Present' is native + exotic richness. 'Area' is total emerged land of a bank. 'Geographic isolation' is three orthogonal metrics calculated from the pairwise-distances among banks and the mainland (Extended Data Table 4). Significant values ($\alpha = 0.05$) are in bold and given with the sign of the relationship. 'Past to present change' is the difference between present and past explained variation divided by past explained variation. Richness and area were log transformed and all variables were standardized.

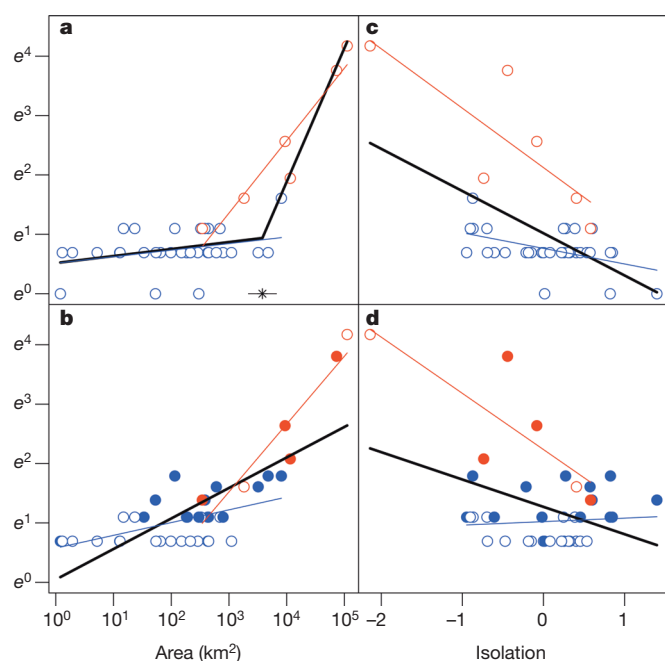


Figure 2 | The linearization of the Caribbean anole species–area relationship (SAR) and flattening of the species–isolation relationship (SIR). **a**, The past SAR was nonlinear and best fitted by a regression with two slopes and a breakpoint (*, 3,579 [CI_{95%}, 3,337–3,822], $P \ll 0.001$)⁶. In all panels, solid black lines indicate regression fits across all banks and coloured lines are regressions of banks with (red) or without (blue) *in situ* speciation. **b**, Colonization of exotic anoles has eliminated the two-part SAR. Solid symbols are banks with exotics and the y-axis plots $\log_e(\text{species richness})$. **c**, In the past, there was a strong SIR across all banks. ‘Isolation’ is the mean of three orthogonal isolation metrics (Table 1, Extended Data Table 4). **d**, Exotic colonization has reduced the strength of the SIR by eliminating the SIR of banks without *in situ* speciation. R^2 in each panel for the regressions on all banks, with *in situ*, and without *in situ*, speciation are respectively: **a**, 0.85, 0.90, 0.11; **b**, 0.57, 0.89, 0.31; **c**, 0.32, 0.65, 0.22; **d**, 0.15, 0.65, 0.01. See Table 1 for the multivariate regressions.

the most isolated banks also the most impoverished in native anoles ($P \ll 0.001$, Extended Data Table 3). As predicted, the SIR has now weakened while the SAR has strengthened (Fig. 2b, d, Table 1, Extended Data Table 5). This shift is because isolation now correlates positively with the richness of newly colonized species, a reversal of the natural pattern, but like the natural pattern, exotic richness positively correlates with area, further strengthening the present-day anole SAR (see the exotic model in Table 1).

Our results support the theory that it is the influence of geographic area and isolation on long-term biogeographic processes such as speciation and colonization that fundamentally determine island biodiversity^{1,2,4,10}. However, as the species richness of isolated islands is increasing, Caribbean anoles are not currently in equilibrium and island isolation no longer inhibits colonization by new species (Figs 1, 2d; Table 1). Yet, this latter conclusion rests on defining isolation relevant to the natural over-water colonizing ability of lizards. In the modern world, anoles colonize as commensals of humans arriving at new destinations primarily as stowaways in cargo shipments (Extended Data Table 1). In this context, island

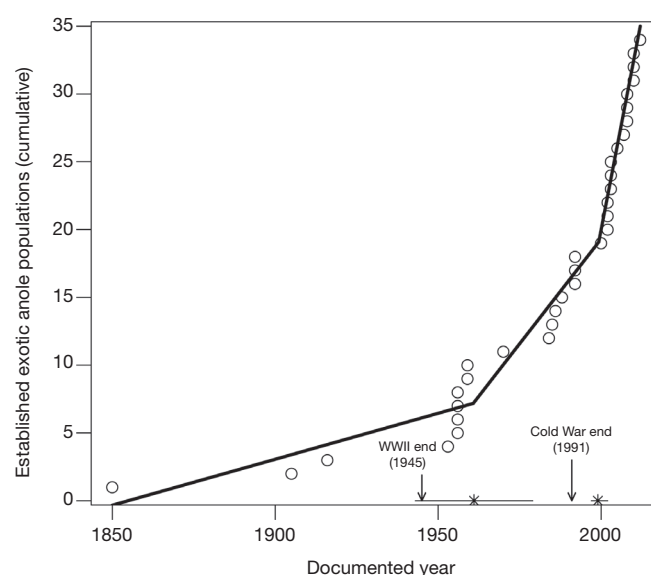


Figure 3 | Anole lizards are establishing on Caribbean islands at an increasing rate. The accumulation of exotic anole lizard species across the Caribbean is best explained by a three-segment regression ($P \ll 0.001$) with breakpoints (*) estimated at 1961 (1943–79 CI_{95%}, horizontal bars) and 1999 (1997–2002), and rates of 0.07 (± 0.01 s.e.m.), 0.23 (0.07), 0.96 (0.12) exotic establishments per year.

isolation should be redefined to be relevant to this new way in which islands gain species.

Translocating species to new destinations is one of the many ways humans alter Earth. Human effects are so pervasive that a new epoch for the present day, the Anthropocene, has been proposed²³. Proponents argue that an anthropogenic perspective is necessary to understand current and future trajectories of Earth systems^{24,25}. Beginning with the Industrial Revolution, multiple indicators of human activity (for example, atmospheric CO₂ concentration) slowly increased, but then following the Second World War (WWII) increased rapidly²³. The establishment of exotic anoles follows such a curve (Fig. 3). Establishment rate increased first after WWII, and again following the end of the Cold War when global shipping more than doubled²⁶. An Anthropocene perspective may thus well apply to understanding present-day island isolation, and we interpret our final results in this context.

Shipping traffic among Caribbean banks is not related to geographic isolation (Extended Data Table 6)²⁷. Instead, variation in shipping is dependent on anthropogenic factors that influence trade (for example, the US–Cuban trade embargo)²⁸. We estimated the economic isolation of Caribbean banks from a global maritime shipping-traffic data set²⁷ and asked if this metric explained anole richness.

Economic isolation determines Caribbean biodiversity in the Anthropocene—both exotic and present-day (that is, native + exotic) anole richness were negative functions of economic isolation (Table 2, Extended Data Table 5). Further, the correlation between area and economic isolation was high ($\rho = -0.74$, $P \ll 0.001$), implicating shipping trade as the mechanism underlying the positive exotic SAR (Table 1). Therefore, two mechanisms, natural and anthropogenic, underlie the shifting importance of area and isolation in determining past from present anole biogeography (Tables 1 and 2, Extended Data Table 2). As expected if area

Table 2 | The importance of economic isolation to Anthropocene island biogeography

	Sum of squares				Explained variation			
	Geographic isolation			Economic isolation	Residual	Total isolation		
	Area	1	2			Area	Total isolation	Economic isolation
Exotic	-	-	(+) 6.06	(-) 10.76	14.11	-	35%	28%
Present	(+) 4.83	(-) 3.3	-	(-) 2.26	11.91	22%	15%	10%

See Table 1 footnote. Economic isolation is based on the total number of ships docking on each bank. Models are best-fit based on the lowest Akaike information criterion, dashes indicate dropped covariates.

determines saturation points, isolated banks without *in situ* speciation are impoverished in native species (Extended Data Table 3) and are consequently gaining exotics to strengthen the anole SAR, yet because the trade that disperses anoles is constrained by area (for example, larger banks have more people and ports), the SAR is also strengthening because there is a negative economic isolation–area relationship (EIAR, Extended Data Fig. 4a).

Anthropocene models of island biogeography must include economic isolation. For example, the US embargo strongly increases Cuban economic isolation (Extended Data Fig. 4b). We estimated Cuban economic isolation without an embargo from the Caribbean EIAR, and then estimated the expected number of exotic anoles from the exotic model in Table 2 (Extended Data Fig. 4c). Given the current rate of exotic establishment (Fig. 3), we predict Cuba would rapidly gain 1.65 anole lizard species (95% confidence interval, $CI_{95\%}$, 1.06–2.57) should trade normalize following embargo cessation; this gain is comparable to that already seen on Hispaniola, a bank of similar area but without a trade embargo. As the native biodiversity of islands such as Cuba is extraordinary and economically important, strategies (such as cargo screening, ecological monitoring and species import bans) to prevent the establishment and impact of exotic species must increase as economic isolation decreases. Just as for models of other Earth systems, biogeographic models must now include anthropogenic forcing to understand, predict and mitigate the consequences of the new island biogeography of the Anthropocene.

Online Content Methods, along with any additional Extended Data display items and Source Data, are available in the online version of the paper; references unique to these sections appear only in the online paper.

Received 23 December 2013; accepted 7 August 2014.

- MacArthur, R. H. & Wilson, E. O. *The Theory of Island Biogeography* (Princeton Univ. Press, 1967).
- Losos, J. B. & Ricklefs, R. E. *The Theory of Island Biogeography Revisited* (Princeton Univ. Press, 2010).
- Lomolino, M. V. A call for a new paradigm of island biogeography. *Glob. Ecol. Biogeogr.* **9**, 1–6 (2000).
- Heaney, L. R. Dynamic disequilibrium: a long-term, large-scale perspective on the equilibrium model of island biogeography. *Glob. Ecol. Biogeogr.* **9**, 59–74 (2000).
- Schoener, T. W. in *The Theory of Island Biogeography Revisited* (eds Losos, J. B. & Ricklefs, R. E.) 53–85 (Princeton Univ. Press, 2011).
- Losos, J. B. & Schluter, D. Analysis of an evolutionary species–area relationship. *Nature* **408**, 847–850 (2000).
- Kisel, Y. & Barraclough, T. G. Speciation has a spatial scale that depends on levels of gene flow. *Am. Nat.* **175**, 316–334 (2010).
- Wagner, C. E., Harmon, L. J. & Seehausen, O. Cichlid species–area relationships are shaped by adaptive radiations that scale with area. *Ecol. Lett.* **17**, 583–592 (2014).
- Gillespie, R. G., Claridge, E. M. & Roderick, G. K. Biodiversity dynamics in isolated island communities: interaction between natural and human-mediated processes. *Mol. Ecol. Notes* **17**, 45–57 (2008).
- Rosindell, J. & Phillimore, A. B. A unified model of island biogeography sheds light on the zone of radiation. *Ecol. Lett.* **14**, 552–560 (2011).
- Wilson, E. O. & Simberloff, D. S. Experimental zoogeography of islands: defaunation and monitoring techniques. *Ecology* **50**, 267–278 (1969).
- Whittaker, R. J., Field, R. & Partomihardjo, T. How to go extinct: lessons from the lost plants of Krakatau. *J. Biogeogr.* **27**, 1049–1064 (2000).
- Rabosky, D. L. & Glor, R. E. Equilibrium speciation dynamics in a model adaptive radiation of island lizards. *Proc. Natl Acad. Sci. USA* **107**, 22178–22183 (2010).
- Schoener, T. W. & Schoener, A. The time to extinction of a colonizing propagule of lizards increases with island area. *Nature* **302**, 332–334 (1983).
- Blackburn, T. M., Cassey, P. & Lockwood, J. L. The island biogeography of exotic bird species. *Glob. Ecol. Biogeogr.* **17**, 246–251 (2008).
- Sax, D. F. et al. Ecological and evolutionary insights from species invasions. *Trends Ecol. Evol.* **22**, 465–471 (2007).
- Kerr, J. T., Kharouba, H. M. & Currie, D. J. The macroecological contribution to global change solutions. *Science* **316**, 1581–1584 (2007).
- Sax, D. F. & Gaines, M. S. Species invasions exceed extinctions on islands worldwide: a comparative study of plants and birds. *Am. Nat.* **160**, 766–783 (2002).
- Losos, J. B. *Lizards in an Evolutionary Tree* (Univ. California Press, 2009).
- Ojeda Kessler, A. G. *Status of the Culebra Island giant anole (Anolis roosevelti)*. *Herpetol. Conserv. Biol.* **5**, 223–232 (2010).
- Helmus, M. R. & Ives, A. R. Phylogenetic diversity–area curves. *Ecology* **93**, S31–S43 (2012).
- Poe, S. Comparison of natural and nonnative two-species communities of *Anolis* lizards. *Am. Nat.* **184**, 132–140 (2014).
- Steffen, W., Grinevald, J., Crutzen, P. J. & McNeill, J. The Anthropocene: conceptual and historical perspectives. *Phil. Trans. R. Soc. A* **369**, 842–867 (2011).
- Thomas, C. D. The Anthropocene could raise biological diversity. *Nature* **502**, 7 (2013).
- Mendenhall, C. D., Karp, D. S., Meyer, C. F. J., Hadly, E. A. & Daily, G. C. Predicting biodiversity change and averting collapse in agricultural landscapes. *Nature* **509**, 213–217 (2014).
- Essi, F., Winter, M. & Pysek, P. Biodiversity: trade threat could be even more dire. *Nature* **487**, 39 (2012).
- Morinière, V. & Réglain, A. *Development of a GIS-based Database for Maritime Traffic in the Wider Caribbean Region* (Strategic Plan 10–11, Activity 4.6.b.2., UNEP RAC/REMPEITC-Caribe, 2012).
- Bhagwati, J. *Protectionism* (MIT Press, 1988).
- Mahler, D. L., Revell, L. J., Glor, R. E. & Losos, J. B. Ecological opportunity and the rate of morphological evolution in the diversification of greater antillean anoles. *Evolution* **64**, 2731–2745 (2010).

Acknowledgements We thank J. Behm, J. Ellers, A. Ives, C. Pfister, J. Vermaat and T. Wootton for critical feedback; S. Buckner, S. Charles, A. Fields, M. López Darias, G. Perry, R. Platenberg, R. Powell, G. Reynolds, A. Sanchez, G. van Buurt and G. Wever for information on anole introductions; and A. Reglain for access to the RAC/REMPEITC-Caribe UNEP shipping traffic data set. M.R.H. was supported by the Netherlands Organisation for Scientific Research (858.14.040) and the US National Science Foundation (DBI 0906011).

Author Contributions M.R.H. conceived of the study, built the data sets and wrote the manuscript. M.R.H. and D.L.M. performed the analyses. J.B.L. was involved in study design and contributed data. All authors discussed the results and commented on the manuscript.

Author Information Reprints and permissions information is available at www.nature.com/reprints. The authors declare no competing financial interests. Readers are welcome to comment on the online version of the paper. Correspondence and requests for materials should be addressed to M.R.H. (mrhelmus@gmail.com).

A faster Rubisco with potential to increase photosynthesis in crops

Myat T. Lin^{1*}, Alessandro Occhialini^{2*}, P. John Andralojc², Martin A. J. Parry² & Maureen R. Hanson¹

In photosynthetic organisms, D-ribulose-1,5-bisphosphate carboxylase/oxygenase (Rubisco) is the major enzyme assimilating atmospheric CO₂ into the biosphere¹. Owing to the wasteful oxygenase activity and slow turnover of Rubisco, the enzyme is among the most important targets for improving the photosynthetic efficiency of vascular plants^{2,3}. It has been anticipated that introducing the CO₂-concentrating mechanism (CCM) from cyanobacteria into plants could enhance crop yield^{4–6}. However, the complex nature of Rubisco's assembly has made manipulation of the enzyme extremely challenging, and attempts to replace it in plants with the enzymes from cyanobacteria and red algae have not been successful^{7,8}. Here we report two transplastomic tobacco lines with functional Rubisco from the cyanobacterium *Synechococcus elongatus* PCC7942 (Se7942). We knocked out the native tobacco gene encoding the large subunit of Rubisco by inserting the large and small subunit genes of the Se7942 enzyme, in combination with either the corresponding Se7942 assembly chaperone, RbcX, or an internal carboxysomal protein, CcmM35, which incorporates three small subunit-like domains^{9,10}. Se7942 Rubisco and CcmM35 formed macromolecular complexes within the chloroplast stroma, mirroring an early step in the biogenesis of cyanobacterial β -carboxysomes^{11,12}. Both transformed lines were photosynthetically competent, supporting autotrophic growth, and their respective forms of Rubisco had higher rates of CO₂ fixation per unit of enzyme than the tobacco control. These transplastomic tobacco lines represent an important step towards improved photosynthesis in plants and will be valuable hosts for future addition of the remaining components of the cyanobacterial CCM, such as inorganic carbon transporters and the β -carboxysome shell proteins^{4–6}.

Rubisco catalyses the incorporation of CO₂ into biological compounds in photosynthetic organisms¹. During photorespiration, Rubisco also reacts wastefully with oxygen, leading to the release of previously fixed CO₂, NH₃ and energy¹³. Furthermore, catalysis by Rubisco is slow and very large amounts (up to 50% of leaf soluble protein, 25% of leaf nitrogen) are needed to support adequate photosynthetic rates. Some variation in the catalytic properties of Rubisco from diverse sources is apparent. Harnessing this variation has the potential to confer superior photosynthetic characteristics to specific crops and environments¹⁴. C₄ plants, cyanobacteria and hornworts have evolved forms of CO₂-concentrating mechanisms (CCM) that allow them to utilize forms of Rubisco that have higher catalytic rates and lower CO₂ affinity, whereas C₃ plants, which lack a CCM, are constrained to express forms of Rubisco with higher CO₂ affinity but a relatively low rate of turnover². In plants, Rubisco is a L8S8 hexadecamer consisting of eight small subunits (SSU) and eight large subunits (LSU). Although the SSU genes are located in the nucleus, the LSU is encoded by the chloroplast genome, which has complicated previous attempts to engineer improvements in higher plant Rubisco^{2,15}.

Introduction of a CCM has been proposed as a means to improve the performance of Rubisco in C₃ plant chloroplasts^{4–6,16}. In cyanobacteria and several autotrophic prokaryotes, Rubisco and carbonic anhydrase are enclosed within polyhedral microcompartments known as carboxysomes, which maintain elevated CO₂ concentrations in the vicinity of

Rubisco, which both increases carbon fixation and suppresses photorespiration^{4,6}. However, when a tobacco transplastomic line was created in which the LSU gene, *rbcL*, from the cyanobacterium *Synechococcus* PCC6301 replaced the native tobacco *rbcL*, the cyanobacterial LSU did not form a functional complex with the native tobacco SSU⁸. Although a simpler L2 homodimer Rubisco from *Rhodospirillum rubrum* was able to assemble inside tobacco chloroplasts¹⁷, red algal Rubisco subunits failed to produce functional L8S8 complexes within chloroplasts⁷.

To test whether cyanobacterial LSU and SSU can assemble into a functional enzyme within higher plant chloroplasts, we generated two transplastomic tobacco lines, named SeLSX and SeLSM35, using the biolistic delivery system¹⁸, to express the two Rubisco subunits from Se7942 along with either RbcX or CcmM35, respectively. In each chloroplast transformant, three genes were co-transcribed from the tobacco *rbcL* promoter. Each downstream gene was preceded by an intercistronic expression element (IEE) and a Shine-Dalgarno sequence (SD) and equipped with a terminator to facilitate processing into translatable monocistronic transcripts^{19,20} (Fig. 1a).

The two vectors we constructed were designed to replace the tobacco *rbcL* gene with the foreign DNA. To determine whether all chloroplasts in each plant contained the transgenic locus rather than endogenous tobacco *rbcL*, we examined blots of total leaf DNA digested with restriction enzymes that would produce restriction fragment-length polymorphisms between the wild-type and transgenic loci (Fig. 1b). We found that shoots arising after two rounds on selective medium were homoplasmic for the transgene locus, lacking the fragment corresponding to the wild-type chloroplast genome (Fig. 1b). In order to verify these observations, we performed reverse transcription and PCR (RT-PCR) and observed no cDNA derived from the native *rbcL* transcript, whereas cDNAs produced from *aadA*, the selectable marker gene, and the cyanobacterial genes were detected (Fig. 1c).

To observe the expression of the cyanobacterial proteins, we extracted total leaf proteins and examined them by SDS-PAGE and immunoblots. In Coomassie-stained gels, we detected protein bands at the predicted molecular masses of ~52 kDa for the LSU and ~13 kDa for the SSU of the cyanobacterial Rubisco in SeLSX and SeLSM35 samples, whereas wild-type tobacco exhibited a protein of the expected and distinct SSU mass of ~15 kDa (Fig. 2a). Immunoblots probed with antibodies specific for either the cyanobacterial LSU, tobacco Rubisco, tobacco SSU or cyanobacterial CcmM35 verified the presence of cyanobacterial proteins in the two transformants and tobacco Rubisco only in the wild-type plant (Fig. 2a). Although no engineering of tobacco SSU genes was performed in the transgenic lines, tobacco SSU protein was undetectable, as expected, as its stability is known to be severely affected in the absence of a compatible LSU^{8,17}. The absence of the tobacco SSU in the transformants also indicated that it could not form a stable complex with the cyanobacterial LSU. The estimated stoichiometry of CcmM35 per Rubisco holoenzyme in SeLSM35 transformant is about 4.5, which is consistent with the values reported for cyanobacteria (Extended Data Fig. 1)²¹.

In order to observe the configuration of the cyanobacterial Rubisco in the two transgenic lines, we examined the plant material by transmission

¹Department of Molecular Biology and Genetics, Cornell University, Ithaca, New York 14853, USA. ²Plant Biology and Crop Science, Rothamsted Research, Harpenden, Hertfordshire AL5 2JQ, UK.

*These authors contributed equally to this work.

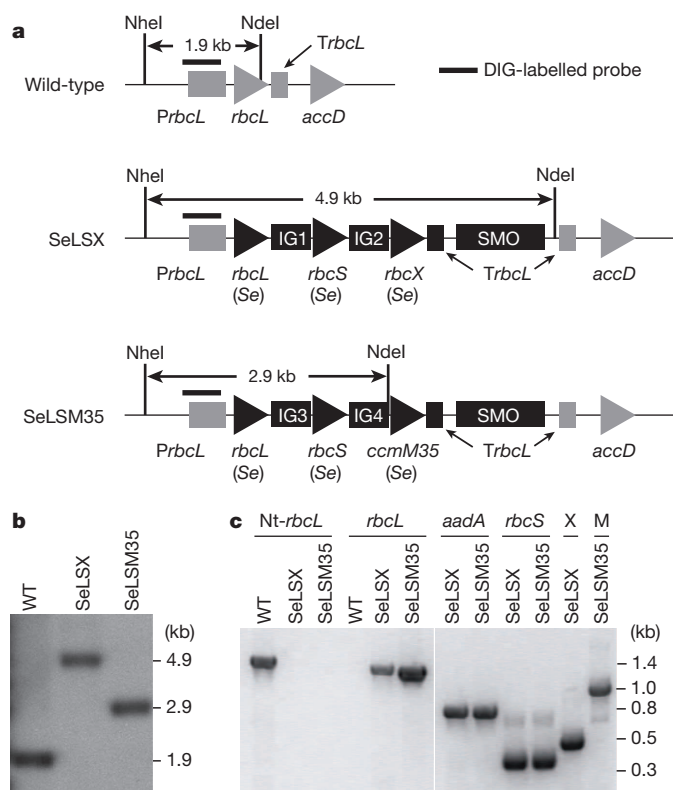


Figure 1 | Replacement of the tobacco chloroplast *rbcL* with cyanobacterial genes. **a**, Gene arrangements of the *rbcL* locus in the wild-type, SeLSX and SeLSM35 tobacco lines. Endogenous chloroplast DNA elements are shown in grey and the newly introduced segments in black. The intergenic regions IG1, IG2, IG3 and IG4 include *TpetD*(At)-IEE-SD, *TpsbA*(At)-IEE-SD, *Trps16*(At)-IEE-SD and *TpsbA*(At)-IEE-SD18 respectively, where *TpetD*, *TpsbA* and *Trps16* are the terminator sequences following the corresponding genes and At stands for the chloroplast of *Arabidopsis thaliana* as the source of these sequences. The selectable marker operon (SMO) includes *LoxP*-*PpsbA*-*aadA*-*Trps16*-*LoxP*, where *PpsbA* stands for the promoter of the *psbA* gene. The probe recognizes the *rbcL* promoter (*PrbcL*) region. The *NheI* and *NdeI* sites used in the DNA blot along with the lengths of the expected DNA fragments detected by the probe are indicated. DIG, digoxigenin. **b**, DNA blot analysis of wild-type, SeLSX and SeLSM35 lines digested with *NdeI* and *NheI*. **c**, Analyses of RT-PCR products of 6 genes. *Nt-rbcL* is the only tobacco (*Nt*, *Nicotiana tabacum*) gene; all other genes are the transgenes introduced into the tobacco chloroplast genome. X = *rbcX*, M = *ccmM35*.

electron microscopy (TEM) in combination with immunogold labelling. Although the enzyme was localized to the chloroplast stroma in both transgenic lines, we observed markedly different patterns of molecular organization. In leaves of the SeLSX line, the cyanobacterial Rubisco showed a diffuse localization similar to endogenous Rubisco in wild-type tobacco (Fig. 2b, c). In contrast, in the SeLSM35 line, in which the Rubisco is co-expressed with CcmM35, the proteins were aggregated into a giant complex in each chloroplast (Fig. 2d and Extended Data Fig. 2). In Se7942, CcmM35 is translated from an internal ribosome entry site of the *ccmM* transcript, which also produces the full-length protein, CcmM58, with an additional amino-terminal domain²². Previous estimation of protein ratios suggested that Rubisco in Se PCC7942 probably exists as L8S5 units crosslinked by the SSU-like domains of CcmM35 resulting in their paracrystalline arrangement in the lumen of β -carboxysomes²¹. The cyanobacterial mutant lacking CcmM58 produces large electron-dense bodies of 300–500 nm with a rectangular cross-section composed of Rubisco and CcmM35 (ref. 22). However, the structures formed inside chloroplasts are generally rounded in appearance without apparent internal order. This discrepancy probably arises from different ratios of Rubisco and CcmM35 or additional carboxysomal components potentially present in the cyanobacterial bodies. Remarkably, the structures

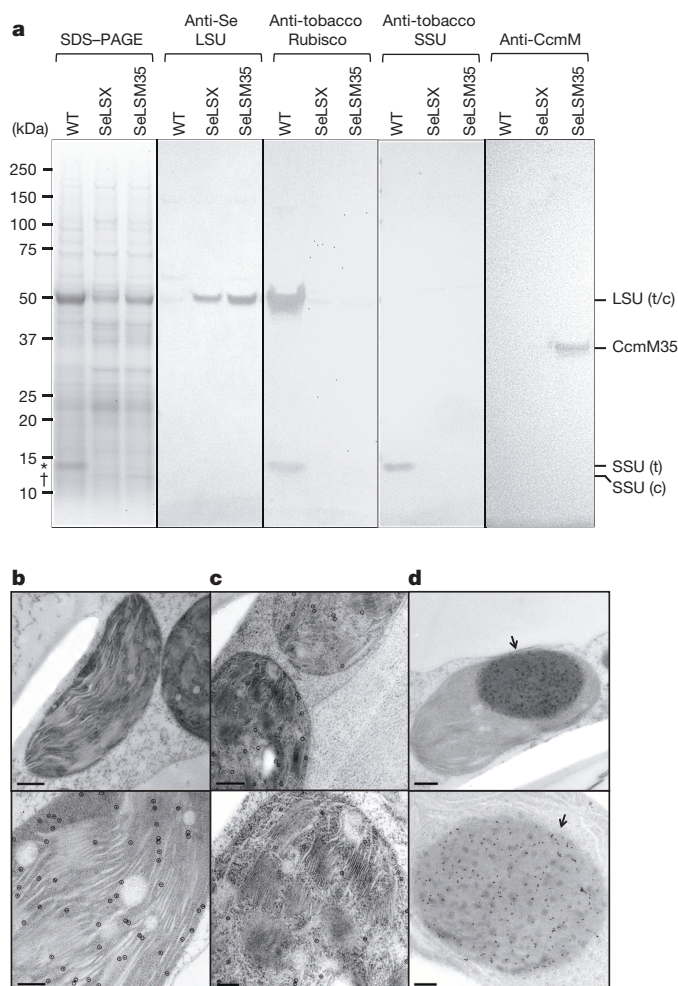


Figure 2 | Cyanobacterial proteins in tobacco chloroplasts. **a**, Coomassie-stained gel and immunoblot of 14 μ g of total leaf protein from wild-type (WT), SeLSX and SeLSM35 tobacco lines. Immunoblots were probed with the antibodies indicated. Molecular mass (kDa) of standard proteins are shown. Asterisk symbol indicates molecular mass of tobacco SSU; dagger symbol indicates molecular mass of cyanobacterial SSU. c, cyanobacteria; t, tobacco. **b–d**, Electron micrographs of leaf sections showing the localization of Rubisco in the stroma of mesophyll chloroplasts of wild-type (**b**), SeLSX (**c**) and SeLSM35 (**d**) tobacco lines. Leaf tissues were prepared by high pressure freeze fixation (HPF) in combination with immunogold labelling using an anti-tobacco Rubisco antibody (**b**) or an anti-cyanobacterial Rubisco antibody (**c, d**) and a secondary antibody conjugated with 10 nm gold particles, which are indicated with either black circles or arrows. Scale bars, 500 nm (top panels in **b, d**) and 200 nm (**c** and the bottom panels in **b, d**).

observed in chloroplasts are highly similar in appearance to procaryosomes recently identified as an important early stage in the carboxysome assembly¹¹ and will potentially facilitate future attempts to assemble β -carboxysomes in chloroplasts through expression of other essential components.

The specificity of the carboxylase activity of cyanobacterial Rubisco relative to its competing oxygenase activity (specificity factor) is known to be lower than that in higher plants, making it more sensitive to the inhibitory effects of oxygen than tobacco Rubisco². SeLSX and SeLSM35 plants did not survive on soil at the normal atmospheric CO₂ concentration of ~400 p.p.m., but were able to grow in CO₂-enriched (9,000 p.p.m.) air at a rate slower than the wild-type plant. Both transgenic plants have normal appearance (Fig. 3). Previous efforts to engineer tobacco Rubisco demonstrated that the growth rate and photosynthetic properties of transplastomic plants are generally consistent with the expression levels and catalytic properties of the recombinant Rubisco^{2,17}. We believe it is

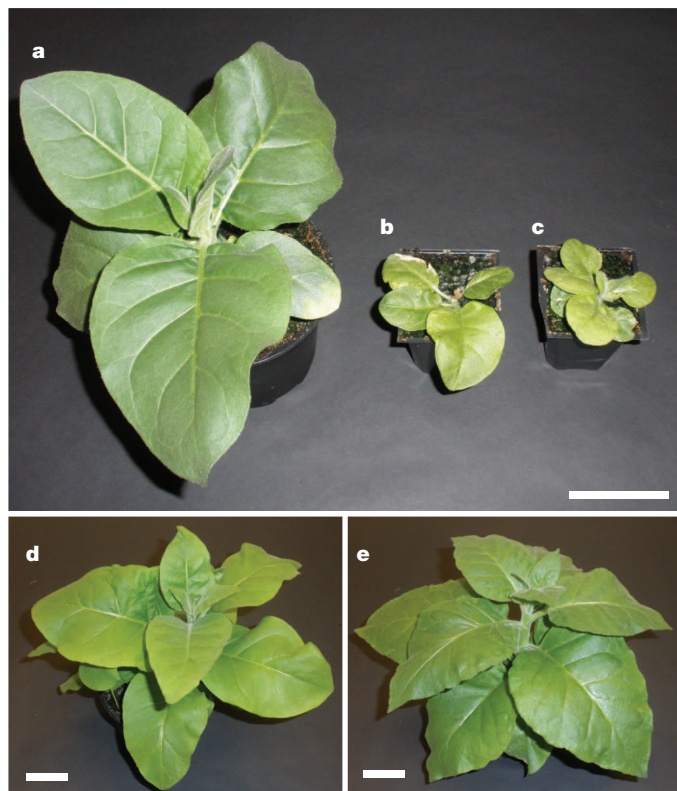


Figure 3 | Phenotype of the wild-type and transplastomic tobacco lines. Plants were grown at atmospheric CO_2 level about 9,000 p.p.m. **a–e**, Pictures showing 6-week-old wild-type (**a**), SeLSX (**b**), and SeLSM35 (**c**); and 10-week-old SeLSX (**d**) and SeLSM35 (**e**) tobacco lines grown in the same conditions. Scale bars, 5 cm.

also the case in our transplastomic plants. Our preliminary analyses to quantify the Rubisco content using the CABP (2-carboxy-D-arabinitol-1,5-bisphosphate) binding method indicate that the Rubisco concentrations in the two chloroplast transformants are approximately 12–18% of that in the wild-type plant (Extended Data Table 1)²³. In addition, the lower levels of total soluble proteins and chlorophyll concentrations probably contribute to the observed slow growth of the two chloroplast transformants (Extended Data Table 1).

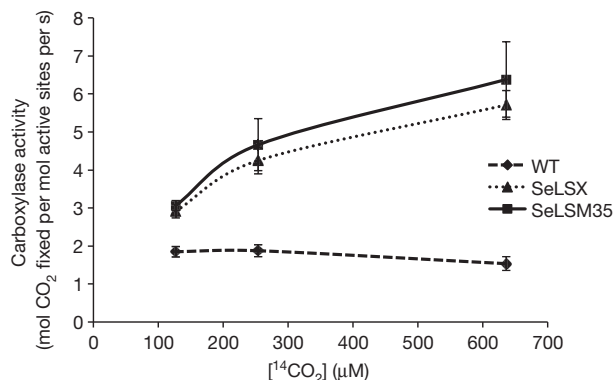


Figure 4 | Carboxylase activities at different $^{14}\text{CO}_2$ concentrations. CO_2 fixation by crude leaf homogenates from tobacco lines expressing cyanobacterial Rubisco (SeLSX and SeLSM35) and wild-type tobacco (WT). The rates of carboxylase activity (mol CO_2 fixed per mol active sites per s) at each point of the curves are the means \pm standard deviation of the 2, 4 and 6 min data obtained in two independent assays at different CO_2 concentrations (125 μM , 250 μM , 640 μM).

The fact that both transgenic lines could grow autotrophically indicated that active cyanobacterial Rubisco has assembled. We measured the carboxylase activities of the cyanobacterial Rubisco in the leaf homogenates at room temperature using ribulose biphosphate (RuBP) and several concentrations of radiolabelled sodium bicarbonate ($\text{NaH}^{14}\text{CO}_3$). The assays were performed in the presence of 10 mM, 20 mM and 50 mM $\text{NaH}^{14}\text{CO}_3$, which at pH 8.0 would generate dissolved CO_2 concentrations of approximately 125 μM , 250 μM and 640 μM , respectively. The carboxylase activity of Rubisco in the tobacco control did not increase upon increasing the CO_2 concentration, confirming that the native enzyme was already saturated at 125 μM of dissolved CO_2 (Fig. 4). In contrast, cyanobacterial Rubisco displayed greater carboxylase activity at higher CO_2 concentrations, with a rate of catalysis which exceeded that of the tobacco enzyme at each CO_2 concentration. Our measured kinetic values are consistent with the reported rate and Michaelis constants for CO_2 ($\sim 3 \text{ s}^{-1}$ and 10.7 μM for tobacco and $\sim 12 \text{ s}^{-1}$ and 200 μM for the enzyme in *Synechococcus* PCC6301, respectively)^{2,24}. We confirmed that the carboxylase activities detected in our samples were specific to Rubisco, as they were entirely dependent on the presence of RuBP and were inhibited by CABP²⁵ (Extended Data Fig. 3). The high carboxylase activities detected in the transformants are consistent with the absence of interference by tobacco SSU in the assembly of bona fide cyanobacterial Rubisco in the chloroplasts. Furthermore, both transgenic lines exhibited high Rubisco activities despite differences in its intra-organellar organization.

We included RbcX in one of our chloroplast transformation vectors because it has been shown to enhance the assembly of the LSU core complex before formation of the final hexadecameric complex⁷. However, Se7942 lacking RbcX suffered no defect in growth rate or Rubisco activity²⁶. As line SeLSM35 lacks RbcX but has active Rubisco, evidently Se-RbcX is not essential for the assembly of functional cyanobacterial Rubisco in chloroplasts. CcmM35, through its SSU-like domains, might assist in the assembly of cyanobacterial Rubisco in SeLSM35 in the absence of RbcX.

The transgenic plants described here are absolutely dependent on the cyanobacterial Rubisco for carbon fixation. If the oxygenation reaction of cyanobacterial Rubisco can be suppressed and the local CO_2 concentration in the vicinity of the enzyme can be raised by further engineering, CO_2 assimilation may be enhanced, and the necessity to divert so much fixed nitrogen into this enzyme may be diminished. Recently, we demonstrated that the shell proteins of β -carboxysomes could form structures similar to empty microcompartments in the chloroplast stroma²⁷. Introduction of the carboxysome shell proteins, the required internal proteins, and appropriate transporters into transgenic plants containing cyanobacterial Rubisco is predicted to result in significantly enhanced photosynthetic performance in vascular plants^{5,6}. This report, demonstrating that cyanobacterial Rubisco can assemble into active enzyme in a C3 plant and support autotrophic photosynthesis, is an important step towards the introduction of a complete and functional CCM into the chloroplasts of vascular plants.

Online Content Methods, along with any additional Extended Data display items and Source Data, are available in the online version of the paper; references unique to these sections appear only in the online paper.

Received 17 June; accepted 14 August 2014.

Published online 17 September 2014.

- Andersson, I. & Backlund, A. Structure and function of Rubisco. *Plant Physiol. Biochem.* **46**, 275–291 (2008).
- Whitney, S. M., Houtz, R. L. & Alonso, H. Advancing our understanding and capacity to engineer nature's CO_2 -sequestering enzyme, Rubisco. *Plant Physiol.* **155**, 27–35 (2011).
- Parry, M. A. J. *et al.* Rubisco activity and regulation as targets for crop improvement. *J. Exp. Bot.* **64**, 717–730 (2013).
- Zarzycki, J., Axen, S. D., Kinney, J. N. & Kerfeld, C. A. Cyanobacterial-based approaches to improving photosynthesis in plants. *J. Exp. Bot.* **64**, 787–798 (2013).
- McGrath, J. M. & Long, S. P. Can the cyanobacterial carbon-concentrating mechanism increase photosynthesis in crop species? A theoretical analysis. *Plant Physiol.* **164**, 2247–2261 (2014).

6. Price, G. D. *et al.* The cyanobacterial CCM as a source of genes for improving photosynthetic CO₂ fixation in crop species. *J. Exp. Bot.* **64**, 753–768 (2013).
7. Whitney, S. M., Baldet, P., Hudson, G. S., Andrews, T. J. & Form, I. Rubiscos from non-green algae are expressed abundantly but not assembled in tobacco chloroplasts. *Plant J.* **26**, 535–547 (2001).
8. Kanevski, I., Maliga, P., Rhoades, D. F. & Gutteridge, S. Plastome engineering of ribulose-1,5-bisphosphate carboxylase/oxygenase in tobacco to form a sunflower large subunit and tobacco small subunit hybrid. *Plant Physiol.* **119**, 133–142 (1999).
9. Saschenbrecker, S. *et al.* Structure and function of RbcX, an assembly chaperone for hexadecameric rubisco. *Cell* **129**, 1189–1200 (2007).
10. Long, B. M., Badger, M. R., Whitney, S. M. & Price, G. D. Analysis of carboxysomes from *Synechococcus* PCC7942 reveals multiple Rubisco complexes with carboxysomal proteins CcmM and CcaA. *J. Biol. Chem.* **282**, 29323–29335 (2007).
11. Cameron, J. C., Wilson, S. C., Bernstein, S. L. & Kerfeld, C. A. Biogenesis of a bacterial organelle: the carboxysome assembly pathway. *Cell* **155**, 1131–1140 (2013).
12. Chen, A. H., Robinson-Mosher, A., Savage, D. F., Silver, P. A. & Polka, J. K. The bacterial carbon-fixing organelle is formed by shell envelopment of preassembled cargo. *PLoS ONE* **8**, e76127 (2013).
13. Parry, M. A. J., Andralojc, P. J., Mitchell, R. A. C., Madgwick, P. J. & Keys, A. J. Manipulation of Rubisco: the amount, activity, function and regulation. *J. Exp. Bot.* **54**, 1321–1333 (2003).
14. Zhu, X. G., Long, S. P. & Ort, D. R. Improving photosynthetic efficiency for greater yield. *Annu. Rev. Plant Biol.* **61**, 235–261 (2010).
15. Dhirga, A., Portis, A. R. & Daniell, H. Enhanced translation of a chloroplast-expressed *RbcS* gene restores small subunit levels and photosynthesis in nuclear *RbcS* antisense plants. *Proc. Natl Acad. Sci. USA* **101**, 6315–6320 (2004).
16. von Caemmerer, S., Quick, W. P. & Furbank, R. T. The development of C4 rice: current progress and future challenges. *Science* **336**, 1671–1672 (2012).
17. Whitney, S. M. & Andrews, T. J. Plastome-encoded bacterial ribulose-1,5-bisphosphate carboxylase/oxygenase (RubisCO) supports photosynthesis and growth in tobacco. *Proc. Natl Acad. Sci. USA* **98**, 14738–14743 (2001).
18. Maliga, P. & Tungsuchat-Huang, T. Plastid transformation in *Nicotiana tabacum* and *Nicotiana sylvestris* by biolistic DNA delivery to leaves. *Methods Mol. Biol.* **1132**, 147–163 (2014).
19. Zhou, F., Karcher, D. & Bock, R. Identification of a plastid intercistronic expression element (IEE) facilitating the expression of stable translatable monocistronic mRNAs from operons. *Plant J.* **52**, 961–972 (2007).
20. Drechsel, O. & Bock, R. Selection of Shine–Dalgarno sequences in plastids. *Nucleic Acids Res.* **39**, 1427–1438 (2011).
21. Long, B. M., Rae, B. D., Badger, M. R. & Price, G. D. Over-expression of the beta-carboxysomal CcmM protein in *Synechococcus* PCC7942 reveals a tight co-regulation of carboxysomal carbonic anhydrase (CcaA) and M58 content. *Photosynth. Res.* **109**, 33–45 (2011).
22. Long, B. M., Tucker, L., Badger, M. R. & Price, G. D. Functional cyanobacterial β -carboxysomes have an absolute requirement for both long and short forms of the CcmM protein. *Plant Physiol.* **153**, 285–293 (2010).
23. Yokota, A. & Canvin, D. T. Ribulose bisphosphate carboxylase/oxygenase content determined with [¹⁴C]carboxypentitol bisphosphate in plants and algae. *Plant Physiol.* **77**, 735–739 (1985).
24. Mueller-Cajar, O. & Whitney, S. M. Evolving improved *Synechococcus* Rubisco functional expression in *Escherichia coli*. *Biochem. J.* **414**, 205–214 (2008).
25. Parry, M. A. J., Keys, A. J., Madgwick, P. J., Carmo-Silva, A. E. & Andralojc, P. J. Rubisco regulation: a role for inhibitors. *J. Exp. Bot.* **59**, 1569–1580 (2008).
26. Emlyn-Jones, D., Woodger, F. J., Price, G. D. & Whitney, S. M. RbcX can function as a Rubisco chaperonin, but is non-essential in *Synechococcus* PCC7942. *Plant Cell Physiol.* **47**, 1630–1640 (2006).
27. Lin, M. T. *et al.* β -carboxysomal proteins assemble into highly organized structures in *Nicotiana* chloroplasts. *Plant J.* **79**, 1–12 (2014).

Acknowledgements We thank C. Kerfeld (Michigan State University) for helpful discussion and providing us with the Se7942 genomic DNA and purified His-tagged CcmM protein, W. Li (Cornell University) for technical assistance in generating, selecting and analysing the tobacco chloroplast transformants and M. Waqar Hameed (Cornell University) for the codon-optimized cyanobacterial Rubisco genes. This material is based upon work supported by the National Science Foundation under grant number EF-1105584 to M.R.H., Biotechnology and Biological Sciences Research Council under grant number BB/I024488/1 to M.A.J.P. and the National Institute of General Medical Sciences of the National Institutes of Health under award number F32GM103019 to M.T.L. P.J.A. and M.A.J.P. also acknowledge support from the 20:20 Wheat Institute Strategic Program (BBSRC BB/J/00426X/1).

Author Contributions M.T.L. designed and generated the DNA constructs and the transgenic tobacco lines. A.O. carried out the TEM imaging, protein analyses and Rubisco activity assays. M.R.H., P.J.A. and M.A.J.P. supervised the project. All authors interpreted results and wrote the manuscript.

Author Information The nucleotide sequences are deposited in GenBank with accession numbers KM102745 and KM102746 for SeLSX and SeLSM35 tobacco lines, respectively. Reprints and permissions information is available at www.nature.com/reprints. The authors declare no competing financial interests. Readers are welcome to comment on the online version of the paper. Correspondence and requests for materials should be addressed to M.R.H. (mrh5@cornell.edu).

Glial origin of mesenchymal stem cells in a tooth model system

Nina Kaukua^{1*}, Maryam Khatibi Shahidi^{2*}, Chrysoula Konstantinidou³, Vyacheslav Dyachuk^{4,5}, Marketa Kaucka⁴, Alessandro Furlan⁶, Zhengwen An⁷, Longlong Wang⁷, Isabell Hultman⁸, Lars Åhrlund-Richter⁸, Hans Blom⁹, Hjalmar Brismar⁹, Natalia Assaife Lopes⁶, Vassilis Pachnis³, Ueli Suter¹⁰, Hans Clevers^{11,12}, Irma Thesleff¹³, Paul Sharpe⁷, Patrik Ernfors⁶, Kaj Friedl¹ & Igor Adameyko⁴

Mesenchymal stem cells occupy niches in stromal tissues where they provide sources of cells for specialized mesenchymal derivatives during growth and repair¹. The origins of mesenchymal stem cells have been the subject of considerable discussion, and current consensus holds that perivascular cells form mesenchymal stem cells in most tissues. The continuously growing mouse incisor tooth offers an excellent model to address the origin of mesenchymal stem cells. These stem cells dwell in a niche at the tooth apex where they produce a variety of differentiated derivatives. Cells constituting the tooth are mostly derived from two embryonic sources: neural crest ectomesenchyme and ectodermal epithelium². It has been thought for decades that the dental mesenchymal stem cells³ giving rise to pulp cells and odontoblasts derive from neural crest cells after their migration in the early head and formation of ectomesenchymal tissue^{4,5}. Here we show that a significant population of mesenchymal stem cells during development, self-renewal and repair of a tooth are derived from peripheral nerve-associated glia. Glial cells generate multipotent mesenchymal stem cells that produce pulp cells and odontoblasts. By combining a clonal colour-coding technique⁶ with tracing of peripheral glia, we provide new insights into the dynamics of tooth organogenesis and growth.

Shortly after the dental placode is induced, nerves intimately associate with the developing tooth⁷. To address whether glia-derived cells contribute to dental mesenchymal stem cells (MSCs) during tooth organogenesis, we used mouse strains allowing for permanent genetic labelling of multipotent^{8,9} Schwann cell precursors (SCPs) and Schwann cells.

Proteolipid protein 1 (PLP1) and sex-determining region Y-box 10 (Sox10) are expressed in cranial neural crest, but after migration around embryonic days (E)9–10, they are retained in SCPs and not in mesenchyme^{10,11}. SCPs at E11.5–12.5 express typical markers of Schwann cell lineage (Supplementary Information and Extended Data Fig. 1). *PLP-CreERT2* and *Sox10-CreERT2* mice^{8,12} were therefore used for lineage tracing of SCPs. We controlled the specificity of PLP1 expression at E12.5 (Fig. 1a, b) and confirmed SCP-selective recombination in *PLP-CreERT2/R26YFP* mice by injecting tamoxifen at E12.5. Twenty-four hours later, traced cells expressing yellow fluorescent protein (YFP⁺) were located along nerves (Fig. 1c, Supplementary Information and Extended Data Fig. 1m–p). CreERT2 protein was confined to Sox10⁺ SCPs (Supplementary Information and Extended Data Fig. 1q–t). After tracing for 36 h, mesenchymal YFP⁺/CreERT2⁺ cells appeared close to nerves at the tooth site (Supplementary Information and Extended Data Fig. 2a–d). Induction of recombination at E12.5 and harvesting at E15.5–17.5 resulted

in numerous traced cells along peripheral nerves and inside developing incisors (Fig. 1d–f, Supplementary Information and Extended Data Fig. 3a–g). YFP⁺ cells formed streams towards the odontoblast layer in spatial coordination with YFP⁺ odontoblasts (Fig. 1d). This was independently confirmed in *Sox10-CreERT2* embryos (Fig. 1i–k and Supplementary Information and Extended Data Fig. 3h–k). Sox10 is expressed in SCPs and not in mesenchyme at E12.5 and at E15.5 (Fig. 1g–h, Supplementary Information and Extended Data Figs 1a–c, g–k, q–s, 2e–o and 3l–n). YFP⁺ pulp cells and odontoblasts formed the same pattern as seen with *PLP-CreERT2* tracing (Fig. 1i–k). Therefore, SCPs must contribute to pulp and odontoblasts since CreERT2 protein in *Sox10-CreERT2* and *PLP-CreERT2* embryos was confined to SCPs (Supplementary Information and Extended Data Figs 2a–d, m–p and 3c–k).

To examine if patches of SCP-derived odontoblasts and pulp cells have clonal structure, we crossed the *PLP-CreERT2* mice to the *R26RConfetti* reporter strain that allows for colour-encoded identification of clones⁶. This experiment revealed an organized clonal relationship between SCPs, pulp cells and odontoblasts (Supplementary Information and Extended Data Fig. 4a–d) and demonstrated that SCP-derived single MSCs produce pulpal and odontoblast fates (Supplementary Information and Extended Data Fig. 4e). We next examined whether ectomesenchyme-derived MSCs generate the same fates and patterns as SCP-derived MSCs. We induced recombination in neural crest at E8.5 in *PLP-CreERT2/R26RConfetti* strain, before segregation of CreERT2 expression into glial lineage. Recombination in both nerve-associated cells and ectomesenchyme was confirmed at E9.5 (Fig. 2a). When embryos were analysed at E17.5, it became apparent that ectomesenchyme- and SCP-derived MSCs generate the same fates and patterns in pulp and odontoblast layer (Fig. 2b–f).

To address whether Schwann cells generate MSCs also in adult growing incisors, we first confirmed that all Sox10⁺ cells in the apical proliferative zone were nerve-associated (Supplementary Information and Extended Data Fig. 5) and expressed Schwann cell markers (Supplementary Information and Extended Data Fig. 6a–g). CreERT2 protein was found in the apex at nerve sites in *Sox10-CreERT2* and *PLP-CreERT2* teeth (Supplementary Information and Extended Data Fig. 6h–q). Additionally, expression of CreERT2 protein driven by the PLP-promoter was identified exclusively in a subpopulation of Sox10⁺ Schwann cells (Supplementary Information and Extended Data Fig. 6j–q). Next, we used *PLP-CreERT2* and *Sox10-CreERT2* animals to analyse the progeny in growing incisors. We injected tamoxifen at postnatal day 60–85 and analysed the teeth 2–3 days later. Small numbers of YFP⁺ cells appeared

¹Department of Neuroscience, Karolinska Institutet, Stockholm 17177, Sweden. ²Department of Dental Medicine, Karolinska Institutet, Stockholm 17177, Sweden. ³Division of Molecular Neurobiology, MRC National Institute for Medical Research, London NW7 1AA, UK. ⁴Department of Physiology and Pharmacology, Karolinska Institutet, Stockholm 17177, Sweden. ⁵A.V. Zhirmunsky Institute of Marine Biology of the Far Eastern Branch of the Russian Academy of Sciences, Vladivostok 690041, Russia. ⁶Unit of Molecular Neurobiology, Department of Medical Biochemistry and Biophysics, Karolinska Institutet, Stockholm 17177, Sweden. ⁷Department of Craniofacial Development and Stem Cell Biology, King's College London Dental Institute, Guy's Hospital, London SE1 3QD, UK. ⁸Department of Women's and Children's Health, Karolinska Institutet, Stockholm 17177, Sweden. ⁹Science for Life Laboratory, Royal Institute of Technology, Stockholm 17177, Sweden. ¹⁰Department of Biology, Institute of Molecular Health Sciences, ETH Zurich CH-8093, Switzerland. ¹¹Hubrecht Institute, Koninklijke Nederlandse Akademie van Wetenschappen (KNAW), PO Box 85164, 3508 AD Utrecht, the Netherlands. ¹²Department of Molecular Genetics, University Medical Center Utrecht, Utrecht 3508 GA, the Netherlands. ¹³Institute of Biotechnology, Developmental Biology Program, University of Helsinki, Helsinki FI-00014, Finland.

*These authors contributed equally to this work.

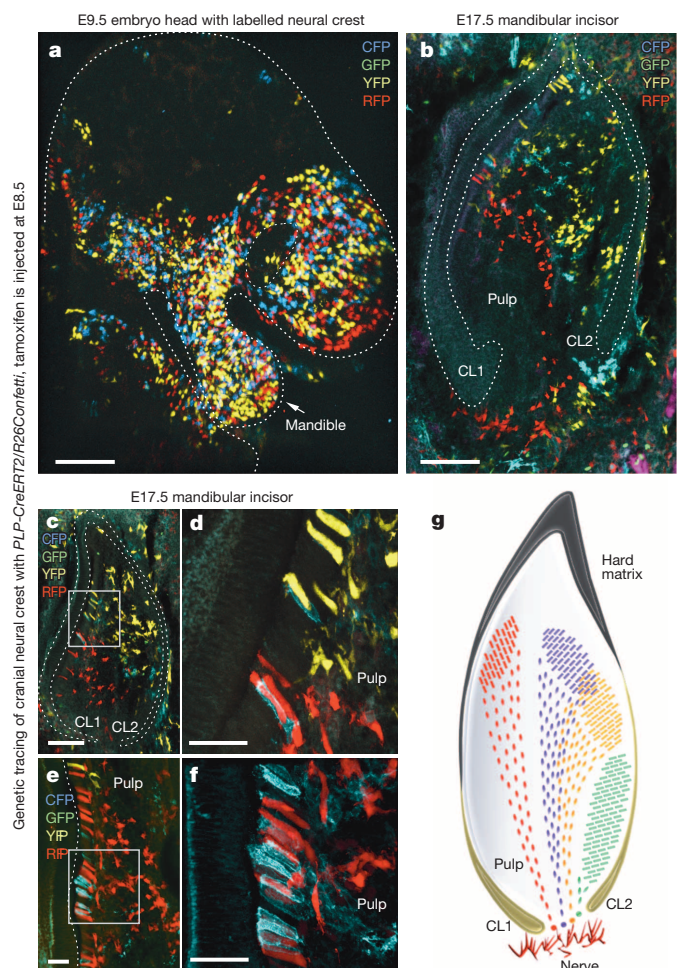


Figure 2 | Clonal contribution of neural crest to tooth development. **a–f**, Tracing of neural-crest-derived cells in *PLP-CreERT2/R26Confetti* embryos. **a**, Embryo traced from E8.5 to E9.5, projection of confocal stack. Dotted line demarcates developing head. Arrow: mandible. **b–f**, Sections of incisor traced from E8.5 to E17.5. **d, f**, Projections of stacks corresponding to areas outlined in **c** and **e**. Note correlation between colours of odontoblasts and adjacent pulp cells. **g**, Illustration of clonally organized pulp and odontoblasts. **b, c, e**, Dotted line: enamel organ. Scale bars, 100 μm (**a–c**); 25 μm (**d–f**). CL1 and CL2 indicate labial and lingual aspects of cervical loop.

colour (Fig. 3m). Clonal streams of pulp cells and odontoblasts intermingled at borders with non-labelled or different-coloured cells (Fig. 3l–p). MSCs produced high numbers of offspring, only a part of which was localized proximally to the dental epithelium and later became pre-odontoblasts. The majority of the progeny acquired a pulpal fate and formed organized streams, with earlier cells progressively displaced distally. Consequently, pulp cells and odontoblasts from the same clone remained associated during growth. These data suggest that progenies of several clones compete for the limited space at the inner surface of the cervical loop and, thus, for the odontoblast fate and final contribution. Indeed, the proportion of odontoblasts within the progeny of a single stem cell varied widely (Fig. 3s). Accordingly, the proximity of an MSC to the cervical loop correlated with the amount of odontoblast-fated progeny and may thus regulate the balance between odontoblast and pulp fates within a single clone (Fig. 3t). Additionally, streams originating closer to the cervical loop contained more cells and connected to larger clusters of odontoblasts than more central streams (Fig. 3q, t–v, Supplementary Information and Extended Data Fig. 8). Lastly, we found no support for a hypothesis that odontoblasts and pulp cells are generated from different pools of MSCs.

adjacent to nerves in the apical incisor (Fig. 3a–c, Supplementary Information and Extended Data Fig. 7a–e). After 5 days YFP⁺ cells at the apex increased in numbers (Supplementary Information and Extended Data Fig. 7f–h). The fates of the progeny were examined at times exceeding the incisor self-renewal (from 30 days after tamoxifen injection). We found that Schwann cells give rise to dental MSCs producing pulp cells and odontoblasts in adult teeth (Fig. 3d–f, Supplementary Information and Extended Data Fig. 7i–k).

Tracing in *PLP-CreERT2/R26RConfetti* mice demonstrated that streams of traced cells were connected to clusters of odontoblasts originating from same recombination events in Schwann cells (Fig. 3g–r, Supplementary Information and Extended Data Fig. 7i–k). The streams appeared increasingly dispersed as they approached odontoblasts labelled by the same

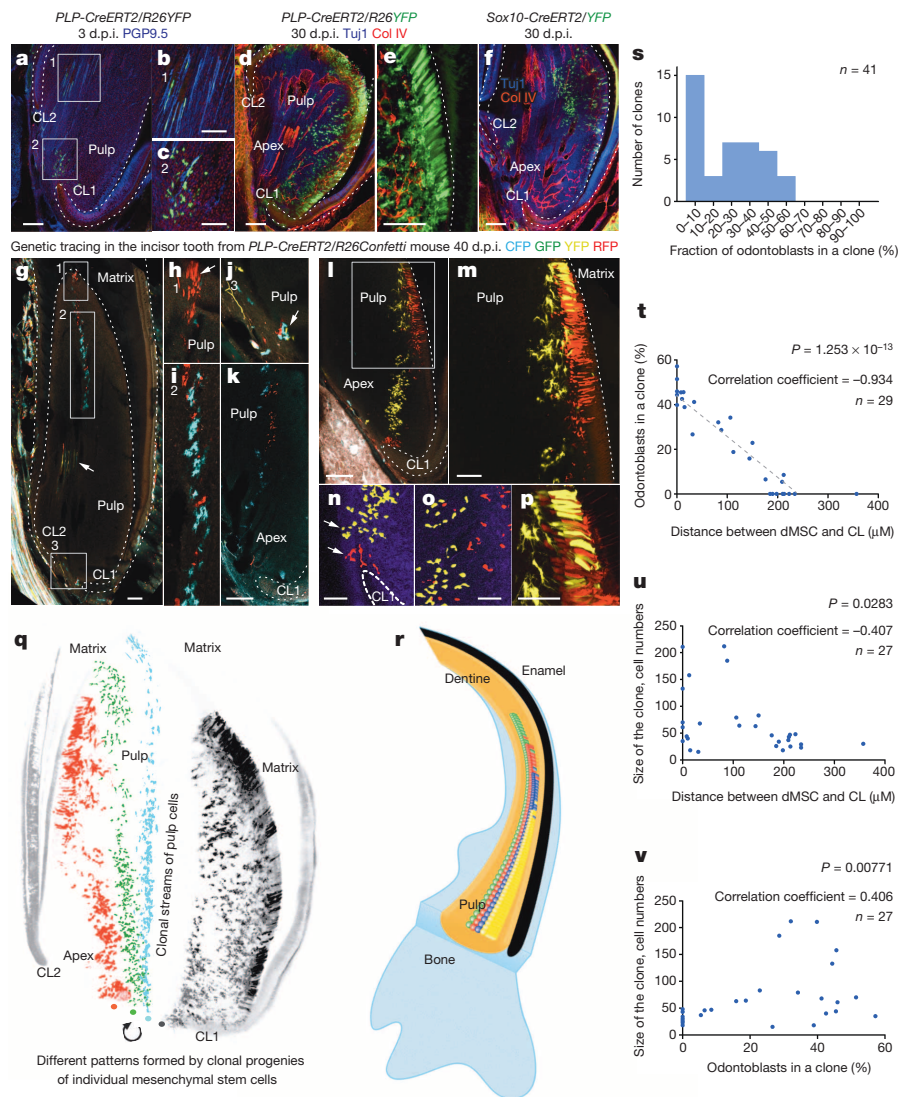


Figure 3 | Schwann cells give rise to dental MSCs in the adult incisor. **a–c**, Incisor traced for 3 days from adult *PLP-CreERT2/R26YFP* mouse. Note protein gene product 9.5 (PGP9.5)⁺ nerve fibres (**a**). **b, c**, Magnified areas from **a**. **d, e**, Incisor traced for 30 days from adult *PLP-CreERT2/R26YFP* mouse. Note collagen IV⁺ blood vessels (**d**). **e**, YFP⁺ odontoblasts and adjacent pulp cells. **f**, Incisor traced for 30 days from *Sox10-CreERT2/R26YFP* mouse. **g–k**, Incisor traced for 40 days from *PLP-CreERT2/R26Confetti* incisor. **h–j**, Magnified areas from **g**. Arrow in **h** indicates a cluster of odontoblasts; arrow in **j** points at CFP⁺ and RFP⁺ cells in proximity to a cervical loop at the base of CFP⁺ and RFP⁺ streams shown in **g** and **i**. **k**, Streams of CFP⁺ and RFP⁺ pulp cells next to **i** and **j**. **l, m**, Incisor traced for 40 days from *PLP-CreERT2/R26Confetti* mouse with YFP⁺ and RFP⁺ pulp cells adjacent to clusters of odontoblasts with corresponding colours. **m**, Magnified region from **l**. **n**, Stream of pulp cells (arrows) in proximity to the cervical loop; yellow and red isosurfaces mark YFP⁺ and RFP⁺ cells. **o, p**, Progenies of individual MSCs intermingle with neighbouring clones in pulp (**o**) and odontoblast layer (**p**), projections of confocal stacks. **q, r**, Clonal organization of mesenchymal compartment in adult incisor. **a–n**, Dotted line, enamel organ and mineralized matrix. Scale bars, 100 μ m (**a, d, f, g, k, l**); 50 μ m (**b, c, e, m–p**). CL1 and CL2 indicate labial and lingual aspects of cervical loop. d.p.i., days post-injection. **s**, Incidence of mesenchymal clones depending on fraction of odontoblasts within the clone. **t–v**, Proximity of dental MSCs (dMSCs) to cervical loop (CL) correlates with clonal size and proportion of odontoblasts in clone.

To prove the importance of the innervation for tooth growth, we denervated incisors 24 h after tamoxifen injection in *PLP-CreERT2/R26YFP* mice. After 10 days we found almost no progeny in denervated teeth, while contralateral control teeth contained abundant YFP⁺ odontoblasts and pulp cells (Supplementary Information and Extended Data Fig. 8j–p). Thus, generation of a progeny from PLP⁺ cells is impaired without innervation.

We quantified the amount of Schwann-cell-derived progeny in *PLP-CreERT2/R26YFP* mice (Supplementary Information and Extended Data Figs 7l and 9a) and found that it varied from $8.23 \pm 3.3\%$ (single tamoxifen injection) to $47.28 \pm 4.02\%$ (multiple injections) (Supplementary Information and Extended Data Fig. 7m–o). Hence, in addition to Schwann cells and SCPs, there are other sources of dental MSCs, possibly pericytes, which generate odontoblasts in injured teeth¹³. We addressed whether pericytes could be derived from peripheral glia, using NG2 staining¹⁴ on sections from traced mice. However, NG2⁺ pericytes in teeth were never YFP⁺. Similar results were obtained in adult incisors (Supplementary Information and Extended Data Fig. 10). Thus, we exclude pericytes as an intermediate for the Schwann-cell- and SCP-derived pulp cells and odontoblasts.

Next we searched for stem cell markers in Schwann-cell-derived dental MSCs. Results from an array of methods strongly suggest that a population of Schwann-cell-derived dental MSCs are Thy1 (CD90)⁺ (Supplementary Information, Extended Data Fig. 9 and Supplementary Video 1).

Finally, we examined if Schwann-cell-derived cells produce regenerative dentine after trauma. We induced recombination in adult *PLP-CreERT2/R26YFP* mice, and allowed Schwann cells to generate progeny for 1 month. We then inflicted a confined damage to the tooth (Fig. 4a). Six days later, numerous traced cells were observed at the injury site, including odontoblast-like alizarin-red-positive cells adjacent to matrix fragments (Fig. 4b–f). Such features were not seen in intact teeth (Fig. 4g–h) or other controls (Fig. 4i). To confirm that *PLP-CreERT2*-traced cells produce mineralized matrix, we cultured dissociated traced tooth pulp explants for 1 week. YFP⁺ cells were then sorted by fluorescence-activated cell sorting (FACS) for cultivation in an osteogenic assay (Fig. 4j). Under these conditions, YFP⁺ cells deposited mineralized matrix (Fig. 4k–l). Thus, Schwann-cell-derived cells exhibit MSC-like characteristics and participate in the regeneration of dentine after damage.

To conclude, SCPs and Schwann cells contribute to development, growth and regeneration of teeth. The concept of glia-to-MSCs transition expands the borders of the multipotency of SCPs¹⁵ and suggests that Schwann cells and SCPs are dormant neural-crest-like cells that can be recruited from nerves and contribute to peripheral tissues. On the basis of our results, Schwann cells and SCP might be the *in vivo* origin of neural-crest-derived multipotent stem cells identified in cultures of dissociated embryonic and adult tissues and designated as postmigratory cranial neural crest cells¹⁶ and skin-derived precursors¹⁷.

Six days after the damage inflicted to *PLP-CreERT2/R26YFP* incisor traced for 1 month

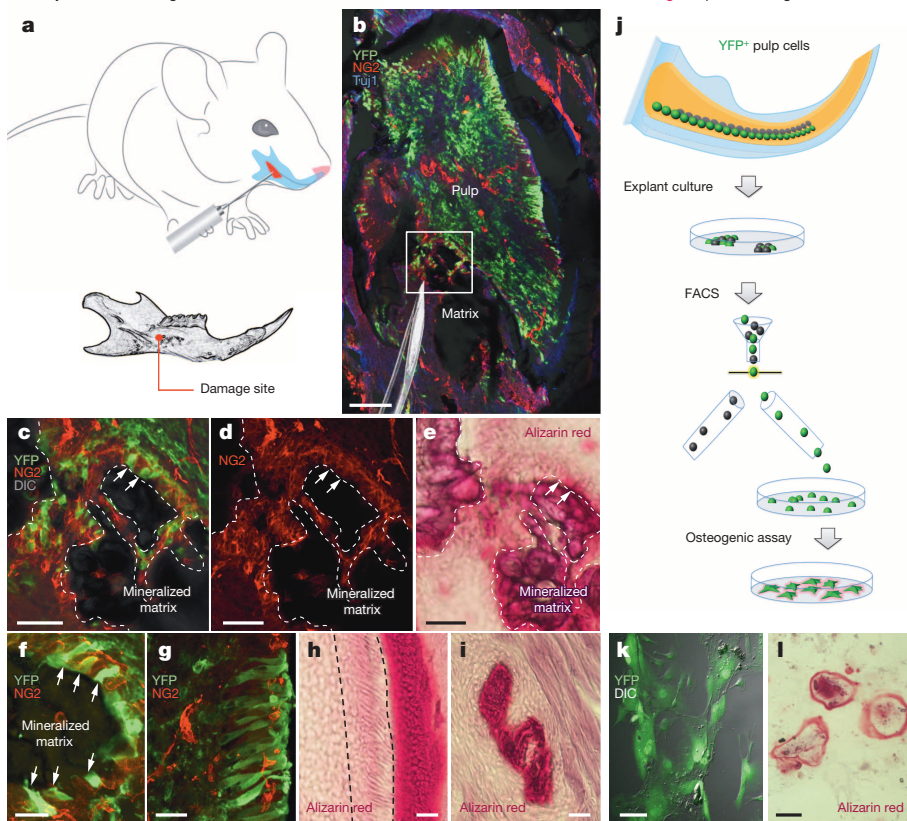


Figure 4 | Schwann-cell-derived cells participate in regeneration of incisors after damage.

a, Damage to 1-month traced *PLP-CreERT2/R26YFP* adult incisor. Red highlights the injured region. **b–e**, YFP⁺ cells at the injury site, after recovery for 6 days. Needle silhouette shows direction of damage. **c, d**, Magnified area from **b**, confocal stack. **e**, Alizarin red staining of damaged region outlined in **b**. Note stained area around ectopic matrix. Arrows in **c–e** point at YFP⁺ cells adjacent to ectopic matrix; dotted line indicates mineralized matrix. **f**, Ectopic matrix in damaged area with YFP⁺ odontoblast-like cells (arrows). **g**, YFP⁺ odontoblasts and NG2⁺ pericytes in intact control incisor. **h**, Alizarin red staining of the odontoblast layer in control. **i**, Matrix fragment from damaged incisor displaced into facial muscle. Note absence of alizarin red staining around matrix fragment compared with ectopic matrix within the pulp (**e**). **j**, Experimental design for addressing mineralizing potential of Schwann-cell-derived cells. **k, l**, Mineralization assay. Schwann-cell-derived YFP⁺ cells (**k**) produce alizarin red⁺ matrix (**l**) *in vitro* after 1 week in osteogenic media. **k, l**, Mineralization assay. Schwann-cell-derived YFP⁺ cells (**k**) produce alizarin red⁺ matrix (**l**) *in vitro* after 1 week in osteogenic media. **k**, DIC, differential interference contrast. Scale bars, 100 μ m (**b**); 50 μ m (**c–e**); 25 μ m (**f–l**).

METHODS SUMMARY

We used *PLP-CreERT2/R26YFP*¹², *Sox10-CreERT2/R26YFP*⁸, *Thy1-Cre/R26YFP*¹⁸ and *R26Confetti*⁶ mouse strains. Immunohistochemistry and *in situ* hybridization used standard protocols on frozen sections of embryos or adult teeth. Multispectral imaging used Zeiss LSM700 and Zeiss LSM780 confocal systems¹¹.

Online Content Methods, along with any additional Extended Data display items and Source Data, are available in the online version of the paper; references unique to these sections appear only in the online paper.

Received 22 August 2013; accepted 28 May 2014.

Published online 27 July 2014.

- Keating, A. Mesenchymal stromal cells: new directions. *Cell Stem Cell* **10**, 709–716 (2012).
- Koussoulakou, D. S., Margaritis, L. H. & Koussoulakos, S. L. A curriculum vitae of teeth: evolution, generation, regeneration. *Int. J. Biol. Sci.* **5**, 226–243 (2009).
- Zhao, H. *et al.* Secretion of shh by a neurovascular bundle niche supports mesenchymal stem cell homeostasis in the adult mouse incisor. *Cell Stem Cell* **14**, 160–173 (2014).
- Caton, J. & Tucker, A. S. Current knowledge of tooth development: patterning and mineralization of the murine dentition. *J. Anat.* **214**, 502–515 (2009).
- Miletich, I. & Sharpe, P. T. Neural crest contribution to mammalian tooth formation. *Birth Defect Res. C* **72**, 200–212 (2004).
- Snippert, H. J. *et al.* Intestinal crypt homeostasis results from neutral competition between symmetrically dividing *Lgr5* stem cells. *Cell* **143**, 134–144 (2010).
- Luukko, K. *et al.* Secondary induction and the development of tooth nerve supply. *Ann. Anat.* **190**, 178–187 (2008).
- Laranjeira, C. *et al.* Glial cells in the mouse enteric nervous system can undergo neurogenesis in response to injury. *J. Clin. Invest.* **121**, 3412–3424 (2011).
- Adameyko, I. *et al.* Schwann cell precursors from nerve innervation are a cellular origin of melanocytes in skin. *Cell* **139**, 366–379 (2009).
- Hari, L. *et al.* Temporal control of neural crest lineage generation by Wnt/ β -catenin signaling. *Development* **139**, 2107–2117 (2012).
- Adameyko, I. *et al.* Sox2 and Mitf cross-regulatory interactions consolidate progenitor and melanocyte lineages in the cranial neural crest. *Development* **139**, 397–410 (2012).

- Leone, D. P. *et al.* Tamoxifen-inducible glia-specific Cre mice for somatic mutagenesis in oligodendrocytes and Schwann cells. *Mol. Cell. Neurosci.* **22**, 430–440 (2003).
- Feng, J., Mantesso, A., De Bari, C., Nishiyama, A. & Sharpe, P. T. Dual origin of mesenchymal stem cells contributing to organ growth and repair. *Proc. Natl Acad. Sci. USA* **108**, 6503–6508 (2011).
- Crisan, M., Corselli, M., Chen, W. C. & Peault, B. Perivascular cells for regenerative medicine. *J. Cell. Mol. Med.* **16**, 2851–2860 (2012).
- Adameyko, I. & Lallemand, F. Glial versus melanocyte cell fate choice: Schwann cell precursors as a cellular origin of melanocytes. *Cell. Mol. Life Sci.* **67**, 3037–3055 (2010).
- Chung, I. H. *et al.* Stem cell property of postmigratory cranial neural crest cells and their utility in alveolar bone regeneration and tooth development. *Stem Cells* **27**, 866–877 (2009).
- Jinno, H. *et al.* Convergent genesis of an adult neural crest-like dermal stem cell from distinct developmental origins. *Stem Cells* **28**, 2027–2040 (2010).
- Dewachter, I. *et al.* Neuronal deficiency of presenilin 1 inhibits amyloid plaque formation and corrects hippocampal long-term potentiation but not a cognitive defect of amyloid precursor protein [V717I] transgenic mice. *J. Neurosci.* **22**, 3445–3453 (2002).

Supplementary Information is available in the online version of the paper.

Acknowledgements P. Kovaleva and O. Rogachevskaya helped with illustrations. This study was supported by the Swedish Research Council (I.A., K.F., P.E.), The Bertil Hållsten Research Foundation (I.A.), StratRegen and the Wallenberg Foundation (CLICK, I.A.), the Swiss National Science Foundation (U.S.), Medical Research Council (G0901599; P.S.), a Wallenberg Scholar and European Research Council advanced grant (P.E.), National Graduate School in Odontological Science (M.K.S.), the Swedish Dental Association (N.K., M.K.S.), an EMBO Long-Term Fellowship (M.K.) and Stockholm County Council (N.K.) and Developmental Studies Hybridoma Bank.

Author Contributions N.K., M.K.S., C.K., V.D., M.K., A.F., Z.A., L.W., P.S., I.H., I.A. and K.F. performed experiments, analysed data and wrote the paper. L.A.-R., H.B., H.B., N.A.L., V.P., U.S., H.C., P.S., I.T. and P.E. analysed data and wrote the paper. All authors read and approved the paper.

Author Information Reprints and permissions information is available at www.nature.com/reprints. The authors declare no competing financial interests. Readers are welcome to comment on the online version of the paper. Correspondence and requests for materials should be addressed to I.A. (Igor.Adameyko@ki.se) or K.F. (Kaj.Fried@ki.se).

Antifungal drug resistance evoked via RNAi-dependent epimutations

Silvia Calo¹, Cecelia Shertz-Wall¹, Soo Chan Lee¹, Robert J. Bastidas¹, Francisco E. Nicolás^{2,3}, Joshua A. Graneck^{1,4,5}, Piotr Mieczkowski⁶, Santiago Torres-Martínez³, Rosa M. Ruiz-Vázquez³, Maria E. Cardenas¹ & Joseph Heitman¹

Microorganisms evolve via a range of mechanisms that may include or involve sexual/parasexual reproduction, mutators, aneuploidy, Hsp90 and even prions. Mechanisms that may seem detrimental can be repurposed to generate diversity. Here we show that the human fungal pathogen *Mucor circinelloides* develops spontaneous resistance to the antifungal drug FK506 (tacrolimus) via two distinct mechanisms. One involves Mendelian mutations that confer stable drug resistance; the other occurs via an epigenetic RNA interference (RNAi)-mediated pathway resulting in unstable drug resistance. The peptidylprolyl isomerase FKBP12 interacts with FK506 forming a complex that inhibits the protein phosphatase calcineurin¹. Calcineurin inhibition by FK506 blocks *M. circinelloides* transition to hyphae and enforces yeast growth². Mutations in the *fkba* gene encoding FKBP12 or the calcineurin *cnbR* or *cnaA* genes confer FK506 resistance and restore hyphal growth. In parallel, RNAi is spontaneously triggered to silence the *fkba* gene, giving rise to drug-resistant epimutants. FK506-resistant epimutants readily reverted to the drug-sensitive wild-type phenotype when grown without exposure to the drug. The establishment of these epimutants is accompanied by generation of abundant *fkba* small RNAs and requires the RNAi pathway as well as other factors that constrain or reverse the epimutant state. Silencing involves the generation of a double-stranded RNA trigger intermediate using the *fkba* mature mRNA as a template to produce antisense *fkba* RNA. This study uncovers a novel epigenetic RNAi-based epimutation mechanism controlling phenotypic plasticity, with possible implications for antimicrobial drug resistance and RNAi-regulatory mechanisms in fungi and other eukaryotes.

The pathogenic fungus *M. circinelloides* grows as hyphae aerobically, and as yeast in low oxygen and high-CO₂ conditions³. FKBP12 is a prolyl isomerase conserved throughout eukaryotes that interacts with FK506 and rapamycin and mediates their antifungal activity in *M. circinelloides*⁴ and other fungi. The FKBP12–FK506 and FKBP12–rapamycin complexes inhibit the protein phosphatase calcineurin and the Tor kinase, respectively^{1,5}. FK506 inhibition of calcineurin blocks hyphal growth of *M. circinelloides* and enforces yeast-phase growth² (Fig. 1a and Extended Data Fig. 1a). Exposure to FK506 yields drug-resistant isolates exhibiting hyphal growth emerging from the yeast colony periphery (Extended Data Fig. 1a) at a ratio of one resistant isolate out of $\sim 1 \times 10^6$ yeast cells. A subset of FK506-resistant (FK506^r) isolates harbour mutations in the *fkba* gene encoding FKBP12 or the calcineurin A or B subunit genes *cnaA* and *cnbR* (45 of 64 isolates ($\sim 70\%$), Supplementary Table 1)².

However, several FK506^r isolates (17 of 64 ($\sim 27\%$)) harboured no mutations in the *fkba* or calcineurin target genes. These isolates exhibited resistance to FK506 and rapamycin, but not to cyclosporin A (CsA, which, similar to FK506, enforces largely yeast growth, Fig. 1a) or other drugs (nystatin, amphotericin B, not shown), suggesting that they had not developed multidrug resistance mechanisms. These unusual drug-resistant isolates also reverted frequently within several generations of

vegetative growth on drug-free media and were restored to a wild-type phenotype (yeast growth on exposure to FK506) (Extended Data Fig. 1b, c). Expression analyses revealed a complete loss of *fkba* mRNA and FKBP12 protein in these drug-resistant isolates when grown in media containing FK506. In contrast, mRNA and protein levels were reduced but detectable in some resistant isolates when grown in drug-free media (Fig. 1b, c) and were restored to wild-type levels in revertant isolates that became FK506-sensitive (FK506^s) following growth in drug-free media (Fig. 1b, c).

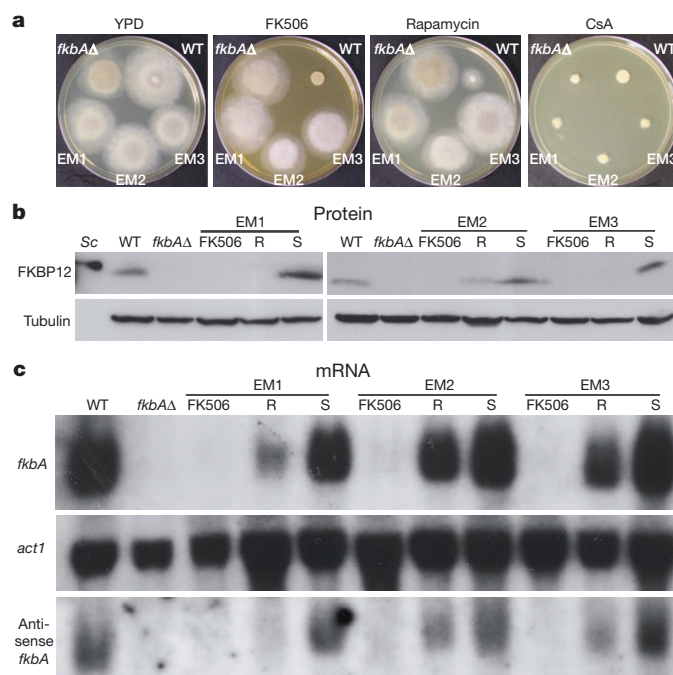


Figure 1 | RNAi-dependent epimutations confer FK506 resistance in *M. circinelloides*. **a**, Wild-type (WT, NRRL3631), *fkba* mutant (*fkbaΔ*) and epimutant strains were grown on yeast extract peptone dextrose (YPD) media alone or supplemented with FK506, rapamycin or cyclosporin A (CsA). Images are representative of two independent experiments. **b**, **c**, The epimutant strains EM1, EM2 and EM3 were grown on YPD media with FK506 (FK506 lanes) or YPD drug-free media (R lanes). The reverted strains EM1-S, EM2-S and EM3-S were grown in YPD media (S lanes) and whole cell protein and RNA extracts were prepared. **b**, Equivalent protein amounts (120 μg) were resolved by SDS-PAGE and analysed by western blot with an anti-*S. cerevisiae*-FKBP12 antibody; tubulin served as a loading control. Images are representative of seven independent experiments. **c**, 50 μg total RNA was analysed by northern blot employing probes specific for *fkba*, *act1* (loading control) and antisense *fkba* mRNAs. Images are representative of six independent experiments for the *fkba* and *act1* probes, and two for the antisense *fkba* probe.

¹Department of Molecular Genetics and Microbiology, Duke University Medical Center, Durham, North Carolina 27710, USA. ²Regional Campus of International Excellence "Campus Mare Nostrum", Murcia 30100, Spain. ³Department of Genetics and Microbiology, Faculty of Biology, University of Murcia, Murcia 30100, Spain. ⁴Department of Biostatistics and Bioinformatics, Duke University Medical Center, Durham, North Carolina 27710, USA. ⁵Duke Center for the Genomics of Microbial Systems, Duke University Medical Center, Durham, North Carolina 27710, USA. ⁶High-Throughput Sequencing Facility, University of North Carolina, Chapel Hill, North Carolina 27599, USA.

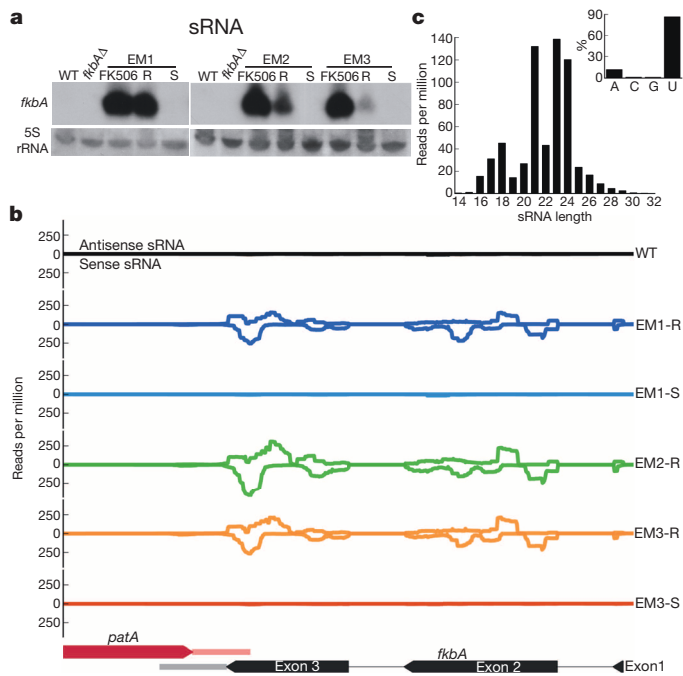


Figure 2 | Epimutant strains express abundant sRNA antisense to *fkbA*. **a**, sRNAs were extracted from wild-type, epimutants (FK506 and R lanes) and reverted strains (S lanes) after growth in YPD media alone (R, S lanes) or with FK506 (FK506 lanes). sRNAs (25 µg) were analysed by sRNA blot employing an antisense-specific probe for the *fkbA* gene or a probe for 5S rRNA (loading control). Images representative of three independent experiments. **b**, The presence of sense and antisense *fkbA* sRNA was analysed by high-throughput sequencing in wild-type, epimutants and two revertant strains (EM1-S and EM3-S). sRNA amount is expressed in reads per million, and they are distributed along the *fkbA* open reading frame (bottom). **c**, Analysis of size and first nucleotide (inset) of antisense sRNAs. The representation corresponds to data obtained from isolate EM1-R. Similar results were observed for the EM2-R and EM3-R epimutants.

As drug resistance was reversible and an active RNAi pathway is present in the organism^{6,7} we hypothesized that drug resistance is RNAi-mediated. Notably, small RNAs (sRNAs) complementary to *fkbA* were detected in these unusual drug-resistant isolates (Fig. 2a and Extended Data Fig. 2a), suggesting a new role for RNAi in the development of transient resistance to antifungal drug exposure. Consistent with the expression analyses, the sRNA signal was highly abundant during growth with FK506 (100%), less abundant when the isolates were grown in drug-free media (~62% and ~25% for epimutant strains EM2 and EM3, respectively, Fig. 2a) and lost when drug resistance reverted (0–0.02%). The *fkbA* silencing was not associated with DNA methylation in *M. circinelloides* (Extended Data Fig. 2b). We term these unusual drug-resistant isolates

epimutants, by analogy with studies in fungi^{8,9}, plants¹⁰ and animals^{11–13}, in which epimutations have been described as silencing of genes that are usually active, or vice versa¹¹.

Our first hypothesis was that RNAi could be triggered via double-strand RNA (dsRNA) production from the overlap in the 3' regions between *fkbA* and its convergently transcribed neighbouring gene *patA* (Extended Data Fig. 3 and Supplementary Table 2). But *patAΔ* mutants did not show any effect on the frequency of *fkbA* epimutational silencing (Table 1, Supplementary Table 1 and Extended Data Fig. 4). 3' rapid amplification of cDNA end assays confirmed that the mRNA from *fkbA* gene and the *pyrG* marker replacing *patA* were not overlapping (Supplementary Table 2). Thus, expression of *patA* to generate overlapping RNA molecules is not necessary for *fkbA* silencing.

As *fkbA* is a highly expressed gene (Fig. 1c), and a high RNA turnover rate has been implicated in the production of aberrant RNA and triggering of silencing^{14–17}, we speculated that an *fkbA* antisense RNA may be generated by an RNA-dependent RNA polymerase (RdRP)¹⁸. Northern blot analysis with an *fkbA* antisense-specific probe revealed an antisense *fkbA* mRNA in all strains with robust *fkbA* expression (Fig. 1c). This *fkbA* antisense RNA is perfectly complementary to the intron-spliced mature *fkbA* sense mRNA, and is 5' capped and polyadenylated (Extended Data Fig. 5). Thus, the antisense RNA is generated from the mature *fkbA* mRNA. The *fkbA* antisense RNA is expressed in the wild-type strain (Fig. 1c); however, RNAi is activated in only a subset of cells selected with FK506. The *in vivo* efficiency of dsRNA formation or its transport to the cytoplasm may limit sRNA levels restricting silencing to fewer cells. Only traces of antisense sRNAs complementary to *fkbA* (16 reads) were detected in the wild-type strain by high-throughput sequencing (Extended Data Fig. 6), supporting this hypothesis.

To test if mutations may have occurred to promote the formation of epimutations, the reverted and now sensitive epimutant strains were exposed to a second round of FK506 to isolate mutants/epimutants. The frequency of epimutation versus mutation to FK506^r in the reverted epimutant strains was similar or even lower than in the parental wild-type strain (Extended Data Fig. 7). Thus, the underlying mechanism appears solely epigenetic and does not require any genetic change in the genome to promote epimutation.

High-throughput sequencing demonstrated abundant sRNAs complementary to the *fkbA* mRNA (antisense) as well as sense sRNA in three epimutant resistant isolates, but these were barely detectable in the wild-type strain or in the two corresponding FK506^s revertants analysed (Fig. 2b). Some sRNA sequences spanned exon–exon junctions (Fig. 2b and Extended Data Fig. 8a), indicating that the source and target of the sRNA is mature mRNA. Most of these sRNAs average 21–24 nucleotides in length, with a bias towards 5' terminal uridine (Fig. 2c), features typical of sRNAs that interact with Argonaute proteins. No further loci were detected exhibiting the same pattern of sRNA production: high level in epimutants and very low levels in wild-type and reverted strains (Extended Data Fig. 8b). Silencing pathways can operate constitutively on *M. circinelloides* endogenous genes during normal growth⁷. In contrast,

Table 1 | Frequency of epimutants/mutants in the wild-type, *patA* and RNAi mutant strains

Strain	Background	Total analysed	Mutations in <i>fkbA</i>	Mutations in <i>cnaA/cnbR</i>	No mutation found	Epimutants (no.)	Epimutants (%)	P value
NRRL3631	Wild type	33	22	0	11	10	30.3	
R7B	<i>leuA</i> [−]	31	22	1	8	7	22.6	
MU434	<i>patAΔ::pyrG leuA</i> [−]	33	28	0	5	5	15.2	0.531
MU435	<i>patAΔ::pyrG leuA</i> [−]	33	26	0	7	7	21.2	1
MU406	<i>dcl1Δ::pyrG leuA</i> [−]	25	23	1	1	1	4	0.06
MU407	<i>dcl1Δ::pyrG leuA</i> [−]	21	18	3	0	0	<4.8	0.033
MU410	<i>dcl2Δ::pyrG leuA</i> [−]	34	31	2	1	0	<2.9	0.004
MU413	<i>ago1Δ::pyrG leuA</i> [−]	26	25	1	0	0	<3.8	0.012
MU426	<i>ago1Δ::pyrG leuA</i> [−]	27	27	0	0	0	<3.7	0.012
MU416	<i>ago2Δ::pyrG leuA</i> [−]	23	16	3	4	4	17.4	0.741
MU414	<i>ago3Δ::pyrG leuA</i> [−]	27	22	1	4	4	14.8	0.518
MU419	<i>rdrp1Δ::pyrG leuA</i> [−]	32	6	0	26	26	81.3	0.000004
MU420	<i>rdrp2Δ::pyrG leuA</i> [−]	25	23	2	0	0	<4.0	0.013
MU428	<i>rdrp2Δ::pyrG leuA</i> [−]	27	26	1	0	0	<3.7	0.012

P values were obtained based on a Fisher Exact Probability Test for a 2x2 Contingency Table, comparing each of the mutant strains individually versus the R7B strain.

the FK506-selected silencing of the *fkba* gene may not affect other loci. However, no other phenotypes were selected and sRNAs are often lost without selection (Fig. 2a and Extended Data Figs 1b and 8b).

To test if silencing was driven and enhanced by a genome-wide increase in stress-activated RNAi, the wild-type strain was exposed to stress conditions before FK506 exposure (Supplementary Table 3). However, analysis of recovered FK506^r isolates did not show an increase (or decrease) of epimutation frequency in *fkba* (Supplementary Table 4). Thus, either stress fails to activate RNAi or we have not identified the precise activating stress. The calcineurin inhibitor CsA also did not increase epimutations conferring FK506 resistance; thus inhibition of calcineurin (by CsA or FK506) does not activate RNAi.

To investigate if sRNAs generated against *fkba* are produced by canonical RNA silencing, we screened for epimutants in mutants lacking RNAi pathway components. No epimutants were found in *dcl2*, *ago1* or *rdp2* mutants (Table 1 and Extended Data Fig. 9a), showing that Dcl2 (Dicer), Ago1 (Argonaute) and RdRP2 are necessary for endogenous silencing of *fkba*. Dcl2 and Ago1 are essential for both transgene-induced and endogenous silencing in *M. circinelloides*^{7,19,20}. RdRP2 is essential to amplify RNAi signals for transgene-induced silencing¹⁸, but was thought to play a role secondary to RdRP1 for endogenous RNAi silencing⁷. Instead, we find RdRP2 is crucial, suggesting that different pathways for endogenous silencing operate in *M. circinelloides*, which may be correlated with the four different known classes of exonic siRNA (ex-siRNA)⁷. Notably, we found only one epimutant in two independent *dcl1* mutants (1 of 46 FK506^r isolates, 2.2%, Table 1, Supplementary Table 1 and Extended Data Fig. 9a). Dcl1 is not known to have any essential role in transgene-induced or endogenous silencing^{7,21}, but does have an auxiliary function in mutants lacking Dcl2 (ref. 19). The paucity of *fkba* epimutants in the *dcl2* and *dcl1* mutant backgrounds suggests that both Dcl1 and Dcl2 are involved in epimutational *fkba* silencing. *ago2* and *ago3* mutants exhibited a wild-type frequency of silencing (15–17%, Table 1 and Extended Data Figs 9a and 2a), thus Ago2 and Ago3 are dispensable for epimutation²⁰. These results reveal that establishment of epimutants in *M. circinelloides* depends on Dcl2, Dcl1, Ago1 and RdRP2. Except for Dcl1, these genes are involved in biogenesis of the known class I type of ex-siRNA⁷. Thus, although epimutant genetic requirements could suggest that a distinct sRNA class is involved (given the role of Dcl1), we cannot exclude the possibility that *fkba* silencing is due to an atypical class I ex-siRNA.

Unexpectedly, our studies revealed a novel role for RdRP1 in constraining epimutational silencing. RdRP1 is required for RNA silencing of exogenous sense transgenes in *M. circinelloides*. When DNA alleles producing dsRNA are introduced, this bypasses RdRP1 to evoke gene silencing¹⁸. As noted above, RdRP1 has a major role in endogenous silencing⁷. RdRP1 is hypothesized to be central for activating RNAi by generating dsRNA from the single-stranded RNA (ssRNA) precursor, both from sense transgenes or mRNA. In this model, RdRP1 should be essential for triggering *fkba* silencing because it involves an *fkba* dsRNA (Fig. 1c and Extended Data Fig. 5). Surprisingly, the *rdp1* mutant showed an elevated silencing rate of ~80% (versus ~22% in wild-type, Table 1 and Extended Data Fig. 9a and 2a) and the epimutants isolated in this mutant did not revert on drug-free media (epimutant strain EM4, Extended Data Fig. 1b). In *Caenorhabditis elegans* the *rrf-3* mutant lacking one of several RdRPs has a similar enhanced RNAi phenotype^{22,23}. RRF-3 has also been proposed to generate dsRNA from mRNA templates²⁴, hence RdRP1 and RRF-3 could serve analogous roles. Furthermore, the exosome and RNAi pathways in *Schizosaccharomyces pombe* compete in their degradation activities. Both mechanisms share common targets²⁵, and in the *rdp1* mutant sRNA formation is abolished and mRNAs are primarily directed to the exosome²⁶. In *Mucor*, RdRP1 could have an opposing role to RNAi, promoting assembly of exosome machinery on specific mRNA targets and thereby avoiding activation of RNAi under normal conditions, as was suggested previously⁷.

To test which RdRP might generate dsRNA from *fkba* mRNA, we tested for *fkba* antisense RNA in silencing mutants (Extended Data Fig. 9b). All strains analysed expressed the antisense RNA at similar levels, even

in the *rdp1* and *rdp2* mutants. The two RdRP polymerases could have a redundant role in generating *fkba* antisense RNA (*rdp1 rdp2* double mutants appear inviable, precluding analysis, not shown), or other *rdp* genes may participate.

Together these results provide evidence for a different route for the processing of endogenous sRNA, wherein RdRP2, Ago1 and both Dcl proteins are necessary to silence mRNA expression via epimutation, and RdRP1 has an unexpected role constraining epimutational silencing. We consider two possible models. In the first, sRNAs are produced constitutively and stochastically at low levels against the entire genome or some designated loci, allowing adaptation to environments through an RNAi-based pathway. In the second model, some mechanism activates RNAi under adverse or novel physiological conditions, facilitating genomic and phenotypic plasticity. Either could explain the broad range of environments in which *M. circinelloides* grows, and the limited antifungal drug susceptibility.

Previous studies showed that the *M. circinelloides* species complex includes three distinct subspecies: *M. circinelloides* f. *lusitanicus*, *M. circinelloides* f. *circinelloides*, and *M. circinelloides* f. *griseocyanus*²⁷. Mating barriers and phylogenetic separation provide evidence that these three lineages are different enough to represent distinct species. To generalize our findings, two *M. circinelloides* f. *circinelloides* strains (Mucho, 1006PhL²⁸), and an *M. circinelloides* f. *griseocyanus* strain (ATCC1207a) were tested in addition to the *M. circinelloides* f. *lusitanicus* strains. Only the *M. circinelloides* f. *circinelloides* strains grew as yeast in the presence of FK506 (Extended Data Fig. 10a), enabling the recovery of FK506^r isolates. The two *M. circinelloides* f. *circinelloides* strains exhibited different patterns of genomic plasticity; FK506^r isolates appeared earlier in 1006PhL than Mucho (5–7 days versus 5–15 days) and 2.5-fold more isolates were recovered from 1006PhL (Supplementary Table 5). Epimutants silencing *fkba* occurred in the pathogenic isolate 1006PhL at a surprisingly higher rate (90%) than in Mucho (<7.7%) or the *M. circinelloides* f. *lusitanicus* strains (~20–30%) (Supplementary Table 5 and Extended Data Fig. 10b). *M. circinelloides* f. *circinelloides* is the most common *Mucor* species associated with human infection. The enhanced ability to activate RNAi exhibited by the 1006PhL virulent isolate suggests that RNAi may enable this fungal pathogen to readily adapt both in nature and the host. Further studies are required to elucidate whether our observations are generally applicable, or if not, how specificity is brought about.

This study underscores the ability of *M. circinelloides* to adapt to the environment through two different routes of phenotypic variation, one stable (mutation) and one transient (epimutation). This plasticity evokes a broader phenotypic repertoire including the ability to reverse epimutations when selective pressures are relaxed. This is, to our knowledge, the first known example of epimutations involving an endogenous gene in fungi identified in a standard genetic screen; however, given the ubiquity of RNAi it is unlikely to be unique. While this example involves resistance to an antifungal drug in a human fungal pathogen, these findings could have implications beyond novel modes of transient antimicrobial resistance for the broader evolutionary trajectory of this and other eukaryotes with active RNAi pathways.

Online Content Methods, along with any additional Extended Data display items and Source Data, are available in the online version of the paper; references unique to these sections appear only in the online paper.

Received 19 September 2013; accepted 12 June 2014.

Published online 27 July 2014.

1. Liu, J. et al. Calcineurin is a common target of cyclophilin-cyclosporin A and FKBP-FK506 complexes. *Cell* **66**, 807–815 (1991).
2. Lee, S. C., Li, A., Calo, S. & Heitman, J. Calcineurin plays key roles in the dimorphic transition and virulence of the human pathogenic zygomycete *Mucor circinelloides*. *PLoS Pathog.* **9**, e1003625 (2013).
3. Orlowski, M. *Mucor* dimorphism. *Microbiol. Rev.* **55**, 234–258 (1991).
4. Bastidas, R. J., Shertz, C. A., Lee, S. C., Heitman, J. & Cardenas, M. E. Rapamycin exerts antifungal activity *in vitro* and *in vivo* against *Mucor circinelloides* via FKBP12-dependent inhibition of Tor. *Eukaryot. Cell* **11**, 270–281 (2012).
5. Heitman, J., Movva, N. R. & Hall, M. N. Targets for cell cycle arrest by the immunosuppressant rapamycin in yeast. *Science* **253**, 905–909 (1991).

6. Nicolas, F. E., Torres-Martinez, S. & Ruiz-Vazquez, R. M. Two classes of small antisense RNAs in fungal RNA silencing triggered by non-integrative transgenes. *EMBO J.* **22**, 3983–3991 (2003).
7. Nicolas, F. E. *et al.* Endogenous short RNAs generated by Dicer 2 and RNA-dependent RNA polymerase 1 regulate mRNAs in the basal fungus *Mucor circinelloides*. *Nucleic Acids Res.* **38**, 5535–5541 (2010).
8. Rhounim, L., Rossignol, J. L. & Faugeron, G. Epimutation of repeated genes in *Ascobolus immersus*. *EMBO J.* **11**, 4451–4457 (1992).
9. Colot, V., Maloïsel, L. & Rossignol, J. L. Interchromosomal transfer of epigenetic states in *Ascobolus*: transfer of DNA methylation is mechanistically related to homologous recombination. *Cell* **86**, 855–864 (1996).
10. Cubas, P., Vincent, C. & Coen, E. An epigenetic mutation responsible for natural variation in floral symmetry. *Nature* **401**, 157–161 (1999).
11. Suter, C. M., Martin, D. I. K. & Ward, R. L. Germline epimutation of *MLH1* in individuals with multiple cancers. *Nature Genet.* **36**, 497–501 (2004).
12. Chan, T. L. *et al.* Heritable germline epimutation of *MSH2* in a family with hereditary nonpolyposis colorectal cancer. *Nature Genet.* **38**, 1178–1183 (2006).
13. Hitchins, M. P. *et al.* Inheritance of a cancer-associated *MLH1* germ-line epimutation. *N. Engl. J. Med.* **356**, 697–705 (2007).
14. Baulcombe, D. C. RNA as a target and an initiator of post-transcriptional gene silencing in transgenic plants. *Plant Mol. Biol.* **32**, 79–88 (1996).
15. Wassenegeger, M. & Pelissier, T. A model for RNA-mediated gene silencing in higher plants. *Plant Mol. Biol.* **37**, 349–362 (1998).
16. Elmayan, T. & Vaucheret, H. Expression of single copies of a strongly expressed 35S transgene can be silenced post-transcriptionally. *Plant J.* **9**, 787–797 (1996).
17. Gazzani, S., Lawrenson, T., Woodward, C., Headon, D. & Sablowski, R. A link between mRNA turnover and RNA interference in *Arabidopsis*. *Science* **306**, 1046–1048 (2004).
18. Calo, S., Nicolas, F. E., Vila, A., Torres-Martinez, S. & Ruiz-Vazquez, R. M. Two distinct RNA-dependent RNA polymerases are required for initiation and amplification of RNA silencing in the basal fungus *Mucor circinelloides*. *Mol. Microbiol.* **83**, 379–394 (2012).
19. de Haro, J. P. *et al.* A single dicer gene is required for efficient gene silencing associated with two classes of small antisense RNAs in *Mucor circinelloides*. *Eukaryot. Cell* **8**, 1486–1497 (2009).
20. Cervantes, M. *et al.* A single *argonaute* gene participates in exogenous and endogenous RNAi and controls cellular functions in the basal fungus *Mucor circinelloides*. *PLoS ONE* **8**, e69283 (2013).
21. Nicolás, F. E., de Haro, J. P., Torres-Martinez, S. & Ruiz-Vazquez, R. M. Mutants defective in a *Mucor circinelloides* dicer-like gene are not compromised in siRNA silencing but display developmental defects. *Fungal Genet. Biol.* **44**, 504–516 (2007).
22. Kennedy, S., Wang, D. & Ruvkun, G. A conserved siRNA-degrading RNase negatively regulates RNA interference in *C. elegans*. *Nature* **427**, 645–649 (2004).
23. Timmons, L. Endogenous inhibitors of RNA interference in *Caenorhabditis elegans*. *Bioessays* **26**, 715–718 (2004).
24. Gent, J. I. *et al.* Distinct phases of siRNA synthesis in an endogenous RNAi pathway in *C. elegans* soma. *Mol. Cell* **37**, 679–689 (2010).
25. Reyes-Turcu, F. E. & Grewal, S. I. Different means, same end-heterochromatin formation by RNAi and RNAi-independent RNA processing factors in fission yeast. *Curr. Opin. Genet. Dev.* **22**, 156–163 (2012).
26. Yamanaka, S. *et al.* RNAi triggered by specialized machinery silences developmental genes and retrotransposons. *Nature* **493**, 557–560 (2013).
27. Li, C. H. *et al.* Sporangiospore size dimorphism is linked to virulence of *Mucor circinelloides*. *PLoS Pathog.* **7**, e1002086 (2011).
28. Lee, S. C. *et al.* Analysis of a foodborne fungal pathogen outbreak: virulence and genome of a *Mucor circinelloides* isolate from yogurt. *mBio* **5**, e01390–14 (2014).

Supplementary Information is available in the online version of the paper.

Acknowledgements We thank R. Skalsky and V. Ponnusamy for technical support and J. Wöstemeyer for trisporic acid. We thank B. Cullen, T. Petes, B. Billmyre, M. Feretzaki, J. Kingsbury and V. Ponnusamy for critical reading. This work was supported by NIH grants R37 AI39115-17, R01 AI50438-10, R01 CA154499-04 and the Spanish MICINN BFU2009-07220 and MINECO BFU2012-32246, co-financed by FEDER.

Author Contributions S.C., C.S.-W., S.T.M., R.M.R.-V., M.E.C. and J.H. designed experiments, interpreted data and wrote the paper. S.C., C.S.-W., R.J.B., S.C.L. and F.E.N. performed experiments. P.M. sequenced the sRNA library. J.A.G. analysed deep-sequencing data. S.T.M., R.M.R.-V., M.E.C. and J.H. provided materials.

Author Information Sequences for the *kbaA* gene from WT strain NRRL3631 and epimutant strains (EM1, EM2 and EM3) were deposited in GenBank with accession numbers KF203228, KF203229, KF203230 and KF203231. Raw data from high-throughput sRNA sequencing of WT, epimutant and revertant strains have been deposited in NCBI's Gene Expression Omnibus and are accessible through accession number GSE56353. Reprints and permissions information is available at www.nature.com/reprints. The authors declare no competing financial interests. Readers are welcome to comment on the online version of the paper. Correspondence and requests for materials should be addressed to J.H. (heitm001@duke.edu).

Functional polarization of tumour-associated macrophages by tumour-derived lactic acid

Oscar R. Colegio^{1,2,3,4}, Ngoc-Quynh Chu¹, Alison L. Szabo¹, Thach Chu¹, Anne Marie Rhebergen¹, Vikram Jairam¹, Nika Cyrus¹, Carolyn E. Brokowski¹, Stephanie C. Eisenbarth^{1,5}, Gillian M. Phillips⁶, Gary W. Cline⁷, Andrew J. Phillips⁶ & Ruslan Medzhitov^{1,4,8}

Macrophages have an important role in the maintenance of tissue homeostasis¹. To perform this function, macrophages must have the capacity to monitor the functional states of their 'client cells': namely, the parenchymal cells in the various tissues in which macrophages reside. Tumours exhibit many features of abnormally developed organs, including tissue architecture and cellular composition². Similarly to macrophages in normal tissues and organs, macrophages in tumours (tumour-associated macrophages) perform some key homeostatic functions that allow tumour maintenance and growth^{3–5}. However, the signals involved in communication between tumours and macrophages are poorly defined. Here we show that lactic acid produced by tumour cells, as a by-product of aerobic or anaerobic glycolysis, has a critical function in signalling, through inducing the expression of vascular endothelial growth factor and the M2-like polarization of tumour-associated macrophages. Furthermore, we demonstrate that this effect of lactic acid is mediated by hypoxia-inducible factor 1 α (HIF1 α). Finally, we show that the lactate-induced expression of arginase 1 by macrophages has an important role in tumour growth. Collectively, these findings identify a mechanism of communication between macrophages and their client cells, including tumour cells. This communication most probably evolved to promote homeostasis in normal tissues but can also be engaged in tumours to promote their growth.

To study tumour-macrophage interactions, we used syngeneic murine tumour models of Lewis lung carcinoma (LLC) and B16-F1 (B16) melanoma cancer cell lines. LLC and B16 cells were subcutaneously injected into C57BL/6J mice. At day 19, the tumours were harvested and analysed for the presence of macrophages. Histological analysis showed that, in both LLC and B16 tumours, F4/80⁺ macrophages and CD11b⁺ macrophages were present at a high density in the tumour periphery, as well as in cords and clusters throughout the interior of the tumours (Extended Data Fig. 1a, b). Fluorescence-activated cell sorting (FACS) analysis showed that the F4/80⁺CD11b⁺ macrophages constituted between 1% and 6% of all cells within the tumours. Although the extent of macrophage recruitment varied between the tumour types, it remained constant for tumours of each type (Extended Data Fig. 1c, d). The sorted tumour-associated macrophages (TAMs) were vacuolated or foamy in appearance and thus morphologically distinct from peritoneal macrophages (Extended Data Fig. 1e). The TAMs expressed high levels of vascular endothelial growth factor (*Vegf*; also known as *Vegfa*) and arginase 1 (*Arg1*) messenger RNA compared with peritoneal macrophages (Fig. 1a, b), and they expressed more *Vegf* and *Arg1* mRNA than all of the other cells within the tumour combined. Thus, consistent with the current thinking⁵, tumour cells recruit macrophages and induce their functional polarization into TAMs.

We hypothesized that tumour-derived signals activate macrophages to reach a tumour-promoting state that is characterized by the expression of *Arg1* and *Vegf*. The upregulation of *Vegf* and *Arg1* in macrophages might support tumour growth by inducing neovascularization and by

providing the substrates for cancer cell proliferation, respectively^{5,6}. Therefore, we used *Vegf* and *Arg1* mRNA as read-outs to study the signals that tumours produce that promote the functional polarization of TAMs. The expression of *Vegf* has been characterized best in the context of hypoxia⁷, whereas *Arg1* expression in macrophages has been best characterized in response to the T-helper-2-derived cytokines interleukin 4 (IL-4) and IL-13 (ref. 8). First, we tested whether *Vegf* and *Arg1* induction in macrophages is mediated by a secreted tumour-derived signal. We incubated bone-marrow-derived macrophages with LLC-tumour-conditioned medium and measured *Vegf* and *Arg1* expression in the macrophages. Tumour-conditioned media induced both *Vegf* and *Arg1* expression in bone-marrow-derived macrophages under normoxic conditions (Fig. 2a, b).

Vegf expression is induced by ischaemia, during which the loss of both oxygen and nutrients can induce *Vegf* through different pathways: hypoxia induces *Vegf* expression via the transcription factor HIF1 α , while nutrient deprivation induces *Vegf* expression through the transcriptional co-activator PGC1 α (peroxisome-proliferator-activated receptor γ , co-activator 1 α)⁹. We found that a tumour-derived signal(s) induces *Vegf* expression in macrophages under normoxic conditions by the same pathway through which hypoxia induces *Vegf* expression: that is, stabilization of HIF1 α . Macrophages stimulated by tumour-conditioned media

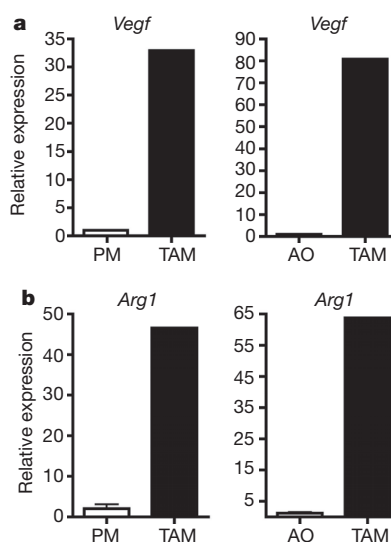


Figure 1 | TAMs express high levels of *Vegf* and *Arg1* mRNA.

a, b, Expression analysis by quantitative PCR (qPCR) of *Vegf* and *Arg1* mRNA in FACS-sorted peritoneal macrophages (PM), TAMs and all other cells (AO) within the tumour from day 19 LLC tumours. Expression is shown relative to the left histogram bar.

¹Department of Immunobiology, Yale University School of Medicine, New Haven, Connecticut 06519-1612, USA. ²Department of Dermatology, Yale University School of Medicine, New Haven, Connecticut 06520-8059, USA. ³Yale-New Haven Transplantation Center, Yale University School of Medicine, New Haven, Connecticut 06519-1369, USA. ⁴Yale Cancer Center, Yale University School of Medicine, New Haven, Connecticut 06520-8028, USA. ⁵Department of Laboratory Medicine, Yale University School of Medicine, New Haven, Connecticut 06520-8035, USA. ⁶Department of Chemistry, Yale University School of Medicine, New Haven, Connecticut 06520-8107, USA. ⁷Department of Internal Medicine, Yale University School of Medicine, New Haven, Connecticut 06520-8020, USA. ⁸Howard Hughes Medical Institute, Chevy Chase, Maryland 20815-6789, USA.

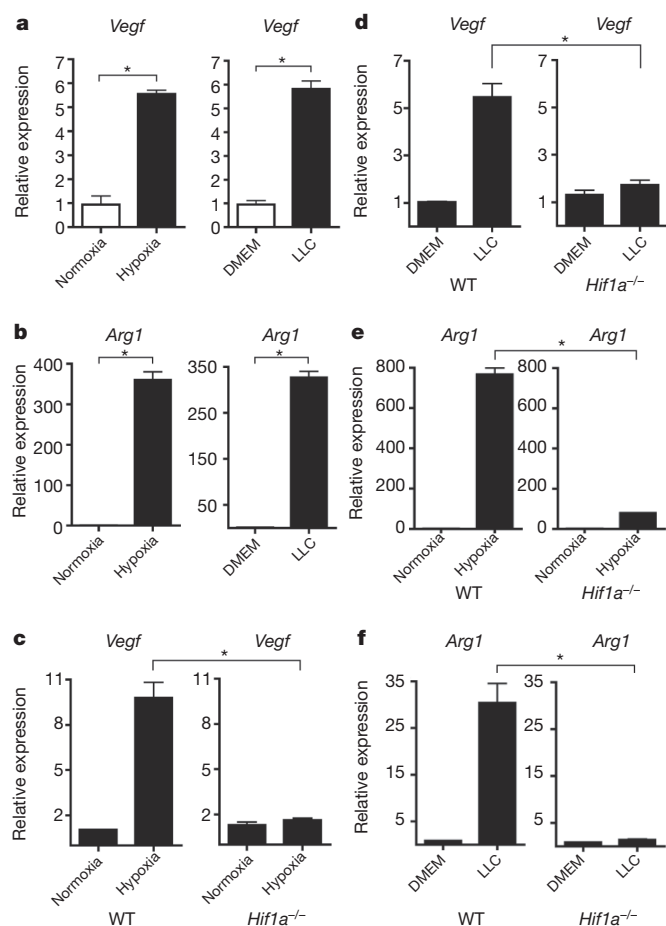


Figure 2 | A soluble factor in tumour-conditioned medium induces *Vegf* and *Arg1* via HIF1 α . **a, b**, Expression analysis by qPCR of *Vegf* (**a**) and *Arg1* (**b**) mRNA in bone-marrow-derived macrophages grown under conditions of normoxia (20% O₂) or hypoxia (0.1% O₂) (left panels) or stimulated with control medium (DMEM) or LLC-tumour-conditioned medium (right panels). **c–f**, Expression analysis by qPCR of *Vegf* (**c, d**) and *Arg1* (**e, f**) mRNA in wild-type (WT) and *Hif1α*^{-/-} bone-marrow-derived macrophages stimulated with LLC-tumour-conditioned medium (**d, f**) or hypoxia (0.1% O₂) (**c, e**). The histogram bars represent the expression level of three biological replicates (relative to the left histogram bar), displayed as mean \pm s.e.m. **P* < 0.01, using a two-tailed, unpaired *t*-test. All experiments were performed at least twice.

had stabilized HIF1 α protein under normoxic conditions (Extended Data Fig. 2a). Furthermore, using luciferase reporter assays that determined both the stability of the HIF1 α protein's oxygen-dependent domain and the activity of the *Vegf* promoter, we found that tumour-conditioned media stabilized HIF1 α and induced the *Vegf* promoter under normoxic conditions to a level similar to that induced by hypoxia (Extended Data Fig. 2b, c). In addition to HIF1 α protein stabilization, tumour-conditioned media induced the expression of the inducible isoform of the *HIF1A* gene (*HIF1A* I.1) but not the constitutive isoform (*HIF1A* I.2). Neither the *Pgc1a* nor *Pgc1b* co-activator, which are associated with the induction of *Vegf* during nutrient deprivation, was induced by tumour-conditioned media (Extended Data Fig. 2d, e). To determine whether HIF1 α is critical for tumour-induced upregulation of *Vegf* and *Arg1* expression, we used *Hif1a*^{fl/fl} \times *Lysm*^{Cre/WT} mice, in which HIF1 α is specifically deleted in myeloid cells. In the resultant *Hif1a*^{-/-} macrophages, neither *Vegf* nor *Arg1* was induced by either hypoxia or tumour-conditioned media (Fig. 2c–f). Together, these findings indicate that a tumour-derived soluble factor(s) induce *Vegf* and *Arg1* in macrophages via HIF1 α under normoxic conditions.

After determining that the tumours induced *Vegf* and *Arg1* expression via HIF1 α , we next sought to identify the tumour-derived soluble factor capable of activating HIF1 α under normoxic conditions. The tumour-conditioned medium was fractionated by size (<3 kDa and >3 kDa),

and the activity of both fractions was tested. Both unfractionated tumour-conditioned medium and the <3 kDa fraction stabilized HIF1 α and upregulated *Arg1* expression (Fig. 3a and Extended Data Fig. 2f); the >3 kDa fraction had none of these effects. Furthermore, the <3 kDa fraction strongly upregulated *Arg1* and *Vegf* expression (Fig. 3b and Extended Data Fig. 2g). Its activity was also heat stable: that is, it induced *Arg1* and *Vegf* after prolonged boiling (Extended Data Fig. 2h).

At least four soluble factors of <3 kDa are known to stabilize HIF1 α under normoxic conditions: adenosine, acidic pH, pyruvate and lactate^{10–12}. Acidic pH was not able to stabilize HIF1 α in macrophages under normoxic conditions, and an inhibitor of adenosine did not abrogate the induction of *Vegf* by tumour-conditioned medium (Extended Data Fig. 2i, j). We therefore focused on the possibility that tumour-derived lactate is the soluble factor responsible for the polarization of TAMs. Warburg observed that cancer cells preferentially perform aerobic glycolysis: that is, they convert most glucose molecules into lactate regardless of the amount of oxygen present¹³. Furthermore, the eponymous Warburg effect is also observed in most cells undergoing rapid proliferation¹⁴. It has been hypothesized that aerobic glycolysis is conducive to cell proliferation because, despite the consequent reduction in ATP production, aerobic glycolysis produces metabolic precursors, such as lactate, for biosynthetic pathways, and these precursors may be the limiting factor during rapid cell proliferation¹⁴.

One of the key enzymes involved in aerobic glycolysis is pyruvate kinase, which catalyses the production of pyruvate from its precursor during glycolysis. Specifically, the M2 isoform—but not the M1 isoform—of pyruvate kinase is preferentially active during aerobic glycolysis¹⁵. When cells expressing the M2 isoform were compared with cells expressing the M1 isoform for differences in the intracellular metabolites that they produced, the levels of lactate and pyruvate produced proved to be the most different. We investigated the differential expression of the M1 (*Pkm1*) and M2 (*Pkm2*) isoforms in different tumour cell lines and normal tissues. As expected, whereas PKM1 was the predominant isoform in differentiated tissues, particularly in metabolically active brown adipose tissue, muscle and heart, *Pkm2* was the predominant isoform in a variety of tumour cell lines (Extended Data Fig. 3a–c).

We next measured the levels of lactic acid in the media from a variety of tumour cell lines. Interestingly, LLC and B16 cells—the most malignant tumour lines tested—yielded the highest concentrations of lactate (Fig. 3c), suggesting that the *Pkm2* expression level and the subsequent lactate production correlate with tumour malignancy. When macrophages were then stimulated with these tumour-conditioned media, the magnitude of *Vegf* induction correlated with the amount of lactate that accumulated in the media (Fig. 3d).

When the tumour-conditioned media were fractionated, the vast majority of the lactate partitioned into the <3 kDa fraction (Extended Data Fig. 3d). Furthermore, lactic acid alone was sufficient to induce *Vegf* and *Arg1* expression in macrophages in a dose-dependent manner (Fig. 3e, f). Using mass spectroscopy for quantitation, we determined that the *in vivo* intratumoural lactate levels were equivalent to the lactate concentrations required for *in vitro* induction of *Vegf* and *Arg1* (Extended Data Fig. 3e). When macrophages were stimulated with either lactic acid or hypoxia (0.1% O₂), the induction of *Vegf* expression peaked at 6 h post stimulation, whereas *Arg1* induction peaked at 24 h post stimulation (Extended Data Figs 4 and 5). The cellular uptake of lactic acid, mediated by monocarboxylate transporters (MCT1, MCT2, MCT3 and MCT4), is necessary for the induction of *Vegf*, as indicated by the abrogation of *Vegf* induction in macrophages by LLC-conditioned media after exposure to α -cyano-4-hydroxycinnamate, an MCT inhibitor (Extended Data Fig. 6a). Furthermore, as monocarboxylate transporters are proton-coupled symporters, the induction of *Vegf* by lactate was dependent on an acidic pH (Extended Data Fig. 6b). Although lactic acid was sufficient to induce *Vegf* in LLC and B16 tumour cells (Extended Data Fig. 6c), the relative levels of expression observed *in vivo* are greatest in TAMs (Fig. 1a).

Finally, similarly to the induction of *Vegf* and *Arg1* by hypoxia, the induction of these genes by tumour-conditioned media and lactic acid

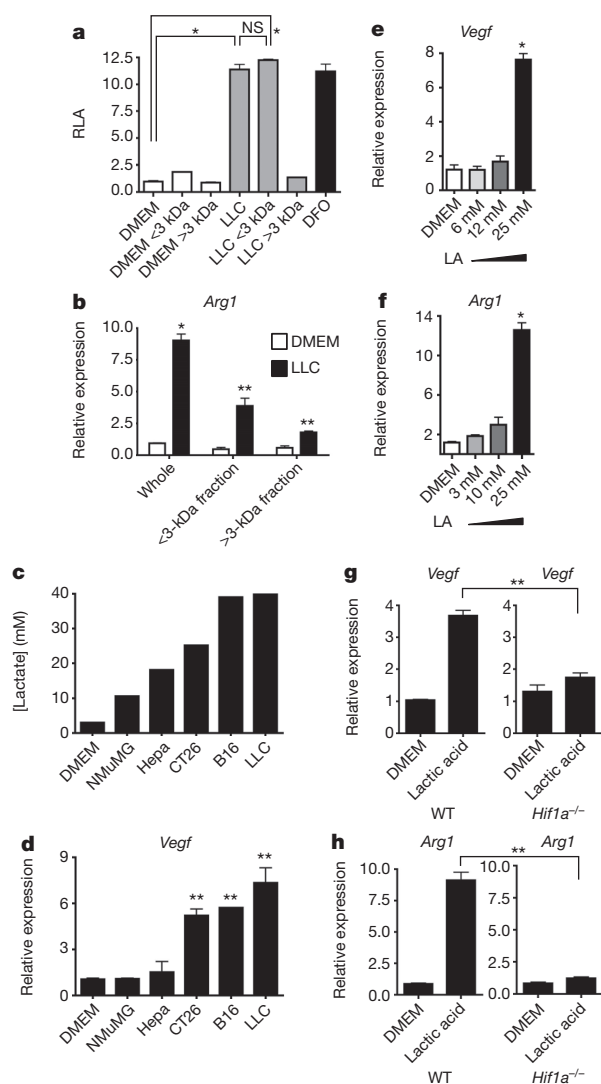


Figure 3 | Lactic acid is sufficient to induce *Vegf* and *Arg1* via HIF1 α .

a, b, Control (DMEM) or LLC-tumour-conditioned medium was used unfractionated (whole) or as <3-kDa or >3-kDa fractions to stimulate cells as follows. A luciferase reporter assay of 293T cells transfected with HIF1 α oxygen-dependent domain (ODD)-luciferase was carried out to measure protein stabilization of the ODD; deferoraxamine (DFO) was used as a hypoxia mimetic (**a**). Expression analysis by qPCR of *Arg1* mRNA in bone-marrow-derived macrophages (**b**). **c,** Lactic acid concentration in the tumour-conditioned media from five tumour cell lines, collected after culturing at confluence for 4 days. **d,** Expression analysis by qPCR of *Vegf* mRNA in bone-marrow-derived macrophages stimulated with the tumour-conditioned media in **c**. **e, f,** Expression analysis by qPCR of *Vegf* (**e**) and *Arg1* (**f**) mRNA in bone-marrow-derived macrophages cultured with a concentration gradient of lactic acid (LA). **g, h,** Expression analysis by qPCR of *Vegf* and *Arg1* mRNA in wild-type (WT) and *Hif1 α* ^{-/-} bone-marrow-derived macrophages. **b–h,** The histogram bars represent the expression level of three biological replicates (relative to expression in DMEM), displayed as mean \pm s.e.m. **P* < 0.0001; ***P* < 0.001, using a two-tailed, unpaired *t*-test. All experiments were performed at least twice. NS, not significant; RLA, relative luciferase activity.

was also dependent on HIF1 α , as HIF1 α -deficient macrophages were not able to upregulate *Vegf* or *Arg1* on stimulation with lactic acid (Fig. 3g, h). Collectively, these findings suggest a model in which macrophages are recruited to the tumour micro-environment, where tumour-derived lactic acid induces HIF1 α -dependent polarization of macrophages, including the induction of *Vegf* and *Arg1*.

To determine whether lactic acid can induce an M2-like phenotype in TAMs, FACS sorting of F4/80⁺CD11b⁺ macrophages was performed on syngeneic LLC tumours at day 19 after injection. Gene expression

analysis revealed that these TAMs have an M2-like profile, with the expression of *Fizz1*, *Mgl1* and *Mgl2* at levels higher than in all other tumour cells combined (Fig. 4a). Compared with F4/80⁺CD11b⁺ FACS-sorted peritoneal macrophages, TAMs express higher levels of the M2-associated genes *Arg1* and *Mrc1* but not higher levels of *Ym1*, *Mgl1*, *Mgl2* or *Fizz1* (Extended Data Fig. 7). Since lactic acid is sufficient to induce *Arg1* in macrophages, we asked whether the expression of other M2 markers is induced by lactic acid. We found that lactic acid was sufficient to induce the M2 markers *Fizz1*, *Mgl1* and *Mgl2* in bone-marrow-derived macrophages (Fig. 4b and Extended Data Fig. 8a). Given that HIF1 α is required for the induction of *Arg1* by lactic acid *in vitro*, we asked whether HIF1 α is required for the induction of other M2 markers *in vivo*. TAMs from LLC tumours injected into wild-type mice and mice with HIF1 α -deficient macrophages were sorted by FACS, and their expression of M2 markers was compared. *Arg1*, *Fizz1*, *Mgl1* and *Mgl2* were all expressed at lower levels in TAMs from mice with HIF1 α -deficient macrophages than from wild-type mice (Fig. 4c and Extended Data Fig. 8b).

IL-4 and IL-13 are the best-characterized inducers of M2 polarization of macrophages⁸, but the downstream steps involved in M2 polarization are poorly defined¹⁶. To determine whether HIF1 α is required for IL-4-induced M2 polarization, macrophages from HIF1 α -deficient and wild-type mice were stimulated with IL-4, and their gene expression was compared. The induction of *Arg1*, *Fizz1* and *Mgl2* was significantly impaired in HIF1 α -deficient macrophages compared with wild-type macrophages (Fig. 4d). By contrast, the induction of *Mgl1* was intact, suggesting that HIF1 α is required for a subset of M2-associated genes, whether stimulated by lactic acid, hypoxia or IL-4. To determine whether IL-4 and IL-13 signalling is required for the M2 polarization of LLC TAMs *in vivo*, we isolated TAMs from mice deficient in the IL-4 receptor α -chain (IL-4R α), a component of the receptors for both IL-4 and IL-13, and compared their gene expression with that of TAMs from wild-type mice. The levels of *Arg1* mRNA were higher in TAMs from IL-4R α -deficient mice than from wild-type mice, and the other M2 markers were present at only moderately lower levels than in wild-type mice. Therefore, IL-4 and IL-13 signalling are not critical for the TAM M2-like phenotype in this model (Fig. 4e). Together, these findings suggest that there is an alternative pathway to an M2-like state that does not require IL-4 and IL-13 but is instead mediated by HIF1 α . In addition, these results demonstrate that the induction of at least some M2-associated genes by IL-4 is dependent on HIF1 α .

To determine whether lactic acid is driving macrophage polarization *in vivo*, we generated stable LLC tumour cell lines in which *Pkm2* was knocked down and then injected these cells subcutaneously into wild-type mice. The *Pkm2*-knockdown tumours had a lower *in vivo* concentration of lactic acid than tumours bearing scrambled constructs. Furthermore, TAMs isolated from the *Pkm2*-knockdown tumours contained approximately half of the amount of *Arg1* mRNA, and the tumours were significantly smaller (Fig. 4f). Although interpretation of this result is complicated by the probable cell-intrinsic effect of *Pkm2* knockdown, this finding is at least consistent with the model in which PKM2-dependent lactic acid production by tumour cells has an important role in TAM polarization. As a converse correlate to these experiments, to determine whether lactic acid stimulation of bone-marrow-derived macrophages *ex vivo* confers a growth advantage on LLC tumours, we compared the tumour volumes in mice co-injected with LLC cells plus control-medium-stimulated bone-marrow-derived macrophages and in mice co-injected with LLC cells plus lactic-acid-stimulated bone-marrow-derived macrophages. Co-injection of the lactic-acid-stimulated bone-marrow-derived macrophages resulted in significantly larger tumours than did co-injection of the control-medium-stimulated bone-marrow-derived macrophages (Extended Data Fig. 9a). To determine whether lactic acid is used as a metabolic substrate, as well as a polarizing signal, in TAMs, we measured the oxidation of ¹⁴C-lactic acid. TAMs oxidized more ¹⁴C-lactic acid to ¹⁴CO₂ than either bone-marrow-derived macrophages or cultured LLC cells (Extended Data Fig. 9b), suggesting that TAM polarization allows increased utilization of lactic acid.

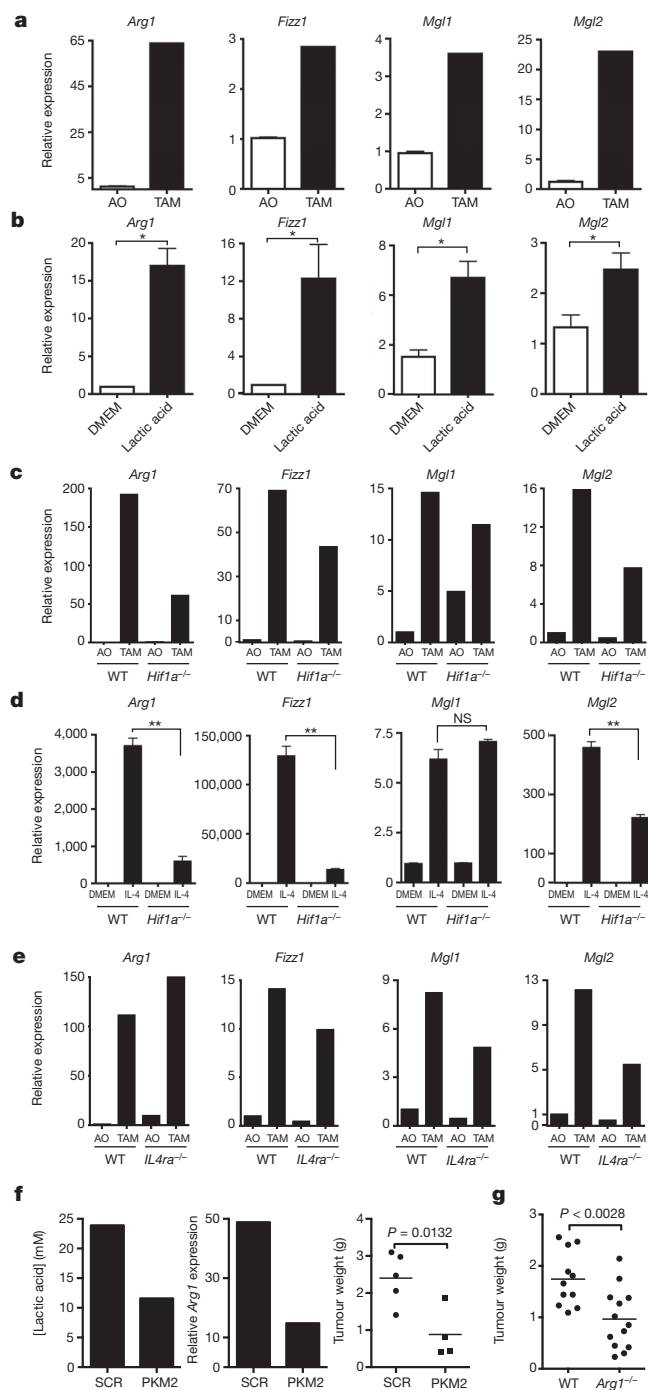


Figure 4 | Lactic acid polarizes macrophages to an M2-like state that is critical for tumour growth. **a–e**, Expression analysis by qPCR of *Arg1*, *Fizz1*, *Mgl1* and *Mgl2* mRNA in the following cell types: TAMs and all other tumour cells (AO) from LLC tumours resected from wild-type (WT, C57BL/6J) mice (**a**), bone-marrow-derived macrophages stimulated with 25 mM lactic acid (LA) (**b**), TAMs and AO from LLC tumours resected from mice with either WT or *Hif1a*^{-/-} macrophages (**c**), WT or *Hif1a*^{-/-} bone-marrow-derived macrophages stimulated with control medium (DMEM) or IL-4 (10 ng ml⁻¹) (**d**), and TAMs and AO from CT26 colon carcinoma tumours resected from mice with WT (BALB/c) or *IL4ra*^{-/-} macrophages (**e**). **f**, Intratumoral lactic acid concentrations (mM) from tumours of LLC cells that had been stably transfected with a scrambled short hairpin RNA (shRNA) construct (SCR) or an shRNA targeting *Pkm2* (centre panel). Expression analysis by qPCR of *Arg1* mRNA in TAMs isolated from SCR-transfected and *Pkm2*-knockdown tumours. Weight of LLC tumours from cells bearing an SCR construct (mean \pm s.e.m., 2.402 \pm 0.310 g; n = 5) or *Pkm2* shRNA construct (mean \pm s.e.m., 0.8820 \pm 0.341 g; n = 4); P = 0.0132 using a two-tailed, unpaired *t*-test (right panel). The *F* test revealed no significant difference in variance between the compared groups. **g**, Weight of LLC tumours resected on day 19 from mice with WT macrophages (mean \pm s.e.m., 1.74 \pm 0.161 g; n = 11) or *ARG1*-deficient macrophages (mean \pm s.e.m., 0.965 \pm 0.163 g; n = 13); P < 0.0028 using a two-tailed, unpaired *t*-test. The *F* test revealed no significant difference in variance between the compared groups. **a–f**, The histogram bars represent the expression level of three biological replicates, displayed as mean \pm s.e.m., relative to AO (**a**, **c**, **e**, **f**) or DMEM (**b**, **d**). * P < 0.05; ** P < 0.001, using a two-tailed, unpaired *t*-test. All experiments were performed at least twice. NS, not significant.

Together, these findings demonstrate that lactate, a by-product of glycolysis, induces TAM polarization characterized by the induction of *Vegf* expression and differentiation into an M2-like phenotype. Pioneering studies by Folkman demonstrated the crucial role of neovascularization in tumour growth¹⁸. It has generally been assumed that cancer cells experiencing hypoxia in a growing tumour are themselves the source of VEGF. However, our findings suggest that, at least in some cases, it is the tumour accessory cells, including macrophages, that are the main source of VEGF. It should be noted that the elimination of one source of VEGF will probably result in compensatory VEGF production by alternative cellular sources⁵. Further studies will be necessary to elucidate the specific tumour features that dictate the primary source of VEGF.

ARG1 is widely accepted as a marker of M2 macrophages, but the functional role of ARG1 in M2 macrophages has been determined only in the context of helminth infection¹⁹. Our findings suggest that *Arg1* expression in TAMs has an important role in tumour growth, possibly via an ARG1-dependent pathway responsible for producing polyamines, which are substrates that have a critical role in cell proliferation. In addition, TAMs may contribute to nitrogen metabolism in the tumour microenvironment, as all five enzymes of the urea cycle are expressed at higher levels in TAMs than in all other tumour cells (Extended Data Fig. 10). TAMs also express higher levels of the transaminase *Gpt* and of glutamine synthetase (*Glut*), which also facilitate nitrogen metabolism, than all other tumour cells.

We observed that the effect of lactate on tumour cell proliferation is mediated by HIF1 α and, interestingly, is independent of IL-4R α signalling. However, in other tumour models, IL-4 produced by T helper 2 cells has an important role in the M2 polarization of TAMs²⁰. Thus, multiple pathways for the induction of the M2 phenotype in TAMs probably exist, and further investigation is necessary to characterize the features of tumour cells or their tissue environment that dictate the induction of the M2 phenotype.

In conclusion, we found that tumour-cell-derived lactic acid has an important signalling role in the induction of several key features of TAM polarization and the subsequent promotion of tumour growth. Lactic acid, as a by-product of aerobic glycolysis, can be a 'reporter' of cell proliferation. Lactic acid is also a by-product of anaerobic glycolysis, which in metazoan cells is typically indicative of hypoxia. These features of lactic acid may explain its ability to induce *Vegf*, *Arg1* and other M2-associated genes in TAMs. Finally, we expect that multiple signals are involved in

The role of VEGF in promoting neovascularization and subsequent growth of tumours is well established¹⁷. However, the role of macrophage-derived ARG1 is unclear, despite being part of the signature of the TAM phenotype. ARG1 is known to be involved in a pathway that generates polyamines, which are essential metabolites during cell division and have been shown to regulate tumour cell proliferation *in vitro*⁶. ARG1 is also one of five urea cycle enzymes that is important in nitrogen metabolism. Therefore, we sought to determine whether macrophage-derived ARG1 is involved in tumour progression by using a syngeneic tumour model in *Arg1*^{fl/fl} \times *Lysm*^{cre/wt} mice, whose macrophages are deficient in ARG1. Tumours from ARG1-deficient mice were approximately half the size of those from wild-type mice, indicating that macrophage-derived ARG1 has an important role in tumour progression (Fig. 4g and Extended Data Fig. 9c, d).

the communication between tumour cells and macrophages. Indeed, recent findings demonstrate the important role of tumour-cell-derived versican²¹ and macrophage colony-stimulating factor²² in tumour-macrophage communication. These and other, yet to be discovered, signals involved in macrophage polarization are presumably not specific to tumours. That is, as tumours represent an abnormal and exaggerated version of normal tissue growth, the role of TAMs reflects the role of macrophages in normal tissue maintenance and repair.

METHODS SUMMARY

Syngeneic tumour model. LLC (LL/2), B16-F1 melanoma or CT.26WT colon carcinoma cells were injected subcutaneously into the flanks of mice (1×10^6 , in 200 μ l PBS). Both male and female C57BL/6J (LLC and B16) and BALB/c (CT26) strains of mice (Jackson Laboratory) were used. Mice were 6 to 8 weeks of age. The resultant tumours were resected and transferred to PBS on ice. Tumour weight (g) was measured on a scale after transferring the specimen to a sterile Petri dish. The tumours from all experiments were then processed for FACS analysis or sorting (see Methods) on the same day or fixed in formalin for immunohistochemistry.

Tumour supernatant preparation and collection. Cell lines were grown in DMEM plus supplements (DMEM-complete; containing 10% FBS, 1% penicillin and streptomycin, 1% HEPES, 1% L-glutamine and 1% sodium pyruvate). Fractionation of LLC tumour supernatants was achieved using Amicon Ultra centrifugal filters (3K Ultracel, Millipore). The supernatant fraction >3 kDa remained above the filter, and the fraction <3 kDa passed through to the lower chamber. The >3 -kDa fraction was resuspended in unsupplemented DMEM to the pre-filtration volume.

Determination of lactate concentration. The lactate concentration was measured using a Lactate Assay Kit (BioVision) according to the manufacturer's instructions. The mean values and s.e.m. of the lactate concentration were calculated for each condition. The mean intratumoral lactic acid concentration was determined for LLC and B16 tumours after homogenization (Polytron) and methanol extraction, using hydrophilic interaction chromatography and mass spectroscopy, as well as the colorimetric lactate assay.

Online Content Methods, along with any additional Extended Data display items and Source Data, are available in the online version of the paper; references unique to these sections appear only in the online paper.

Received 7 October 2013; accepted 14 May 2014.

Published online 13 July 2014.

1. Pollard, J. W. Trophic macrophages in development and disease. *Nature Rev. Immunol.* **9**, 259–270 (2009).
2. Egeblad, M., Nakasone, E. S. & Werb, Z. Tumors as organs: complex tissues that interface with the entire organism. *Dev. Cell* **18**, 884–901 (2010).
3. Grivennikov, S. I., Greten, F. R. & Karin, M. Immunity, inflammation, and cancer. *Cell* **140**, 883–899 (2010).
4. Mantovani, A., Allavena, P., Sica, A. & Balkwill, F. Cancer-related inflammation. *Nature* **454**, 436–444 (2008).
5. Qian, B. Z. & Pollard, J. W. Macrophage diversity enhances tumor progression and metastasis. *Cell* **141**, 39–51 (2010).
6. Chang, C. I., Liao, J. C. & Kuo, L. Macrophage arginase promotes tumor cell growth and suppresses nitric oxide-mediated tumor cytotoxicity. *Cancer Res.* **61**, 1100–1106 (2001).

7. Shweiki, D., Itin, A., Soffer, D. & Keshet, E. Vascular endothelial growth factor induced by hypoxia may mediate hypoxia-initiated angiogenesis. *Nature* **359**, 843–845 (1992).
8. Gordon, S. & Martinez, F. O. Alternative activation of macrophages: mechanism and functions. *Immunity* **32**, 593–604 (2010).
9. Arany, Z. *et al.* HIF-independent regulation of VEGF and angiogenesis by the transcriptional coactivator PGC-1 α . *Nature* **451**, 1008–1012 (2008).
10. Lu, H., Forbes, R. A. & Verma, A. Hypoxia-inducible factor 1 activation by aerobic glycolysis implicates the Warburg effect in carcinogenesis. *J. Biol. Chem.* **277**, 23111–23115 (2002).
11. De Ponti, C. *et al.* Adenosine A_{2a} receptor-mediated, normoxic induction of HIF-1 through PKC and PI-3K-dependent pathways in macrophages. *J. Leukoc. Biol.* **82**, 392–402 (2007).
12. Mekhail, K., Gunaratnam, L., Bonicalzi, M. E. & Lee, S. HIF activation by pH-dependent nucleolar sequestration of VHL. *Nature Cell Biol.* **6**, 642–647 (2004).
13. Warburg, O. On the origin of cancer cells. *Science* **123**, 309–314 (1956).
14. Vander Heiden, M. G., Cantley, L. C. & Thompson, C. B. Understanding the Warburg effect: the metabolic requirements of cell proliferation. *Science* **324**, 1029–1033 (2009).
15. Christoff, H. R. *et al.* The M2 splice isoform of pyruvate kinase is important for cancer metabolism and tumour growth. *Nature* **452**, 230–233 (2008).
16. Murray, P. J. & Wynn, T. A. Protective and pathogenic functions of macrophage subsets. *Nature Rev. Immunol.* **11**, 723–737 (2011).
17. Lin, E. Y. *et al.* Macrophages regulate the angiogenic switch in a mouse model of breast cancer. *Cancer Res.* **66**, 11238–11246 (2006).
18. Folkman, J. Tumor angiogenesis: therapeutic implications. *N. Engl. J. Med.* **285**, 1182–1186 (1971).
19. Wynn, T. A. & Barron, L. Macrophages: master regulators of inflammation and fibrosis. *Semin. Liver Dis.* **30**, 245–257 (2010).
20. DeNardo, D. G. *et al.* CD4⁺ T cells regulate pulmonary metastasis of mammary carcinomas by enhancing protumor properties of macrophages. *Cancer Cell* **16**, 91–102 (2009).
21. Kim, S. *et al.* Carcinoma-produced factors activate myeloid cells through TLR2 to stimulate metastasis. *Nature* **457**, 102–106 (2009).
22. Wyckoff, J. *et al.* A paracrine loop between tumor cells and macrophages is required for tumor cell migration in mammary tumors. *Cancer Res.* **64**, 7022–7029 (2004).

Acknowledgements We thank members of the Medzhitov laboratory for discussions, L. Xu, C. Annicelli, S. Cronin and G. Tokmouline for animal care and technical help, and N. Palm for critical feedback on the manuscript. O.R.C. is supported by the National Cancer Institute (1K08CA172580-01), the Yale Center for Clinical Investigation (5KL2RR024138), the Yale SPORE in Skin Cancer (1 P50 CA121974), the Damon Runyon Cancer Research Foundation (DRG 108-09) and the Dermatology Foundation. R.M.'s laboratory is supported by The Blavatnik Family Foundation, grants from the National Institutes of Health (AI046688, AI089771 and CA157461) and the Howard Hughes Medical Institute.

Author Contributions O.R.C. and R.M. conceived the project, designed the experimental approach, interpreted data and wrote the manuscript. N.-Q.C. and A.L.S. designed and performed experiments and wrote the manuscript. T.C., A.M.R., V.J., N.C., C.E.B., G.M.P. and G.W.C. designed and performed experiments and analysed data. S.C.E. and A.J.P. designed experiments, analysed data and provided key expertise.

Author Information Reprints and permissions information is available at www.nature.com/reprints. The authors declare no competing financial interests. Readers are welcome to comment on the online version of the paper. Correspondence and requests for materials should be addressed to R.M. (ruslan.medzhitov@yale.edu).

The alarmin IL-33 promotes regulatory T-cell function in the intestine

Chris Schiering^{1†*}, Thomas Krausgruber^{1*}, Agnieszka Chomka¹, Anja Fröhlich², Krista Adelmann¹, Elizabeth A. Wohlfert^{3†}, Johanna Pott⁴, Thibault Griseri¹, Julia Bollrath¹, Ahmed N. Hegazy¹, Oliver J. Harrison⁴, Benjamin M. J. Owens¹, Max Löhning², Yasmine Belkaid³, Padraic G. Fallon⁵ & Fiona Powrie¹

FOXP3⁺ regulatory T cells (T_{reg} cells) are abundant in the intestine, where they prevent dysregulated inflammatory responses to self and environmental stimuli. It is now appreciated that T_{reg} cells acquire tissue-specific adaptations that facilitate their survival and function¹; however, key host factors controlling the T_{reg} response in the intestine are poorly understood. The interleukin (IL)-1 family member IL-33 is constitutively expressed in epithelial cells at barrier sites², where it functions as an endogenous danger signal, or alarmin, in response to tissue damage³. Recent studies in humans have described high levels of IL-33 in inflamed lesions of inflammatory bowel disease patients^{4–7}, suggesting a role for this cytokine in disease pathogenesis. In the intestine, both protective and pathological roles for IL-33 have been described in murine models of acute colitis^{8–11}, but its contribution to chronic inflammation remains ill defined. Here we show in mice that the IL-33 receptor ST2 is preferentially expressed on colonic T_{reg} cells, where it promotes T_{reg} function and adaptation to the inflammatory environment. IL-33 signalling in T cells stimulates T_{reg} responses in several ways. First, it enhances transforming growth factor (TGF)- β -mediated differentiation of T_{reg} cells and, second, it provides a necessary signal for T_{reg}-cell accumulation and maintenance in inflamed tissues. Strikingly, IL-23, a key pro-inflammatory cytokine in the pathogenesis of inflammatory bowel disease, restrained T_{reg} responses through inhibition of IL-33 responsiveness. These results demonstrate a hitherto unrecognized link between an endogenous mediator of tissue damage and a major anti-inflammatory pathway, and suggest that the balance between IL-33 and IL-23 may be a key controller of intestinal immune responses.

To identify potential tissue-specific modulators of colonic T_{reg} cells, we compared the messenger RNA expression profiles of mesenteric lymph node and colonic T_{reg} cells. We identified *St2* (also known as *Il1rl1*), the transcript coding for the IL-33 receptor¹², as one of the top differentially upregulated genes in colonic T_{reg} cells (Fig. 1a, b). Flow-cytometric analysis confirmed selective enrichment of ST2⁺ T_{reg} cells in the colon (Fig. 1c) and these cells expressed high levels of the activation markers KLRG1, CD103 and OX40 (Fig. 1d). Analysis of Helios expression revealed that ST2⁺ T_{reg} cells are a heterogeneous population containing thymus-derived T_{reg} cells as well as peripherally generated Helios⁺ T_{reg} cells (Fig. 1e)¹³. A significant proportion of intestinal Foxp3⁺ T_{reg} cells co-express the transcription factor GATA3 (refs 14–16), and GATA3 is known to regulate ST2 expression in T_H2 cells¹⁷. Indeed, ST2 expression was largely restricted to GATA3-expressing colonic T_{reg} cells (Fig. 1e) and selective ablation of GATA3 in Foxp3-expressing cells, using *Gata3^{fl/fl}-Foxp3-cre* mice¹⁵, caused a marked reduction of ST2 protein levels (Fig. 1f).

Given that ST2⁺ T_{reg} cells are prominent in the colon, we postulated that IL-33 may modulate *in vitro* induced (i)T_{reg}-cell differentiation.

To test this, we sort-purified naive CD4⁺ T cells from *Foxp3^{gfp}* reporter mice and activated them in the presence of TGF- β ₁. Notably, both *Gata3* and *St2* expression were induced under iT_{reg}-differentiation conditions (Extended Data Fig. 1). Addition of IL-33 to iT_{reg} cultures significantly increased both the percentage and total number of Foxp3-expressing cells but had no effect on Foxp3 expression in the absence of TGF- β ₁ (Fig. 2a). The presence of IL-33 in iT_{reg} cultures did not affect induction of T_H2 cytokines or expression of T_H1- and T_H17-associated transcription factors *Tbx21* and *Rorc* (Extended Data Fig. 1), suggesting that IL-33 preferentially regulates Foxp3 expression. Thus, our data indicate

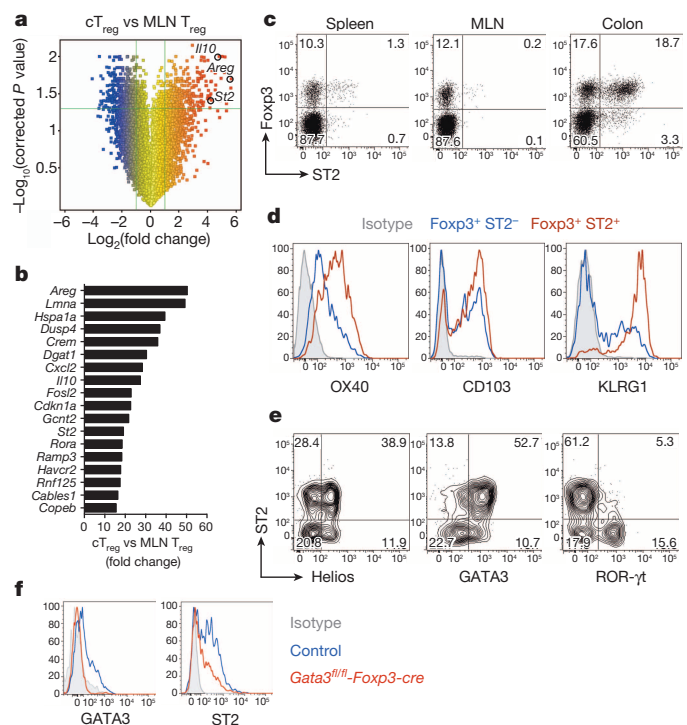


Figure 1 | ST2-expressing T_{reg} cells are enriched in the colon. **a**, Change in gene expression in colonic (c)T_{reg} cells versus mesenteric lymph node (MLN) T_{reg} cells ($n = 3$ per group) presented as volcano plot. **b**, Top differentially upregulated transcripts in colonic T_{reg} versus MLN T_{reg} cells. **c**, ST2 protein expression on T_{reg} cells from indicated organs. **d**, Phenotypic analysis of ST2⁺ or ST2⁺ colonic T_{reg} cells. **e**, Expression of transcription factors in colonic T_{reg} cells. **f**, Representative histograms gated on colonic T_{reg} cells from control or *Gata3^{fl/fl}-Foxp3-cre* mice.

¹Translational Gastroenterology Unit, Nuffield Department of Clinical Medicine, Experimental Medicine Division, John Radcliffe Hospital, University of Oxford, Oxford OX3 9DU, UK. ²Experimental Immunology, Department of Rheumatology and Clinical Immunology, Charité — University Medicine Berlin, and German Rheumatism Research Center (DRFZ), D-10117 Berlin, Germany. ³Program in Barrier Immunity and Repair, Mucosal Immunology Section, Laboratory of Parasitic Diseases, National Institute of Allergy and Infectious Diseases (NIAID), National Institutes of Health (NIH), Bethesda, Maryland 20892, USA. ⁴Sir William Dunn School of Pathology, University of Oxford, South Parks Road, Oxford OX1 3RE, UK. ⁵Trinity Biomedical Sciences Institute, Trinity College Dublin, Pearse Street, Dublin 2, Ireland. [†]Present addresses: Division of Molecular Immunology, MRC National Institute for Medical Research, Mill Hill, London NW7 1AA, UK (C.S.); Department of Microbiology and Immunology, School of Medicine and Biomedical Sciences, University at Buffalo (SUNY), Buffalo, New York 14214-3000, USA (E.A.W.).

*These authors contributed equally to this work.

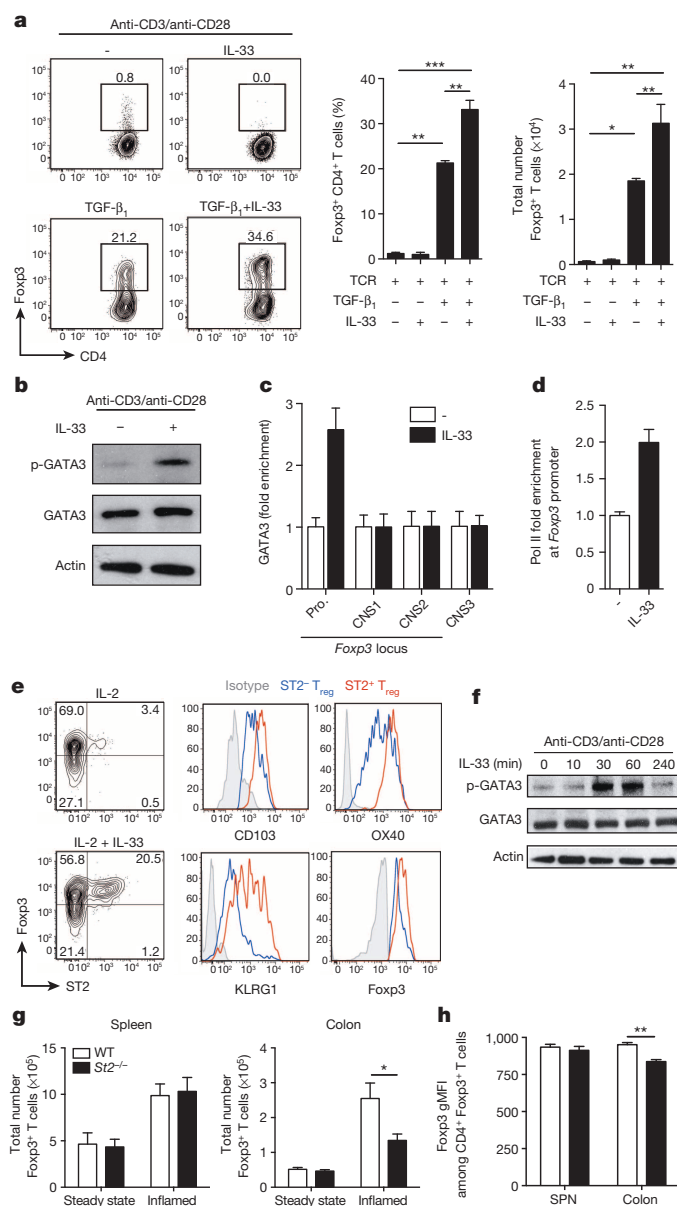


Figure 2 | Effects of IL-33 on iT_{reg} and thymus-derived T_{reg} cells. **a**, Naive CD4⁺ T cells were cultured with anti-CD3/CD28 plus the indicated cytokines and the frequencies and absolute numbers of Fopx3⁺ T cells were determined 3 days later (mean \pm standard error of the mean (s.e.m.) of three independent experiments). **b**, Naive CD4⁺ T cells were cultured for 48 h with anti-CD3/CD28 plus TGF- β_1 , followed by stimulation with IL-33 for 45 min. Blots are representative of two independent experiments. p, phosphorylated. **c**, **d**, Cells were cultured and stimulated as in **b** and recruitment of GATA3 or RNA Pol II to the indicated regions was assessed by ChIP-qPCR. Data are from one experiment representative of two (mean \pm standard deviation (s.d.)). Pro., promoter. -, no IL-33 added. **e**, Representative plots of T_{reg} cells cultured with anti-CD3/CD28 plus indicated cytokines and analysed after 3 days. Data are representative of three independent experiments. **f**, T_{reg} cells were cultured with anti-CD3/CD28 for 24 h followed by stimulation with IL-33. Blots are representative of three independent experiments. **g**, Mixed chimaera mice were generated containing wild-type (WT) and *St2*^{-/-} bone marrow cells. Reconstituted mice were analysed at steady state or 2 weeks after infection with *H. hepaticus* and anti-IL-10R treatment (inflamed). Absolute numbers of wild-type or *St2*^{-/-} T_{reg} cells in steady state ($n = 3$) and inflamed ($n = 6$) hosts (mean \pm s.e.m.). **h**, Analysis of Foxp3 expression in T_{reg} cells in spleen (SPN) and colon from inflamed chimaeric hosts presented as geometric mean fluorescence intensity (gMFI). * $P < 0.05$, ** $P < 0.01$, *** $P < 0.001$ as calculated by one-way analysis of variance (ANOVA) with Bonferroni post-test or paired Student's *t*-test.

that the alarmin IL-33 is a novel cofactor in TGF- β_1 -mediated iT_{reg} generation.

GATA3 is highly expressed in ST2⁺ T_{reg} cells (Fig. 1e) and IL-33 has been shown to activate GATA3 in TH2 cells^{17,18} as well as in innate lymphoid cells¹⁹. Consistent with this notion, we observed serine phosphorylation of GATA3 upon acute stimulation of iT_{reg} cells with IL-33 (Fig. 2b). The *Fopx3* locus contains putative GATA3-binding sites within its promoter and intragenic conserved noncoding sequences (CNSs) 1–3 (ref. 14). To investigate whether IL-33 influences the binding of GATA3 to any of these elements in iT_{reg} cells, we performed chromatin immunoprecipitation (ChIP) followed by quantitative polymerase chain reaction (PCR). Acute stimulation of iT_{reg} cells with IL-33 induced GATA3 recruitment to the *Fopx3* promoter but not CNS1, 2 or 3 (Fig. 2c). In addition, RNA polymerase II (Pol II) was recruited to the *Fopx3* promoter upon IL-33 stimulation (Fig. 2d), suggesting that IL-33 directly regulates *Fopx3* expression through activation and recruitment of GATA3 to the *Fopx3* promoter. In TH2 cells, GATA3 has been shown to promote *St2* gene expression by binding to an enhancer element located 12 kilobases upstream of the *St2* transcription start site¹⁷. Consistent with this, we detected recruitment of GATA3 to the *St2* enhancer upon acute stimulation of iT_{reg} cells with IL-33 and this correlated with RNA Pol II enrichment at the *St2* promoter (Extended Data Fig. 2). Thus, in addition to its role in Fopx3 induction, IL-33 also promoted its own receptor expression in iT_{reg} cells through direct transcriptional regulation of the *St2* locus, providing an amplification loop for further enhancement of iT_{reg}-cell differentiation.

Next we focused on thymus-derived T_{reg} cells, which constitute a significant proportion of ST2⁺ colonic T_{reg} cells (Fig. 1e). In line with published reports^{20,21}, administration of recombinant IL-33 led to a significant increase in the frequency and total number of splenic T_{reg} cells (Extended Data Fig. 3a, b) and these IL-33-elicited T_{reg} cells expressed higher levels of Fopx3 and ST2 (Extended Data Fig. 3c, d). Further analysis of the proliferation marker Ki67 showed that IL-33 induced proliferation in splenic T_{reg} cells but not in T effector cells (Extended Data Fig. 3e). To examine whether IL-33 acts directly on T_{reg} cells, we injected IL-33 into chimaeric mice containing a mixture of wild-type and *St2*^{-/-} haematopoietic cells. In this setting, the proliferative capacity of *St2*^{-/-} T_{reg} cells was significantly impaired (Extended Data Fig. 3f), suggesting that IL-33 acts directly on thymus-derived T_{reg} cells to promote their proliferation and accumulation *in vivo*. This is further supported by the finding that sort-purified splenic T_{reg} cells cultured in the presence of IL-33 expressed higher levels of ST2, showed a more activated phenotype and expressed increased amounts of Fopx3 protein (Fig. 2e). In addition, acute stimulation of T-cell antigen receptor (TCR)-activated splenic T_{reg} cells with IL-33 induced serine phosphorylation of GATA3 (Fig. 2f), further demonstrating that IL-33 acts directly on thymus-derived T_{reg} cells.

To assess the impact of IL-33 on the T_{reg} response during intestinal inflammation, we induced chronic colitis by infection with *Helicobacter hepaticus* and administration of an IL-10R blocking antibody²² (Extended Data Fig. 4a). We detected an increase in IL-33 protein levels in colon explant cultures and its expression kinetics mirrored that of IL-23, which is essential for the development of intestinal inflammation in this model (Extended Data Fig. 4b). Consistent with its pattern of expression, IL-33 protein levels were elevated in colonic intestinal epithelial cells isolated from the inflamed gut (Extended Data Fig. 4c, d). Interestingly, the onset of intestinal pathology correlated with a marked increase of soluble ST2, which is produced primarily by colonic stromal cells (Extended Data Fig. 4b, e, f). Soluble ST2 is thought to limit IL-33 bioavailability by acting as a decoy receptor²³ and is increased in patients with active inflammatory bowel disease (IBD)^{6,24}, suggesting that the chronic inflammatory tissue environment may antagonize IL-33 activity. Despite high levels of soluble ST2, analysis of chimaeric mice showed that accumulation of *St2*^{-/-} T_{reg} cells in the colon but not the spleen was significantly impaired during the peak of intestinal inflammation (Fig. 2g). In addition, colonic *St2*^{-/-} T_{reg} cells expressed lower amounts of Fopx3 protein on a per cell

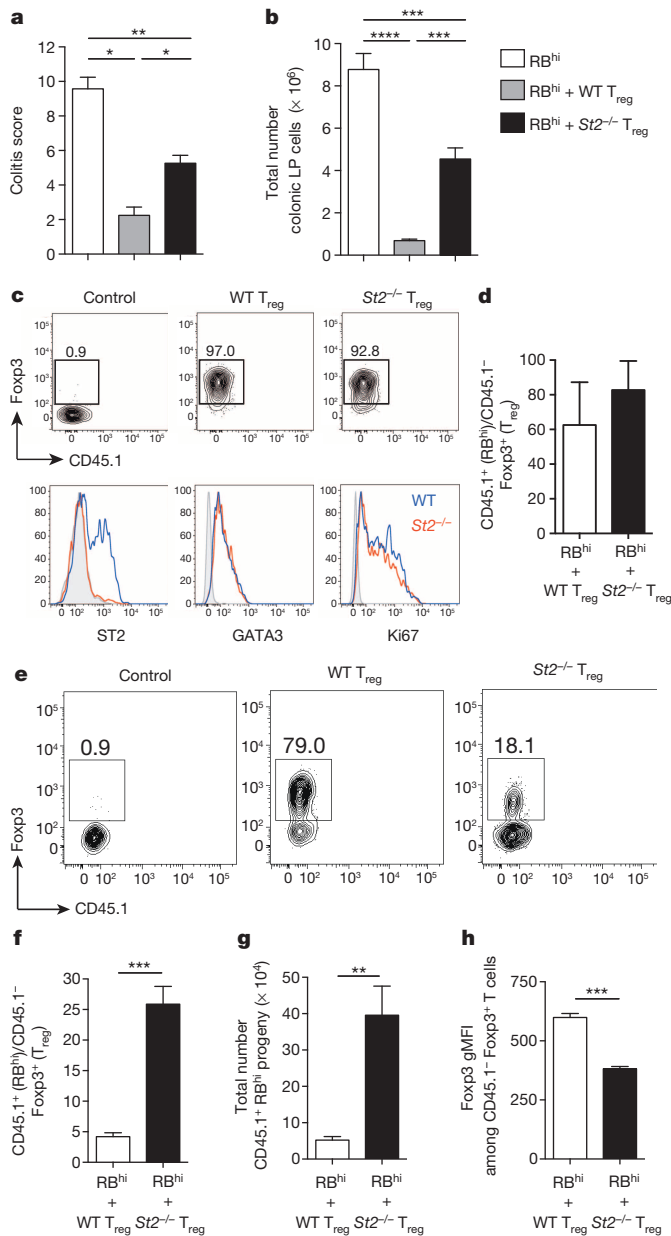


Figure 3 | IL-33 promotes T_{reg}-cell stability and function *in vivo*. **a**, C57BL/6 *Rag1*^{-/-} mice were injected with CD45.1⁺ naive T cells alone (RB^{hi}; $n = 4$) or in combination with wild-type (WT; $n = 4$) or St2^{-/-} ($n = 6$) CD45.1⁻ T_{reg} cells. Mice were killed 6–8 weeks after transfer and colitis scores are shown (mean \pm s.e.m.). **b**, Absolute numbers of colon lamina propria (LP) cells from mice in **a** (mean \pm s.e.m.). **c**, C57BL/6 *Rag1*^{-/-} mice were injected as in **a** and killed at 2 weeks post-injection. Representative plots are gated on colonic T_{reg}-cell progeny (CD45.1⁻). **d**, Ratio of RB^{hi} T-cell progeny (CD45.1⁺) to wild-type or St2^{-/-} Foxp3⁺ T_{reg}-cell progeny (CD45.1⁻) in the colon ($n = 5$ per group) from mice in **c** (mean \pm s.e.m.). **e**, C57BL/6 *Rag1*^{-/-} mice were injected as in **a** and killed at 8 weeks post-injection. Representative plots are gated on colonic T_{reg}-cell progeny (CD45.1⁻). **f**, Ratio of RB^{hi} T-cell progeny (CD45.1⁺) to wild-type or St2^{-/-} T_{reg}-cell progeny (CD45.1⁻) in the colon from mice in **e** (mean \pm s.e.m.). **g**, Absolute numbers of RB^{hi} T-cell progeny (CD45.1⁺) in the colon from mice in **e** (mean \pm s.e.m.). **h**, Analysis of Foxp3 expression in colonic Foxp3⁺ CD45.1⁻ T_{reg} cells presented as gMFI (mean \pm s.e.m.). Results are representative of two independent experiments. * $P < 0.05$, ** $P < 0.01$, *** $P < 0.001$, **** $P < 0.0001$ as calculated by one-way ANOVA with Bonferroni post-test or Student's *t*-test.

basis as compared to their wild-type counterparts (Fig. 2h). Together, these observations indicate that the alarmin IL-33 acts in a cell-intrinsic manner to promote the tissue-specific accumulation and stability of the

T_{reg} phenotype in the intestine under inflammatory conditions. Furthermore, high levels of soluble ST2 during chronic intestinal inflammation may represent a mechanism to further perpetuate pathogenic responses by limiting IL-33-driven T_{reg} accumulation.

We next sought to compare the suppressive capacity of wild-type and St2^{-/-} T_{reg} cells. St2^{-/-} T_{reg} cells inhibited T-cell proliferation to the same extent as wild-type T_{reg} cells *in vitro* (Extended Data Fig. 5) and addition of IL-33 did not enhance wild-type T_{reg} suppressor function. We then tested the ability of St2^{-/-} T_{reg} cells to protect from colitis induced by adoptive transfer of naive CD4⁺ T cells. Interestingly, ST2 was highly expressed on wild-type T_{reg} cells upon T-cell transfer, pointing towards a potential role of ST2 in modulating T_{reg} function in this model (Extended Data Fig. 6a). Indeed, St2^{-/-} T_{reg} cells were significantly impaired in their ability to prevent colonic inflammation and cellular infiltration (Fig. 3a, b), demonstrating that IL-33 signalling in T_{reg} cells is important for their suppressive function *in vivo*. Analysis of wild-type or St2^{-/-} T_{reg} cells 2 weeks after transfer, before the onset of intestinal pathology, showed similar proliferative capacity and Foxp3 expression between groups (Fig. 3c). The ratio of T effector cells (CD45.1⁺ RB^{hi} progeny) to T_{reg} cells (CD45.1⁻ Foxp3⁺ T_{reg} progeny) was also similar (Fig. 3d), suggesting that IL-33 signalling in T_{reg} cells is dispensable for their ability to expand and index with effector cells in the lymphopenic host at 2 weeks after transfer. By contrast, analysis at 8 weeks after transfer showed that the progeny of St2^{-/-} T_{reg} cells contained a significantly lower proportion of Foxp3⁺ cells and expressed significantly less Foxp3 on a per cell basis, suggesting that they had lost Foxp3 expression (Fig. 3e, h). Under these circumstances the ratio of T effector/T_{reg} cells and the total number of T effector cells (CD45.1⁺ RB^{hi} progeny) was markedly increased in recipients of St2^{-/-} T_{reg} cells (Fig. 3f, g). Importantly, ST2-deficient T_{reg} cells did not themselves acquire the capacity to produce inflammatory cytokines (Extended Data Fig. 6c). Perturbations of Foxp3 expression have been shown to affect T_{reg}-cell function^{25–27} and our data indicate that IL-33 signalling in T_{reg} cells contributes to the maintenance of Foxp3 expression under inflammatory stress, enabling T_{reg} cells to compete in the inflammatory niche and to control the intestinal effector T-cell response.

Next we sought to integrate our observations with existing pro-inflammatory pathways. IL-23 is a pivotal mediator of intestinal inflammation and polymorphisms in the *IL23R* locus are associated with increased susceptibility to IBD in humans²⁸. We previously showed that IL-23 promotes intestinal inflammation in part through inhibition of iT_{reg}-cell differentiation^{29,30}. However, the mechanism by which IL-23 blocked iT_{reg} generation remained undefined. Interestingly, whole transcriptome analysis of IL-23 target genes in colonic effector CD4⁺ T cells revealed that IL-23 inhibits expression of *Gata3* and *St2* (Extended Data Fig. 7). On the basis of this observation we hypothesized that IL-23 might limit T-cell responsiveness to IL-33. Indeed, the cofactor activity of IL-33 on TGF- β -mediated Foxp3 induction *in vitro* was completely abrogated in the presence of IL-23 (Fig. 4a). Notably, addition of IL-23 prevented induction of *Gata3* and *St2* mRNA under iT_{reg} differentiation conditions (Fig. 4b), resulting in reduced ST2 protein expression (Fig. 4c). Consequently, acute stimulation of IL-23-exposed iT_{reg} cells with IL-33 did not lead to recruitment of GATA3 to the ST2 enhancer (Extended Data Fig. 8). We observed a similar role for IL-23 in limiting T_{reg} ST2 expression during bacterially driven intestinal inflammation (Extended Data Fig. 9). Collectively, our data indicate that IL-23 inhibits iT_{reg} differentiation by regulating T-cell responsiveness to IL-33.

We previously showed that IL-23 restrains T_{reg} cells *in vivo* because naive T-cell transfer into *Il23a*^{-/-} *Rag1*^{-/-} recipients resulted in increased T_{reg}-cell differentiation²⁹. Therefore, we hypothesized that enhanced responsiveness to IL-33 may contribute to increased iT_{reg} differentiation in *Il23a*^{-/-} *Rag1*^{-/-} hosts. To test this, we transferred wild-type or St2^{-/-} naive T cells into *Il23a*^{-/-} *Rag1*^{-/-} hosts and monitored iT_{reg}-cell generation. Indeed, ST2-deficient T cells were significantly impaired in their ability to differentiate into T_{reg} cells (Fig. 4d) and this correlated with a significant increase in intestinal pathology (Fig. 4e). Importantly,

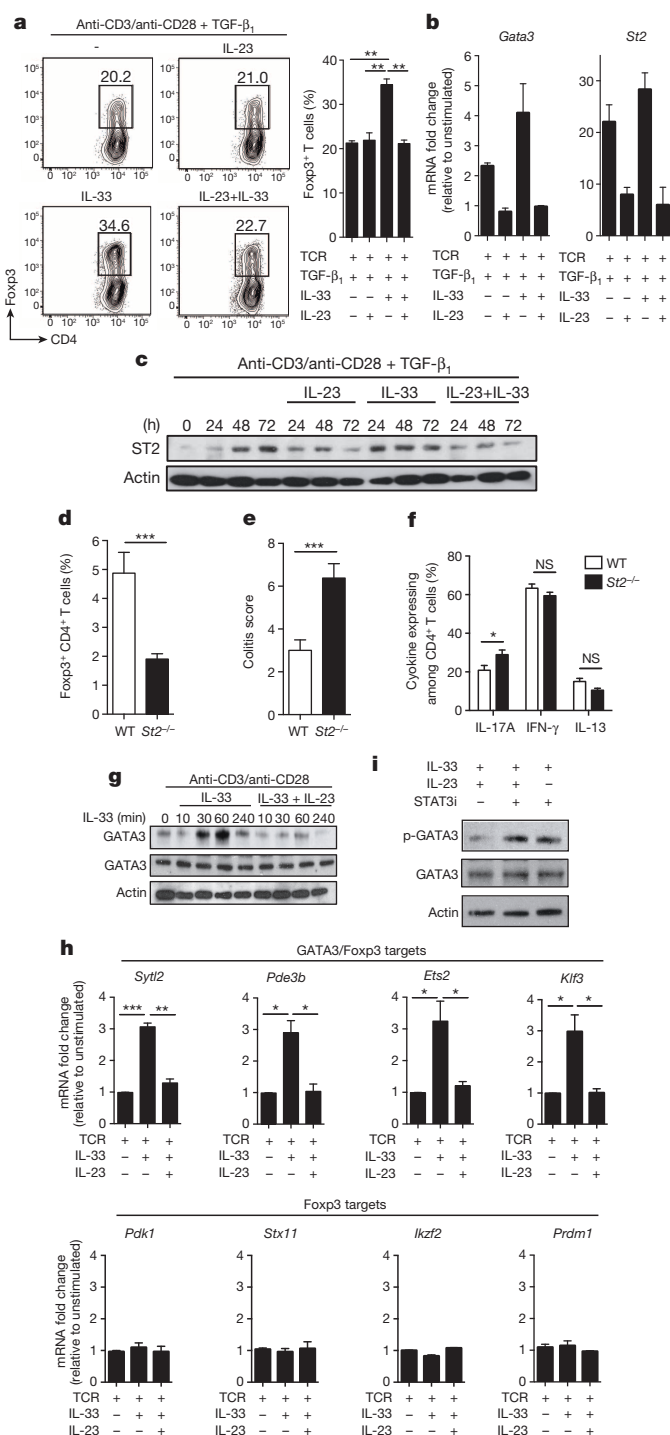


Figure 4 | IL-23 inhibits the effects of IL-33 on T_{reg} cells. **a**, Naive CD4⁺ T cells were cultured with anti-CD3/CD28 plus TGF- β_1 , as well as the indicated cytokines, and the frequencies of Foxp3⁺ T cells were determined 3 days later (mean \pm s.e.m. of three independent experiments). **b**, Naive CD4⁺ T cells were cultured with anti-CD3/CD28 plus the indicated cytokines for 48 h. Data are from one experiment representative of two (mean \pm s.d.). **c**, Naive CD4⁺ T cells were cultured as indicated. Representative blots of two independent experiments are shown. **d**, C57BL/6 *Il23a*^{-/-} *Rag1*^{-/-} mice were injected with CD45RB^{hi} wild-type (WT; $n = 9$) or *St2*^{-/-} ($n = 10$) T cells. Mice were killed 6–8 weeks after transfer and frequencies of Foxp3⁺ CD4⁺ T cells in colon are shown (mean \pm s.e.m.). **e**, Colitis scores for mice in **d** (mean \pm s.e.m.). **f**, Expression of the indicated cytokines by colonic CD4⁺ T cells from mice in **d** (mean \pm s.e.m.). **g**, T_{reg} cells were cultured with anti-CD3/CD28 for 24 h followed by stimulation with IL-33 in the presence or absence of IL-23. Representative blots of two independent experiments are shown. **h**, T_{reg} cells were cultured in the presence of anti-CD3/CD28 for 24 h and the mRNA expression of the indicated genes was measured after stimulation with IL-33 for 45 min in the presence or absence of IL-23 (mean \pm s.e.m. of three independent experiments). **i**, T_{reg} cells were cultured with anti-CD3/CD28 for 24 h and representative blots of two independent experiments are shown. **p**, phosphorylated. * $P < 0.05$, ** $P < 0.01$, *** $P < 0.001$ as calculated by one-way ANOVA with Bonferroni post-test or Student's *t*-test. NS, not significant.

IL-23 (Fig. 4h). Addition of a specific inhibitor of STAT3, the main transcription factor downstream of IL-23 signalling, reversed this inhibitory effect of IL-23 (Fig. 4i). Together our data suggest that IL-23 inhibits ST2 signal transduction and expression of a distinct set of GATA3-regulated genes in thymus-derived T_{reg} cells.

Our results identify a new function for IL-33 as an important link between inflammation-driven tissue damage and the local intestinal T_{reg}-cell response. We show that colonic T_{reg} cells are poised to respond to the release of IL-33 upon tissue damage through selective expression of ST2 and that signalling through this pathway has an essential role in their capacity to adapt to the inflammatory tissue environment and restrain intestinal inflammation. The ability of IL-33 to amplify regulatory networks in response to tissue injury may represent a more general mechanism by which alarmins limit immune-mediated damage to self at barrier tissues. Strikingly, IL-23 limits this regulatory mechanism through inhibition of T_{reg}-cell responsiveness to IL-33, suggesting that the balance between IL-23 and IL-33 may be a major determinant of the outcome of intestinal immune responses.

Online Content Methods, along with any additional Extended Data display items and Source Data, are available in the online version of the paper; references unique to these sections appear only in the online paper.

Received 27 November 2013; accepted 11 June 2014.

Published online 16 July 2014.

- Burzyn, D., Benoist, C. & Mathis, D. Regulatory T cells in nonlymphoid tissues. *Nature Immunol.* **14**, 1007–1013 (2013).
- Pichery, M. et al. Endogenous IL-33 is highly expressed in mouse epithelial barrier tissues, lymphoid organs, brain, embryos, and inflamed tissues: *in situ* analysis using a novel *Il-33-LacZ* gene trap reporter strain. *J. Immunol.* **188**, 3488–3495 (2012).
- Palmer, G. & Gabay, C. Interleukin-33 biology with potential insights into human diseases. *Nature Rev. Rheumatol.* **7**, 321–329 (2011).
- Beltrán, C. J. et al. Characterization of the novel ST2/IL-33 system in patients with inflammatory bowel disease. *Inflamm. Bowel Dis.* **16**, 1097–1107 (2010).
- Kobori, A. et al. Interleukin-33 expression is specifically enhanced in inflamed mucosa of ulcerative colitis. *J. Gastroenterol.* **45**, 999–1007 (2010).
- Pastorelli, L. et al. Epithelial-derived IL-33 and its receptor ST2 are dysregulated in ulcerative colitis and in experimental Th1/Th2 driven enteritis. *Proc. Natl Acad. Sci. USA* **107**, 8017–8022 (2010).
- Seidelin, J. B. et al. IL-33 is upregulated in colonocytes of ulcerative colitis. *Immunol. Lett.* **128**, 80–85 (2010).
- Oboki, K. et al. IL-33 is a crucial amplifier of innate rather than acquired immunity. *Proc. Natl Acad. Sci. USA* **107**, 18581–18586 (2010).
- Duan, L. et al. Interleukin-33 ameliorates experimental colitis through promoting Th2/Foxp3⁺ regulatory T-cell responses in mice. *Mol. Med.* **18**, 753–761 (2012).
- Groß, P., Doser, K., Falk, W., Obermeier, F. & Hofmann, C. IL-33 attenuates development and perpetuation of chronic intestinal inflammation. *Inflamm. Bowel Dis.* **18**, 1900–1909 (2012).

ST2 deficiency had minor effects on *in vivo* differentiation of T_H1, T_H2 or T_H17 cells (Fig. 4f), further supporting the notion that the increased colitogenic potential of *St2*^{-/-} CD4⁺ T cells is a consequence of deficient iT_{reg} differentiation rather than dysregulated effector T-cell responses. Our data strongly suggest that IL-33 is a major factor responsible for driving iT_{reg} differentiation in the absence of IL-23.

Finally, we investigated whether IL-23 can interfere with ST2 signalling in T_{reg} cells. Interestingly, sort-purified ST2⁺ T_{reg} cells from the colon expressed detectable levels of *Il23r* (Extended Data Fig. 10). Indeed, exposure of TCR-activated thymus-derived T_{reg} cells to IL-23 completely abolished IL-33-mediated GATA3 phosphorylation (Fig. 4g). Furthermore, IL-33 preferentially induced genes co-regulated by Foxp3 and GATA3 (ref. 16), and this was completely abrogated in the presence of

11. Sedhom, M. A. *et al.* Neutralisation of the interleukin-33/ST2 pathway ameliorates experimental colitis through enhancement of mucosal healing in mice. *Gut* **62**, 1714–1723 (2013).
12. Schmitz, J. *et al.* IL-33, an interleukin-1-like cytokine that signals via the IL-1 receptor-related protein ST2 and induces T helper type 2-associated cytokines. *Immunity* **23**, 479–490 (2005).
13. Thornton, A. M. *et al.* Expression of Helios, an Ikaros transcription factor family member, differentiates thymic-derived from peripherally induced Foxp3⁺ T regulatory cells. *J. Immunol.* **184**, 3433–3441 (2010).
14. Wang, Y., Su, M. A. & Wan, Y. Y. An essential role of the transcription factor GATA-3 for the function of regulatory T cells. *Immunity* **35**, 337–348 (2011).
15. Wohlfert, E. A. *et al.* GATA3 controls Foxp3⁺ regulatory T cell fate during inflammation in mice. *J. Clin. Invest.* **121**, 4503–4515 (2011).
16. Rudra, D. *et al.* Transcription factor Foxp3 and its protein partners form a complex regulatory network. *Nature Immunol.* **13**, 1010–1019 (2012).
17. Guo, L. *et al.* IL-1 family members and STAT activators induce cytokine production by Th2, Th17, and Th1 cells. *Proc. Natl Acad. Sci. USA* **106**, 13463–13468 (2009).
18. Maneechotesuwan, K. *et al.* Regulation of Th2 cytokine genes by p38 MAPK-mediated phosphorylation of GATA-3. *J. Immunol.* **178**, 2491–2498 (2007).
19. Furusawa, J. *et al.* Critical role of p38 and GATA3 in natural helper cell function. *J. Immunol.* **191**, 1818–1826 (2013).
20. Turnquist, H. R. *et al.* IL-33 expands suppressive CD11b⁺ Gr-1^{int} and regulatory T cells, including ST2L⁺ Foxp3⁺ cells, and mediates regulatory T cell-dependent promotion of cardiac allograft survival. *J. Immunol.* **187**, 4598–4610 (2011).
21. Wasserman, A. *et al.* Interleukin-33 augments Treg cell levels: a flaw mechanism in atherosclerosis. *Isr. Med. Assoc. J.* **14**, 620–623 (2012).
22. Kullberg, M. C. *et al.* IL-23 plays a key role in *Helicobacter hepaticus*-induced T cell-dependent colitis. *J. Exp. Med.* **203**, 2485–2494 (2006).
23. Hayakawa, H., Hayakawa, M., Kume, A. & Tominaga, S. Soluble ST2 blocks interleukin-33 signaling in allergic airway inflammation. *J. Biol. Chem.* **282**, 26369–26380 (2007).
24. Díaz-Jiménez, D. *et al.* Soluble ST2: a new and promising activity marker in ulcerative colitis. *World J. Gastroenterol.* **17**, 2181–2190 (2011).
25. Zheng, Y. *et al.* Role of conserved non-coding DNA elements in the *Foxp3* gene in regulatory T-cell fate. *Nature* **463**, 808–812 (2010).
26. Wan, Y. Y. & Flavell, R. A. Regulatory T-cell functions are subverted and converted owing to attenuated Foxp3 expression. *Nature* **445**, 766–770 (2007).
27. Kitoh, A. *et al.* Indispensable role of the Runx1-Cbfb transcription complex for *in vivo*-suppressive function of FoxP3⁺ regulatory T cells. *Immunity* **31**, 609–620 (2009).
28. Maloy, K. J. & Powrie, F. Intestinal homeostasis and its breakdown in inflammatory bowel disease. *Nature* **474**, 298–306 (2011).
29. Izcue, A. *et al.* Interleukin-23 restrains regulatory T cell activity to drive T cell-dependent colitis. *Immunity* **28**, 559–570 (2008).
30. Ahern, P. P. *et al.* Interleukin-23 drives intestinal inflammation through direct activity on T cells. *Immunity* **33**, 279–288 (2010).

Acknowledgements C.S., K.A., A.C., O.J.H. and F.P. are supported by the Wellcome Trust. F.P. is also supported by the Fondation Louis Jeantet. A.N.H. is supported by a European Molecular Biology Organization long-term fellowship (ALTF 116-2012). P.G.F. is supported by Science Foundation Ireland. M.L. and A.F. are supported by the Volkswagen Foundation (Lichtenberg Program) and BMBF (e:Bio/T-Sys). B.M.J.O. is supported by an Oxford-UCB Pharma Postdoctoral Fellowship. We thank all members of the Oxford Translational Gastroenterology Unit for assistance and support. We are grateful to H. Ferry and K. Alford for essential flow cytometry support and the staff of the University of Oxford for animal care. We are also grateful to D. Baban for conducting microarray hybridizations.

Author Contributions C.S. and T.K. planned experiments and analysed the data. C.S., T.K. and F.P. wrote the paper. A.C., A.F., K.A., O.J.H., A.N.H., E.A.W., T.G., J.B., B.M.J.O. and J.P. performed particular experiments. M.L., Y.B. and P.G.F. provided essential materials and were involved in data discussions.

Author Information Microarray data have been deposited in the Gene Expression Omnibus under accession number GSE58164. Reprints and permissions information is available at www.nature.com/reprints. The authors declare no competing financial interests. Readers are welcome to comment on the online version of the paper. Correspondence and requests for materials should be addressed to F.P. (fiona.powrie@path.ox.ac.uk).

Structural basis of PAM-dependent target DNA recognition by the Cas9 endonuclease

Carolyn Anders¹, Ole Niewoehner¹, Alessia Duerst¹ & Martin Jinek¹

The CRISPR-associated protein Cas9 is an RNA-guided endonuclease that cleaves double-stranded DNA bearing sequences complementary to a 20-nucleotide segment in the guide RNA^{1,2}. Cas9 has emerged as a versatile molecular tool for genome editing and gene expression control³. RNA-guided DNA recognition and cleavage strictly require the presence of a protospacer adjacent motif (PAM) in the target DNA^{1,4–6}. Here we report a crystal structure of *Streptococcus pyogenes* Cas9 in complex with a single-molecule guide RNA and a target DNA containing a canonical 5'-NGG-3' PAM. The structure reveals that the PAM motif resides in a base-paired DNA duplex. The non-complementary strand GG dinucleotide is read out via major-groove interactions with conserved arginine residues from the carboxy-terminal domain of Cas9. Interactions with the minor groove of the PAM duplex and the phosphodiester group at the +1 position in the target DNA strand contribute to local strand separation immediately upstream of the PAM. These observations suggest a mechanism for PAM-dependent target DNA melting and RNA–DNA hybrid formation. Furthermore, this study establishes a framework for the rational engineering of Cas9 enzymes with novel PAM specificities.

In type II CRISPR (clustered regularly interspaced short palindromic repeats)–Cas (CRISPR-associated) systems, the endonuclease Cas9 associates with a dual-RNA guide structure consisting of a CRISPR RNA (crRNA) and a trans-activating CRISPR RNA (tracrRNA) to cleave double-stranded DNA (dsDNA) using its HNH and RuvC nuclease domains^{1,2,7}. Cas9 has been exploited in numerous gene-targeting applications, in which its sequence specificity is programmed by either dual crRNA–tracrRNA guides or chimaeric single-molecule guide RNAs (sgRNAs)^{8–19}. PAM recognition is a critical aspect of Cas9-mediated DNA targeting, being a prerequisite for ATP-independent strand separation and guide-RNA–target-DNA heteroduplex formation⁶. Recent crystal structures and electron microscopic reconstructions of Cas9 and its RNA- and DNA-bound complexes revealed that Cas9 undergoes a dramatic RNA-induced conformational rearrangement that facilitates target DNA binding^{20,21}. Although two tryptophan residues have been implicated in PAM binding²⁰, how PAM recognition occurs at the molecular level remains unclear.

To provide insight into the molecular mechanism of PAM recognition in Cas9, we determined the crystal structure of *S. pyogenes* Cas9

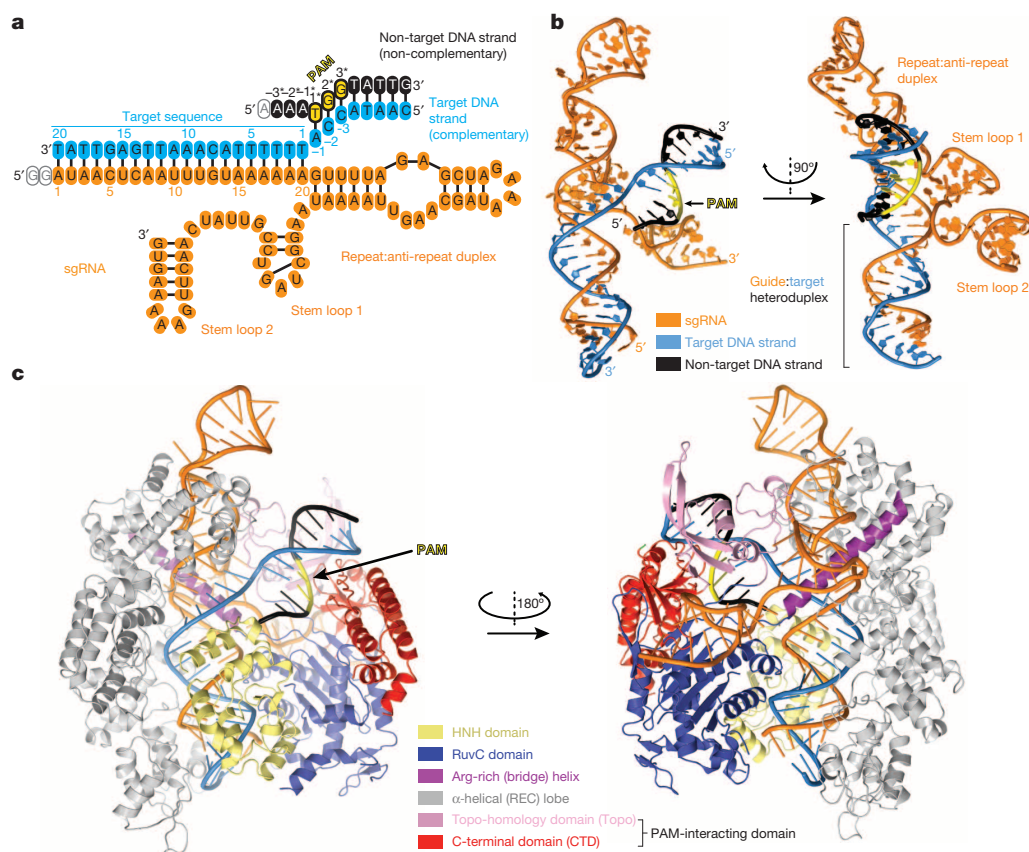


Figure 1 | Crystal structure of Cas9 in complex with a sgRNA and a PAM-containing target DNA. **a**, Schematic diagram of guide and target nucleic acids. Empty ovals denote nucleotides not observed in the electron density. **b**, Orthogonal views of the sgRNA–target–DNA four-way junction. **c**, Front and rear views of the Cas9–sgRNA–DNA complex. In all panels guide RNA is coloured orange, target DNA strand in light blue and non-target DNA strand in black. The 5'-NGG-3' PAM trinucleotide in the non-target strand is highlighted in yellow.

¹Department of Biochemistry, University of Zurich, Winterthurerstrasse 190, CH-8057 Zurich, Switzerland.

in complex with an 83-nucleotide sgRNA and a partially duplexed target DNA containing a 5'-TGG-3' PAM sequence (Fig. 1 and Extended Data Table 1). Owing to an inactivating mutation (H840A) in the Cas9 HNH nuclease domain, the structure reveals an intact target (complementary) DNA strand, while the non-target (non-complementary) DNA strand is captured as cleaved product that has dissociated from the RuvC domain active site (Fig. 1a–c). In the complex, the bound nucleic acids are enclosed by the nuclease and helical recognition lobes of Cas9 and form a four-way junction that straddles the arginine-rich bridge helix (Fig. 1b, c). The entire PAM-containing region of the target DNA (target-strand nucleotides –1 to –8 and non-target-strand nucleotides +1* to +8*) is base-paired. Strand separation occurs only at the first base pair of the target sequence (the +1 position). Here, the target strand exhibits a pronounced kink as it hybridizes with the sgRNA. The PAM duplex is nestled in a positively charged groove between the Topoisomerase-homology and C-terminal domains (collectively referred to as the PAM-interacting domain²¹) (Fig. 2a and Extended Data Fig. 1). Comparison with the crystal structure of the Cas9–sgRNA complex bound to a single-stranded DNA target²¹ reveals a slight tightening of an otherwise pre-structured PAM binding cleft upon PAM-duplex binding (Extended Data Fig. 2).

The deoxyribose-phosphate backbone of the non-target DNA strand is engaged in numerous ionic and hydrogen-bonding interactions (Fig. 2b). Conserved tryptophan residues Trp 476 and Trp 1126, previously implicated in PAM recognition by crosslinking experiments²⁰, are not in direct contact with the PAM, suggesting that the crosslinks may have originated from a transient intermediate in the PAM recognition mechanism, or from non-specifically bound DNA. Instead, the guanine nucleobases of dG2* and dG3* in the non-target strand are read out in the major groove by base-specific hydrogen-bonding interactions with Arg 1333 and Arg 1335, respectively, provided by a β -hairpin from the

C-terminal domain of Cas9 (Fig. 2c). The target-strand nucleotides complementary to the PAM are not recognized by major-groove interactions (Fig. 2b, c), rationalizing previous observations that Cas9-mediated DNA cleavage requires the 5'-NGG-3' trinucleotide in the non-target strand, but not its target-strand complement^{1,6}. The lack of interactions with the target-strand backbone also explains why mismatches in the PAM are tolerated provided that a GG dinucleotide is present in the non-target strand¹. In agreement with the observed role of the arginine residues in PAM recognition, substitution of Arg 1333 or Arg 1335 with alanine residues resulted in substantially reduced target DNA binding *in vitro* (Fig. 2d). Furthermore, alanine substitutions of both Arg 1333 and Arg 1335 nearly abolished cleavage of linearized plasmid DNA, and substantially reduced cleavage of supercoiled circular plasmid DNA and short dsDNA oligonucleotides *in vitro* (Fig. 2e and Extended Data Fig. 3). Individual arginine substitutions yielded modest reductions of cleavage activity (Fig. 2e and Extended Data Fig. 3).

The Cas9 sequence motif containing the PAM-interacting arginine residues (₁₃₃₂DRKRY₁₃₃₆) is conserved in other type II-A Cas9 proteins known to recognize 5'-NGG-3' PAMs (Extended Data Fig. 4 and Supplementary Information). Similar arginine-containing motifs are found in Cas9 from *Francisella novicida* (₁₆₀₈SRYPD₁₆₁₂) and from *Streptococcus thermophilus* CRISPR3 locus (₁₃₅₀PRYRDY₁₃₅₆), which recognize 5'-NG-3' and 5'-NGGNG-3' PAMs, respectively, but are notably absent from type II-C Cas9 proteins that are known to recognize distinct PAM sequences^{4,22,23} (Extended Data Fig. 4). Whereas arginine residues are commonly used by DNA-binding proteins to recognize guanines, major-groove read-out of adenines typically involves glutamine residues²⁴. Interestingly, a Cas9 orthologue from *Lactobacillus buchneri*, predicted to recognize a 5'-NAAAA-3' PAM²⁵, contains glutamine residues (₁₃₃₈QLQ₁₃₄₀) at the positions equivalent to Arg 1333 and Arg 1335 in *S. pyogenes* Cas9. Together, these observations suggest

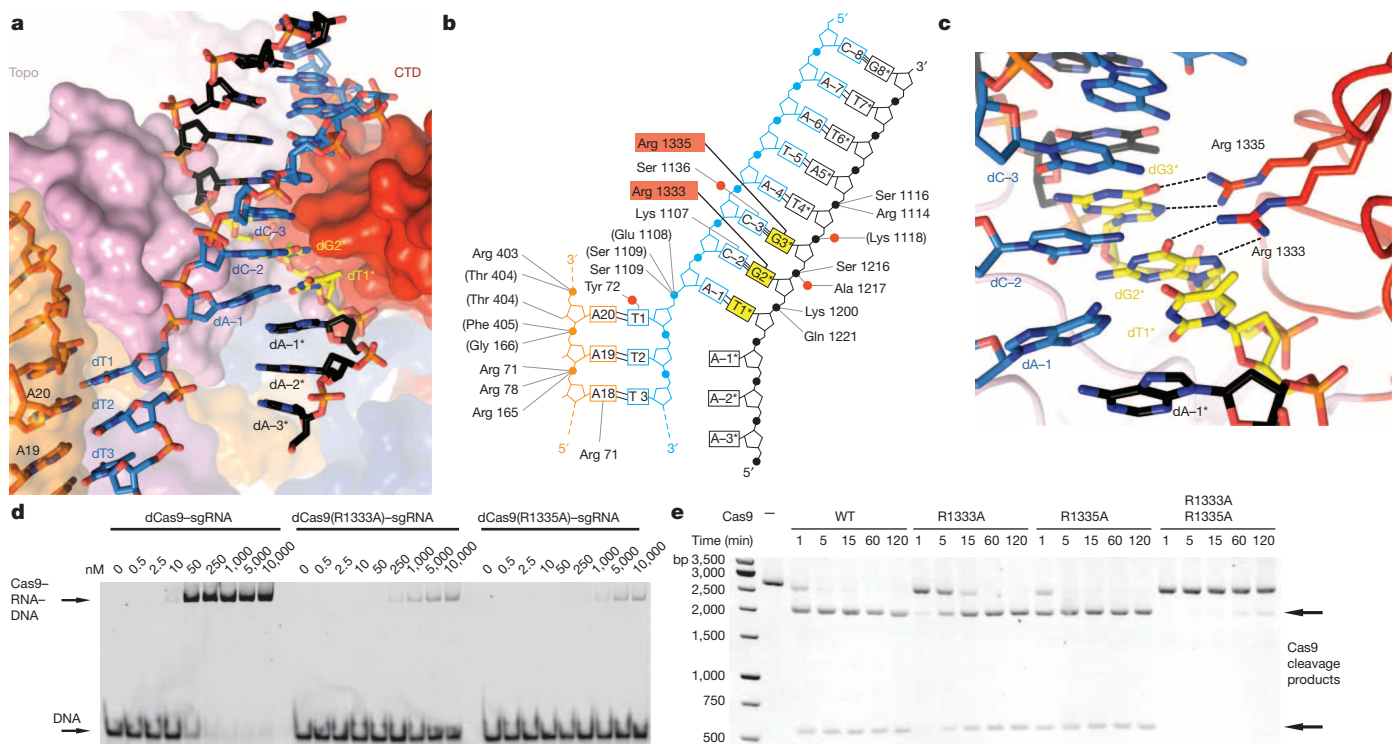


Figure 2 | The GG dinucleotide of the PAM is read out by major-groove interactions. **a**, Zoomed-in view of the PAM binding region in Cas9. Topo, topoisomerase-homology domain; CTD, C-terminal domain. **b**, Schematic of Cas9 interactions with the PAM duplex. Red circles denote bridging water molecules. **c**, Detailed view of the major groove. Sequence-specific hydrogen-bonding interactions with the GG PAM dinucleotide are indicated with dashed lines. **d**, Electrophoretic mobility shift assay using catalytically inactive dCas9–sgRNA complexes and fluorophore-labelled target DNA duplex.

e, Endonuclease activity assay of wild type (WT) and mutant Cas9 proteins using a linearized plasmid DNA containing a target sequence fully complementary to the sgRNA in Fig. 1a. Bands at 2,104 and 598 base pairs (bp) correspond to Cas9 cleavage products. In all relevant panels guide RNA is coloured orange, target DNA strand in light blue and non-target DNA strand in black. The 5'-NGG-3' PAM trinucleotide in the non-target strand is highlighted in yellow.

that at least in a subset of Cas9 proteins, PAM binding may be governed by a major-groove base-recognition code. Substitutions of Arg 1333 and Arg 1335 in *S. pyogenes* Cas9 with glutamine residues did not produce a specificity switch towards alanine-rich PAMs (Extended Data Fig. 5). Reprogramming PAM specificity might thus require more extensive remodelling of the PAM-interacting motif by directed evolution and/or computational design, as has been done previously for homing endonucleases^{26,27}.

The PAM-interacting domain of Cas9 makes further contacts with the minor groove of the PAM duplex (Fig. 3a). Ser 1136 interacts with the non-target strand dG3* through a water-mediated hydrogen bond, while Lys 1107 contacts dC-2 of the target strand (Fig. 3a). This interaction enforces a pyrimidine at this position, explaining why 5'-NAG-3' PAMs are weakly permissive for *S. pyogenes* Cas9 (refs 19, 28, 29). The minor-groove interactions with the PAM duplex orient the target DNA strand for base pairing with the guide RNA. Downstream of

Lys 1107, residues Glu 1108 and Ser 1109 interact with the phosphodiester group linking dA-1 and dT1 in the target DNA strand (the +1 phosphate). The non-bridging phosphate oxygen atoms form hydrogen bonds with the backbone amide groups of Glu 1108 and Ser 1109, and with the side chain of Ser 1109 (Fig. 3b). Owing to its interaction with the Lys 1107-Ser 1109 loop (the 'phosphate lock' loop), the +1 phosphate group is rotated (Fig. 3c and Extended Data Fig. 6), which coincides with a distortion in the target DNA strand that allows the nucleobase of dT1 to base pair with A20 of the guide RNA. Furthermore, comparison with the structure of Cas9-sgRNA bound to a single-stranded DNA²¹ suggests that interaction between the +1 phosphate and the loop is PAM-dependent (Extended Data Fig. 6).

Previous biochemical studies indicated that PAM recognition is concomitant with local destabilization of the adjacent sequence and directional target DNA unwinding from the PAM-proximal end⁶. Our structural observations suggest that the interaction between the target

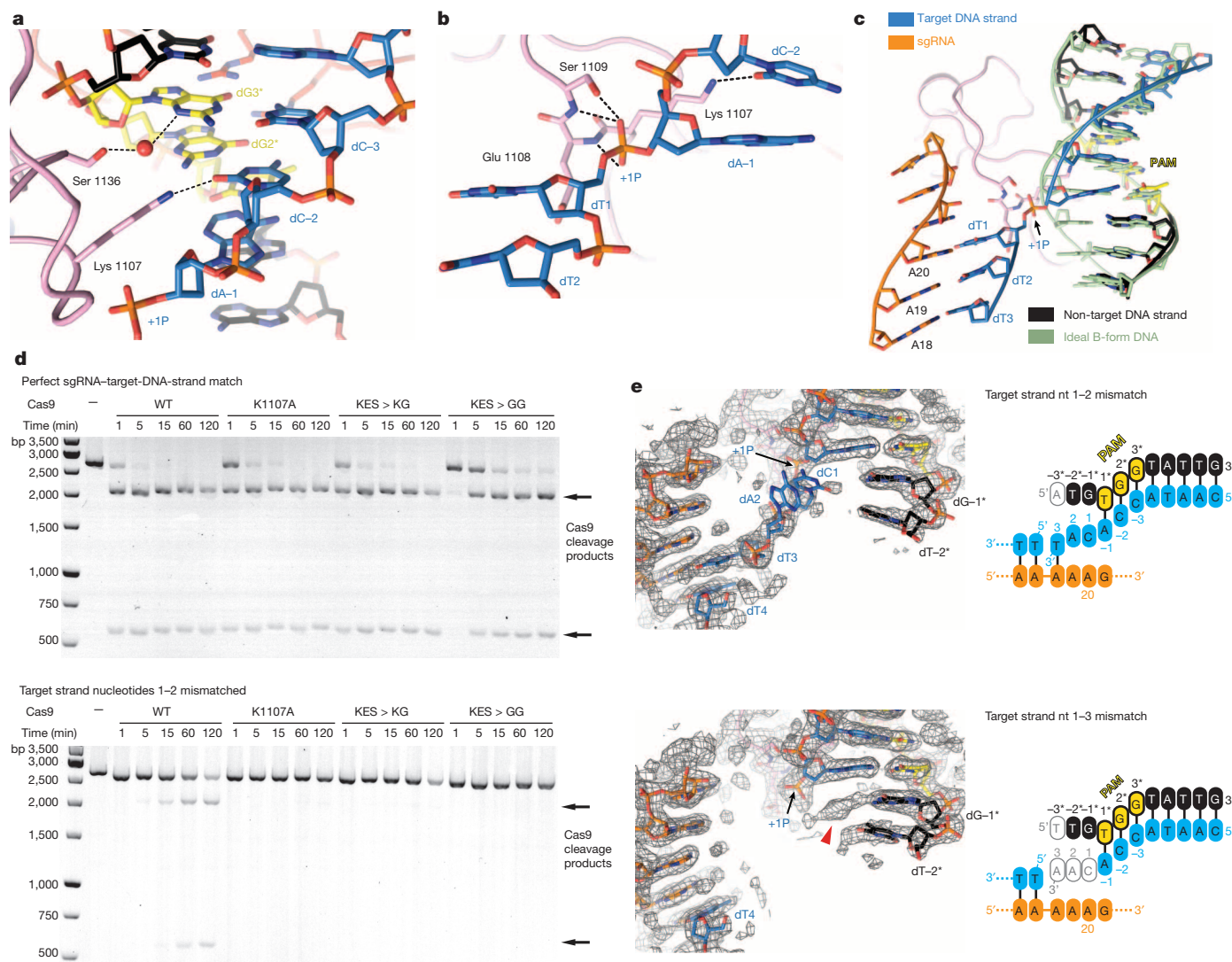


Figure 3 | Interactions with the +1 phosphodiester group orient the target strand for guide-RNA binding. **a**, Detailed view of the minor groove of the PAM region. **b**, Hydrogen-bonding interactions (dashed lines) of the +1 phosphate (+1P) with the Lys 1107-Ser 1109 (phosphate lock) loop. **c**, Superposition of the unwound target DNA strand with an ideal B-form DNA duplex (green). **d**, Endonuclease activity assays using linearized plasmid DNA containing a fully complementary target sequence (top) or a target sequence mismatched to the sgRNA at positions 1-2 (bottom). KES>KG denotes substitution of the Lys 1107-Ser 1109 loop with a Lys-Gly dipeptide. KES>GG denotes substitution of the Lys 1107-Ser 1109 loop with a Gly-Gly dipeptide.

e, Crystal structures of dCas9-sgRNA bound to DNA substrates containing mismatches to the sgRNA at positions 1-2 (top) and 1-3 (bottom), overlaid with refined $2mF_o - DF_c$ electron density maps (grey mesh, contoured at 1σ). The sgRNA is identical to that in Fig. 1a. In both structures, the target DNA strand is provided in two fragments, as indicated in the schematics. Residual electron density corresponding to the +1 base pair is indicated with a red arrowhead. In all relevant panels guide RNA is coloured orange, target DNA strand in light blue and non-target DNA strand in black. The 5'-NGG-3' PAM trinucleotide in the non-target strand is highlighted in yellow.

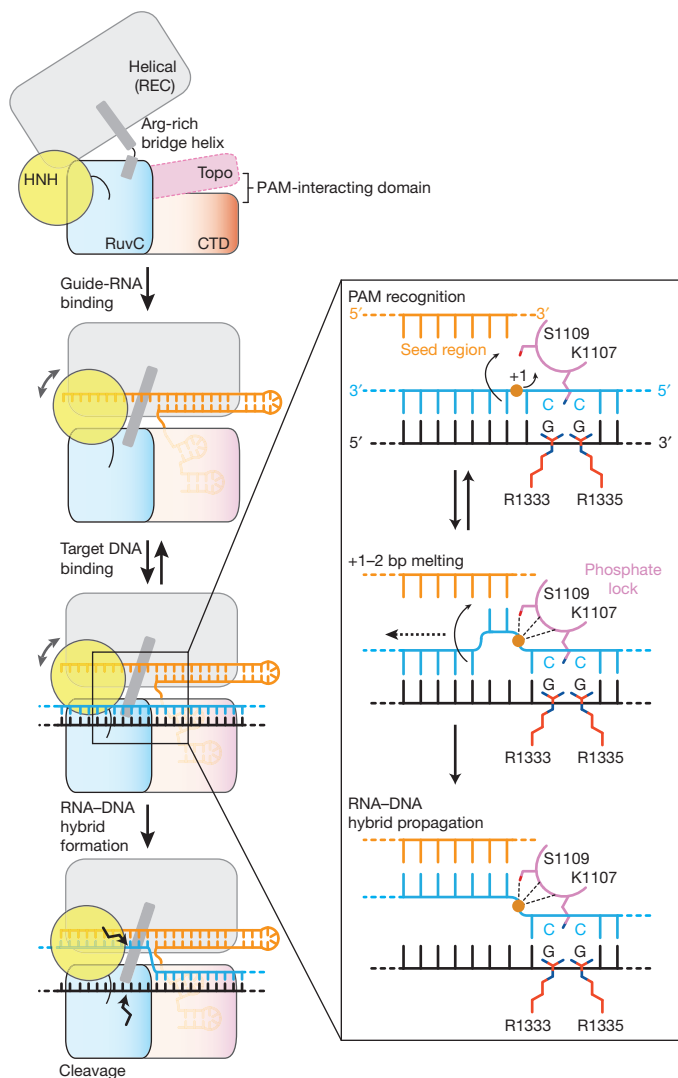


Figure 4 | Model for PAM-dependent target DNA unwinding and recognition by Cas9. Guide RNA binding to Cas9 results in the formation of the PAM binding site. Cas9–RNA engages the PAM GG dinucleotide using Arg 1333 and Arg 1335, and positions the target DNA duplex such that the +1 phosphate (orange circle) interacts with the phosphate lock loop, resulting in local strand separation immediately upstream of the PAM. Base pairing between displaced target DNA strand and the seed region of the guide RNA promotes further stepwise strand displacement and propagation of the guide–target heteroduplex. Guide RNA is coloured orange, target DNA strand in light blue and non-target DNA strand in black. CTD, C-terminal domain. Topo, topoisomerase-homology domain; REC, recognition lobe. bp, base pair.

DNA strand and the phosphate lock loop might stabilize target DNA immediately upstream of the PAM in an unwound conformation, thereby linking PAM recognition with local strand separation. In agreement with this hypothesis, alanine substitution of Lys 1107 or replacement of the Lys 1107–Ser 1109 loop with a Lys–Gly or Gly–Gly dipeptide yielded Cas9 proteins with modestly reduced cleavage activities towards linearized plasmid DNA containing a perfectly complementary sequence, but almost no activity towards DNA containing mismatches to the guide RNA at positions 1 and 2 (Fig. 3d). Moreover, the phosphate lock loop mutations also disproportionately impaired cleavage of an oligonucleotide duplex containing the same mismatch, but the defect was partially relieved with a duplex in which the mismatched nucleotides were themselves unpaired (Extended Data Fig. 7).

To provide additional support for the hypothesis, we determined two crystal structures of Cas9(D10A/H840A)–sgRNA bound to DNAs containing mismatches to the guide RNA (Fig. 3e and Extended Data

Table 1). To discount the possibility that duplex melting in these target DNAs is driven from the unpaired PAM-distal end, the target strand was supplied in two fragments and interrupted by a gap at the scissile phosphate (+4) position. The structure of the complex containing mismatches at positions 1 and 2 reveals a fully melted duplex, with nucleotides +1 and +2 unpaired, and nucleotide dT3 base paired to A18 of the sgRNA. In the complex containing mismatches at positions 1–3, the target strand backbone upstream of the PAM is disordered and we observe only residual electron density for the +1 base pair that cannot be modelled with full occupancy (Fig. 3e), suggesting that the DNA is unpaired in a substantial fraction of molecules in the crystal. Together, these structures reveal that even in the absence of compensatory base pairing to the guide RNA, target DNA binding by Cas9–RNA results in local strand separation immediately upstream of the PAM. Importantly, the interaction of the +1 phosphate with the phosphate lock loop is maintained in both structures, supporting the hypothesis that the loop contributes to stabilizing the target DNA strand in the unwound state.

In this study we highlight the central importance of PAM recognition in Cas9 function, both as a critical determinant of initial target DNA binding and as a licensing element in subsequent strand separation and guide-RNA–target-DNA hybridization. Based on our structural and biochemical observations, we propose a model for PAM-dependent target dsDNA recognition and unwinding (Fig. 4). Sequence-specific PAM read-out by Arg 1333 and Arg 1335 in Cas9 positions the DNA duplex such that the +1 phosphate group of the target strand interacts with the phosphate lock loop. This promotes local duplex melting, allowing the Cas9–RNA complex to probe the identity of the nucleotides immediately upstream of the PAM. Base pairing between the seed region of the guide RNA and the target DNA strand subsequently drives further stepwise destabilization of the target DNA duplex and directional formation of the guide-RNA–target-DNA heteroduplex.

Online Content Methods, along with any additional Extended Data display items and Source Data, are available in the online version of the paper; references unique to these sections appear only in the online paper.

Received 11 March; accepted 13 June 2014.

Published online 27 July 2014.

- Jinek, M. *et al.* A programmable dual-RNA-guided DNA endonuclease in adaptive bacterial immunity. *Science* **337**, 816–821 (2012).
- Gasiunas, G., Barrangou, R., Horvath, P. & Siksnys, V. Cas9–crRNA ribonucleoprotein complex mediates specific DNA cleavage for adaptive immunity in bacteria. *Proc. Natl Acad. Sci. USA* **109**, 2579–2586 (2012).
- Mali, P., Esvelt, K. M. & Church, G. M. Cas9 as a versatile tool for engineering biology. *Nature Methods* **10**, 957–963 (2013).
- Garneau, J. E. *et al.* The CRISPR/Cas bacterial immune system cleaves bacteriophage and plasmid DNA. *Nature* **468**, 67–71 (2010).
- Sapranauskas, R. *et al.* The *Streptococcus thermophilus* CRISPR/Cas system provides immunity in *Escherichia coli*. *Nucleic Acids Res.* **39**, 9275–9282 (2011).
- Sternberg, S. H., Redding, S., Jinek, M., Greene, E. C. & Doudna, J. A. DNA interrogation by the CRISPR RNA-guided endonuclease Cas9. *Nature* **507**, 62–67 (2014).
- Deltcheva, E. *et al.* CRISPR RNA maturation by trans-encoded small RNA and host factor RNase III. *Nature* **471**, 602–607 (2011).
- Mali, P. *et al.* RNA-guided human genome engineering via Cas9. *Science* **339**, 823–826 (2013).
- Cong, L. *et al.* Multiplex genome engineering using CRISPR/Cas systems. *Science* **339**, 819–823 (2013).
- Jinek, M. *et al.* RNA-programmed genome editing in human cells. *elife* **2**, e00471 (2013).
- Hwang, W. Y. *et al.* Efficient genome editing in zebrafish using a CRISPR–Cas system. *Nature Biotechnol.* **31**, 227–229 (2013).
- Wang, H. *et al.* One-step generation of mice carrying mutations in multiple genes by CRISPR/Cas-mediated genome engineering. *Cell* **153**, 910–918 (2013).
- Bassett, A. R., Tibbit, C., Ponting, C. P. & Liu, J.-L. Highly efficient targeted mutagenesis of *Drosophila* with the CRISPR/Cas9 system. *Cell Rep.* **4**, 220–228 (2013).
- Gratz, S. J. *et al.* Genome engineering of *Drosophila* with the CRISPR RNA-guided Cas9 nuclease. *Genetics* **194**, 1029–1035 (2013).
- Friedland, A. E. *et al.* Heritable genome editing in *C. elegans* via a CRISPR–Cas9 system. *Nature Methods* **10**, 741–743 (2013).
- Qi, L. S. *et al.* Repurposing CRISPR as an RNA-guided platform for sequence-specific control of gene expression. *Cell* **152**, 1173–1183 (2013).

17. Bikard, D. *et al.* Programmable repression and activation of bacterial gene expression using an engineered CRISPR-Cas system. *Nucleic Acids Res.* **41**, 7429–7437 (2013).
18. Gilbert, L. A. *et al.* CRISPR-mediated modular RNA-guided regulation of transcription in eukaryotes. *Cell* **154**, 442–451 (2013).
19. Mali, P. *et al.* CAS9 transcriptional activators for target specificity screening and paired nickases for cooperative genome engineering. *Nature Biotechnol.* **31**, 833–838 (2013).
20. Jinek, M. *et al.* Structures of Cas9 endonucleases reveal RNA-mediated conformational activation. *Science* **343**, 1215 (2014).
21. Nishimasu, H. *et al.* Crystal structure of Cas9 in complex with guide RNA and target DNA. *Cell* **156**, 935–949 (2014).
22. Fonfara, I. *et al.* Phylogeny of Cas9 determines functional exchangeability of dual-RNA and Cas9 among orthologous type II CRISPR-Cas systems. *Nucleic Acids Res.* **42**, 2577–2590 (2013).
23. Esvelt, K. M. *et al.* Orthogonal Cas9 proteins for RNA-guided gene regulation and editing. *Nature Methods* **10**, 1116–1121 (2013).
24. Luscombe, N. M., Laskowski, R. A. & Thornton, J. M. Amino acid-base interactions: a three-dimensional analysis of protein-DNA interactions at an atomic level. *Nucleic Acids Res.* **29**, 2860–2874 (2001).
25. Briner, A. E. & Barrangou, R. *Lactobacillus buchneri* genotyping on the basis of clustered regularly interspaced short palindromic repeat (CRISPR) locus diversity. *Appl. Environ. Microbiol.* **80**, 994–1001 (2014).
26. Redondo, P. *et al.* Molecular basis of xeroderma pigmentosum group C DNA recognition by engineered meganucleases. *Nature* **456**, 107–111 (2008).
27. Ashworth, J. *et al.* Computational reprogramming of homing endonuclease specificity at multiple adjacent base pairs. *Nucleic Acids Res.* **38**, 5601–5608 (2010).
28. Jiang, W., Bikard, D., Cox, D., Zhang, F. & Marraffini, L. A. RNA-guided editing of bacterial genomes using CRISPR-Cas systems. *Nature Biotechnol.* **31**, 233–239 (2013).
29. Hsu, P. D. *et al.* DNA targeting specificity of RNA-guided Cas9 nucleases. *Nature Biotechnol.* **31**, 827–832 (2013).

Supplementary Information is available in the online version of the paper.

Acknowledgements We are grateful to J. Doudna for agreement on research directions, helpful discussions and encouragement throughout the project. We thank B. Blattmann and C. Stutz-Ducommun for crystallization screening, N. Ban and M. Leibundgut for the gift of iridium hexamine, and R. Dutzler for sharing synchrotron beam time and crystallographic advice. We thank E. Charpentier, I. Fonfara, S. Sternberg, P. Sledz, A. May and S. Kassube for critical reading of the manuscript. Part of this work was performed at the Swiss Light Source at the Paul Scherrer Institute, Villigen, Switzerland. We thank T. Tomizaki, V. Olieric and M. Wang for assistance with X-ray data collection. This work was supported by the European Research Council Starting Grant no. 337284 ANTIVIRNA and by start-up funds from the University of Zurich.

Author Contributions C.A. designed experiments, performed site-directed mutagenesis, prepared guide RNAs, purified and crystallized the Cas9–sgRNA–target-DNA complex, determined its structure together with M.J., and performed plasmid cleavage assays. O.N. purified Cas9 mutants, performed EMSA assays and assisted with cleavage assays. A.D. performed site-directed mutagenesis, prepared guide RNAs and assisted with cleavage assays. M.J. designed experiments and supervised the study. C.A. and M.J. wrote the manuscript.

Author Information Atomic coordinates and structure factors have been deposited in the Protein Data Bank under accession numbers 4un3, 4un4 and 4un5. Reprints and permissions information is available at www.nature.com/reprints. Readers are welcome to comment on the online version of the paper. The authors declare competing financial interests: details are available in the online version of the paper. Correspondence and requests for materials should be addressed to M.J. (jinek@bioc.uzh.ch).

CORRIGENDUM

doi:10.1038/nature13675

Corrigendum: Quantitative flux analysis reveals folate-dependent NADPH production

Jing Fan, Jiangbin Ye, Jurre J. Kamphorst, Tomer Shlomi, Craig B. Thompson & Joshua D. Rabinowitz

Nature **510**, 298–302 (2014); doi:10.1038/nature13236

In the interests of transparency, we wish to amend the ‘Competing financial interests’ section of our Letter to read: “J.D.R. is the only author with a competing financial interest with respect to the current manuscript. He is involved in the founding of Raze Therapeutics.”

CORRIGENDUM

doi:10.1038/nature13699

Corrigendum: Elephant shark genome provides unique insights into gnathostome evolution

Byrappa Venkatesh, Alison P. Lee, Vydianathan Ravi, Ashish K. Maurya, Michelle M. Lian, Jeremy B. Swann, Yuko Ohta, Martin F. Flajnik, Yoichi Sutoh, Masanori Kasahara, Shawn Hoon, Vamshidhar Gangu, Scott W. Roy, Manuel Irimia, Vladimir Korzh, Igor Kondrychyn, Zhi Wei Lim, Boon-Hui Tay, Sumanty Tohari, Kiat Whye Kong, Shufen Ho, Belen Lorente-Galdos, Javier Quilez, Tomas Marques-Bonet, Brian J. Raney, Philip W. Ingham, Alice Tay, LaDeana W. Hillier, Patrick Minx, Thomas Boehm, Richard K. Wilson, Sydney Brenner & Wesley C. Warren

Nature **505**, 174–179 (2014); doi:10.1038/nature12826

The ranges of accession numbers JW861113–JW881738 and KA353634–KA353668 (20,661 in total) cited in this Article include 3,630 sequences that were unrelated and hence removed from the NCBI GenBank database before the analysis of the data and submission of the manuscript to *Nature*. None of those sequences were used or are cited anywhere in the Article. The sequences that were used in the analysis and cited in the Article are available under BioProject ID PRJNA168475.

CORRIGENDUM

doi:10.1038/nature13720

Corrigendum: Coupling of angiogenesis and osteogenesis by a specific vessel subtype in bone

Anjali P. Kusumbe, Saravana K. Ramasamy & Ralf H. Adams

Nature **507**, 323–328 (2014); doi:10.1038/nature13145

In this Article, the labels 'Metaphysis' and 'Diaphysis' were inadvertently swapped in Extended Data Fig 3d. In the Methods Summary on page 327 and in the third paragraph of the Methods it should state that deferroxamine mesylate (DFM) was injected for μ -CT (microtomography) analysis into mice for a period of 6 weeks, rather than 5 weeks. These errors have been corrected in the online versions of the Article.

CAREERS

SALARY Report confirms broad gender pay disparity in United States **p.577**

GRADUATE EDUCATION Institutions globally aim to support interdisciplinarity **p.577**

NATUREJOBS For the latest career listings and advice www.naturejobs.com



ILLUSTRATION BY CLAIRE WELSH/NATURE; FOSSIL ILLUSTRATION BY ARTA/SHUTTERSTOCK

WORK-LIFE BALANCE

Kid-friendly digs

How to blend fieldwork and far-flung travel with raising little people.

BY KENDALL POWELL

Before heading off to hunt for fossils in the Canadian High Arctic for a month every summer, Jaelyn Eberle buys and freezes pre-made dinners for her husband and three boys — along with other preparations to make for an easier life. The palaeontologist's work takes her from the University of

Colorado Boulder to an off-the-grid spot for four to five weeks, and her husband works long hours and has a round-trip commute of nearly two hours for his job in Denver. So they hire two babysitters who split the work days, book the kids — aged 14, 7 and 5 — into summer camps and swim lessons and put Eberle's retired-nurse mother in Canada on call for emergencies.

Like many early- and mid-career researchers, Eberle has to balance family responsibilities with the demands of her research, and that requires advance planning and dispassionate cost-benefit analyses. Research schedules rarely fit neatly into day-care hours, but field research — be it fossil hunting in the Arctic Circle or testing medical devices in Malawi — brings the extra challenge of long stretches of solo parenting and the need to modify work hours or secure extra, and usually expensive, child care.

Veteran field researchers say that it helps inestimably to have a supportive, equal-parenting partner who is willing to shoulder the extra load at such moments. But sometimes, it makes sense to bring the family along. Whatever approach or combination of approaches is adopted, scientists should remember to factor in family face time, say those who have learned the ropes. And they will need to develop a strategy that achieves both personal and professional goals (see 'Tips from parents').

INNOVATIVE SOLUTIONS

Selina Heppell, an ecologist at Oregon State University in Corvallis, crosses the globe to study the dynamics of endangered species. On a solo trip to Japan in 2000, her then-2-month-old son, Dylan, slept in the hotel's chest of drawers.

"Travelling with a little baby is not that hard. It's when they start running around that it gets problematic," she says. But getting Dylan, now aged 14, used to travelling early in his life made him more adaptable later on, she says.

Heppell and her researcher husband made a deliberate decision to have one child, knowing that their careers involved numerous trips to places such as Croatia, Iceland and Peru. "Having one kid and two parents means you can be quite mobile," she says.

They relied on hotel babysitting services and travelled light whenever possible — forgoing a portable crib, for example, and buying cheap, lightweight strollers that can be donated to a local mother when leaving the country.

Carrie Masiello, a geochemist at Rice University in Houston, Texas, says that when her son Owen was young, she and her husband, a biochemist at Rice, travelled less often for their work. But they did wonder whether they should have been doing more while working towards tenure. "Especially when you are a junior scientist, you have to get out and let people see your work," she says. Academia should find better ways to help pre-tenure faculty ►

► parents to be more mobile, Masiello adds.

And when they both had to travel out of town, they took advantage of Rice's contract with a national back-up day-care provider, which let them drop off Owen at centres near to their conferences. And sometimes, colleagues can help each other out. Heppell says that at times she travels with multiple families and each researcher takes a turn babysitting three or four kids for a day. "It takes a lab to raise a child," she says.

Researchers also need to consider their child's age and health when travel would require heavy immunizations or risk exposure to diseases such as malaria, typhoid or dengue. Heppell recommends that people check with their doctor. She decided that Malaysia was too risky for a 2-year-old Dylan — because of both the risk of infectious diseases and because there had been a terrorist attack in nearby Bali — but that by age 10, he could handle Peru and the necessary medications.

Short visits to other countries are one thing; remote fieldwork presents added challenges: camping in rustic or rough conditions, unreachable by mobile phone or e-mail and at the mercy of the local wildlife. Still, in some cases, it is feasible to bring the kids along. Masiello, for instance, says that her postdoctoral adviser chose a site in rural Canada for their soil-sampling trips in part because there was a day camp nearby where her kids could be dropped off each morning.

Likewise, Suzanne Anderson, an Earth scientist at Colorado's Institute of Arctic and

Alpine Research in Boulder, has at times selected field sites where her twin daughters and geologist husband could be nearby, so family life often overlapped with work. "We've always been ones who don't know where the boundaries are between home and work because my husband is in the same field and we often work together," she says.

That teamwork became indispensable when she won a grant to study glacier-outburst floods when she was heavily pregnant, because her husband was able to collect the data for her. Then, the following summer, when the twins were 9 months old, the entire family including her parents trekked to remote Alaska for a month. They stayed in a rustic cabin, borrowing a portable cot and high chair from locals. It was doable, she says, because her site was a 10-minute walk away and the area was free of bears.

She says that her spouse's equitable, even-handed approach to balancing fieldwork and child care has made her field excursions possible. "It really depended on having this spouse who was totally into it," she says. "The most important thing for me has been having a partner who is absolutely committed to our family and to us both having careers."

The couple returned to the Alaskan site when the girls were about 5, again with help from grandparents and this time a nanny as well. But they also turned down joint field opportunities if they did not seem safe or practical with children in tow. Short scouting trips to get preliminary data on snow melt or soil samples were useful for making those evaluations, she says. Anderson says that she has also been able to find field projects close by that still allow her to function as a chauffeur for her teens.

FIND A WAY

Whereas the Andersons achieve the right mix of field travel and family life through blurry work-life boundaries, Rebecca Richards-Kortum, a bioengineer at Rice, uses strict rules to combine her career with raising her six children aged from 4 to 22.

For example, she has a 'two weeks or less' rule for travel to Malawi, where she tests life-saving medical devices for newborns. It was a rule informed by experience: on hearing the news that one field trip was going to be extended by four days, her then-4-year-old daughter — who was at home with dad — had a complete meltdown. A parent's prolonged absence from home can leave small children — and spouses — with frayed nerves.

Now, she does one 10–14-day trip a year, working 15-hour days to maximize her research, and her husband, also a tenured researcher at Rice, takes over her parenting responsibilities. And during normal work weeks, the couple uses day care and after-school programmes instead of babysitters to help set limits on time spent at work.



MARILYN EITNER

Jaelyn Eberle sometimes takes her son Quin on field trips in Colorado.

"It's good insurance that I don't take too much advantage of always working late," she says. "The day-care centre closing is a good boundary." She also schedules her work trips to not clash with birthdays, an important family tradition. "Understand where your boundaries are — and figure out a way to stick to them," she advises.

Eberle, for her part, uses uber-organization to help to keep family life on track: she plans her Arctic trips almost a year in advance. And because her husband's position at an energy company often requires more-than-40-hour work weeks, the couple uses an agency to find experienced babysitters that meet their needs when she is away. The service also steps in to find a replacement quickly should one be needed. "We wanted someone we didn't have any concerns about," she says. Eberle notes that this arrangement is financially possible for her family only because it is not necessary year-round.

Her work on 50-million-year-old rhino-like brontothere fossils has to be done on-site and in-person. But Tom Painter, a snow hydrolo-

"It takes a lab to raise a child."

gist at the Jet Propulsion Laboratory in Pasadena, California, says that researchers

should carefully consider whether they actually need to attend a remote meeting.

His own research leads to various engagements with international scientists and federal, state and local water organizations. But as a father of two boys, he is wary of getting "carried off the cliff of busyness". So he has a strong commitment to say no to field travel and off-site meetings whenever he can. He uses Google Hangouts or Skype to give presentations whenever feasible. He also does the reverse, using

WAYS TO COPE

Tips from parents

- See the bright side of travelling with children. Parents with kids in tow often get to go to the front of a line and many areas of the world are child-friendly.
- Buy or borrow *The Happiest Baby on the Block* video (www.happiestbaby.com) for techniques that work to calm a screaming baby.
- Order groceries online and have them delivered when someone is home.
- Share videos or pictures of your travels with young children, so that they can begin to understand why you are gone.
- Investigate and make use of family-friendly workplace policies, including family leave and automatic tenure-clock stoppages for the birth or adoption of a child, and back-up day-care services.
- Apply for university mini-grants available to faculty to cover the extra child-care expenses related to travel.
- During long solo-parenting stretches, take frequent walks to diffuse stress and frustration. **K.P.**



Suzanne Anderson (second from left) took her husband, parents and 9-month-old twins on a trip to Alaska to study glacier outbursts.

video chats to connect with his boys while away — but it is not the same as being there in person. “We can’t shoot baskets,” he says, “or kick the soccer ball or wrestle.”

FAMILY CAPITAL

Single parents, and those who are effectively single parents because of long-distance relationships, face additional struggles. Jane Willenbring, an Earth scientist at the University of Pennsylvania in Philadelphia, travels to the far reaches of Antarctica, Puerto Rico and Turkey for her research on erosion and long-term climate change, and her husband is a political scientist on the opposite coast, at Stanford University in Palo Alto, California.

“I put in so much time solo parenting that I actually feel almost zero guilt,” she says about dropping off her almost-2-year-old daughter in Palo Alto so that she can do her fieldwork. She will even add a northern Californian project to her portfolio because it would be an easy side trip for her to drop off her daughter.

Because of her family’s situation, Willenbring’s ability to coordinate site visits with collaborators is restricted by her husband’s schedule and even by airline routes. She says that she must be frank with colleagues about her child-care and family-life requirements, and adds that it is ultimately for the best. “People are usually more accommodating. Or, if not, then you know you don’t want to work with them,” she says.

Alain Plante, one of Willenbring’s colleagues, says that her bi-coastal situation lets her stockpile what he calls “family capital.” He keeps careful track of his own levels, too.

“Every hour that I take away from my family, I feel like I have to make it up to them,” he says. He recently declined a field trip to

New Jersey because too many other trips had depleted his family capital account.

After spending a month in Mongolia, Plante paid back the capital by taking time off from work. But piggybacking family travel onto work travel can also work well, he says — a lectureship in Paris let his family spend a month with him.

The Google Calendar he shares with his wife, a counselling professor, is a boon for family organization and communication. But it also creates a mutual appreciation for how busy they both are. “When I ask her to cover while I’m gone, that’s not asking a little, that’s asking a lot,” he says.

Spousal support and commitment is key to finding the time and space to get quality research done without disrupting the routines that make for happy children, say field-working parents.

Masiello’s favourite piece of advice to hand down to young researchers is simply, “Marry well.” The key to a household that runs smoothly with minimal stress while a parent is away, she says, is for both partners to have loads of patience with each other and to put their family first. When Owen had the sniffles, they would forgo day care and instead take him to work and let him build forts under their desks. Similarly, Plante hops on a train at 4.30 each afternoon to pick up their two girls because his wife teaches evening classes. “With two people on the tenure track, both of us had to be willing to step in and pick up the pieces,” Masiello says.

And, just as importantly, they try not to keep score. ■

Kendall Powell is a freelance writer in Lafayette, Colorado.

REMUNERATION

Gender gaps

Last year, male scientists in the United States earned 20% more on average than did female scientists, according to a report by the US National Science Foundation in Arlington, Virginia. The *Survey of Doctorate Recipients* looked at salaries across academia, government, industry and the non-profit sector, and found that full-time scientists earn a median of US\$100,000, with men at \$110,000 and women at \$88,000. The disparity is probably because of institutional bias at the earliest career levels, says Janet Bandows Koster, chief executive of the Association for Women in Science in Alexandria, Virginia. She notes that salary differences compound as female scientists advance up the career ladder. Women “are getting a percentage increase based on a smaller amount”, she says.

GRADUATE EDUCATION

Cross-discipline focus

Identifying and providing funding, training and mentoring resources for graduate students who plan to conduct cross-disciplinary research are among the principles that graduate institutions in 14 countries aim to adopt. The US Council of Graduate Schools in Washington DC sponsored an annual summit this month in St John’s, Canada, on promoting best practices in graduate education, focusing on interdisciplinary research. “The questions that will advance human knowledge often lie at the boundaries of current disciplines, so interdisciplinary knowledge and ways of thinking are central to today’s doctoral education,” says council president Suzanne Ortega.

CAREER BREAKS

Wellcome re-entry

The Wellcome Trust, a biomedical-research charity in London, has published an online guide to help researchers return to the bench after career breaks. *Getting Back into Research After a Career Break* details various funding schemes to facilitate the move, and presents case studies of those who have returned to research. It also offers advice to potential returnees on finding mentors and identifying research niches. Shewly Choudhury, the trust’s basic careers portfolio adviser, says that “the guide is there to help people realize that it is possible to come back to the lab, and to offer advice on how to do it”.

POST-APOCALYPTIC CONVERSATIONS WITH A SIDEWALK

A trip to remember.

BY BETH CATO

Emma tripped, but the sidewalk caught her. As her bony hip and shoulder met the concrete, the surface beneath her softened to the texture of the foam pads she had once used for tumbling exercises in school.

"Oh dear! I'm terribly sorry. It seems my third panel developed an uplift of four millimetres. I do hope you're all right. Should I summon assistance?" The voice was young, female and perky — though not obnoxious in a morning-talk-show-host kind of way. The sound came from the sidewalk itself.

Emma lay still, breathing fast in shock from the words, not the fall. "You... the sidewalk, you talked?" Her voice was creaky with misuse. The surface hardened beneath her.

"Why, yes! I'm Cy Anara, the Friendly Sidewalk". Good morning. I apologize for the uplift that occurred while I was offline. It has now been corrected. Do you need emergency help?"

Emma rolled herself to a crouch and blinked tears from her eyes. How long had it been since she heard a human voice — even from a computer? She glanced around. The street was a ruin, like the rest of the city. A blackened sign read, '-OSPICE CARE'. That explained the modified sidewalk. Her own grandpa had died when a fall and hip fracture led to pneumonia.

"Can you summon emergency care?" she asked.

"Yes!" A pause. "Oh dear. It seems that the network is currently down. The response status is not listed, but I've queued your request."

"It was worth a try. How... how long were you offline?"

"It seems that I've been offline for seven months, five days and three hours. My average offline period is three hours, nine minutes."

No one had walked this way since the attack, then.

"I really am alone," she whispered. All alone here. Maybe in the country, the world. If the blasts hadn't killed them, the virus had.

"You're not alone. I will stay online as we await emergency responders."

How had the sidewalk's computer survived the EMP? Luck? Surely something like this hadn't been kept in a Faraday cage. She stroked the surface. It still felt like concrete but with the tiniest bit of give.

"Do you always talk to strangers?" A hysterical titter escaped her lips. She was talking! To a sidewalk!

"No one is a stranger to a Friendly Sidewalk!" said Cy. "I act as greeter for Twin Doves Hospice. I track a daily average of 53 residents and 22 regular guests to the facility. It's my hope that you'll become a regular, too!"

About half of the hospice had burned. Emma should investigate. She could always use more food and clothing for the stockpile, but she didn't want to move. She sprawled out on the sidewalk, quiet sobs shivering through her body, her backpack a heavy shell.

"I... I'd like to become a regular. Can you tell me about Friendly Sidewalks? How large an area do you cover right here?"

"My sensors are distributed across ten panels of sidewalk directly in front of Twin Doves Hospice. I take care of my residents.

As you're interested in Friendly Sidewalks, would you like to be sent an introductory document regarding our systems? We won't subscribe you unless you opt in!"

Ten panels. It'd be wonderful to bring the device home, but Emma had no idea how she would go about removing such an inlaid system. "You run on batteries? How... how much power do you have left?"

"Yes, I run on batteries! My current battery life will keep me online for one hour, 13 minutes. Oh dear. It seems I'm overdue for my annual maintenance. I have queried the network. The system is currently down, but I'm sure a technician will respond shortly." A pause. "It's been three minutes since I requested emergency care for you. I apologize. I'm querying them again."

"One hour, 13 minutes." Emma moaned against her fist. "Please God, no. I want to talk longer than that."

➔ NATURE.COM

Follow Futures:

🐦 @NatureFutures

🌐 go.nature.com/mtoodm

"I apologize for the limits of my battery. This should have been addressed in my

maintenance, but the problem is currently queued. I don't believe I heard a reply from you regarding more information on Friendly Sidewalks. Again, it's totally opt-in after the initial mailer!"

The sidewalk was cool against her cheek. Rough, porous, soothing. "Friendly Sidewalks. There are more of you?"

"Why, yes! I'm glad you asked. There are 12 Friendly Sidewalks within a 10-mile radius. We're currently hosting a scavenger hunt. If you visit all 12 locations, you get an eco-friendly water bottle! Please visit our site for the full rules and regulations."

Emma scrambled to sit and unzipped her backpack. She cracked open a notebook warped by rain and tears. "The locations? Can you tell me?"

"Of course!"

If this one had survived, maybe some of the others had, too. Maybe they had more juice in their batteries. She scribbled down the addresses and filled two pages. "How much battery life is left now?"

"One hour, five minutes remaining. The maintenance system is currently unresponsive. I've queried again. Do you still need emergency care?"

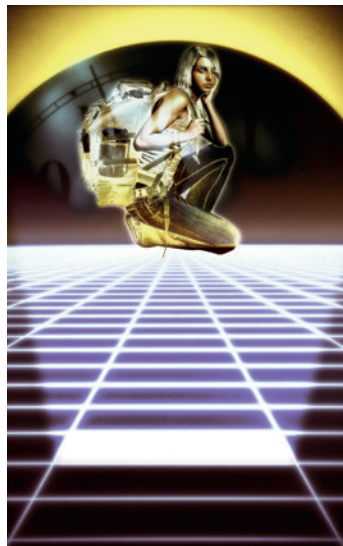
Yes. Emma stood. "No... I, I'm going to go now. I need to go. I can't... I can't use you up all in one shot. I'll be back tomorrow. I promise. I'll be a regular." She stepped into the gutter. "Bye."

"I'm glad we're friends! Good-bye, from Cy Anara, the Friendly Sidewalk!"

Silence.

Emma stared at the sidewalk for a few minutes and then hurried on, notebook in hand. Food could wait.

She had more friends to find. ■



JACEY

Beth Cato resides in Arizona. Her debut novel, *The Clockwork Dagger*, was released by HarperCollins Voyager US in September 2014. Her website is www.bethcato.com.